

FIELD OF SCIENCE - NATURAL SCIENCES

SCIENTIFIC DISCIPLINE - PHYSICAL SCIENCES

DOCTORAL THESIS

Electron States Confined in Electrostatic Quantum Dots Defined within Phosphorene

Author: Tanmay Thakur

Supervisor: Prof. dr hab. inż. Bartłomiej Szafran

Completed in: Faculty of Physics and Applied Computer Science

Abstract

Phosphorene, a two-dimensional form of black phosphorus, offers unique opportunities for quantum device applications due to its pronounced in-plane anisotropy. In this thesis, we investigate how this anisotropy influences electronic and spin properties in phosphorene quantum dots and rings, focusing on key phenomena such as Aharonov-Bohm oscillations (Chapter. 5), Wigner molecule formation (Chapter. 6), vortex structures (Chapter. 7), Nagaoka ferromagnetism (Chapter. 8), and electrical spin manipulation (Chapter. 9). Through a combination of theoretical modeling, configuration interaction methods, and time-dependent simulations (Chapter. 3), we capture the intricate many-body effects that emerge from strong electron-electron interactions. Our results show that anisotropy can significantly modify interference patterns, stabilize correlated electron configurations, and enable tunable spin states, suggesting new strategies for controlling quantum behavior in quantum dot systems. These findings, presented through a collection of five published articles, highlight phosphorene's potential as a platform for next-generation quantum devices, while also pointing to promising avenues for future research, including experimental validation. By demonstrating the feasibility of engineering anisotropy-driven phenomena, this work lays the groundwork for leveraging phosphorene's unique properties in a broad range of nano-electronic and quantum applications.

Streszczenie

Fosforen, dwuwymiarowa forma czarnego fosforu, oferuje unikalne możliwości zastosowań w urządzeniach kwantowych ze względu na wyraźną anizotropię w płaszczyźnie. W niniejszej rozprawie badamy, w jaki sposób ta anizotropia wpływa na właściwości elektronowe i spinowe fosforowych kropek kwantowych i pierścieni, koncentrując się na kluczowych zjawiskach, takich jak oscylacje Aharonova-Bohma (rozdział. 5), tworzenie molekuł Wignera (Rozdział.6), struktury wirowe (Rozdział.7), ferromagnetyzm Nagaoki (Rozdział.8) i elektryczna manipulacja spinem (Rozdział.9). Dzięki połączeniu modelowania teoretycznego, metod interakcji konfiguracyjnych i symulacji zależnych od czasu (Rozdział. 3), uchwyciliśmy skomplikowane efekty wielu ciał, które wyłaniają się z silnych oddziaływań elektron-elektron. Nasze wyniki pokazują, że anizotropia może znacząco modyfikować wzorce interferencyjne, stabilizować skorelowane konfiguracje elektronowe i umożliwiać przestrajalne stany spinowe, sugerując nowe strategie kontrolowania zachowania kwantowego w układach kropek kwantowych. Odkrycia te podkreślają potencjał fosforenu jako platformy dla urządzeń kwantowych nowej generacji, wskazując jednocześnie obiecujące kierunki przyszłych badań, w tym weryfikację eksperymentalną. Demonstrując wykonalność inżynierii zjawisk napędzanych anizotropią, praca ta kładzie podwaliny pod wykorzystanie unikalnych właściwości fosforenu w szerokim zakresie zastosowań nanoelektronicznych i kwantowych.

Acknowledgments

I would like to express my deepest gratitude to everyone who has supported me throughout my thesis journey. First and foremost, I am profoundly thankful to my supervisor prof. Bartłomiej Szafran, whose unwavering support and insightful guidance have been important in shaping this work. His readiness to provide opportunities for learning and his belief in my abilities have not only enriched my academic experience but have also helped me grow personally. His work inspires me and I am truly grateful for his encouragement in every single way. I would like to thank prof. Francois Peeters for the support, hospitality and possibility to work in Condensed Matter Theory Group at University of Antwerp. I also extend my thanks to prof. Diego Rabelo da Costa and prof. Andre Chaves for guidance and scientific discussions.

I must also extend my heartfelt thanks to Pragati who has been a constant pillar of strength for me. Her support and motivation have been invaluable and I will forever be grateful for her belief in me. My friends and colleagues, deserve special mention as well. The stimulating scientific discussions and collaborative spirit we shared have significantly enriched my research. Their willingness to engage in thoughtful debates and share their insights has broadened my understanding and pushed me to explore new ideas.

Lastly, I am immensely grateful to my family for their unwavering support and sacrifice. Their decision to support my studies abroad has opened doors to opportunities I could only dream of. Their constant encouragement and belief in my potential have provided the strong foundation needed to embark on and complete this journey. To everyone who contributed to this milestone in my life, thank you. Your support has been my constant inspiration, and I share this achievement with all of you.

More crucially, this work was supported by the National Science Centre (NCN) according to decision DEC-2019/35/O/ST3/00097. Research was partly supported by program "Excellence initiative - research university" for the AGH University of Krakow and Polish National Agency for Academic Exchange (NAWA) under program Zagraniczne Staże Doktorskie NAWA Preludium BIS 1 according to decision PP-N/STA/2021/1/00076/DEC/1. I gratefully acknowledge Poland's high-performance computing infrastructure PLGrid (HPC Center Cyfronet) for providing computer facilities and support within computational grant no. PLG/2024/017175.

Contents

Li	st of l	Figures	xi
1	Intr	roduction	1
2	Qua	antum Confinement	9
	2.1	Introduction to Quantum Confinement	9
		2.1.1 Quantum Confinement: Theory	9
		2.1.2 Quantum Confinement: Experiments	10
	2.2	A Review of Confined Systems	11
		2.2.1 Quantum Dots	11
		2.2.2 Quantum Rings	16
		2.2.3 Multiple Quantum Dots	18
3	Met	hodology	23
	3.1	Theoretical Model	23
	3.2	Configuration Interaction	24
	3.3	Time Dependent Calculations	27
4	Sun	nmary of Articles	29
	4.1	Aharonov-Bohm oscillations in phosphorene quantum rings: mass anisotropy compensa- tion by confinement potential	
		Thakur, T., & Szafran, B. Physical Review B, 105(16), 165309 (2022)	29
	4.2	Wigner molecules in phosphorene quantum dots	
		Thakur, T., & Szafran, B. Physical Review B, 106(20), 205304 (2022)	30
	4.3	Vortex structure in Wigner molecules	
		Thakur, T., & Szafran, B. Scientific Reports, 13(1), 9707 (2023).	31
	4.4	Nagaoka ferromagnetism in an array of phosphorene quantum dots	
		Thakur, T., & Szafran, B. Scientific Reports, 13(1), 18796 (2023).	32
	4.5	Electrical manipulation of the spins in phosphorene double quantum dots	
		Thakur, T., Peeters, F. M., & Szafran, B. Scientific Reports, 14(1), 18966 (2024)	33
5	Aha	ronov-Bohm oscillations in phosphorene quantum rings: mass anisotropy compensation	
	by c	confinement potential	35

6	Wigner molecules in phosphorene quantum dots	43
7	Vortex structure in Wigner molecules	57
8	Nagaoka ferromagnetism in an array of phosphorene quantum dots	73
9	Electrical manipulation of the spins in phosphorene double quantum dots	85
10	Summary & Conclusions	101
Bil	bliography	103

List of Figures

1.1	(a) An illustration of the phosphorene crystal structure with views from three axes and a 3d representation. The direction 'a' is the zigzag crystal direction, and direction 'c' is the armchair crystal direction. (b) Shows ADF-STEM image of black phosphorus depicting the puckered structure as in the illustration above. The image is reprinted with permission from Ref [21] by R. Wu <i>et.al.</i> Copyright 2015, American Vacuum Society	2
1.2	(a) The ARPES image depicting the band structure of bulk BP. The curvature of bands in ZT' and ZU direction is largely different. The experiment performed by L. Li $et~al.$ in Ref [1] and reproduced with permission from Springer Nature. (b) μ -ARPES image 2-layer showing anisotropy of bands. Images from Ref.[24]. Copyright 2023 Margot et.al. (Licensed under CC-BY 4.0). (c) The DFT-calculated (dashed lines) and GW-calculated (solid lines) band structures of monolayer black phosphorus. Reprinted with permission from Ref. [25]. Copyright 2014 by the American Physical Society. (d) Shows the PL spectra of BP for 1 to 5 layers, depicting the variability of bandgap with the number of layers. The spectra were obtained by Ref. [26] copyright 2015, Jiong Yang $et~al.$ (Licensed under CC BY-NC-SA 4.0).	3
1.3	(a) and (b) depict the plateaus in the resistance with voltage and magnetic field for a black phosphorus field-effect transistor (FET), the plateaus illustrate the quantum Hall effect in black phosphorus, revealing its true 2D nature. Reprinted (adapted) with permission from Ref. [27] by G. Long. <i>et al.</i> Copyright 2016 American Chemical Society	5
2.1	(a) A schematic of typical gated quantum dot device. Gate changes the confinement potential and source and drain leads are used to measure the quantum transport of the electron. Bottom part of schematic shows possible energy levels of the source, QD and drain. (b) SEM of a single QD device quipped with transport measurements fabricated using silicon nanowire by Angus <i>et al.</i> [33]. (c) Vertical architecture single QD in GaAs heterostructures by Kouwenhoven <i>et al.</i> [115]. (d) Single QD device with quantum point contact as means of measurements using GaAs based heterostructures by Vandersypen <i>et al.</i> [117]. (b) Reprinted (adapted) with permission from Ref. [33]; Copyright 2007 American Chemical Society. (c) Used with permission of IOP Publishing, Ltd, from Ref. [115]; permission conveyed through Copyright Clearance Center, Inc. (d) Reprinted from Ref. [117], with the permission from AIP Publishing.	12

LIST OF FIGURES xii

2.2	(a) Topography of the WSe_2/WS_2 moiré superlattice. (b) dI/dV maps of the Wigner crys-	
	tal formed at the filling factor of $n=2/3$ in the superlattice shown in (a). (c) Topography of	
	ultra clean bilayer graphene. (d) δI_{dc} maps showing the Wigner crystallization in the same	
	region as (c). (a,b) were reproduced with permission from Springer Nature from Ref. [76].	
	(c,d) were reproduced with permission from Springer Nature from Ref. [162]	15
2.3	(a) AFM image of QRs formed with help of Stranski-Krastanov growth model. (b) Micro-	
	graph of the quantum ring taken with the unbiased AFM-tip showing white oxide layer	
	'written' onto the surface creating depletion region in 2DEG underneath. (c) Transmission	
	electron microscope image of GaAs/AlAs core-multishell nanowires. (d) SEM image of a	
	closed-loop Aharonov Bohm interferometer depicting the gates to form the ring-form po-	
	tential minima for electron in 2DEG underneath. (a) Reprinted (adapted) with permission	
	from Ref. [195]. Copyright 2008 American Chemical Society. (b) Reproduced with permis-	
	sion from Springer Nature from Ref. [105]. (c) Reprinted (adapted) with permission from	
	Ref. [198]. Copyright 2018 WILEY-VCH Verlag GmbH & Co. KGaA, Weinheim. (d) Re-	
	produced with permission from Springer Nature from Ref. [190]	17
2.4	(a) Charge stability diagram obtained for double quantum dots in bilayer graphene. (b) A	
	closer look at the transport current plot as a function of left and right gate voltages illustrating	
	spin blockade phenomena. Inset shows the schematic of process at blue (\Diamond) and pink (+)	
	points. (a) Reprinted (adapted) with permission from Ref. [199]. Copyright 2020 American	
	Chemical Society. (b) Reprinted figure with permission from Ref. [200]. Copyright 2005 by	
	the American Physical Society.	19
2.5	(a) False-color SEM image of array of nine quantum dots with overlapping gate architecture	
	with three charge sensor QDs in undoped Si/SiGe heterostructures. (b) False-color SEM	
	image of the crossbar array device employing 16 coupled quantum dots with four charge	
	sensors in each corner of the array on Ge/SiGe heterostructures. (a) Reprinted figure with	
	permission from Ref. [103]. Copyright 2016 by the American Physical Society. (b) Figure	
	adapted from Ref. [104] (Licensed under CC BY).	19
2.6	SEM image of QD array device utilized to simulate and test the Nagaoka theorem with	
	real electrons. Inset shows the schematic of the array showing the relevant tunnel couplings	
	and on-site interaction parameters from Hubbard model. Reproduce with permission from	
	Springer Nature from Ref. [212]	21
3.1	Phosphorene crystal structure illustrated with the tight-binding hopping parameters given in	
	Table. 3.1	23

Chapter 1

Introduction

In the domain where quantum mechanics intersects with material science, two-dimensional (2D) materials present remarkable new properties. Among these atomically thin structures, phosphorene [1]—the monolayer form of black phosphorus—has emerged as a promising candidate for next-generation nanoelectronics. Its unique characteristics position it between the gapless graphene [2] and the wider-gap transition metal dichalcogenides, offering new possibilities for electronic and optoelectronic applications.

The isolation of the first graphene flakes in 2004 [2] transformed the landscape of material science, leading to the rapid emergence of a new frontier in this field. The fabrication of 2D materials opened novel lines of inquiry and exploration, as these materials exhibit properties fundamentally linked to their low dimensionality that are often absent in their bulk counterparts. The electronic structures of 2D materials can be significantly altered by external factors such as strain or electric fields. Many 2D materials exhibit direct band gaps, allowing for greater efficiency in optoelectronic applications. Quantum confinement to a plane leads to a modified density of states, which can enhance many-body effects. Surface effects, negligible in bulk, become dominant in 2D materials, profoundly affecting properties like chemical reactivity and electrical conductivity. In few-layer 2D materials, weak van der Waals interactions between layers allow for layer-dependent properties and facilitate the engineering of heterostructures. These unique characteristics of 2D materials indicate potential for both exciting new physics and novel applications across various technological domains.

This paradigm shift in material science, while largely driven by graphene's exotic properties, was also propelled by other newly discovered 2D materials in their monolayer forms. These include transition metal dichalcogenides (TMDs) [4–6] with stoichiometry MX₂ such as MoS₂ [3]; transition metal oxides [7] like MoO₃ [8, 10]; hexagonal boron nitride (h-BN) [9]; MXenes [11] and elemental 2D materials such as phosphorene, silicene [12, 13], germanene [14] and stanene [15]. Notably, MXenes, silicene, germanene, and stanene do not exist in layered bulk form in nature. These atomically thin layered materials are artificially synthesized on substrates via chemical vapor deposition or epitaxial growth. The stability issues [16, 17] and lack of free-standing forms in nature have limited the potential of these materials. Only stanene as a free-standing form [15], synthesized using an unconventional technique employing femtosecond laser ablation; and silicene in encapsulated form [13], synthesized with epitaxial growth have been reported. Black phosphorus, on the other hand, is the thermodynamically most stable allotrope of phosphorus and is demon-

strated to be air-stable for many days using encapsulation by h-BN or Al₂O₃ layers [18–20]. Thus, graphene and black phosphorus stand out as the only stable elemental 2D materials derived from naturally occurring layered solids, offering a unique platform for exploring fundamental physics due to their chemical simplicity compared to compound 2D materials like TMDs or hBN.

Black Phosphorus

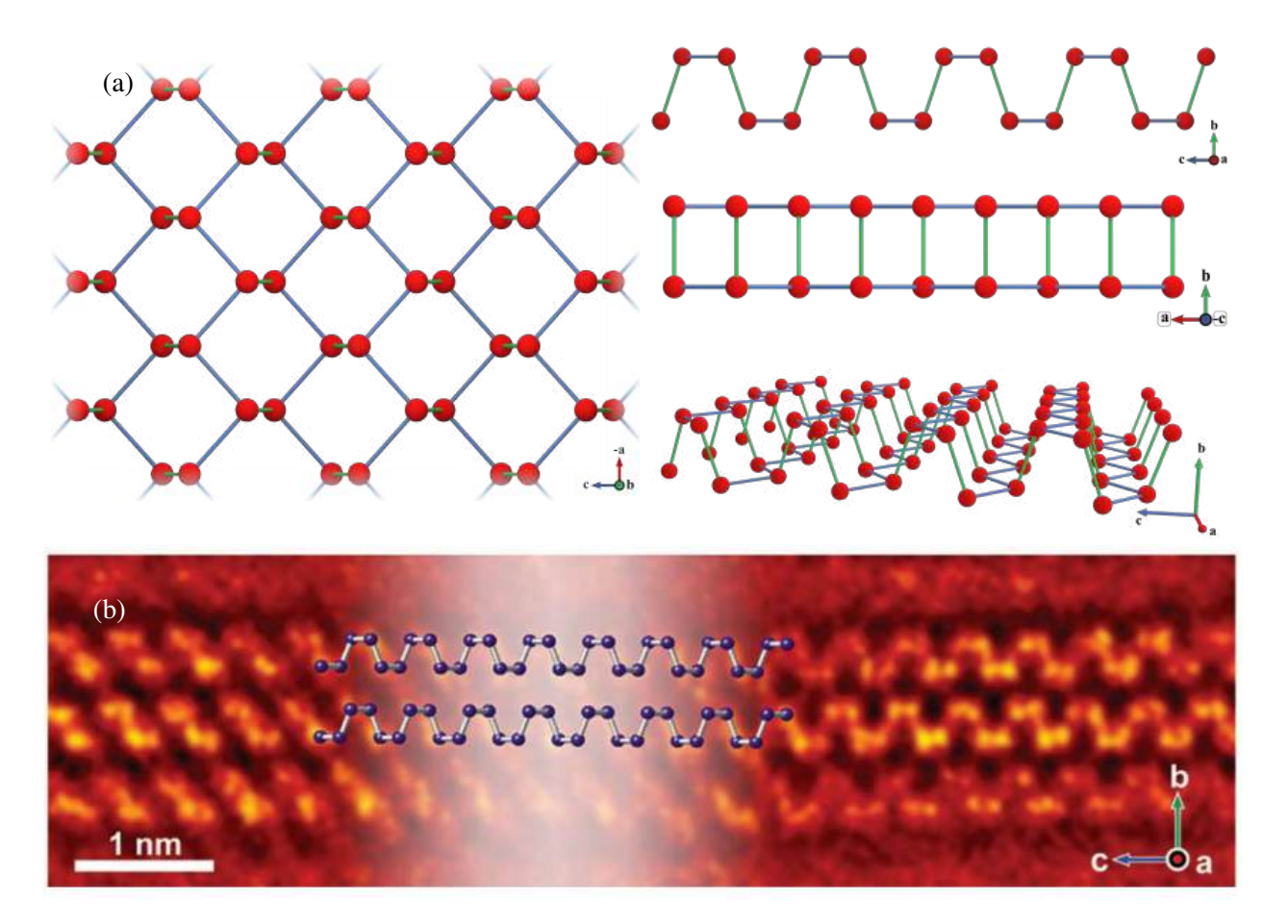


Figure 1.1: (a) An illustration of the phosphorene crystal structure with views from three axes and a 3d representation. The direction 'a' is the zigzag crystal direction, and direction 'c' is the armchair crystal direction. (b) Shows ADF-STEM image of black phosphorus depicting the puckered structure as in the illustration above. The image is reprinted with permission from Ref [21] by R. Wu *et.al.* Copyright 2015, American Vacuum Society.

The monolayer form of black phosphorus (BP), known as phosphorene, was first reported in theoretical and experimental studies in 2014 [1]. Unlike the planar structure of graphene, phosphorene forms a puckered honeycomb lattice. Atomic-resolution ADF-STEM of black phosphorus reported in Ref. [21] reveals its puckered crystal structure [See Fig. 1.1(b)]. In this structure, each phosphorus atom is sp³ hybridized and bonded to three neighboring atoms, resulting in a nonplanar configuration. Black phosphorus belongs to the 2D orthorhombic lattice system with in-plane lattice parameters of a ≈ 3.31 Å, $c \approx 4.34$ Å and an interlayer

distance, $b/2 \approx 5.4$ Å [21]. The crystal exhibits two distinct in-plane directions: zigzag and armchair, as illustrated in Fig. 1.1(a). In few-layer systems, the layers are stacked via van der Waals interactions, with each layer shifted relative to adjacent layers, forming an AB stacking arrangement [23].

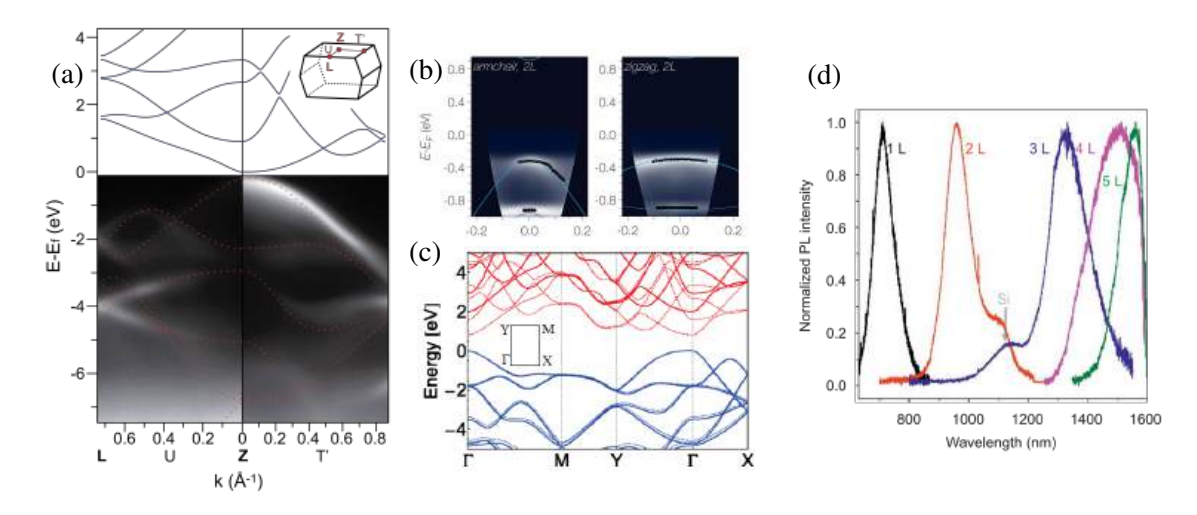


Figure 1.2: (a) The ARPES image depicting the band structure of bulk BP. The curvature of bands in ZT' and ZU direction is largely different. The experiment performed by L. Li *et al.* in Ref [1] and reproduced with permission from Springer Nature. (b) μ -ARPES image 2-layer showing anisotropy of bands. Images from Ref.[24]. Copyright 2023 Margot et.al. (Licensed under CC-BY 4.0). (c) The DFT-calculated (dashed lines) and GW-calculated (solid lines) band structures of monolayer black phosphorus. Reprinted with permission from Ref. [25]. Copyright 2014 by the American Physical Society. (d) Shows the PL spectra of BP for 1 to 5 layers, depicting the variability of bandgap with the number of layers. The spectra were obtained by Ref. [26] copyright 2015, Jiong Yang *et al.*(Licensed under CC BY-NC-SA 4.0).

This anisotropic crystal structure gives rise to highly anisotropic electronic, optical, and mechanical properties, making phosphorene a unique and fascinating candidate for both applications and fundamental physics studies, and setting it apart within the diverse landscape of 2D materials. The anisotropy is evident in the band structure of black phosphorus in two orthogonal reciprocal lattice directions reported using angle-resolved photoemission spectroscopy (ARPES) in Fig. 1.2(a). The potential and limitations of phosphorene can be contextualized by comparing it to other prominent 2D materials, viz. graphene, MoS₂, and h-BN. These materials span a spectrum of electronic behaviors—from semi-metallic zero gap graphene to wide gap insulator h-BN—with phosphorene and MoS₂ occupying intermediate positions as semiconductors.

Apart from h-BN with band gap of about 5.9 eV (bulk, indirect) to 6.1 eV (monolayer, direct), Table 1.1 shows key properties of other three materials as reported in several works. The experimental and theoretical works reveal that BP has a highly tunable direct bandgap (0.3-2.0 eV) and remains direct from monolayer to bulk forms unlike MoS₂. The tunability of the band gap with number of layers can be seen from the photoluminescence spectrum obtained by Yang *et al.* in Fig. 1.2(b) The wide range of direct band gap allows for efficient light emission and absorption, crucial for optical applications across a broad spectral range. The thermal conductivity of both materials is of similar orders, nevertheless, much lower than that of graphene, but phosphorene shows a large anisotropy in the conductivity depending on the crystal direction.

Property	Black Phosphorus	Graphene	MoS_2
Lattice Structure	Orthorhombic (cmce)	Hexagonal (P6 ₃ /mmc)	Hexagonal (P6 ₃ /mmc)
Electronic Structure	Semiconductor	Semimetal	Semiconductor
Bulk Bandgap	0.3 eV (Direct) [25, 36]	0 eV	1.29 eV (Indirect) [3]
Monolayer Bandgap	1.1-2.0 eV	0 eV	∼1.9 eV
	(Direct) [25, 36, 37]		(Direct, few layers) [3]
Mobility (cm ² /Vs)	~1000 (10 nm, RT) [1]	~200,000	79 (few-layer, RT) [58]
	200-300 (5 nm, RT) [36, 38]	(suspended) [50]	100 (20-30 nm) [59]
	4000 (1.5 K, ~10 nm) [18]	2,000-5,000	40 (35 nm) [60]
	Theoretical:	(on substrate) [9]	130 (theoretical) [61]
	10,000-26,000 [39]		
Thermal Conductivity	Zigzag: ∼40	$(4.84 \text{ to } 5.3) \times 10^3 \text{ [51]}$	~52 (few-layer) [62]
$(W m^{-1} K^{-1})$	Armchair: ∼20		44-50 (4-layer)
	(>15 nm) [40]		48-52 (7-layer) [63]
	Zigzag: ∼86		
	Armchair: ∼34		
	(>100 nm) [41]		
	Zigzag: 30.15		
	Armchair: 13.65		
	(theoretical, monolayer) [42]		
Electrical Conductiv-	Up to 250 (< 20 nm, RT) [38]	$\sim 1.46 \times 10^4$	$(1.3 - 2) \times 10^{-5}$
ity (S/cm)		(graphene on Cu) [52]	[58, 64]
Seebeck Coefficient	~335 (bulk, RT) [43]	~100	-400 to -100,000
(μV/K)	\sim 175 (monolayer, theory) [44]	(monolayer, RT) [53]	(monolayer) [65]
			Up to 250 (monolayer,
			RT)
			Up to 550 (few-layer,
			RT) [66]
Spin-Orbit Coupling	Armchair: 1.7	27.26×10^{-3} [54]	0.27 to 2.5
(meV·Å) (Theory)	Zigzag: 14	(at 50/300 V/nm)	$(MoS_2 / Bi_2Te_3$
	(at electric field 2.6 V/cm) [45]	0.106×10^{-3} [55]	heterostructures,
	Armchair: -1.79	(at 50/300 V/nm)	intrinsic field) [67]
	Zigzag: 1.03		
	(at electric field 0.1 V/cm) [46]		
Exfoliation Energy	22 [47]	21 [47]	18 [47]
(meV/Å ²) (Theory)			
Current On/Off Ratio	$\sim 10^5 (6.5 \text{ nm, RT}) [1]$	no real 'off' state	upto 2.1 ×10 ⁷ [68, 69]
	$\sim 2 \times 10^3$ (6-10 nm, RT) [48]	100 (bilayer, RT) [56]	
	$\sim 1 \times 10^7 \ (< 8$ nm, RT) [49]	70 (nanoribbon, RT) [57]	

Table 1.1: Comparison of key properties for phosphorene, graphene, and MoS_2 . RT: Room temperature, all values from experiments unless mentioned otherwise

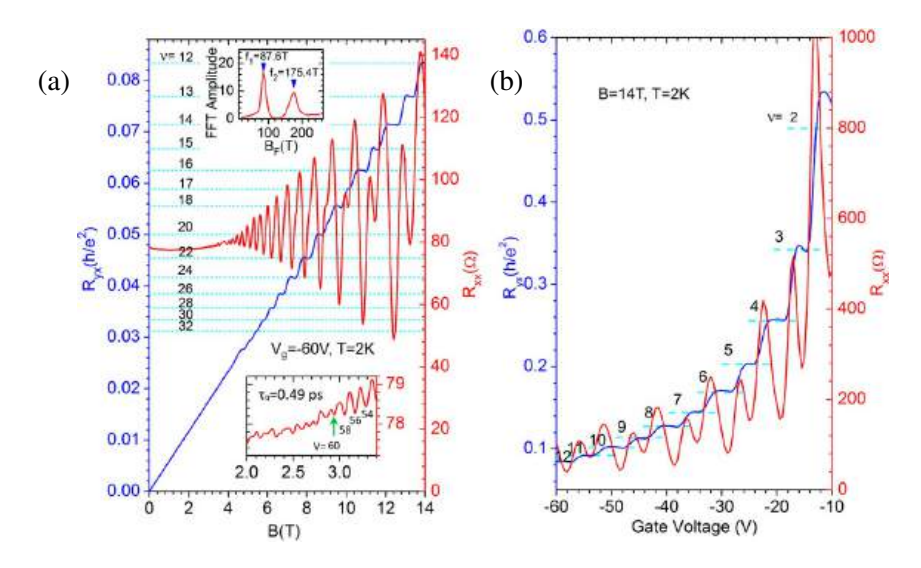


Figure 1.3: (a) and (b) depict the plateaus in the resistance with voltage and magnetic field for a black phosphorus field-effect transistor (FET), the plateaus illustrate the quantum Hall effect in black phosphorus, revealing its true 2D nature. Reprinted (adapted) with permission from Ref. [27] by G. Long. *et al.* Copyright 2016 American Chemical Society.

This anisotropy can be exploited in applications where directional heat flow is required, which is not possible using MoS_2 or graphene.

The band extrema at Γ point (see Fig. 1.2) is not exactly parabolic in both planar directions, leading to anisotropic effective masses. Consequently, all the characteristic lengths associated with phosphorene will also be anisotropic. The thermal de Broglie wavelength [81] and Thomas-Fermi screening length [82–85] change with anisotropy and reduced dimensionality. Theoretical calculations have shown the effective masses of phosphorene to exhibit strong anisotropy with $m_{zz}/m_{ac}=7.75$ [77], 6.59 [39], 5.1 [74]; and experimentally extracted $m_{zz}=0.9m_e$ and $m_{ac}=0.18m_e$ with ratio $m_{zz}/m_{ac}=5.0$ for 4-layers of black phosphorus [25]. As an example, at temperature of 4K, and with the effective masses $m_{zz}=0.85m_e$ and $m_{ac}=0.17m_e$ [75] (notably much larger than isotropic effective mass of GaAs), the thermal de Broglie wavelengths for phosphorene would be $\lambda_{ac}\approx 90$ nm in armchair direction and $\lambda_{zz}\approx 40$ nm in zigzag direction. These effects in the phosphorene significantly influence the transport properties, many-body effects and quantum interference phenomena, as can be seen from the properties in Table 1.1 and further chapters of this thesis.

For electronic applications, phosphorene demonstrates promising characteristics for field-effect transistors (FETs). Its high carrier mobility ($\sim 1000~\rm cm^2/Vs$ for 10 nm samples) approaches that of graphene on substrate while maintaining a significant bandgap, which is crucial for achieving high on/off ratios (10^5). This combination addresses the limitations of graphene's lack of bandgap and MoS₂'s lower mobility. In 2019, long-term air-stable FETs made using black phosphorus, approaching the ballistic limit were reported [22, 49]. While phosphorene transistors show promising potential, there's still room for improvement to match the best silicon devices. However, phosphorene's performance is already within a useful range for many applications. Phosphorene's electrical conductivity (up to 250 S/cm for thin flakes) and moderate Seebeck coefficient ($\sim 335~\mu V/K$) also suggest potential for thermoelectric applications. In the quantum regime,

the anisotropic extrinsic Rashba spin-orbit coupling provides a platform for spin-based quantum information processing, where the strong anisotropy offers a unique opportunity for engineering qubits with novel characteristics, as will be discussed in this thesis. Additionally, the gated system made of BP has been reported to exhibit quantum Hall effect, with Landau level filling factor observed up to $\nu=2$ [27] as shown in Fig. 1.2(c, d). There have even been reports of fractional quantum Hall effect in BP indicating that electrons are strongly interacting and that the material can host topological states and superconductivity [28]. The underlying physics in phosphorene is very rich, and experiments can reveal new quantum phenomena.

As we move from bulk to 2D materials, quantum confinement effects become increasingly prominent, giving rise to new and intriguing physics with potential applications. An even more confined form of black phosphorus appeared as nanocrystals or quantum dots (QDs). These nanocrystals have already enhanced the material's optoelectronic properties to produce highly efficient blue light-emitting elements [29, 30]. The exceptional performance of phosphorene in FETs, coupled with the enhanced properties observed in more confined nanostructures, naturally directs research towards even greater confinement in the form of quantum dots. The dots, functioning as artificial atoms, represent the maximum degree of electronic confinement and provide an ideal platform for studying quantum phenomena and developing quantum technologies.

Motivation of the thesis

While nanocrystal QDs have shown promise, gate-defined quantum dots offer additional advantages for precise quantum state manipulation. Electrostatic quantum dots, created through local electrostatic potential or gates, similar to FETs, have been shown to exhibit extraordinary properties in some materials like MoS₂ [31], WSe₂ [32], intrinsic silicon [33], carbon nanotubes [34], and various other 2D materials [35]. These gate-defined quantum dots offer an ideal platform to further exploit phosphorene's unique electronic properties at the nanoscale, as they have an advantage over the ensemble of nanocrystal QDs through their ability for precise control and measurements. Nanocrystal QD ensembles, due to their size distribution, as seen in Ref. [29], can be studied using optical spectroscopy. However, they suffers from inhomogeneous broadening, which limits the measurement precision. On the other hand, transport spectroscopy on the gated electrostatic QDs [31–35] is performed on a single dot. In the weak coupling limit, this technique resolves the spectra, including the excited states with the precision down to a fraction of a μ eV. This method determines the gate voltages for which the confined chemical potentials align the transport window, defined by the chemical potentials of the source and the drain. Furthermore, the charging diagram, particularly as a function of the external magnetic field, provides insights into the single-electron spectra, the evolution of the confined system from zero magnetic field to integer and fractional quantum Hall regime, electronelectron interactions, spin interactions, and the coupling of separate QDs to form artificial molecules. These high-precision measurements and charging diagrams are crucial for accurately determining energy levels, studying complex quantum interactions, and observing subtle quantum effects, all of which are essential for developing quantum technologies and understanding quantum phenomena in phosphorene.

At the start of this PhD project, there was no literature addressing properties of quantum dots defined in phosphorene by electrostatic potential, albeit a large attention was attracted by nanoflakes in spite of the fact that the gating technology for phosphorene transistors was already mature. This PhD research aimed

to provide a theoretical description of the electron states confined in electrostatic quantum dots in phosphorene, with special attention paid to the effects of the effective mass anisotropy. The anisotropy of the conduction band leads lowers the symmetry of states confined in radially symmetric systems and is relevant for e.g. Quantum rings and Aharonov-Bohm oscillations in the ring-like confinement. The heavy electron effective masses can enhance the electron-electron interactions and produce strongly correlated states that can be discussed in the context of Wigner molecules and fractional quantum Hall states. Crystal anisotropy enables charge density distribution in the Wigner phase in real space to be studied using the scanning probe techniques [76]. Additionally, the electron-electron interactions can also be tuned and manipulated by adjusting the orientation of QDs in space with gates. Such tuning can optimize certain properties of interest, for example, Nagaoka ferromagnetism in QD array or induce Wigner crystallization with a specific orientation. The ttransport spectroscopy provides precise measurements to study spin-orbit interaction effects and the anisotropy can be utilized for engineering QD qubits with properties tunable with orientations.

Chapter 2

Quantum Confinement

In this chapter, we review the fundamental theoretical concepts and the quantum confined systems that we consider for our subsequent investigations in phosphorene. To establish concrete foundation for the concepts and terminologies which will be used for the rest of this PhD thesis, we begin by briefly discussing the idea of confinement, a fundamental principle that plays an important role in understanding the quantum properties of low-dimensional materials.

2.1 Introduction to Quantum Confinement

2.1.1 Quantum Confinement: Theory

A state of a system in quantum physics is represented by the wavefunction $\psi(q)$ (q denotes set of coordinates), with the quantity $|\psi(q)|^2 dq$ being the probability to find the system in the volume element dq. Now, if for $q \to \infty$, $|\psi(q)|^2 \to 0$ i.e. the system cannot extend to infinity—the state of the system is said to be a bound or confined.

The number of bound states depends on the potential shape. Infinite wells support infinite bound states, while finite wells allow only a limited number. In atoms, the Coulomb potential, 1/r, supports an infinite number of bound states, as do potentials that vanish asymptotically as $\sim r^{-s}$ with s < 2 [78]. In contrast, quantum dots with electrostatic confinement lack singularities and have rapidly vanishing potentials, leading to only a finite number of bound states. This distinction is crucial for designing quantum devices, affecting available energy levels for quantum state manipulation and spectroscopy. Despite of the fundamental differences in confinement of atoms and quantum dots, both exhibit discrete energy levels, shell structure, strong interactions and excitation properties from external fields, hence quantum dots are aptly referred to as the artificial atoms.

Although the principles of quantum confinement are similar to those in atomic systems and other text-book examples, their behavior in solid-state environments introduces additional complexities due to the underlying crystalline medium. The periodic potential of a perfect lattice in the material modulates the free particle wavefunction of the electron resulting in the 'Bloch states'. The confinement potential is then acting on these Bloch electrons with modified momentum and the effective mass. The energy scale of the potential created by a lattice of atomic nuclei typically ranges from 1-10 eV, whereas the scale of confinement poten-

tial introduced by gating is on the order of few hundred meV. Also, the size of the artificial confinement is much larger than the periodicity of the crystal.

The continuum of the energies available to a free electron is replaced by a few discrete levels or bands of nearly continuous energies. Meanwhile, the parabolic dispersion curve is also is modified depending on the material's properties. These distinct electronic structures and carrier distributions in different material classes significantly influence the behavior under quantum confinement. In metals, where the Fermi energy lies within the band, the free electron density is very high ($\sim 10^{23}~{\rm cm}^{-3}$) [79], resulting in short Thomas-Fermi screening length(\sim Å) making the electrostatic confinement very difficult. On the other hand in insulators, the large band gap prevents the availability of mobile carriers in the conduction band for confinement. Semiconductors, with their Fermi level in the band gap and moderate carrier densities, have an ideal setting for electrostatic quantum confinement. The relatively small density of carriers can be effectively manipulated by external fields, and the generally parabolic band structure near extrema allows for well-defined confined states.

Constraining a quantum system to a 2D plane instead of a three-dimensional space induces significant changes in confinement. In bulk materials, the density of states, g(E), can be evaluated within the nearly free electron approximation framework. The change in dimensionality is clearly reflected in the energy dependence of the density of states. For a 3D system, the dependence is given by $g_{3D}(E) \sim E^{1/2}$, while for 2D materials like phosphorene, $g_{2D}(E) \sim \Theta(E-E_n)$ where Θ represents the Heaviside step function at subband energies E_n , for a nanowire $g_{1D}(E) \sim (E-E_{n,m})^{-1/2}\Theta(E-E_{n,m})$ and for confined system like quantum dot $g_{0D}(E) \sim \delta(E-E_{n,m,l})$ [80].

Phosphorene's anisotropic masses [75] further increase the complexity of the problem by breaking symmetry and influence various physical properties. Together with the low dimensionality and anisotropy, quantum confinement in phosphorene leads to various interesting and unique results which will be discussed later in later sections of this thesis.

2.1.2 Quantum Confinement: Experiments

While the theoretical understanding on the confinement is necessary, it is not sufficient. The ultimate determining factors for quantum confinement arise from experimental design and implementation constraints. Material imperfections, particularly point defects, introduce local potential perturbations that significantly modify the electronic structure [86–88]. Even an isolated point defect is expected to impact switching in ferroelectric devices [89], while structural defects in 2D materials can substantially alter their intrinsic properties [90]. Along with the effects from the imperfections and defects in the crystal of target material, the environmental factors such as temperature [91] and mismatch effect [92] can induce strain perturbing the band structure. The gates and the material can induce a charge fluctuations, which alters the confinement potential by adding noise to the ideal static potential [93, 94]. The design and the scale of confinement are governed by the geometry of the gates and dots, their capacitance and the tunnel resistance [95]. Measuring different properties of a quantum dot requires transport spectroscopy [96–99], which comes with its own limitations. Consequently, the design of quantum confinement must also adhere to the constraints imposed by transport spectroscopy measurements.

Nevertheless, many of these limitations can be effectively managed, making it possible to experimentally realize single quantum dot [99], double dots [100–102], an array of dots [103, 104] or even a non-elementary ring-shaped confinement [105] (of the order of hundreds nm) experimentally. Beyond the mere possibility of confinement, experimental techniques in this field have matured over many years, making them a well-established tool rather than a barrier to studying quantum confinement in phosphorene. Therefore, throughout this PhD thesis, it is assumed that experimental techniques can generally be figured out and the focus of this thesis is purely on the theoretical understanding of the physics involved in confinement in phosphorene. In many cases, this understanding remains valid at the quantum scale of the dot, irrespective of its exact dimensions.

2.2 A Review of Confined Systems

2.2.1 Quantum Dots

As discussed earlier, a quantum dot is equivalent to an artificial atom where the motion of electron or the where particle motion is restricted in all spatial dimensions through a confining potential. In 2D materials like phosphorene, where carriers are inherently planar, additional confinement is achieved via nanostructure fabrication or electrostatic gating, or a combination of both. Nanoflakes (~ 5nm) are widely studied [30, 106–114] and are relatively easy to fabricate; but limit precise quantum state control, typically requiring ensemble optical spectroscopy, where inhomogeneous broadening reduces accuracy. In contrast, electrostatic gating enables precise control and high-resolution transport spectroscopy, making it ideal approach for investigating rich physics introduced by phosphorene's anisotropic effective masses.

Gate-defined electrostatic quantum dots, typically fabricated with characteristic dimensions of \sim 100nm, function as artificial charge containment systems for conduction band electrons. As these charge islands are further reduced in size by manipulating the confinement potential, the capacitance, C, reduces to a very small value (about 10^{-3} pF), thereby increasing the energy cost of adding the extra electron to the charge container. At this stage, if the charging energy exceeds the thermal energy of the electrons, i.e. $e^2/C \gg k_B T$, the system enters the Coulomb blockade regime—a quantum mechanical state where electron occupation remains constant and isolated from environmental electrons. This phenomenon forms the fundamental basis for precise measurement and control of single-electron states in gate-defined quantum dots.

The experimental investigation of these systems is usually conducted through tunneling, precisely controlled through capacitive coupling to metallic gates. A prototypical experimental configuration uses a transistor-like geometry using source and drain electrodes for transport measurements, complemented by gate electrodes for potential modulation as shown in Fig. 2.1(a). The confinement potential is induced in the material via the gate structures, while the transport properties are generally measured through current flow in source and drain gates. The discrete nature of the QD energy levels manifests in suppressed current through the source-QD-drain channel until sufficient source-drain bias is applied to overcome the energy level difference. Through careful engineering of tunnel barriers, single-electron tunneling can be achieved,

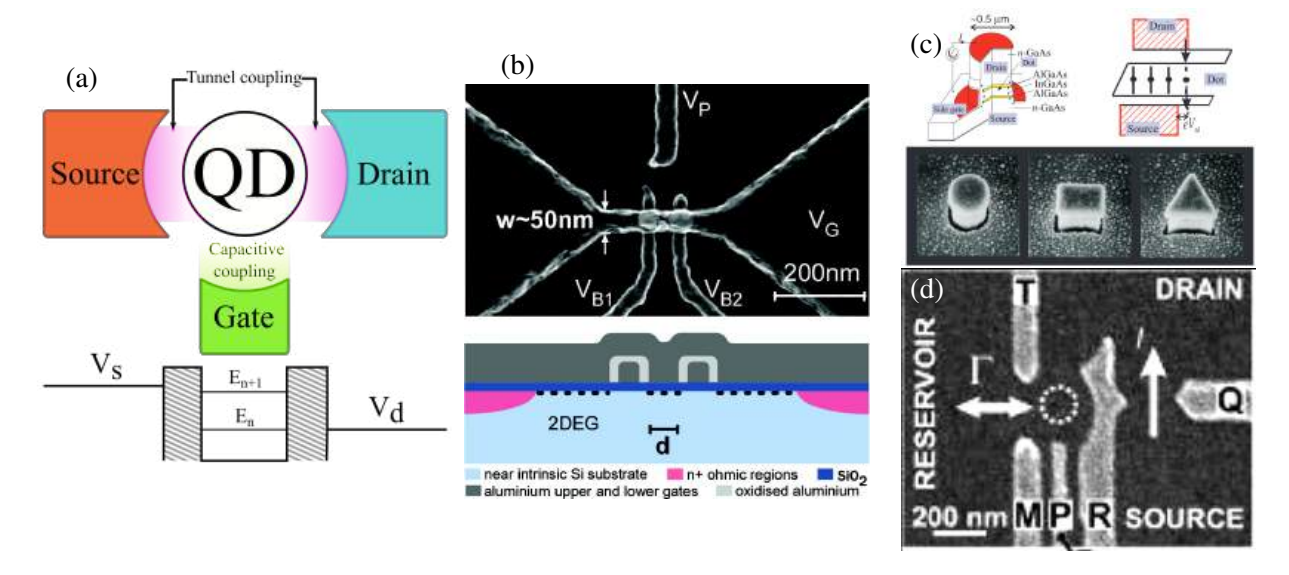


Figure 2.1: (a) A schematic of typical gated quantum dot device. Gate changes the confinement potential and source and drain leads are used to measure the quantum transport of the electron. Bottom part of schematic shows possible energy levels of the source, QD and drain. (b) SEM of a single QD device quipped with transport measurements fabricated using silicon nanowire by Angus *et al.* [33]. (c) Vertical architecture single QD in GaAs heterostructures by Kouwenhoven *et al.* [115]. (d) Single QD device with quantum point contact as means of measurements using GaAs based heterostructures by Vandersypen *et al.* [117]. (b) Reprinted (adapted) with permission from Ref. [33]; Copyright 2007 American Chemical Society. (c) Used with permission of IOP Publishing, Ltd, from Ref. [115]; permission conveyed through Copyright Clearance Center, Inc. (d) Reprinted from Ref. [117], with the permission from AIP Publishing.

enabling precise control over electron occupation down to the few-electron regime. A much detailed review on the theory of quantum dots for transport spectroscopy can be found in Ref. [95, 115].

The prototypical tunneling measurement shown in Fig. 2.1(b) can be implemented experimentally in various ways. Few of the experiments which employed gated quantum dots largely similar to the schematic is shown in Fig. 2.1. Angus *et al.* [33] fabricated a single gated quantum dot using silicon nanowire, scanning electron microscopy (SEM) micrograph of such a device is shown in Fig. 2.1(a). Here, electron motion is restricted to one dimension and further confined by barrier gates V_{B1} and V_{B2} , forming the quantum dot. The dot's occupation and potential are controlled via the plunger gate V_P and the connecting gate V_G , while transport measurements are conducted by varying the source-drain bias. A similar but more intricate setup was designed for forming a quantum dot in suspended bilayer graphene [116]. Both of these serve as examples of quantum dot devices with lateral geometry. In contrast, an equivalent setup can be formed with vertical geometry as demonstrated by Kouwenhoven *et al.* [115] with GaAs heterostructures shown in Fig. 2.1(c). The general principles of the measurements remain exactly the same as those for lateral geometry. The SEM images at bottom of Fig. 2.1(c) illustrate the control over the shape of the dots created using gating techniques. The current measurements in the transport spectroscopy discussed affect the quantum state of the dot. A much favorable type of measurement can be done using quantum point contact [117], wherein the measurement is done in form of charge sensing. SEM of one such experiment on GaAs het-

erostructures is shown in Fig. 2.1(d). The gates T, M, and R define the the quantum dot (shown as dotted circle), gates R and Q make a quantum point contact and the gate P is the plunger gate. All these experiments demonstrate the maturity of technology involved in fabricating gated quantum dots and the possibility to perform such experiments based on phosphorene.

Transport spectroscopy in electrostatically defined quantum dots provides high-precision insights into quantum confinement, probing both single-particle and many-body states. With energy resolution down to the μ eV scale, it advances fundamental quantum physics and material-specific studies. Excited state spectroscopy through transport measurements has provided detailed maps of quantum dot energy levels for 1 to 12 electrons in a single dot, analyzing both single-particle and collective excitations through singlet-triplet transitions, as well as spin polarizations and Hund's rule for QD [118]. A spin in the quantum dot acts as a magnetic impurity and couples with electrons in the leads, enabling direct observation of the Kondo effect (manifested as conductivity in the zero-bias regime) in various flavors [119, 120]. The ability to achieve near complete control over the spin of individual electrons paves the way for investigating single-spin dynamics in solid-state environments [121]. Beyond spin degrees of freedom, gated quantum dots enable precise manipulation and readout of valley states as well as the valley-orbit and valley-spin coupling in the system [122–126]. The spin qubit formed in a gated quantum dot can be benchmarked and utilized for phase-sensitive coherence measurements, facilitating the creation of high-fidelity quantum gates with superior performances [127–129]. Specially designed and biased quantum dots can also function as nanoscale charge-sensing devices [130, 131]. Additionally, quantum chaotic systems can be studied within quantum dots [132-135]. The quenching of kinetic energy in magnetic field, along with electron occupation control, allows the electrostatic quantum dots to reveal the effects of strong correlation effects and many body physics, including fraction quantum Hall effect and Wigner crystallization at a finite scales [136–140].

In this thesis, we specifically study theoretically strongly correlated state of Wigner molecules, a finite form of Wigner crystallization and also the vortex structure in these Wigner molecules inside quantum dot. The high anisotropic mass and anisotropy of phosphorene is expected to reveal rich physical phenomena, with gating techniques increasing feasibility of observing these theoretical results in experiments. We will now discuss the Wigner molecules and vortex structures in phosphorene quantum dot.

Wigner Molecules

Electron-electron interactions often dictate a material's electronic properties, sometimes beyond single-particle band theory. While weak interactions allow a quasiparticle description, strong interactions induce complex phenomena, altering electronic, magnetic, and structural behavior. For instance, various kinds of exchange interaction along with repulsion between the electrons in material can lead to ferromagnetic, antiferromagnetic, ferrimagnetic or even exotic phases like skyrmions and spiral orders [144–149]. In certain rare-earth compounds, strong interactions between localized and conduction electrons can lead to the formation of heavy fermions, where quasiparticles acquire a thermal effective mass on the order of 1000 times the bare electron mass [150, 151]. Additionally, strong correlations can result in the fractionalization of electron charge and spin, leading to novel quantum states [152, 153]. Moreover, in narrow-band materials, strong on-site Coulomb repulsion can induce Mott insulating behavior, where electron localization prevents

conduction despite a partially filled electronic band [154, 155]. In contrast, at low electron densities, long-range Coulomb repulsion can dominate kinetic energy, resulting in Wigner crystallization, where electrons arrange themselves into a periodic lattice to minimize energy [156–159]. In 3D, strong interactions give rise to emergent states like heavy fermions and Mott insulators. Lower dimensions enhance interactions, leading to fractional quantum Hall states and Wigner crystallization (for low densities) in 2D, and spin-charge separation in 1D Luttinger liquids. In a quantum dot, where the electron interactions are the strongest, the opportunity to study these emergent phenomena is presented.

Wigner crystallization occurs in low density electron systems where the electron electron interaction energy is higher than the Fermi level. The onset of such crystallization is characterized by the dimensionless Wigner-Seitz radius, r_s , which must exceed a critical value of approximately 37 (in atomic units) to ensure sufficiently low electron density [160, 161]. However, observing a true Wigner crystal in real materials is extremely challenging due to multiple disruptive factors. Quantum and thermal fluctuations destabilize the long-range order necessary for crystallization, while impurities, defects, and disorder can further disrupt Wigner ordering by pinning electrons in random positions rather than allowing them to form a well-defined lattice. Additionally, background charge screening from the lattice or surrounding electron gas weakens Coulomb interactions, reducing the tendency for crystallization. Imaging 2D Wigner crystals is challenging because the measurement technique must balance high spatial resolution, single-electron sensitivity, and minimal disturbance to the electron lattice. The high sensitivity requires strong coupling to the crystal, while low perturbation demands weak coupling, creating a trade-off between the two. Nevertheless, electrons in a moiré superlattice can have sufficiently large charge density variations to be observed using STM with graphene sensing layer and has been observed only recently in 2021 by Li et al. [76]. Fig. 2.2(a) shows the topography image of the moiré superlattice formed using the WSe₂/WS₂ heterostructures underneath graphene monolayer. Likewise, Fig. 2.2(b) shows the dI/dV maps of the Wigner crystal formed at the filling factor of n = 2/3. These electron crystal structures are shaped by a moiré superlattice potential that traps electrons rather than the crystallization due to repulsion which can form even in absence of a periodic potential.

Therefore, direct observation of Wigner crystal had not been ideally realized during this stage of the PhD work. Only recently in 2024, after this PhD's work on Wigner molecules, Tsui *et al.* finally directly observed the Wigner crystal states with the predicted triangular lattice independent from the underlying lattice [162]. Fig. 2.2(c) shows the topography of the underlying lattice of ultra clean bilayer graphene, while Fig. 2.2(d) shows spatially resolved tunneling current modulation δI_{dc} within the same area clearly indicating Wigner crystal structure.

Gated quantum dots offer a more feasible opportunity to explore strong electron interactions by enabling the study of Wigner crystallization in its finite form, i.e. Wigner molecules. The ability to tune both the dot size and electron occupation in a QD makes it possible to achieve the low-density criterion required for Wigner ordering. In QDs with an isotropic effective mass, the confined charge density mirrors the symmetry of the confinement potential. So for these circular QDs, the Wigner phase only occurs in inner coordinates of the dot. Along with this, quantum fluctuations and charge sensitivity pose challenges for direct observation of electron density in quantum dots. Nevertheless, gated quantum dots show signatures of spatially correlated

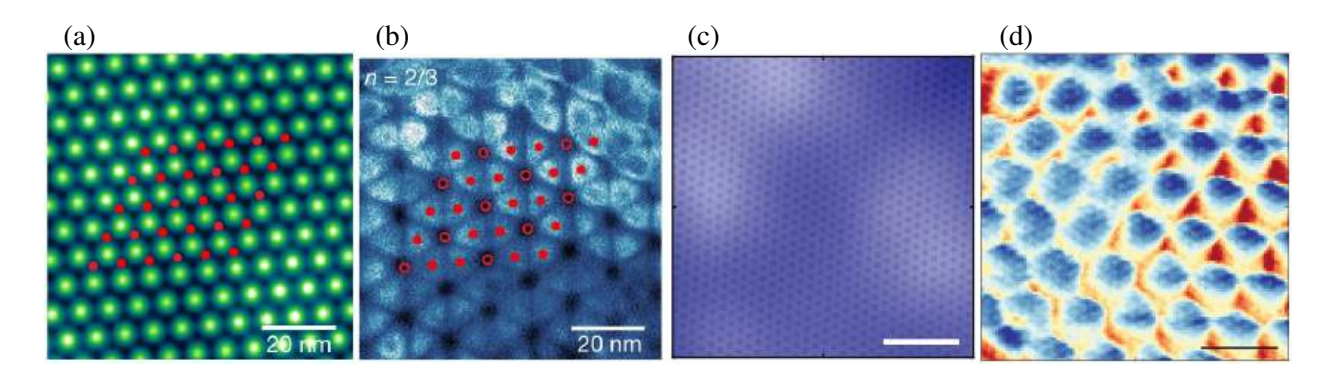


Figure 2.2: (a) Topography of the WSe_2/WS_2 moiré superlattice. (b) dI/dV maps of the Wigner crystal formed at the filling factor of n=2/3 in the superlattice shown in (a). (c) Topography of ultra clean bilayer graphene. (d) δI_{dc} maps showing the Wigner crystallization in the same region as (c). (a,b) were reproduced with permission from Springer Nature from Ref. [76]. (c,d) were reproduced with permission from Springer Nature from Ref. [162].

states in the excitation spectra [163] and lower symmetry Wigner molecules are predicted to appear in laboratory frame [164, 165].

The effective mass of electron in phosphorene [75] is much larger than that of electrons in 2DEG fabricated with commonly used GaAs heterostructures [165]. The higher effective mass resulting in stronger correlations and anisotropy lowering the symmetry. Both these favorable conditions are naturally fulfilled by gated quantum dots in phosphorene. We therefore examine the circular and rectangular confinement potential of the quantum dot for various number of electrons and predict the observation of Wigner molecules in laboratory frame along with the clear spectral signatures within the transport spectroscopy resolutions. Later in 2024, using the moiré superlattices with twisted WS₂, a crystal made of Wigner molecules was directly observed [166].

Vortices in FQHE

Wigner molecules are an emergent correlated state in confined geometries purely driven by Coulomb interaction. As strong magnetic fields are applied to these electron arrangements, the system transitions from purely Coulomb driven spatial ordering to a regime where both interaction and magnetic effects interplay. At sufficiently high magnetic fields, the kinetic energy is quenched to the lowest Landau level, and the strongly correlated electrons in Wigner molecules begin to exhibit fractional quantum Hall characteristics. QDs provide a perfect chance to study these interplay of magnetic field and Wigner crystallization in a controlled, measurable environment.

The integer quantum Hall effect (IQHE) occurs when a two-dimensional electron gas is subjected to a strong perpendicular magnetic field at low temperatures, leading to quantized Hall conductivity [167]. The system's energy levels (Landau levels) are quantized as $E_n=\hbar\omega_c^2(n+1/2)$ where $\omega_c=eB/m$ and B is applied magnetic field. The discrete energy is contributed by harmonic oscillators centered at $x_0=l_B^2k_y$, where $l_B=\sqrt{\hbar/eB}$ is called the magnetic length. Therefore, ideally all the electrons with any momentum k_y will have the same energy given by E_n . The Landau level is highly degenerate, containing $eB/2\pi\hbar$ states

per unit area. The number of Landau levels filled is then defined as the 'fill factor', ν , and is exactly quantized to integers. When the Fermi level lies between Landau levels, the bulk is insulating, and Hall conductivity is quantized. When it aligns with a Landau level, extended edge states contribute to conduction, producing peaks in longitudinal conductivity. In realistic systems with disorder or finite temperature, Landau levels broaden, leading to Hall conductivity plateaus at exactly $\sigma_{xy} = \nu \hbar/e^2$.

When the interaction between electrons are considered at high magnetic fields, electrons try to minimize Coulomb repulsion, exchange interactions become important, new collective excitations or quasiparticles with fractional charge and statistics appear [168, 169]. This leads to plateaus forming at exactly fractional filling factor $\nu = a/b$ where p,q are integers [170, 171]. For only odd q fractions, the Laughlin wavefunction $\psi = \prod (z_j - z_k)^{(2p+1)} \exp(1/4\sum |z_l|^2)$ with coordinates of electrons $z_j = x_j + iy_j$ and filling factor is an excellent approximation to describe the system at filling factor $\nu = 1/(2p+1)$, where electrons at fixed positions impose zeros of order 2p+1, reflecting strong correlations beyond Pauli exclusion and Coulomb repulsion. In the composite fermion approach, electrons bind to 2n vortices, reducing the Aharonov-Bohm phase and experiencing an effective magnetic field $B^* = B - 2n\phi_0$, mapping the fractional QHE to an integer QHE of composite fermions [172, 173]. Regardless of the specific theoretical framework, the emergence of zeros and vortex clusters remains essential for describing the fundamental physics of the system.

The small size of the system of gated quantum dot allows to investigate the fraction quantum Hall regime accurately using exact diagonalization. With exact diagonalization, fractional fillings factors beyond the Laughlin's description can also be studied. Similar to Wigner molecules, structure of vortices and the underlying physics have been discussed for circular quantum dots with isotropic effective mass [174, 175]. At extremely high magnetic fields in a QD, the kinetic energy is quenched in the lowest Landau level and the correlations and interactions dominate. The anisotropy of phosphorene allows the Wigner molecules to appear in lab frame and thus the FQHE can be studied near this regime. Both these strongly correlated phenomena were separately investigated for anisotropic materials or Fermi surfaces [141–143]. In phosphorene quantum dots, the interplay of extremely strong magnetic fields and tightly confined electrons is expected to give rise to rich and complex physics, significantly different from conventional quantum dot systems. Therefore, we study the cluster of vortices in Wigner molecules formed in gated phosphorene QD.

2.2.2 Quantum Rings

Quantum rings (QR) are nanoscale structures where charge carriers are confined to a ring-like geometry. Unlike quantum dots, quantum rings allow for electron motion along a closed loop. Similar to QDs, however, quantum rings can give insight into various unique phenomena and be utilized for applications.

The wavefunction of electrons traveling around the ring acquires a quantum phase dependent on the magnetic flux threading the ring, providing a tool to investigate the effect of electromagnetic fields on a quantum object. This phase, known as Aharonov-Bohm phase [176], although not observable, results in distinctive behavior due to quantum interference. The distinct behavior manifests as oscillations in discrete energy levels and in the current or conductivity as a function of the magnetic flux in the transport measurements [177–180]. An ideal one dimensional quantum ring with a circumference L will have energy levels given by $E_n = (n + \Phi/\Phi_0) h^2/2mL^2$, where $\Phi_0 = h/e$ is the flux quantum. Therefore, many-body ground

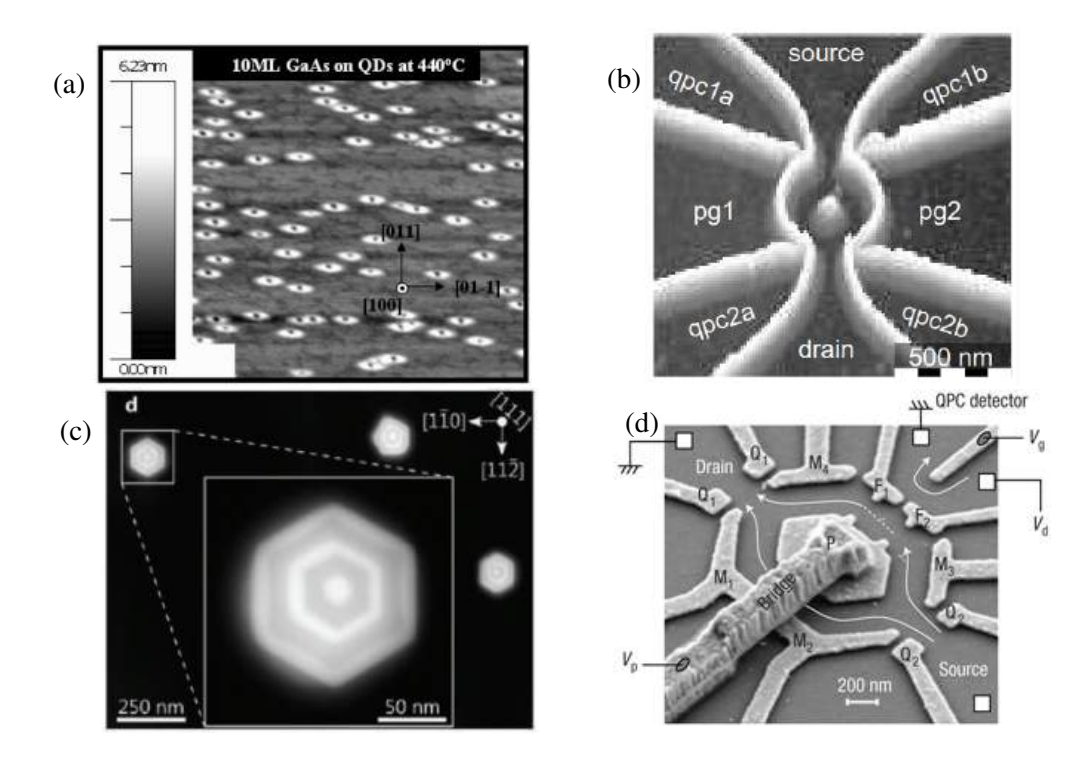


Figure 2.3: (a) AFM image of QRs formed with help of Stranski-Krastanov growth model. (b) Micrograph of the quantum ring taken with the unbiased AFM-tip showing white oxide layer 'written' onto the surface creating depletion region in 2DEG underneath. (c) Transmission electron microscope image of GaAs/AlAs core—multishell nanowires. (d) SEM image of a closed-loop Aharonov Bohm interferometer depicting the gates to form the ring-form potential minima for electron in 2DEG underneath. (a) Reprinted (adapted) with permission from Ref. [195]. Copyright 2008 American Chemical Society. (b) Reproduced with permission from Springer Nature from Ref. [105]. (c) Reprinted (adapted) with permission from Ref. [198]. Copyright 2018 WILEY-VCH Verlag GmbH & Co. KGaA, Weinheim. (d) Reproduced with permission from Springer Nature from Ref. [190].

state of electrons inside a QR has a non-dissipative current even without the presence of voltage difference [181–183]. The electrons maintain their phase throughout the system and hence QRs can be used to study quantum coherence and interference phenomena. Additionally, the geometry of quantum rings naturally leads to periodic boundary conditions, making them excellent tools to investigate topological quantum phases and geometric phases [184–186]. Due to their coherence properties, QRs can thus be used as qubits in quantum computing architectures, as well as magnetic field sensors [188, 189] and nanoscale interferometers [190, 191].

Quantum rings can be fabricated using several experimental techniques, each with distinct advantages. One common method involves the self-assembly of semiconductor quantum dots through strain-driven growth or Stranski-Krastanov (SK) growth [192], where specific growth conditions lead to the formation of ring-like structures [193, 194]. Lee et.al. [195], using this method has demonstrated formation of In-GaAs quantum rings transformed from InAs quantum dots as shown in Fig. 2.3(a). Another widely used technique is lithographic patterning, where electron beam lithography (EBL) and etching processes define nanoscale ring geometries on a semiconductor substrate [196]. Fuhrer et.al. fabricated on AlGaAs-GaAs

heterostructures and locally oxidized surface of the heterostructures by applying a voltage between the conductive tip of an atomic force microscope (AFM) and the 2DEG [105, 197]. This resulted in depletion of 2DEG underneath the oxidized part, thus 'writing' the quantum ring structure onto the surface as shown in Fig. 2.3(b). Additionally, nanowire-based quantum rings can be created by selective material deposition around a nanowire core [198] as shown in Fig. 2.3(c). The self-assembled QRs, while produce high quality QR, lack in control over individual ring placement and uniformity. In contrast, nanowire-based quantum rings are prone to defects and lithography techniques can also suffer from etching induced defects. Electrostatic gating techniques allow for dynamic tuning of quantum ring structures in two-dimensional electron gases (2DEGs). Using this approach, Chang et.al. created an Aharonov-Bohm interferometer formed by gating GaAs/AlGaAs heterostructures [190] as shown in Fig. 2.3(d). While each method enables the study of quantum interference effects, persistent currents, and Aharonov-Bohm oscillations, this PhD work is focused on electrostatic gating due to its high control and tunability for investigating the physical phenomena theoretically. The current state of the art techniques thus enable the fabrication of gated quantum rings in phosphorene.

2.2.3 Multiple Quantum Dots

Building on the understanding of single-gated quantum dots in phosphorene (Section. 2.2.1), multiple quantum dots add complexity and tunability, forming artificial molecules that enable studies of coupling, electron correlations, and emergent few-electron effects. By controlling the interdot tunneling through the gates, as described in Fig. 2.1, along with the charge distributions via confinement gates, and spin interactions with electric and magnetic fields; multiple quantum dots serve as a platform for investigating molecular-like states, quantum coherence, and exotic magnetic phenomena. Their behavior is particularly sensitive to the underlying material properties, including anisotropic effective mass and strong electron-electron interactions, making phosphorene-based multiple quantum dots a promising candidate for studying correlated electron physics as well as potential quantum computing applications. To investigate this behavior experimentally and understand the properties of these gated quantum dots, transport measurements are crucial.

By tuning the gate voltages relative to the discrete energy levels in the quantum dots, one can measure conductivity as a function of these voltages to obtain a charge stability diagram. This diagram reveals the Coulomb blockade (described in Sec. 2.2.1) and the electron occupation in each QD. Fig. 2.4(a) shows the charge stability diagram for a double quantum dot fabricated in bilayer graphene [199]. The numbers '(1,2)' indicate the range of voltage where the left dot is occupied with one electron and right with two. Suppressed current regions correspond to energy gaps between charge states, while finer voltage resolution reveals Pauli spin blockade [Fig. 2.4(b)] shows the suppression of current due to the spin blockade along with the schematic of the process [200]. This occurs when a triplet state cannot transition to a singlet due to spin conservation, enabling electron spin readout. Such behavior facilitates studies of charge transport, spin physics, magnetic ordering, and quantum information applications.

Achieving precise control over charge and spin states in quantum dots requires sophisticated fabrication techniques. Nevertheless, recent advancements in material engineering and gate control have enabled the realization of highly tunable multidot arrays. In 2016, Zajac et.al. fabricated a 12-dot scalable device featur-

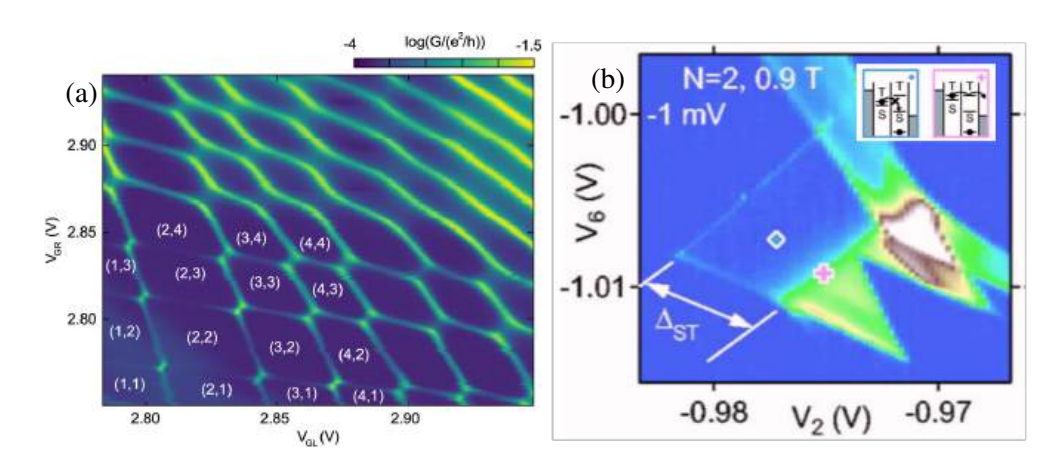


Figure 2.4: (a) Charge stability diagram obtained for double quantum dots in bilayer graphene. (b) A closer look at the transport current plot as a function of left and right gate voltages illustrating spin blockade phenomena. Inset shows the schematic of process at blue (\Diamond) and pink (+) points. (a) Reprinted (adapted) with permission from Ref. [199]. Copyright 2020 American Chemical Society. (b) Reprinted figure with permission from Ref. [200]. Copyright 2005 by the American Physical Society.

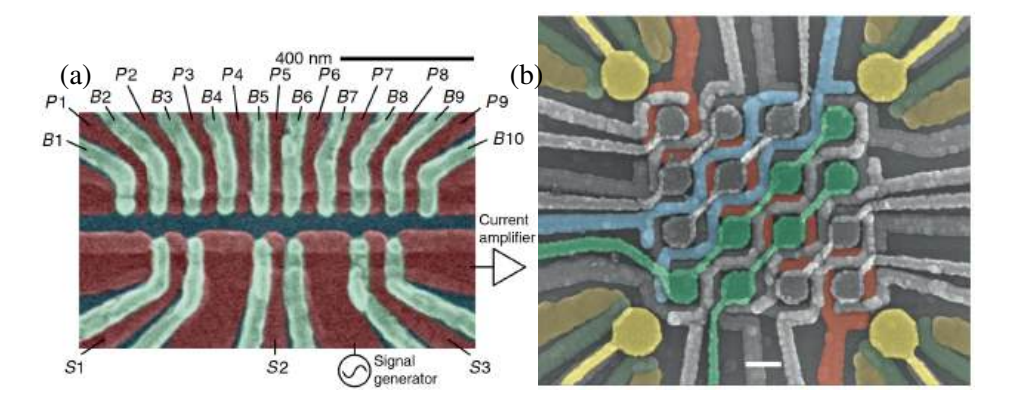


Figure 2.5: (a) False-color SEM image of array of nine quantum dots with overlapping gate architecture with three charge sensor QDs in undoped Si/SiGe heterostructures. (b) False-color SEM image of the crossbar array device employing 16 coupled quantum dots with four charge sensors in each corner of the array on Ge/SiGe heterostructures. (a) Reprinted figure with permission from Ref. [103]. Copyright 2016 by the American Physical Society. (b) Figure adapted from Ref. [104] (Licensed under CC BY).

ing nine dots in array and remaining three as charge sensors, demonstrating high degree of control over the occupation of the dots [103]. The device is shown in Fig. 2.5(a), fabricated in Si/SiGe heterostructures. An even more complex device consisting of quantum dots in 4x4 array was fabricated on Ge/SiGe heterostructures using the crossbar control approach as shown in Fig. 2.5. Using this method, Borsoi et.al. were able to control the dot occupancies to an odd charge occupancies as well as selectively tune the interdot coupling inspired from dynamic random-access memories [104].

Phosphorene based quantum dots is an especially compelling platform for exploring the underlying physics due to their highly anisotropic electronic properties and intrinsic spin-orbit coupling. The interplay between strong electron-electron interactions and the directional dependence of the effective mass in phosphorene quantum dots introduces novel regimes of confinement, potentially modifying charge stability patterns and spin blockade characteristics. This thesis investigates phosphorene as a next-generation quantum dot material, which enables unconventional charge and spin dynamics not present in isotropic systems. As fabrication techniques advance, leveraging the unique properties studied in this thesis may open new avenues for quantum computing and strongly correlated electron physics. Specifically, we delve into Nagaoka ferromagnetism and spin control via electric dipole spin resonance.

Nagaoka Ferromagnetism

Nagaoka theorem provides a rigorous mathematical framework demonstrating how a ferromagnetic ground state can emerge in a nearly half-filled Hubbard model under certain conditions [201]. Specifically, in the limit of an infinite onsite Coulomb repulsion $(U \to \infty)$ and a single hole doped into a half-filled lattice, the system favors a fully spin-polarized state. This effect arises from the delocalization of the hole, which is more efficient when the other electron spins are aligned, preventing destructive quantum interference. Such a system is crucial to understand itinerant ferromagnetism and strongly correlated electron systems [202].

QD arrays, as discussed earlier in Sec. 2.2.3, turn out to be ideal platform for experimentally exploring Nagaoka ferromagnetism due to their tunable electronic properties. The tunable voltages controlling the electron occupation in each dot and the tunneling coupling between these dots, make it possible to physically simulate the lattice models such as Hubbard model [203–205]. One of the significant applications of quantum simulators is in studying strongly correlated electron systems, where conventional computational techniques, such as mean-field approximations or density functional theory (DFT), often fail. Many forms of quantum simulators have been developed and are reviewed in Ref. [206, 207]. Cold atom systems, for example, have been used to realize the Fermi-Hubbard model, providing insights into phenomena like Mott insulators and high-temperature superconductivity [208, 209]. Similarly, quantum dot arrays have been used to realize Fermi-Hubbard model and its emergent phases, but with a better control over single sites, higher operating temperatures, faster operations due to strong coupling and integration with already advanced semiconductor technologies [210, 211]. In particular, small quantum dot arrays such as triangular or square arrangements, allow direct realization of Nagaoka's conditions, where a single hole in the half filled system can induce spin alignment. Dehollain et.al. tested and observed the Nagaoka ferromagnetism in quantum dot array formed in AlGaAs/GaAs heterostructure [212], the confined electrons having isotropic

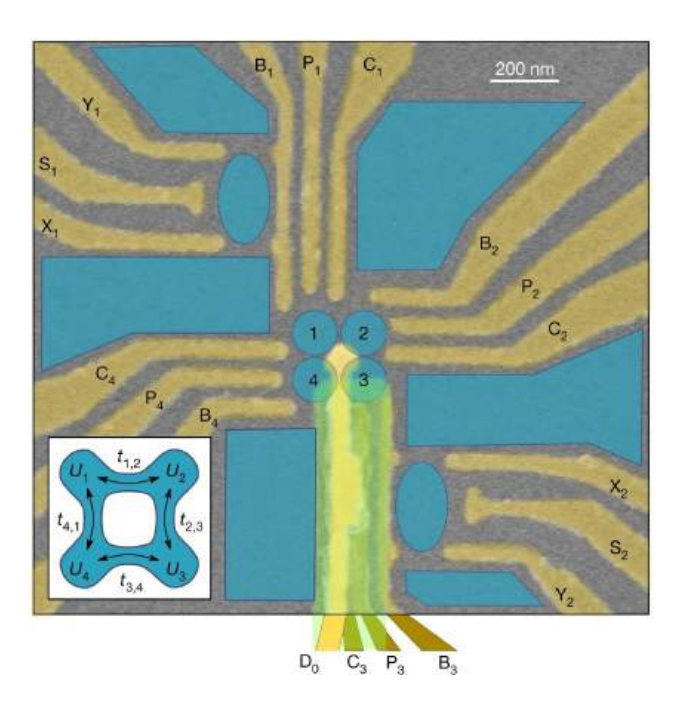


Figure 2.6: SEM image of QD array device utilized to simulate and test the Nagaoka theorem with real electrons. Inset shows the schematic of the array showing the relevant tunnel couplings and on-site interaction parameters from Hubbard model. Reproduce with permission from Springer Nature from Ref. [212].

effective mass, lower than that of phosphorene and isotropic hopping parameters. Fig. 2.6 shows the SEM image of the QD array fabricated with gating to tune the hopping and confinement of the confined electrons.

While Nagaoka's theorem predicts ferromagnetism in an idealized scenario, real materials and quantum dot arrays often exhibit competing interactions that give rise to different magnetic orders. In the presence of strong superexchange interactions or lower hopping amplitudes, an antiferromagnetic ground state may be favored. Additionally, spin-orbit coupling and disorder can destabilize Nagaoka ferromagnetism, leading to more complex magnetic textures. Defects or impurities in the material can affect the electron densities and interference to subvert the spin polarization. In cases where one of the hopping is slowly removed to break the loop, the itinerant ferromagnetism may be lost providing proof for Lieb-Mattis theorem. This thesis specifically tests the robustness of Nagaoka ferromagnetism against these two competing factors.

Electric Dipole Spin Resonance

Nagaoka ferromagnetism is examined through itinerant electrons and strong correlations, where the spin polarization state is an emergent collective spin state. On the other hand, selective coherent spin manipulation (which are crucial for spin qubit implementations) can also be explored using multiple coupled quantum dots. While spin-orbit coupling (SOC) in materials might compete with the collective Nagaoka ordering, it can be exploited for the selective spin manipulation. SOC provides the coupling between the electron's motion and spin, facilitating the spin control through external electric fields via 'Electric Dipole Spin Resonance (EDSR)'.

Spin-orbit coupling (SOC) in semiconductors arises from intrinsic and extrinsic factors like inversion asymmetry or band distortion at interfaces, giving rise to phenomena such as the spin Hall effect, spin-orbit

torques, and the broader field of spin-orbitronics [213]. In quantum dots, Rashba SOC plays a key role in electron dipole spin resonance (EDSR) and spin control. In EDSR, an alternating electric field induces electron oscillations, causing spin rotations via SOC. A full spin flip occurs when the AC field frequency matches the spin transition energy. In gated quantum dots, these spin transitions are directly observable in transport spectroscopy, as discussed earlier.

Experimental realization of the spin manipulation in QD systems is already within the design limits of gating techniques [219]. Nowack et.al. achieved coherent control of an electron's spin with electric fields mediated by spin-orbit interactions [220]. A similar spin qubit was fabricated in silicon metal-oxide semiconductor QD, with artificially induced SOC through micromagnet, but was driven predominantly by 'flopping' a single electron between two quantum dots [221]. A much more complex driving via subharmonics of the resonant frequency was achieved in GaAs double QD system through enhancement from Landau-Zener-Stückelberg-Majorana interference [222]. Many other forms of spin qubits with varying degrees of advantages and disadvantages are reviewed in Ref. [223–225].

Most of the double QD systems are fabricated in III-V semiconductor heterostructures and they suffer from dephasing due to electron-nucleus effects [214–216]. Spin qubits benefit from longer spin coherence time, which allows for more reliable and coherent quantum gate operations. Therefore, faster spin operations are generally sought after to overcome the difficulty of dephasing [216, 217]. Phosphorene, on the other hand, has the bottom of conduction bands contributed majorly from p-orbitals [218], eliminating the extra effort to overcome the dephasing barrier. The much larger effective mass of phosphorene compared to GaAs may lead to strong driving with smaller amplitudes of electric fields, enabling fast spin manipulations anyway. Additionally, the anisotropic effective mass and the anisotropic spin orbit coupling in phosphorene can allow accommodating spin qubits with varying characteristics in a single material by just changing the orientation of gating or QDs. We therefore study a system of gated double QD in phosphorene driven by AC electric field.

Chapter 3

Methodology

After establishing the theoretical framework that describes electron correlations and quantum confinement in electrostatic quantum dots, we turn to numerical methods to quantitatively analyze our system. For each system described in Sec. 2.2, a model Hamiltonian describing the quantum system is constructed.

3.1 Theoretical Model

The tight-binding approach offers a microscopic description of the electronic structure, accounting for the atomic-scale details of phosphorene's puckered honeycomb lattice. This method is particularly useful for capturing the material's inherent anisotropy and complex band structure. The model Hamiltonian used is given by

$$H_{TB} = \sum_{ij} t_{ij} \, p_{ij} \, c_i^{\dagger} c_j + \sum_i V_i \, c_i^{\dagger} c_i + \frac{g\mu_B \, \sigma_z}{2}. \tag{3.1}$$

Here t_{ij} are hopping parameters from site i to j, V_i is external potential at site i and the third part is the Zeeman splitting term, with the magnetic field pointing in z direction. The term p_{ij} is the Peierls phase which takes into account the extra phase acquired by electron when it moves from site i to j in magnetic field B due to the symmetric gauge $\mathbf{A} = (By/2, Bx/2, 0)$ and is given by $p_{ij} = \exp{(i\frac{e}{\hbar}\int_{\vec{r}_i^j}^{\vec{r}_j^j} \vec{A} \cdot \vec{dl})}$.

	$r_{kl}(\mathrm{nm})$	$t_{kl}(\mathrm{eV})$
t_1	0.222	-1.22
t_2	0.224	3.665
t_3	0.334	-0.205
t_4	0.347	-0.105
t_5	0.423	-0.055

Table 3.1: Distances r_{ij} and their respective hopping energies t_{ij} between sites for monolayer black phosphorus [226].

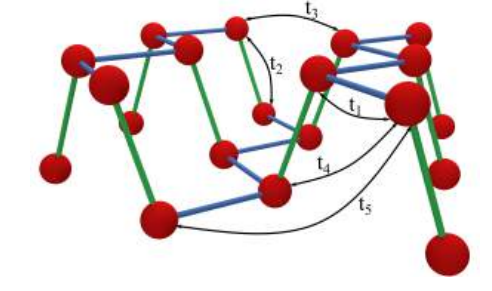


Figure 3.1: Phosphorene crystal structure illustrated with the tight-binding hopping parameters given in Table. 3.1.

The hopping parameters are taken from Ref. [226] and values are listed in Table. 3.1. We use tight-binding method to obtain the energy spectrum in the case of quantum rings and Wigner molecules. However,

for studying larger and larger systems, the computational demands of tight-binding calculations can become prohibitive.

In contrast, effective mass models provide a more computationally efficient framework for investigating quantum confinement in phosphorene. These models approximate the band structure near the relevant energy extrema, allowing for the study of larger systems and more complex confinement geometries. We describe the system in effective mass approximation using the simplest approach given by the Hamiltonian

$$h = \left(-i\hbar \frac{\partial}{\partial x} + eA_x\right)^2 / 2m_x + \left(-i\hbar \frac{\partial}{\partial y} + eA_y\right)^2 / 2m_y + V_{\text{ext}}(x,y) + g\mu_B B\sigma_z/2 \ . \tag{3.2}$$

Where the effective masses are calculated for the conduction lowest band near the extrema.

In phosphorene however, the bands are anisotropic and deviate from parabolic near conduction and valence band extrema [see Fig. 1.2(a)]. A precise continuum model description would therefore require coupling of conduction and valence bands, like $k \cdot p$ model [70]. However, this coupling remains small in phosphorene due to its large band gap [71, 72] and the nearly linear Landau levels in monolayer phosphorene [73, 74] make the nonlinear correction negligible as well. As a result, the single-band effective mass approximation accurately reproduces the energy levels of confined systems [75]. The single-band effective mass approach is especially valuable for phosphorene due to its strongly anisotropic band structure, which can be captured through crystal direction dependent effective masses. The effective masses we use throughout this thesis are $m_{ac} = m_x = 0.17037m_e$ and $m_{zz} = m_y = 0.85327m_e$. A detailed comparison of the charging spectrum calculated using tight-binding Hamiltonian in Eq. 3.1 and using single-band effective mass Hamiltonian in Eq. 3.2 is given in Chapter. 5. By using this model, the low-energy spectrum of confined systems can be obtained with good agreement to tight-binding results, while avoiding the additional computational cost of the full tight-binding method.

The differential equation or the eigenvalue problem can be solved numerically through various methods. For a system of non-interacting electrons or a single electron, we simply discretize the real space in a gauge invariant way [227] and employ the tight-binding model in Eq. 3.1 or the single-band effective mass model on Eq. 3.2 to solve the differential equation with finite difference method. These single electron energies and eigenstates obtained are used to study quantum ring with single electron. For rest of results for system with multiple electrons, we use a technique called 'configuration interaction' to investigate interaction, correlations and many-body effects.

3.2 Configuration Interaction

The general many-body Hamiltonian comprises of kinetic energy, external potential energy and interaction energy terms and can be written as:

$$H = \sum_{i} h_i(\mathbf{r}) + \sum_{i,j>i} V_{\text{int}}(r_{ij}).$$
(3.3)

When the interaction potential energy $V_{\rm int}$ is of the scale of external potential $V_{\rm ext}$, the energy contributions from interactions are no longer perturbative. For eg. the electrostatic interaction energy for classical point electrons just 50 nm (10 nm) apart in Al_2O_3 is already ~ 3 meV (~ 16 meV). A Gaussian wavepacket

of electron with effective mass $0.1m_e$ in harmonic potential spread across 50 nm (10 nm) will have kinetic energy of scale ~ 0.08 meV (~ 1.91 meV). Furthermore, the antisymmetrization requirement for fermionic wavefunctions imposes constraints on single electron calculations, as exchange effects fundamentally alter the system's behavior, necessitating multi-electron approaches.

Mean-field methods like Hartree-Fock and density functional theory use approximate exchange-correlation energies and efficiently handle weak to moderate interactions, while quantum Monte Carlo technique extends these capabilities into more strongly correlated regimes and are beneficial especially for systems with large number (> 10) number of electrons [228–234]. Strong-coupling models such as the Hubbard model capture key features of extreme electron-electron interactions but often simplify the underlying physics. In contrast, exact diagonalization combined with full configuration interaction provides an essentially exact treatment for small systems, fully accounting for all many-body effects without relying on approximations, making it superior and within computational reach for studying very small systems like a few-electron quantum dot in the strong-correlation limit [235].

We describe here the full configuration interaction method mathematically. In our method, we mostly use exact diagonalization to obtain the numerical set of eigenfunctions and energies for single electron system. In principle, this can also be done in any favorable basis such as polynomials and Gaussians as performed in the analysis of vortex structures in Wigner molecules (c.f. Chapter. 7). For n_e electrons in the system, the electrons motion is correlated due to Coulomb repulsion as well as exchange is also correlated due to Pauli exclusion principle. Unlike the Hatree-Fock method where only one Slater determinant is used, full configuration interaction wavefunctions are constructed with linear combination of all possible Slater determinants. Thus, interaction potential and Slater determinants handles the electron correlations and exchange correlations. The general state is given by,

$$|\Psi\rangle = \sum_{i} c_{i} |D_{i}\rangle \tag{3.4}$$

where,
$$|D_i\rangle = \frac{1}{\sqrt{n_e!}} \sum_{p_i \in \mathfrak{S}_{n_e}} sgn(p_i) \prod_{l}^{n_e} |\phi_{p_i(l)}^{(i)}\rangle$$
 (3.5)

and
$$h|\phi_i\rangle = \varepsilon_i |\phi_i\rangle$$
. (3.6)

The single electron exactly diagonalized orthonormal eigenstates (orbitals) $|\phi_i\rangle$ are used to create Slater determinants $|D_i\rangle$. In above Eq. 3.5, ' $p_i(l)$ ' is the index at lth position of p_i permutation out of total $n_e!$ permutations in the symmetric group \mathfrak{S}_{n_e} and $1/\sqrt{n_e!}$ is the normalization factor. Matrix elements of single particle and two particle operator in this general state $|\Psi\rangle$ can be calculated using Slater-Condon rules, eliminating all the inner products where three or more orbitals differ [236]. The surviving matrix elements are:

For diagonal:

$$\langle D_i | H | D_i \rangle = \sum_{i}^{n_e} \varepsilon_i \tag{3.7}$$

For non-diagonals:

$$\langle D_{i}|H|D_{j}\rangle = \sum_{p_{i} \in \mathfrak{S}_{n_{e}}} \prod_{l} \prod_{m} sgn(p_{j}) \langle \phi_{\mathbb{I}(l)}^{(i)}(r_{l})| \sum_{a,b>a}^{n_{e}} V_{\text{int}}(r_{ab}) |\phi_{p_{j}(m)}^{(j)}(r_{m})\rangle$$

$$= \sum_{p_{i} \in \mathfrak{S}_{n_{e}}} \sum_{a,b>a}^{n_{e}} sgn(p_{j})$$

$$\langle \phi_{\mathbb{I}(a)}^{(i)}(r_{a}) \phi_{\mathbb{I}(b)}^{(i)}(r_{b})|V_{\text{int}}(r_{ab}) |\phi_{p_{j}(a)}^{(j)}(r_{a})\phi_{p_{j}(b)}^{(j)}(r_{b})\rangle$$

$$(3.8)$$

where $V_{\rm int}(r_{ab})=1/4\pi\epsilon\cdot 1/|r_{ab}|$ where we consider phosphorene is embedded in Al_2O_3 with $\epsilon=9.1\,\epsilon_0$ [237] and the integral near $r_{ab}=0$ is calculated using Monte Carlo integration. This matrix constructed using the basis of all combinations of Slater determinants or configurations, is then exactly diagonalized to obtain many electron eigenstates and energies. As the number of single electron eigenstates used to construct the basis is increased (gets closer to a complete set), the ideal solution of the full configuration interaction method approaches the exact solution. This convergence can easily be seen in the ground state energy. Along with the Slater-Condon rules for determinants, each state that electron a and b are in must have same spin state on either side of the inner product, i.e. in Eq. 3.8, spin eigenvalue of $|\phi_{\mathbb{I}(a)}^{(i)}(r_a)\rangle$ must be the same as spin eigenvalue of $|\phi_{p_j(a)}^{(j)}(r_a)\rangle$, given spin is a good quantum number. Later, we introduce Rashba spin-orbit coupling in Chapter. 9 where the spin is not a good quantum number and the integration is over both spinor wavefunctions of single-electron eigenfunctions. Similar symmetry considerations on parity can further simplify the matrix constructions when applicable.

The diagonalization is performed numerically using Lanczos algorithm [238, 239] using the ARPACK library for Fortran. It is possible to further speedup the calculations at expense of accuracy by restricting the value of excited orbitals, i.e. $p_j(a)$ or $p_j(b)$ to perform 'restricted configuration interaction' method [236]. The number of single-electron eigenstates, the highest excited state index, and the density of the discretized grid are carefully balanced to ensure convergence while minimizing computational cost. The convergence can be further improved by introducing an extra repulsive potential at center of the QD to mimic the repulsion of electrons at single electron calculation stage, and its contributions can be removed for multi-electron calculations. This technique was especially used to calculate the convergent solutions for Wigner molecules. Electron density and pair correlation functions were calculated in similar way as Eq. 3.8.

3.3 Time Dependent Calculations

For the time evolution and spin manipulation by electric dipole spin resonance (EDSR) in quantum dots, we use the time dependent Scrödinger equation with the Hamiltonian where constant and time dependent part are separable as

$$H(t) = H_0 + V'(t). (3.9)$$

This H_0 can be single electron or multi-electron Hamiltonian. If the eigenstates of the Hamiltonian H_0 are $|n\rangle$ such that, $H_0|n\rangle = E_n|n\rangle$, we use the ansatz for wavefunction as linear combination of the stationary eigenstates with the time evolution governed of the states $|n\rangle$ only governed by the time independent part and that of coefficients governed only by the time dependent potential V'(t). The ansatz is given as

$$|\Phi(t)\rangle = \sum_{n} g_n(t) e^{-iE_n t/\hbar} |n\rangle$$
 (3.10)

Using the time dependent Scrödinger equation with Hamiltonian H(t), we can obtain a set of coupled differential equations for evolution of each coefficient,

$$-i\hbar \frac{\partial g_m(t)}{\partial t} = \sum_n \langle m|V'(t)|n\rangle e^{-i(E_m - E_n)t/\hbar} g_n(t) \quad . \tag{3.11}$$

This set of differential equations is then solved using Crank-Nicholson scheme numerically to obtain the occupancy $|g_n(t)|^2$ in nth state at any time t.

For single electron, the transition matrix element $T_{nm}^{(1e)} = \langle m|V'(t)|n\rangle$ can be calculated easily since the eigenstates are known from exact diagonalization. Transition matrix elements for multi-electron case can be calculated, similar to Eq. 3.8.

$$\langle \Psi | V'(t) | \Psi \rangle = \sum_{i,j} \sum_{p_i \in \mathfrak{S}_{n_c}} \prod_{l}^{n_e} \prod_{m}^{n_e} c_i^* c_j \, sgn(p_j) \, \langle \phi_{\mathbb{I}(l)}^{(i)}(r_l) | V'(t) | \phi_{p_j(m)}^{(j)}(r_m) \rangle \tag{3.12}$$

We studied EDSR system with a sinusoidally oscillation polarized electric field. Thus substituting the form of time dependence $V'(t) = \sum_i eFr_i \sin(\omega t)$ we get.

$$\langle \Psi|V'(t)|\Psi\rangle = \sum_{i,j} \sum_{p_i \in \mathfrak{S}_{n_e}} \prod_{l} \prod_{m} \sum_{m} c_i^* c_j \, sgn(p_j) \, \langle \phi_{\mathbb{I}(l)}^{(i)}(r_l)| \sum_{i_e}^{n_e} eFr_i \sin(\omega t) \, |\phi_{p_j(m)}^{(j)}(r_m)\rangle$$

$$= \sum_{i,j} \sum_{p_i \in \mathfrak{S}_{n_e}} \sum_{i_e}^{n_e} c_i^* c_j \, sgn(p_j) \, \langle \phi_{\mathbb{I}(i_e)}^{(i)}(r_{i_e}) \, | \, eFr_i \sin(\omega t) \, |\phi_{p_j(i_e)}^{(j)}(r_{i_e})\rangle$$

$$= \sum_{i,j} \sum_{p_i \in \mathfrak{S}_{n_e}} \sum_{i_e}^{n_e} c_i^* c_j \, sgn(p_j) \, T_{\mathbb{I}(i_e),p_j(i_e)}^{(1e)}$$

$$(3.13)$$

Using these tools along with the results from full configuration interaction, we studied the resonance spectrum and the spin flip times of a double quantum dot system in phosphorene.

Chapter 4

Summary of Articles

4.1 Aharonov-Bohm oscillations in phosphorene quantum rings: mass anisotropy compensation by confinement potential

Thakur, T., & Szafran, B. Physical Review B, 105(16), 165309 (2022).

We investigate the Aharonov-Bohm (AB) effect in a quantum ring electrostatically defined in a phosphorene monolayer. The strong anisotropy of effective masses in phosphorene disrupts the usual persistent current circulation in a circular quantum ring, preventing ground state AB oscillations. However, we demonstrate that by deforming the confinement potential into an elliptical shape, the anisotropy can be compensated, restoring oscillatory behavior and ground-state parity transformations with AB periodicity.

We employ both tight-binding and effective mass models to analyze the system. We find that for a specific ratio of the ellipse's semi-axes, the spectrum of the system becomes identical to that of a circular quantum ring with an isotropic effective mass. This is explained by the identification of a generalized angular momentum operator that commutes with the continuum Hamiltonian for this special ratio, leading to level crossings rather than avoided crossings for states of the same parity and spin. Additionally, we analytically show that in the limit of diminishing width of the ring, the energy spectrum of compensated Hamiltonian approaches that of ideal 1D quantum ring.

The paper further explores the two-electron case, where Coulomb interactions break the commutation of the modified angular momentum operator with the Hamiltonian. However, AB oscillations in the ground state energy still appear, albeit not as clearly as in the single-electron case, when the confinement potential is properly tuned. The results are discussed in the context of potential experimental realizations, suggesting that these effects could be observed using transport spectroscopy techniques. The study provides a theoretical framework for engineering quantum rings in phosphorene that exhibit AB oscillations despite strong mass anisotropy. However, the results are not limited to phosphorene, as the treatment is general and valid for any material with anisotropic effective masses.

4.2 Wigner molecules in phosphorene quantum dots

Thakur, T., & Szafran, B. Physical Review B, 106(20), 205304 (2022).

We investigate the formation of Wigner molecules from up to five electrons in electrostatically confined phosphorene quantum dots. Due to the large effective masses in phosphorene, electron charge separation occurs even in relatively small quantum dots, facilitating the observation of Wigner crystallization. The study finds that the anisotropic effective mass in phosphorene allows Wigner molecules to form in the laboratory frame, with charge density distributions that do not always reflect the symmetry of the confinement potential due to an extra asymmetry introduced by the effective mass anisotropy.

For circular quantum dots, we find that Wigner molecules form for two and four electrons but not for three and five electrons. A system with five electrons shows a transition between two charge configurations as the magnetic field is varied, one with well-separated single electron islands (Wigner molecule) and another where the charge configuration is a superposition of equivalent charge configurations. The study also explores elongated quantum dots, showing that Wigner molecule formation is more favorable when the longer axis is aligned with the zigzag direction (where the effective mass is heavier), while alignment along the armchair direction suppresses crystallization due to the lower effective mass.

The results highlight spectral signatures of Wigner crystallization, such as nearly degenerate ground states at zero magnetic field, spin polarization at low magnetic fields, and distinct energy gaps between low-energy states. These features suggest that transport spectroscopy could be used to experimentally confirm Wigner molecule formation in phosphorene quantum dots. The existence of Wigner molecules for two and four electrons and not for three, indicates that inter-electron distance is not the only factor for the formation of these structures. The study uses a configuration interaction approach with an optimized single-electron basis to handle strong electron-electron interactions efficiently.

4.3 Vortex structure in Wigner molecules

Thakur, T., & Szafran, B. Scientific Reports, 13(1), 9707 (2023).

This article investigates how vortices, zeros in the many-body wave function with associated phase windings, form and evolve within Wigner molecules in quantum dots under high magnetic fields. We focus on the role of anisotropy, either from the external confinement or the electron effective mass, in controlling the spatial arrangement of these vortices. In isotropic systems, vortex rearrangements occur abruptly at angular momentum transitions, whereas, in anisotropic settings the evolution is smooth as the magnetic field varies.

For a system with an isotropic effective mass, the study shows that extra vortices initially emerge at the edges of the confined electron system under fractional quantum Hall conditions and then gradually migrate toward the electrons. In this case, the vortices are typically aligned along a line perpendicular to the axis of a linear Wigner molecule, shifting to lie along the molecule's axis at the lowest Landau level filling factor $\nu \approx 1/5$. By contrast in phosphorene, where the effective mass is strongly anisotropic, the vortex behavior depends critically on the orientation of the Wigner molecule. When the molecule is aligned along the armchair direction, the vortices remain off the axis, while for alignment along the zigzag direction the vortices transfer to the axis already at a filling factor of $nu \approx 1/3$. This transfer process is accompanied by the creation and subsequent annihilation of an antivortex near an electron's position.

Overall, the work provides a detailed theoretical analysis using exact diagonalization and a configuration interaction approach, of how magnetic field, electron correlations, and anisotropy interplay to determine the vortex structure in Wigner molecules. These insights deepen our understanding of fractional quantum Hall states and Wigner crystallization in low-dimensional systems, and they may help guide future experiments aiming to resolve vortex configurations in anisotropic materials like phosphorene.

4.4 Nagaoka ferromagnetism in an array of phosphorene quantum dots

Thakur, T., & Szafran, B. Scientific Reports, 13(1), 18796 (2023).

In this article, we explore how a nearly half-filled array of quantum dots in phosphorene can exhibit itinerant ferromagnetism driven by strong electron—electron interactions. Using a continuum effective mass Hamiltonian, we study a square array of four quantum dots populated with three electrons. This configuration is ideal for investigating Nagaoka ferromagnetism as per the theorem's conditions of one less than half. According to the theorem the interactions should promote a fully spin-polarized state

The study models the quantum dots with Gaussian confinement potentials, and the geometry of the array, specifically the separations in the armchair (μ_x) and zigzag (μ_y) directions plays a crucial role in compensating for the anisotropic hopping. By varying these parameters, we construct a phase diagram that maps the transition between low-spin and high-spin (Nagaoka ferromagnetic) ground states. The results reveal that an optimized geometry, with $\mu_x=6.8$ nm and $\mu_x=5.2$ nm, can yield a Nagaoka gap as large as approximately $230~\mu eV$, a value that is promising for experimental observation.

Furthermore, the paper investigates the robustness of the ferromagnetic state against structural imperfections. When one quantum dot is shifted, thereby transitioning the array from a square to a quasi one dimensional chain, the ferromagnetic ordering is suppressed (in agreement with Lieb-Mattis theorem). Shifts along the zigzag direction proving more effective in destabilizing the high spin state than those along the armchair direction. Similarly, the study examines potential detuning of one dot and finds that while moderate detuning leaves the ferromagnetic state intact, larger detuning that either traps an electron or effectively removes a dot from the low-energy sector leads to a transition to a low spin ground state. We showed that the mechanisms breaking the Nagaoka ordering are different for positive and negative detuning, and hence the transition occurs for uneven values of detuning.

Overall, the work demonstrates that by judiciously tuning the geometry of the quantum dot array, one can overcome the challenges imposed by effective mass anisotropy in phosphorene to stabilize Nagaoka ferromagnetism. It also tests the robustness of this spin polarized ordering against the position and detuning of one of the quantum dots, while suggesting mechanisms for the resultant states.

4.5 Electrical manipulation of the spins in phosphorene double quantum dots

Thakur, T., Peeters, F. M., & Szafran, B. Scientific Reports, 14(1), 18966 (2024).

We study how electron spins can be controlled using AC electric fields in a double quantum dot system formed in monolayer phosphorene. Exploiting the inherent anisotropy of phosphorene, both in its effective masses (light along the armchair direction, heavy along the zigzag) and its predicted anisotropic spin—orbit coupling, we study electric dipole spin resonance (EDSR) driven by an oscillating electric field. We employ a single-band effective mass Hamiltonian combined with configuration interaction techniques to simulate the time evolution of a two-electron system and analyze singlet—triplet transitions.

The interplay of spin-orbit coupling and asymmetry in the confinement potential results in avoided crossings between the singlet and triplet states, with the dipole transition matrix elements showing a maximum peak at specific potential detuning. This peak corresponds to a region where the detuning flips the ground state spin of the system, and thus becoming most effective detuning to control spins using electric fields.

The study reveals that by adjusting the external AC field near and away from this regime, coherent spin-flip transitions (Rabi oscillations) can be induced on a sub-nanosecond timescale, a favorable characteristic for qubit applications. Furthermore, we compare dots arranged along different crystallographic axes, demonstrating that the orientation significantly influences interdot tunneling and the rates of spin transitions. We find that detuning can be used as a knob to turn the same quantum dots to function as spin-like and charge-like qubits, with the advantage of stability against charge noise and fast spin-flip times respectively.

We also discuss higher-order (multi-photon) and Landau-Zener-Stückelberg-Majorana transitions, illustrating how these processes can be leveraged to further control the spin dynamics. Overall, the work shows that phosphorene double quantum dots in phosphorene offer a promising platform for fast, electrically driven spin manipulation with the potential for high fidelity and tunability, making them attractive for quantum computing applications.

Chapter 5

Aharonov-Bohm oscillations in phosphorene quantum rings: mass anisotropy compensation by confinement potential

Reprinted with permission from Thakur, T., & Szafran, B. Aharonov-Bohm oscillations in phosphorene quantum rings: Mass anisotropy compensation by confinement potential. Physical Review B, 105(16), 165309 (2022). Copyright 2022 by the American Physical Society.

Aharonov-Bohm oscillations in phosphorene quantum rings: Mass anisotropy compensation by confinement potential

Tanmay Thakur o and Bartłomiej Szafran o

Faculty of Physics and Applied Computer Science, AGH University of Science and Technology, al. Mickiewicza 30, 30-059 Kraków, Poland



(Received 22 December 2021; revised 5 April 2022; accepted 8 April 2022; published 22 April 2022)

We consider the Aharonov-Bohm (AB) effect on a confined electron ground state in a quantum ring defined electrostatically within the phosphorene monolayer. The strong anisotropy of effective masses in phosphorene quenches ground-state oscillations for a circular ring because of interrupted persistent current circulation around the ring. An elliptic deformation of the confinement potential can compensate for the anisotropy of the effective masses and produce ground-state parity transformations with the AB periodicity. Moreover, a specific ratio of the semiaxes is determined for which the spectrum becomes identical to that of a circular quantum ring and an isotropic effective mass. We identify a generalized angular momentum operator which commutes with the continuum Hamiltonian for the chosen ratio of the semiaxes that closes the avoided crossings of energy levels for states of the same parity and spin. Ground-state oscillations for the two-electron ground state are also discussed.

DOI: 10.1103/PhysRevB.105.165309

I. INTRODUCTION

Phosphorene [1] or a monolayer form of black phosphorus [2-4] is extensively studied for optics [5], field-effect transistors [2,6,7], and quantum Hall effects [8–10]. Unlike the half-metallic graphene, phosphorene is a direct gap semiconductor that can host the electrostatic lateral confinement of electrons. The electrostatic fields produce a clean confinement in gated two-dimensional systems for the investigation of the single-electron and interaction effects [11] in carrier traps. A particular form of the lateral confinement that attracts a lot of attention is the quantum ring [12]. The annular confinement allows for persistent current circulation in the presence of an external magnetic field, with the spectrum and magnetic response which is periodic with the Aharonov-Bohm periodicity [13]. The periodicity of the spectrum of a phosphorene ring defined as a rectangular flake of the crystal with a central opening has been studied in Ref. [14], including the effect of the zigzag and armchair edges of the crystal. The purpose of this paper is to investigate a clean quantum ring defined within phosphorene by an external potential that keeps the electrons off the edges of the crystal and is not affected by its details.

The anisotropy of the phosphorene crystal structure [4] results in a strongly anisotropic electron effective mass [2,15– 18] that is much larger along the zigzag chains of ions [16] than in the perpendicular direction. The anisotropy prevents the persistent current flow in the electron ground state confined in a circular ring. However, current circulation can be restored by deforming the confinement potential to an elliptic form. Then, the spectrum acquires a braided pattern of evenand odd-parity energy levels, which cross with the Aharonov-Bohm period. Moreover, we propose a geometry for the elliptic confinement in which a modified angular momentum operator, with one of the Cartesian coordinates rescaled, commutes with the Hamiltonian and the energy spectrum becomes

similar to the one of an electron in a circular quantum ring with isotropic effective mass. For a confined electron pair interacting with the Coulomb potential, the operator no longer commutes with the Hamiltonian, but the Aharonov-Bohm oscillations of the ground-state energy appear for a tuned confinement potential.

II. THEORY

A. Tight-binding model

We work with the phosphorene monolayer (see Fig. 1) using the Hamiltonian

$$H_{\rm TB} = \sum_{kl} t_{kl} p_{kl} c_k^{\dagger} c_l + \sum_k V_k c_k^{\dagger} c_k + g \mu_B B \sigma_z / 2, \qquad (1)$$

where the first sum describes the hopping between the neighboring atoms. The values for t_{kl} (see Table I) are taken from the five-parameter effective tight-binding Hamiltonian of Ref. [17]. The positions of the ions in the phosphorene crystal [3] are plotted in Fig. 1 with the zigzag chains oriented along the y direction. In Eq. (1), p_{kl} are the Peierls phase shifts that the electron acquires from the vector potential along the line between k and l ions, $p_{kl}=e^{i\frac{\epsilon}{\hbar}\int_{\tilde{r}_k}^{\tilde{r}_l}\tilde{A}\cdot d\tilde{l}}$. We consider the magnetic field perpendicular to the monolayer (0, 0, B)with the vector potential taken in the symmetric gauge A = $(-\frac{By}{2}, \frac{Bx}{2}, 0)$. In Eq. (1), V_k stands for the external potential on the ion k. The spin Zeeman effect is introduced by the last term of the Hamiltonian.

The g factor for phosphorene of $g \approx 2.03$ was determined using the $\mathbf{k} \cdot \mathbf{p}$ theory by Junior et al. [19]. Zhou et al. [20] indicated the value of g = 2.14 for monolayer black phosphorus. On the other hand, experiments have determined the value of $g = 2 \pm 0.1$ [21] and $g \approx 1.8-2.7$ [22] and some have even reported $g = 5.7 \pm 0.7$ at low filling factors [23].

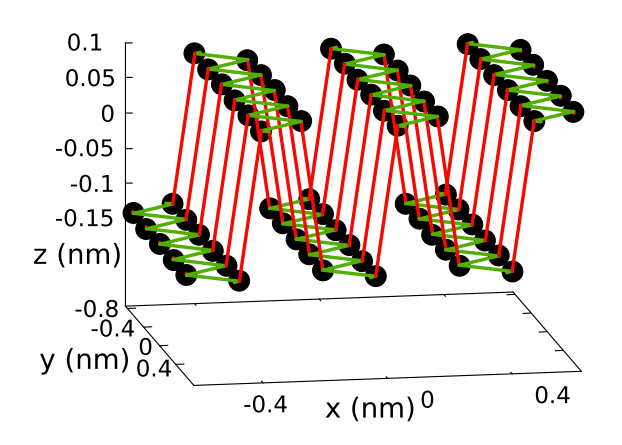


FIG. 1. Ions in phosphorene monolayer placed on two planes separated by a distance of 0.213 nm. The lines link the neighbor ions with the largest hopping energies (in-plane neighbors, green lines, hopping energy -1.22 eV) and (neighbors of separate planes, red lines, hopping energy 3.665 eV) (see Table I).

Nevertheless, the spin Zeeman term produces only a linear shift in the energy defining the spin splitting. The magnetic field promotes the spin-down energy levels to the ground state sooner or later on the magnetic field scale. We focus on avoided crossings or crossings of the states of the polarized spin. The absence or presence of Aharonov-Bohm oscillations will not be affected by the value of the g factor. Therefore, the spin Zeeman term is calculated with the value g=2.

B. Effective-mass Hamiltonian

Part of the results of this work is obtained in the continuum approximation to the tight-binding Hamiltonian. We use a single-band effective-mass operator,

$$H_{\rm em} = \left(-i\hbar \frac{\partial}{\partial x} + eA_x\right)^2 / 2m_x + \left(-i\hbar \frac{\partial}{\partial y} + eA_y\right)^2 / 2m_y + V(x, y) + g\mu_B B\sigma_z/2, \tag{2}$$

with the effective-mass parameters derived by fitting the tight-binding spectrum to the harmonic oscillator spectrum in Ref. [24] with mass about five times heavier for the carrier motion along the zigzag chains of the crystal (see Fig. 1), $m_x = 0.170\,37m_0$ and $m_y = 0.853\,27m_0$. The effective-mass Hamiltonian is diagonalized using the finite-difference technique.

TABLE I. Hopping energies according to Ref. [17] for a single black phosphorus layer. The left column shows the distance between the ions and the right column the hopping energy t_{kl} applied in the tight-binding Hamiltonian (1).

r_{kl} (nm)	t_{kl} (eV)
0.222	-1.22
0.224	3.665
0.334	-0.205
0.347	-0.105
0.423	-0.055

C. Confinement potential

We attempt to compensate for the anisotropy of the effective masses by the anisotropy of the confinement potential. For that purpose, we use the following external potential,

$$V(x, y) = \frac{1}{2} m_x \omega^2 [\rho(x, y) - R]^2, \tag{3}$$

with $\rho(x, y) = \sqrt{x^2 + y^2/\alpha}$, where α is a parameter that controls the anisotropy of the potential. The potential vanishes for points (x, y) forming an ellipse,

$$\frac{x^2}{R^2} + \frac{y^2}{\alpha R^2} = 1. {4}$$

We take the confinement energy $\hbar\omega=6$ meV. Changing α we keep the area within the ellipse fixed taking $R=\alpha^{-1/4}R_c$, with $R_c=30$ nm, so that the number of magnetic flux quanta threading the ellipse is the same for a given magnetic field B independent of α . For $R_c=30$ nm a flux quantum threads the ring at 1.43 T, which is the period of the energy spectrum on the B scale for a strictly one-dimensional (1D) circular quantum ring. We use $\alpha \le 1$ so that the half length of the major axis a of the ellipse is oriented along the x axis $a=R=\alpha^{-1/4}R_c$ and the half length of the minor axis is $b=\sqrt{\alpha}R=\alpha^{1/4}R_c$.

In this work, we focus on the confined electron states of the conduction band. In the continuum Hamiltonian, the bottom of the conduction band is set as the reference energy level. The tight-binding spectrum produces the conduction- and valenceband extrema spaced by the energy gap. For a finite flake, the spectrum also contains in-gap states that are localized at the edge of the flake and the spectrum is not symmetric with respect to the center of the energy gap [14]. Reference [14], which used the same tight-binding parametrization [17], provides the lowest conduction-band state energy level of ≈0.4 eV for a square flake with a side length of 8 nm in the absence of an external potential. In this paper, we are interested in states confined in the external potential that are independent of the details of the edge and thus correspond to an infinite crystal. However, the calculations are carried out in an elliptical flake for which the position of the ions satisfies the condition $x^2 + y^2/\alpha < R_s^2$. We take the flake large enough to contain all the discussed states within the confinement potential so that the results are independent of R_s . However, for V=0, the conduction-band states occupy the entire flake, and the results depend on R_s [25]. The dependence on the lowest-energy level in R_s is well approximated by the dependence $E_0(R_s) =$ $C/R_s^2 + E_{\infty}$, where C = 673.31 (meV nm²) and $E_{\infty} = 340$ meV. The R_s^{-2} dependence is due to the finite-size effect, that is, the kinetic energy due to localization in a finite flake, and $E_{\infty} = 340 \text{ meV}$ is the estimated position of the bottom of the conduction band for an infinite crystal. In the results presented in the following we shift down the tight-binding energies by E_{∞} .

III. RESULTS AND DISCUSSION

A. Single-electron solutions

The low-energy spectrum of a circular ring ($\alpha = 1$) is plotted in Fig. 2(a) [Fig. 2(b)] for the tight-binding (TB) model (continuum model). The TB results [Fig. 2(a)] here and below

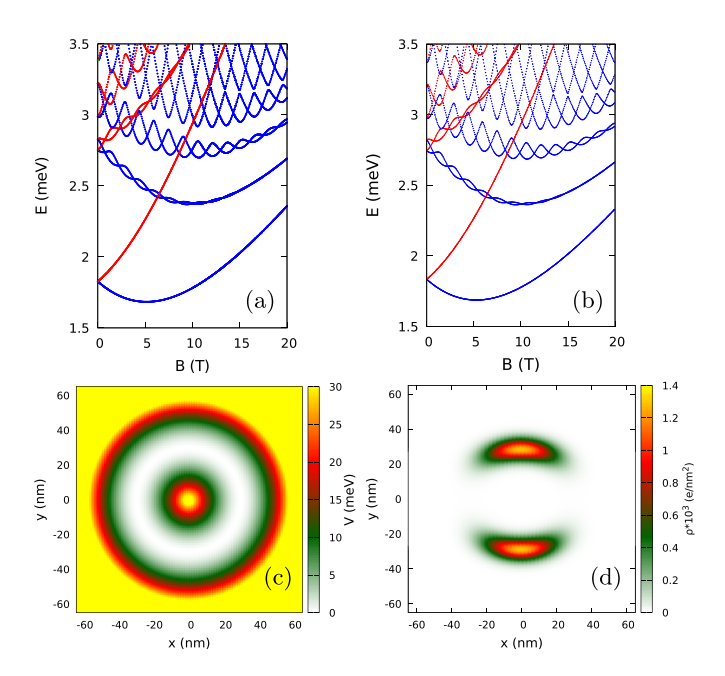


FIG. 2. (a) The tight-binding and (b) continuum Hamiltonian eigenvalues for $\alpha=1$. The blue and red lines show the spin-down and spin-up energy levels, respectively. The tight-binding energy levels in (a) were shifted down by $E_{\infty}=340$ meV (see text in Sec. II B). (c) shows the confinement potential and (d) the ground-state charge density for B=0 calculated using the continuum model.

are shifted down by 340 meV. The results of both approaches are nearly identical. The ground state of a circular ring is localized in two islands near the y axis on the opposite sides of the ring center [Fig. 2(c)]. The wave function confinement implies a contribution to the kinetic energy which is large along the x axis due to the low value of mass m_x . In consequence the ground-state wave function is far from the x axis, and no persistent current circulation is possible in the ground-state.

The lowest spin-up and spin-down energy levels of Figs. 2(a) and 2(b) are twofold degenerate with respect to the parity. Degeneracy results from the lack of tunneling of the wave function across the x axis [Fig. 2(d)]. In the excited state part of the spectrum, one can see pairs of energy levels that cross in a braidlike pattern. The corresponding states have opposite parities, hence the crossings of the levels. These oscillations are reminiscent of the angular momentum transitions for a circular ring with isotropic effective mass [12,26].

With $\alpha < 1$ the confinement area on the y axis becomes thinner and the one along the x axis wider [see Fig. 3(c) for $\alpha = 1.2 \frac{m_x}{m_y}$]. The confinement energy along the y axis increases and that along the x axis decreases. The x axis is now accessible for the ground-state electron [Fig. 3(d)]. The ground-state degeneracy is lifted, and the ground-state crossings of energy levels of opposite parity are observed [Fig. 3(a,b)].

In Fig. 4(a) we plotted a magnified view of the low-energy part of the spectrum. By Δ_0 we denote the energy splitting of the lowest even- and odd-parity energy levels taken at B=0, which defines the range of the ground-state energy oscillations as functions in the external magnetic field. The braided two energy levels cross with the Aharonov-Bohm period. The

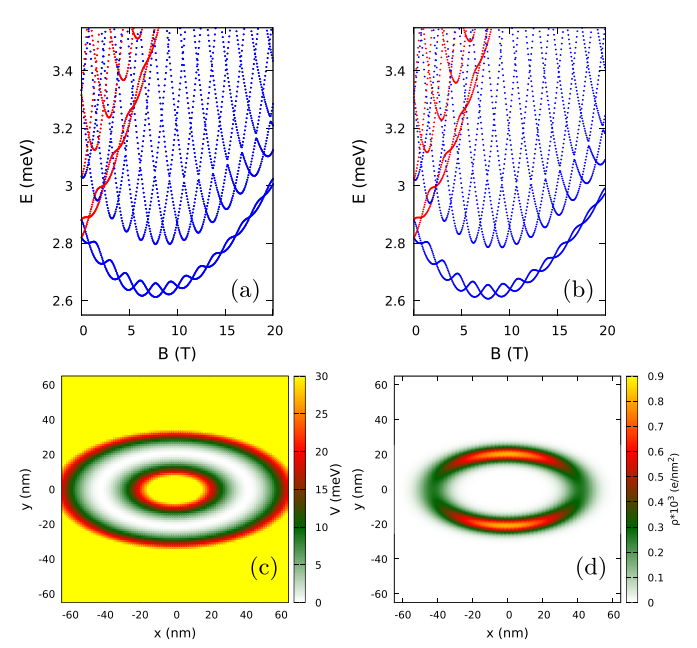


FIG. 3. Same as Fig. 2 only for $\alpha = 1.2 \frac{m_x}{m_y}$.

second quantity marked in Fig. 4(a) by Δ_e is the width of the avoided crossing of even-parity energy levels taken at $B \simeq 7.75$ T.

Decreasing the anisotropy parameter to $\alpha = \frac{m_x}{m_y}$ we find that the ground-state charge density [Fig. 5(d)] is constant along the confinement potential minimum [Fig. 5(c)]. The continuum spectrum [Fig. 5(b)] contains crossings of energy levels in the entire spectrum. For the tight-binding model [see also Fig. 4(b)] we find the parity-related crossings of the energy levels in the ground state as in Fig. 3, and only narrow avoided crossings are found between the first and second

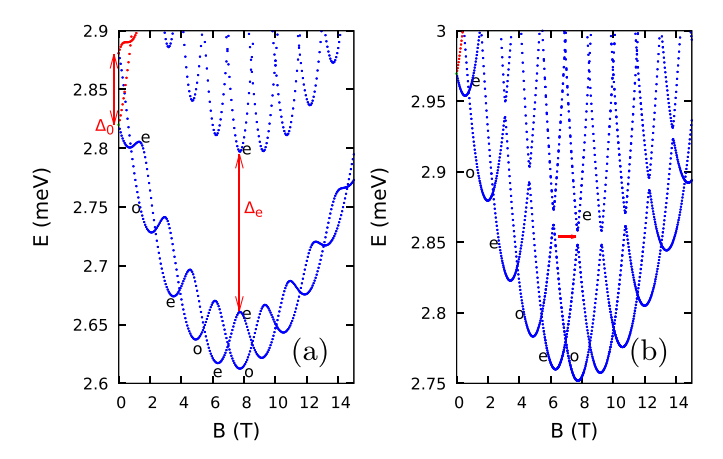


FIG. 4. Magnified view of the low-energy part of the tight-binding spectrum for (a) $\alpha=1.2\frac{m_x}{m_y}$ and (b) $\alpha=\frac{m_x}{m_y}$ [Fig. 6(a)]. Letters "e" and "o" near the energy levels in (a) mark the even- and odd-parity energy levels that are eigenstates of the parity operator with the eigenvalues +1 and -1, respectively. Δ_0 is the even-odd-parity splitting at B=0 and Δ_e is the width of the avoided crossing between the lowest even-parity energy levels for $B\simeq 7.75$ T. The red arrow in (b) shows the avoided crossing Δ_e , here of the width of 13 μeV (see Table II).

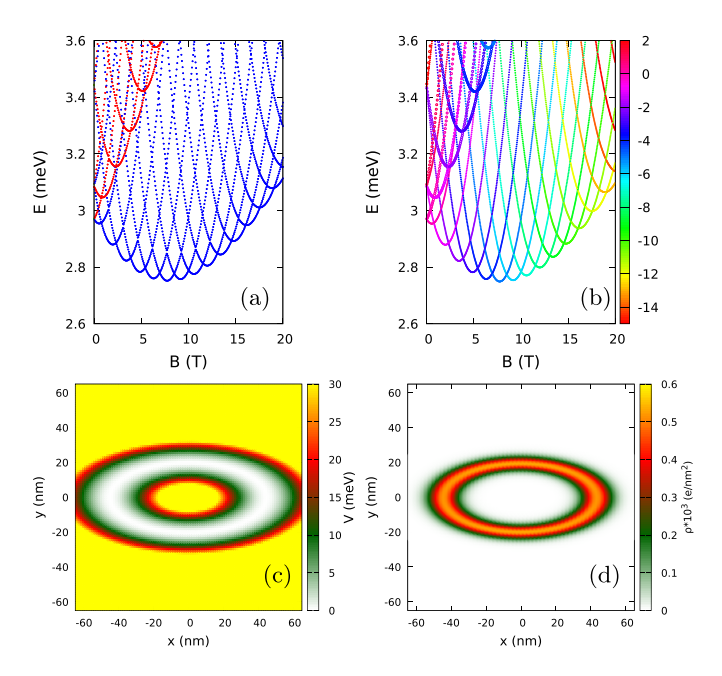


FIG. 5. Same as Fig. 2 only for $\alpha = \frac{m_x}{m_y}$. In (b) the colors indicate the eigenvalue of the angular momentum l_z' operator, and in (a) the colors describe the spin as in Fig. 2.

excited energy levels of the same parity. The one marked by the red arrow in Fig. 4(b) corresponds to $\Delta_e = 13~\mu eV$. Δ_e attains its minimal value for $\alpha = \frac{m_x}{my}$. Values of Δ_0 and Δ_e calculated with the tight-binding approach for varied α are summarized in Table II.

B. Angular momentum in the rescaled space

The crossings of the energy levels in the spectrum of Fig. 5(b) suggest that an additional symmetry is present in addition to the parity. With the substitution $y' = y/\sqrt{\alpha}$ and $\alpha = \frac{m_x}{m_y}$ the Hamiltonian (2) becomes

$$H_{\text{em}} = -\frac{\hbar^2}{2m_x} \left(\frac{\partial^2}{\partial x^2} + \frac{\partial^2}{\partial y'^2} \right) + \frac{e^2 B^2}{8m_y} (x^2 + y'^2) + \frac{eB}{2\sqrt{m_x m_y}} l_z' + V(\rho' - R) + g\mu_B B \sigma_z / 2, \quad (5)$$

TABLE II. The spacing Δ_0 between the lowest-energy levels of even and odd parity for B=0 [see Fig. 4(a)] and the Δ_e width of the avoided crossing between the two lowest-energy levels of even parity [Fig. 4(a)] as a function of the eccentricity parameter α for $B \simeq 7.75$ T. The results are calculated with the tight-binding approach.

α	$\alpha/(m_x/m_y)$	$\Delta_0 \; (\text{meV})$	$\Delta_e ({ m meV})$
1	2.238	0.001	0.673
0.894	2	0.012	0.414
0.536	1.2	0.061	0.137
0.469	1.05	0.096	0.046
0.447	1	0.113	0.013
0.424	0.95	0.104	0.028

with $\rho' = \sqrt{x^2 + y'^2}$ and the z component angular momentum operator in the deformed space $l_z' = i\hbar(y'\frac{\partial}{\partial x} - x\frac{\partial}{\partial y'})$. The confinement potential acquires circular symmetry upon rescaling of the y coordinate and the Hamiltonian commutes with l_z' operator. The crossings of the eigenstates of the effective-mass Hamiltonian are due to the symmetry which upon rescaling of the y coordinate is no longer hidden. The l_z' eigenvalues are given by color in Fig. 5(b). The ground state undergoes l_z' angular momentum transitions similar to the ones found for circular quantum rings with isotropic electron effective mass [26]. Note that the applicability of the l_z' operator is not limited to quantum rings, but it can also be used to any potential profile which is radially symmetric for the rescaled y coordinate.

C. 1D limit

For a narrow radial confinement (large ω) the low-energy part of the spectrum occupies the same state of radial quantization and there is essentially one degree of freedom of motion along the ring. The Hamiltonian (5) put in circular coordinates reads

$$H_{\text{em}} = -\frac{\hbar^2}{2m_x} \left(\frac{1}{\rho'} \frac{\partial}{\partial \rho'} + \frac{\partial^2}{\partial \rho'^2} - \frac{l_z'^2}{\rho'^2} \right) + \frac{B}{2\sqrt{m_x m_y}} l_z' + \frac{e^2 B^2}{8m_y} \rho'^2 + V(\rho' - R),$$
 (6)

where we neglected the spin Zeeman term. For strong confinement (large ω) the radial profile of the wave function no longer depends on l_z' or B. Then, the terms with the derivatives with respect to ρ' and the external potential produce the same energy contribution for all the states involved. With this contribution set as the reference energy level, we obtain the energy spectrum of the form

$$E(l_z', B) = \frac{\hbar^2 l_z^2}{2m_x R^2} + \frac{e^2 B^2}{8m_y} R^2 + \frac{eB}{2\mu} l_z', \tag{7}$$

where $\mu = \sqrt{m_x m_y}$. With $R = (\frac{m_y}{m_x})^{1/4} R_c$ one obtains an expression that is symmetric in the effective masses,

$$E(l'_z, B) = \frac{\hbar^2 l'^2_z}{2\mu R_c^2} + \frac{e^2 B^2}{8\mu} R_c^2 + \frac{eB}{2\mu} l'_z$$

$$= \frac{\hbar^2}{2\mu R_z^2} \left(\frac{\Phi}{\Phi_0} + l'_z\right)^2, \tag{8}$$

where $\Phi_0 = \frac{h}{e} = \frac{2\pi\hbar}{e}$ is the flux quantum and $\Phi = B\pi R_c^2$. The final result with the geometric average of the effective masses is identical to that of the circular ring with an isotropic effective mass [26].

Figure 6 shows the 2D continuum Hamiltonian (6) spectra with the spin Zeeman effect excluded for $\hbar\omega=6$ meV in Fig. 6(a), $\hbar\omega=120$ meV in Fig. 6(b), and the results of the 1D formula in Fig. 6(c). In Fig. 6(a) we see a diamagnetic shift of the spectrum to higher energy. The period of the Aharonov-Bohm oscillations is slightly larger than in the 1D results due to compression of the wave function by the external magnetic field that decreases average ρ' below R_c . For the radial wave

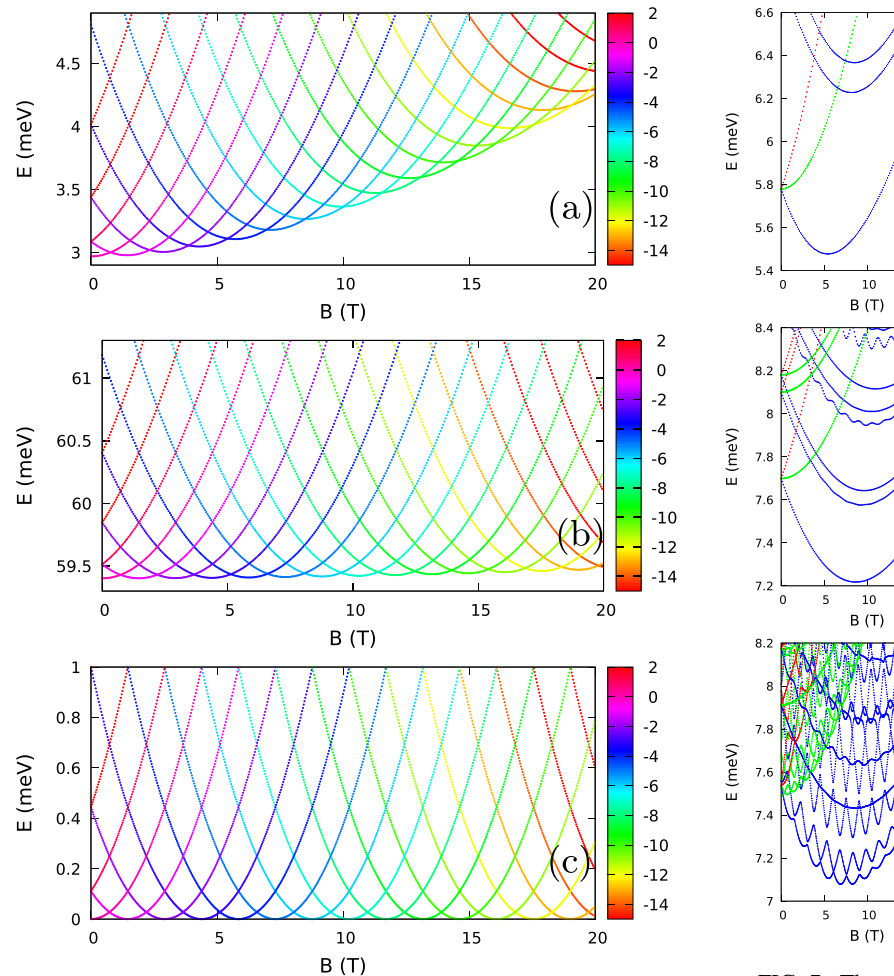


FIG. 6. The energy spectrum of Hamiltonian (5) with g=0 for (a) $\hbar\omega=6$ meV, (b) $\hbar\omega=120$ meV, and (c) the 1D formula (8). The color of the lines gives the l_z' operator eigenvalue.

function confined stronger around R_c in Fig. 6(b), we see the results approach the results for the analytical formula (8).

D. Two-electron spectrum

The electron-electron interaction potential does not commute with the l_z^\prime operator, so the presence of the ground-state oscillations is not given *a priori*. We calculated the two-electron energy spectrum in the continuum approach using the Hamiltonian

$$H_{2e} = H_{\text{em}}(\mathbf{r}_1) + H_{\text{em}}(\mathbf{r}_2) + \frac{e^2}{4\pi\epsilon_0\epsilon} \frac{1}{r_{12}},$$
 (9)

where $H_{\rm em}$ is the single-electron Hamiltonian (2), and $\epsilon = 12$ is taken. The two-electron Hamiltonian is diagonalized in the basis of the two-electron Slater determinants constructed from the 30 lowest-energy single-electron eigenfunctions of Hamiltonian (2).

For both $\alpha = 1$ [Fig. 7(a)] and $\alpha = \frac{m_x}{m_y}$ [Fig. 7(c)] at B = 0 the ground state is fourfold degenerate, with singlet-and triplet-energy levels of the same energy. The exchange interaction is zero since the electrons form single-electron islands that are completely separated. For $\alpha = 1$ the lo-

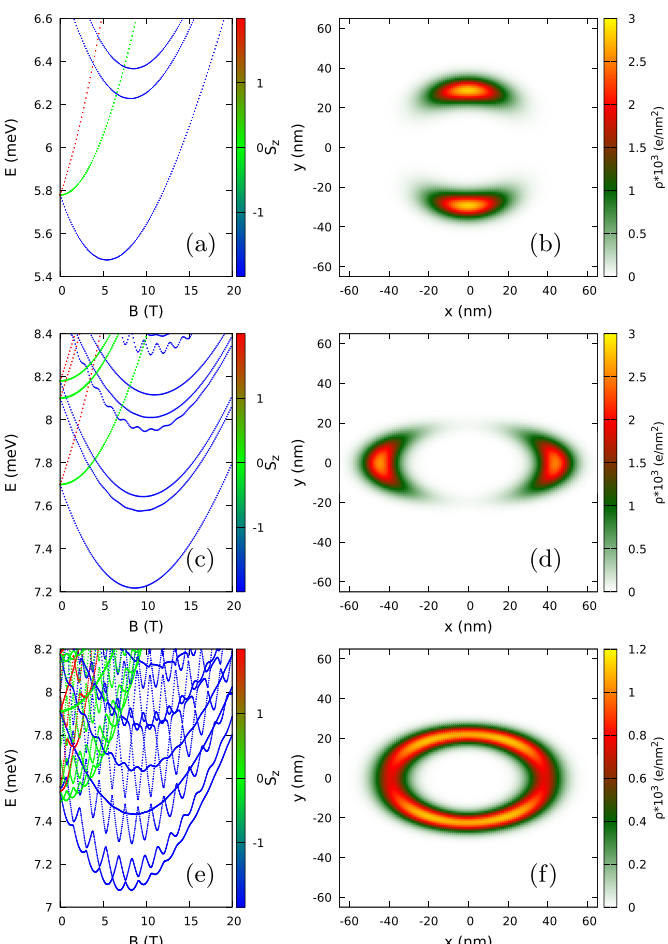


FIG. 7. The two-electron energy spectrum [(a), (c), (e)] and the ground-state charge density [(b), (d), (f)] calculated using continuum model for (a), (b) B=0 and $\alpha=1$, (c), (d) $\alpha=\frac{m_x}{m_y}$, and for (e), (f) $\alpha=1.7\frac{m_x}{m_y}$. In (a), (c), and (e) the color of the lines corresponds to the *z* component of the total spin.

calization of the charge density formed a single-electron island already without interaction [Fig. 2(d)]. For $\alpha = \frac{m_x}{m_y}$ the electron-electron interaction separates the electron density to the opposite ends of the longer semiaxis of the ellipse [Fig. 7(d)]. A more or less uniform electron distribution is obtained for $\alpha = 1.7 \frac{m_x}{m_y}$ [Fig. 7(f)]. In this case, the ground state for B = 0 is a singlet which is not degenerate with the triplet. The field of about 0.5 T promotes the triplet to the ground state. Periodic avoided crossings are observed in the ground state, which are similar to the ones found for a system with an isotropic effective mass but in an anisotropic quantum ring [27]. For the circular ring, the triplet energy levels correspond to odd values of the total angular momentum (L) [28] that correspond to the negative parity $(-1)^L$. In our two-electron system, only the parity is a good quantum number. In Fig. 7(e) we see a series of avoided crossings between the ground state and the first excited state. The avoided crossings obtained for the spin-polarized two-electron levels are observed due to the same—odd—parity of these levels, which is in contrast to the single-electron ground state where the crossings of energy

levels corresponding to opposite parity were observed in the ground state.

E. Discussion

The spectra of confined quantum rings are experimentally studied for annular-shaped traps defined in gated two-dimensional electron gas [29]. The current transport for electron traps weakly coupled to the electron reservoirs is governed by the Coulomb blockade [11,30], with the singleelectron current passing through the system only when the chemical potential of the confined N-electron system falls within the transport window defined by the Fermi levels of the source and drain. The technique can also be used for detection of the excited part of the spectra when the corresponding energy level enters the transport window [29,30]. The transport spectroscopy allows for reconstruction of the energy spectra with a precision of the order of a few μ eV [29] with the Aharonov-Bohm periodicity as the signature of the angular confinement. The gated quantum rings can exhibit an elliptically deformed confinement potential as in Ref. [29] in particular.

The gating techniques for phosphorene have been developed [2,6,7] and applied for fabrication of the field-effect transistors. The ringlike potential can be defined electrostatically in a plane plate capacitor system with a tubular electrode protruding from one of the plate electrodes with the phosphorene layer embedded in a dielectric [31,32]. For a similar gating system defined for electrons on liquid helium surface, see, e.g., Ref. [33].

The results of this paper indicate the way to observe the Aharonov-Bohm effect for the system confined by the external potential in phosphorene. For circular quantum rings the Aharonov-Bohm oscillations can only be observed in the excited part of the spectrum since in the degenerate ground state the electron density forms separated islands and the persistent current circulation is interrupted. For an elliptical deformation of the confinement potential, the oscillations of the ground-state parity appear with the Aharonov-Bohm periodicity. The amplitude of these oscillations has been determined (see Δ_0 in Table II). Based on results of Ref. [29] one can expect that for $\alpha \leq 1.2 \frac{m_x}{m_y}$ the ground-state oscillation should enter the experimental resolution.

For a specifically chosen eccentricity parameter α one can reduce the spectra to those that are characteristic to a circular quantum ring with an isotropic effective mass. We explained this effect analytically in the effective-mass approximation that indicates an additional symmetry found for a value of α and the spectra that agree with the tight-binding ones up to an avoided crossing in the excited energy spectra found in the latter, which is minimal for the optimal value of $\alpha = \frac{m_x}{m_y}$ (see Δ_e in Table II). The width of the avoided crossing should also be accessible for an experimental study.

IV. SUMMARY AND CONCLUSIONS

We have studied the ground-state energy oscillations in a quantum ring potential defined within monolayer black phosphorus with the tight-binding and effective-mass models. In a circular quantum ring, the strong anisotropy of the effective mass produces a ground state localized along the axis related to the heavier mass. The current circulation around is possible for an elliptic ring. A braided pattern of evenand odd-parity energy levels is then observed in the ground state with crossings appearing with the Aharonov-Bohm periodicity. In particular, for the ellipse with the ratio of the semiaxes equal to the effective-masses ratio, the electron density becomes uniform along the ring. Then, the single-electron energy spectrum becomes similar to that of a circular quantum ring with an isotropic effective mass equal to the geometric average of the effective masses along the two crystal directions. We demonstrated that the angular momentum in the rescaled space l_z^\prime is definite in the single-electron Hamiltonian eigenstates. We provided an analytical formula for the spectrum in the 1D limit. The applicability of the l_z' operator exceeds the quantum rings and can be used for modeling other confined systems in phosphorene. For two electrons, an elliptical deformation of the ring produces avoided crossings in the ground state due to the same parity of low-energy spin-polarized states appearing periodically on the magnetic field scale.

ACKNOWLEDGMENTS

This work was supported by the National Science Centre (NCN) according to decision DEC-2019/35/O/ST3/00097. Calculations were performed on the PLGrid infrastructure.

^[1] H. Liu, A. T. Neal, Z. Zhu, Z. Luo, X. Xu, D. Tomanek, and P. D. Ye, ACS Nano 8, 4033 (2014).

^[2] L. Li, Y. Yu, G. J. Ye, Q. Ge, X. Ou, H. Wu, D. Feng, X. H. Chen, and Y. Zhang, Nat. Nanotechnol. 9, 372 (2014).

^[3] S. Fukuoka, T. Taen, and T. Osada, J. Phys. Soc. Jpn. 84, 121004 (2015).

^[4] M. Akhtar, G. Anderson, R. Zhao, A. Alruqi, J. E. Mroczkowska, G. Sumanasekera, and J. B. Jasinski, npj 2D Mater. Appl. 1, 5 (2017).

^[5] G. Zhang, S. Huang, F. Wang, and H. Yan, Laser Photonics Rev. 15, 2000399 (2021).

^[6] D. He, Y. Wang, Y. Huang, Y. Shi, X. Wang, and X. Duan, Nano Lett. 19, 331 (2019).

^[7] X. Li, Z. Yu, X. Xiong, T. Li, T. Gao, R. Wang, R. Huang, and Y. Wu, Sci. Adv. 5, eaau3194 (2019).

^[8] G. Long, D. Maryenko, J. Shen, S. Xu, J. Hou, Z. Wu, W. K. Wong, T. Han, J. Lin, Y. Cai, R. Lortz, and N. Wang, Nano Lett. 16, 7768 (2016).

^[9] G. Long, D. Maryenko, S. Pezzini, S. Xu, Z. Wu, T. Han, J. Lin, C. Cheng, Y. Cai, U. Zeitler, and N. Wang, Phys. Rev. B 96, 155448 (2017).

^[10] J. Yang, S. Tran, J. Wu, S. Che, P. Stepanov, T. Taniguchi, K. Watanabe, H. Baek, D. Smirnov, R. Chen, and C. N. Lau, Nano Lett. 18, 229 (2018).

^[11] R. Hanson, L. P. Kouwenhoven, J. R. Petta, S. Tarucha, and L. M. K. Vandersypen, Rev. Mod. Phys. 79, 1217 (2007).

- [12] V. M. Fomin, Physics of Quantum Rings (Springer, Cham, 2018).
- [13] Y. Aharonov and D. Bohm, Phys. Rev. 115, 485 (1959).
- [14] L. L. Li, D. Moldovan, P. Vasilopoulos, and F. M. Peeters, Phys. Rev. B 95, 205426 (2017).
- [15] R. Schuster, J. Trinckauf, C. Habenicht, M. Knupfer, and B. Büchner, Phys. Rev. Lett. 115, 026404 (2015).
- [16] J. Qiao, X. Kong, Z. X. Hu, F. Yang, and W. Ji, Nat. Commun. 5, 4475 (2014).
- [17] A. N. Rudenko and M. I. Katsnelson, Phys. Rev. B 89, 201408(R) (2014).
- [18] A. N. Rudenko, S. Yuan, and M. I. Katsnelson, Phys. Rev. B 92, 085419(R) (2015).
- [19] P. E. Faria Junior, M. Kurpas, M. Gmitra, and J. Fabian, Phys. Rev. B 100, 115203 (2019).
- [20] X. Zhou, W. K. Lou, D. Zhang, F. Cheng, G. Zhou, and K. Chang, Phys. Rev. B 95, 045408 (2017).
- [21] L. Li, F. Yang, G. J. Ye, Z. Zhang, Z. Zhu, W. Lou, X. Zhou, L. Li, K. Watanabe, T. Taniguchi, and K. Chang, Nat. Nanotechnol. 11, 593 (2016).
- [22] N. Gillgren, D. Wickramaratne, Y. Shi, T. Espiritu, J. Yang, J. Hu, J. Wei, X. Liu, Z. Mao, K. Watanabe, and T. Taniguchi, 2D Mater. 2, 011001 (2014).
- [23] F. Yang, Z. Zhang, N. Z. Wang, G. J. Ye, W. Lou, X. Zhou, K. Watanabe, T. Taniguchi, K. Chang, X. H. Chen, and Y. Zhang, Nano Lett. 18, 6611 (2018).

- [24] B. Szafran, Phys. Rev. B 101, 235313 (2020).
- [25] With $\alpha = \frac{m_x}{m_y}$ for $R_s = 25, 30, 35, \dots, 70$ (in nm) we obtain the lowest conduction-band energy level at 341.066, 340.764, 340.559, 340.415, 340.328, 340.266, 340.184, 340.161, and 340.138 (in meV), respectively.
- [26] S. Viefers, P. Koskinen, P. S. Deo, and M. Manninen, *Physica E* **21**, 1 (2004).
- [27] V. M. Fomin, V. N. Gladilin, J. T. Devreese, N. A. J. M. Kleemans, and P. M. Koenraad, Phys. Rev. B 77, 205326 (2008).
- [28] J.-L. Zhu, Z. Dai, and X. Hu, Phys. Rev. B 68, 045324 (2003).
- [29] A. Fuhrer, S. Luescher, T. Ihn, T. Heinzel, K. Ensslin, W. Wegscheider, and M. Bichler, Nature (London) 413, 822 (2001).
- [30] L. P. Kouwenhoven, C. M. Marcus, P. L. McEuen, S. Tarucha, R. M. Westervelt, and N. S. Wingreen, Electron transport in quantum dots, in *Mesoscopic Electron Transport*, edited by L. L. Sohn, L. P. Kouwenhoven, and G. Schön, NATO Advanced Studies Institute, Series E: Applied Sciences, Vol. 345 (Springer, Dordrecht, 1997).
- [31] W. Dickerson, V. Tayari, I. Fakih, A. Korinek, M. Caporali, M. Serrano-Ruiz, M. Peruzzini, S. Heun, G. A. Botton, and T. Szkopek, Appl. Phys. Lett. 112, 173101 (2018).
- [32] B. Deng, V. Tran, Y. Xie, H. Jiang, L. Cheng, Q. Guo, X. Wang, H Tian, S. J. Koester, H. Wang, J. J. Cha, Q. Xia, L. Yang, and F. Xia, Nat. Commun. 8, 14474 (2017).
- [33] B. Szafran, Phys. Rev. B 104, 235402 (2021).

Chapter 6

Wigner molecules in phosphorene quantum dots

Reprinted with permission from Thakur, T., & Szafran, B. Wigner molecules in phosphorene quantum dots. Physical Review B, 106(20), 205304 (2022). Copyright 2022 by the American Physical Society.

Wigner molecules in phosphorene quantum dots

Tanmay Thakur o and Bartlomiej Szafran o

AGH University of Science and Technology, Faculty of Physics and Applied Computer Science, al. Mickiewicza 30, 30-059 Kraków, Poland



(Received 17 June 2022; revised 2 November 2022; accepted 9 November 2022; published 17 November 2022)

We study Wigner crystallization of electron systems in phosphorene quantum dots with the confinement of an electrostatic origin with both circular and elongated geometry. The large effective masses in phosphorene promote the separation of the electron charges already for quantum dots of relatively small size. The anisotropy of the effective mass allows for the formation of Wigner molecules in the laboratory frame with a confined charge density that has lower symmetry than the confinement potential. We find that in circular quantum dots separate single-electron islands are formed for two and four confined electrons but not for three trapped carriers. The spectral signatures of the Wigner crystallization to be resolved by transport spectroscopy are discussed. Systems with Wigner molecule states are characterized by a nearly degenerate ground state at B = 0 and are easily spin-polarized by the external magnetic field. In electron systems for which the single-electron islands are not formed, a more even distribution of excited states at B = 0 is observed, and the confined system undergoes ground-state symmetry transitions at magnetic fields of the order of 1 T. The system of five electrons in a circular quantum dot is indicated as a special case with two charge configurations that appear in the ground state as the magnetic field is changed: one with the single electron islands formed in the laboratory frame and the other where only the pair-correlation function in the inner coordinates of the system has a molecular form as for three electrons. The formation of Wigner molecules of quasi-1D form is easier for the orientation of elongated quantum dots along the zigzag direction with heavier electron mass. The smaller electron effective mass along the armchair direction allows for freezing out the transverse degree of freedom in the electron motion. Calculations are performed with a version of the configuration interaction approach that uses a single-electron basis that is preoptimized to account for the relatively large area occupied by strongly interacting electrons allowing for convergence speed-up.

DOI: 10.1103/PhysRevB.106.205304

I. INTRODUCTION

Electron gas with Coulomb interactions dominating over the kinetic energies forms a Wigner crystal [1–4]. Its finite counterparts, e.g., Wigner molecules [5–21] are formed in quantum dots at low electron numbers in spatially large systems [5] or in a strong magnetic field that promotes the single-electron localization [22,23].

The confined charge density in quantum dots defined in materials with isotropic effective mass reproduces the symmetry of confinement potential. For this reason in circular quantum dots, separation of the electrons in the Wigner phase occurs only in the inner coordinates of the system spanned by relative electron-electron distances [22]. For lowered symmetry, the Wigner molecules can appear in the laboratory frame [24], with the special case of one-dimensional systems that is studied with much of attention [6,9,16,20,21].

Phosphorene [25–28] is a particularly interesting material for Wigner-molecule physics due to the large electron effective masses and their strong anisotropy [29–35] Large masses reduce the kinetic energy as compared to the electron-electron interaction energy. Lowering the Hamiltonian symmetry by the effective mass anisotropy is promising for observation of the Wigner molecules in the laboratory frame.

Phosphorene quantum dots [36–43] in the form of small flakes have been extensively studied, in particular from

the point of view of optical properties. In this work we consider a clean electrostatic confinement that keeps the confined electrons off the edge of the flake. In finite sheets of graphene, the edges inhibit the Wigner crystallization [12]. Advanced phosphorene gating techniques have been developed [26,28,44–46] for, e.g., fabrication of the field-effect transistors [26,44,45] and experimental studies of the quantum Hall effects [47–50] are carried out. Therefore the formation of clean electrostatic quantum dots [51] in phosphorene is within experimental reach.

Ordering of the electron charge in Wigner molecules of single-electron islands in quasi 1D systems [6,9,16,20,21] reduces the electron-electron interaction energy at the cost of increasing the kinetic energy due to the electron localization. In GaAs systems with low electron band effective mass of 0.067m₀, conditions for Wigner molecule formation occur only in very long systems of hundreds of nanometers [16] already for four electrons. On the other hand, the light electron mass in GaAs favors the reduction of the 2D confinement to an effectively 1D form with all the electrons occupying the same state of quantization for the transverse motion. Hence, the large effective masses in phosphorene are promising for producing the Wigner molecules in systems of relatively small sizes, but may inhibit formation of 1D confinement.

In this paper, we consider the formation of Wigner molecules in the laboratory frame for a few electrons confined

in circular and elongated quantum dots for varied confinement orientation and look for spectral signatures of Wigner crystallization to be experimentally resolved. We use the configuration interaction approach [7,52–55] that requires an optimized single-electron basis [56–58] for convergence due to the strong electron-electron interaction effects [59] in phosphorene.

This paper is organized as follows. In the Theory section, we describe the applied computational approach. In the Results section, we first describe the results for circular quantum dots and next the Wigner molecules in quasi-one-dimensional confinement oriented along the zigzag and armchair crystal directions. Section IV contains the discussion of the experimentally accessible signatures of the Wigner molecule formation in the laboratory frame. Summary and conclusions are given in Section V. In the Appendix, we include details on the single-electron wave functions used for optimization of the basis, the choice of the computational box, and the spectra without the Zeeman interaction.

II. THEORY

In this section, we describe the finite difference method applied to the continuum Hamiltonian of a single electron in phosporene (Sec. II A), the model potential (Sec. II B), and the configuration interaction approach (Sec. II C) with optimization of the single-electron basis allowing for faster convergence of the configuration interaction approach. Section II D describes the formula for extraction of the charge density and pair correlation functions for discussion of the Wigner crystallization of the confined system.

A. Single-electron Hamiltonian

We use the single-band approximation for Hamiltonian describing the electrons of the conduction band of monolayer phosphorene [35,60]

$$H_{0} = \left(-i\hbar \frac{\partial}{\partial x} + eA_{x}\right)^{2} / 2m_{x} + \left(-i\hbar \frac{\partial}{\partial y} + eA_{y}\right)^{2} / 2m_{y} + W(x, y) + g\mu_{B}B\sigma_{z}/2,$$
(1)

where W(x, y) is the confinement potential. In Eq. (1), we use the effective masses $m_x = 0.17037m_0$ for the armchair crystal direction (x) and $m_y = 0.85327m_0$ for the zigzag direction (y). The values for the masses were determined in Ref. [35] by fitting the confined energy spectra of the continuum singleband Hamiltonian to the results of the tight-binding method. A detailed comparison of the spectra as obtained by the continuum model to the tight-binding ones is given in Ref. [35] for the harmonic oscillator potential and in Ref. [60] for the annular confinement. In Eq. (1), we take the Landé factor $g = g_0 = 2$ after the k · p theory of Ref. [33]. The values of experimentally extracted g-factors vary; in particular an increase with respect to g_0 was reported [59] at low filling factors, which is attributed [33,59] to strong electron-electron interaction effects in black phosphorus. The electron-electron interaction in this work is treated in an exact manner. The spin Zeeman term leads to the spin polarization of the confined system. The exact value of the magnetic field producing the spin polarization is affected by the adopted g-factor value,

but no qualitative effect for the Wigner crystallization of the charge density is expected as long as the spin-orbit coupling is absent. The spectral features of Wigner crystallization for g = 0 are discussed in Appendix.

We work with a square mesh with a spacing Δx in both the x and y directions. The Hamiltonian acting on the wave function $\Psi_{\mu,\eta} = \Psi(x_\mu,x_\eta) = \Psi(\mu\Delta x,\eta\Delta x)$ in the finite-difference approach reads

$$H_{0}\Psi_{\mu,\eta} \equiv \frac{\hbar^{2}}{2m_{x}\Delta x^{2}} (2\Psi_{\mu,\eta} - C_{y}\Psi_{\mu,\eta-1} - C_{y}^{*}\psi_{\mu,\eta+1})$$

$$+ \frac{\hbar^{2}}{2m_{y}\Delta x^{2}} (2\Psi_{\mu,\eta} - C_{x}\Psi_{\mu-1,\eta} - C_{x}^{*}\psi_{\mu+1,\eta})$$

$$+ W_{\mu,\eta}\Psi_{\mu,\eta} + \frac{g\mu_{B}B}{2}\sigma_{z},$$
(2)

where $C_x = \exp(-i\frac{e}{\hbar}\Delta x A_x)$ and $C_y = \exp(-i\frac{e}{\hbar}\Delta x A_y)$ introduce the Peierls phases [61] for the description of the orbital effects of the perpendicular magnetic field (0, 0, B). For calculation of the phase shifts, we use the symmetric gauge $\mathbf{A} = (A_x, A_y, A_z) = (-By/2, Bx/2, 0)$. Hamiltonian (2) is diagonalized in a finite computational box with the infinite quantum well set at the end of the box (see Appendix).

B. Model potential

For evaluation of a realistic confinement potential W, we use a simple model with a phosphorene plane embedded in a Al₂O₃ dielectric that fills the area between two parallel electrodes [Figs. 1(a) and 1(b)]. A higher (lower) potential energy for electrons is introduced at the top (bottom) electrode. The bottom electrode is grounded and contains a protrusion that approaches the phosphorene layer. As a result, the electrostatic potential within phosphorene forms a cavity that traps the electrons of the conduction band. The model is a variation [62,63] of a gated GaAs quantum dot of Ref. [64]. Below we use two models: one with a circular protrusion [Fig. 1(a)] and the other with a rectangular one [Fig. 1(b)]. The latter is used in the following to study the case close to the 1D confinement. The confinement potential to be used in the Hamiltonian is given by $W(x, y) = -eV(x, y, z_p)$, with the electrostatic potential V that we evaluate by solving the Laplace equation $-\nabla^2 V = 0$ and z_p is the coordinate of the phosphorene layer. For evaluation of the potential we use the finite element method similar to the one applied in Ref. [63] for a charge-neutral phosphorene plane. The confinement potential at the monolayer is plotted in Fig. 1(c) for the circular protrusion of Fig. 1(a) and in Fig. 1(d) for the rectangular protrusion of Fig. 1(b).

C. Diagonalization of the N-electron Hamiltonian

The system of N-confined electrons is described with the Hamiltonian

$$H_N = \sum_{i=1}^{N} H_0(i) + \sum_{j>i}^{N} \frac{e^2}{4\pi \epsilon_0 \epsilon \, r_{ij}} \,. \tag{3}$$

We take the dielectric constant $\epsilon = 9$ assuming that the phosphorene is embedded in Al_2O_3 .

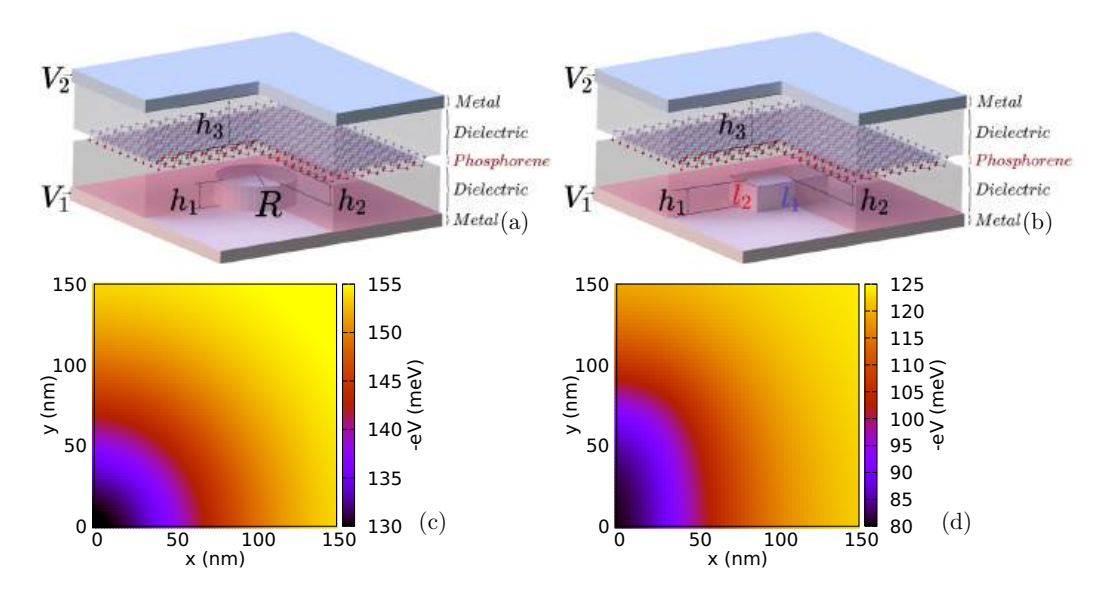


FIG. 1. Schematics of model systems for evaluation of the confinement potential. The phosphorene monolayer is embedded in a dielectric that fills the space between electrodes of the plane capacitor configuration. The lower metal electrode contains a circular (a) or rectangular (b) protrusion. The upper electrode is kept at a higher potential energy $-eV_2 = 0.25$ eV for the electrons than the lower one $-eV_1 = 0$. The protrusion introduces an inhomogeneity of the electric field within the capacitor that forms the confinement potential for the electrons of the conduction band. We use $h_1 + h_2 + h_3 = 150$ nm and $h_1 = 50$ nm. For the circular protrusion (a) we take $h_2 = 50$ nm and for the rectangular one (b) $h_2 = 30$ nm. The radius of the protrusion in (a) is R = 50 nm, and the sides of the rectangle in (b) have lengths $l_1 = 80$ nm and $l_2 = 30$ nm. The confinement potential on the phosphorene plane is plotted in (c) and (d) for the circular and rectangular protrusions, respectively. The origin in (c) and (d) is the symmetry center of the protrusion.

standard configuration-interaction [7,52–55] the N-electron Hamiltonian is diagonalized on the basis of Slater determinants constructed with the single-electron Hamiltonian H_0 eigenstates. Each of the Slater determinants defines a configuration, e.g., a distribution of electrons over the single-electron states. The number of Slater determinants to be used in the calculation is established by a study of the convergence of the energy estimates. Reaching convergence in the present calculation is challenging because of the strong electron-electron interaction in phosphorene [59]. The energy of the ground state estimated for N=4 at B = 0 in the circular potential of Fig. 1(c) is plotted with the black line in Fig. 2(a) as a function of the number of the lowest-energy single-electron states ν that span the Slater determinant basis. The Hamiltonian H_N commutes with the operator of the z component of the total spin and also with the parity operator due to the point symmetry of the potential. The symmetries allow for a few-fold reduction of the number of basis elements. In Fig. 2, the four-electron ground state at B = 0 is the spin singlet $S_z = 0$ of an even spatial parity. Only Slater determinants of these symmetries contribute to the ground-state wave function. For $\nu = 60$, the Slater determinants set counts $\binom{60}{4} = 487 635$ elements, of which only about 94 500 determinants correspond to $S_z = 0$ and either even or odd parity. The right vertical axis in Fig. 2(a) shows the number of Slater determinants of the spin-parity symmetry that are compatible with and contribute to the ground state.

The convergence of the CI method using the H_0 single-electron eigenstates (black line in Fig. 2(a)) is slow. The electron-electron interaction has a pronounced effect on the electron localization, since the electrons in phospho-

rene are quite heavy as compared to those in, e.g., GaAs, and the deformation of the charge density in terms of the single-electron energy is cheap. This in turn results in a high numerical cost of the convergent calculations that require a large number of single-electron states to be included in the convergent basis. Therefore, due to the strong electronelectron interaction, the set of H_0 eigenstates is not the best starting point for a convergent CI calculation. The literature indicates a number of methods to speed-up the convergence, including the HF+CI method [56-58] where the basis for the CI method is based on the Hartree-Fock single-electron spin-orbitals. In the HF+CI approach, the mean-field effects of the electron-electron interaction are accounted for already in the single-electron basis and the CI is responsible only for description of the electron-electron correlation effects that evade the mean-field treatment. The HF charge density in the unrestricted version of the method breaks the symmetry of the confinement potential and its restoration is challenging [65,66] on its own at the CI stage. Convergence speed-up by the choice of the single-electron basis is achieved [67,68] with the natural orbitals [69,70] introduced by Löwdin [71].

In this work, we apply a simple approach that allows for the convergence speed-up by replacing the potential W in H_0 by another potential that produces single-electron wave functions of the low-energy spectrum that cover a larger area than the ones for the bare potential W. For preparation of the single-electron basis, we diagonalize the single-electron Hamiltonian H_0' with the potential

$$W' = W + V_0 \exp(-(x^2 + y^2)/d^2).$$
 (4)

The H'_0 , eigenfunctions are used for the Slater determinants to diagonalize the Hamiltonian H_N . V_0 and d of Eq. (4) are

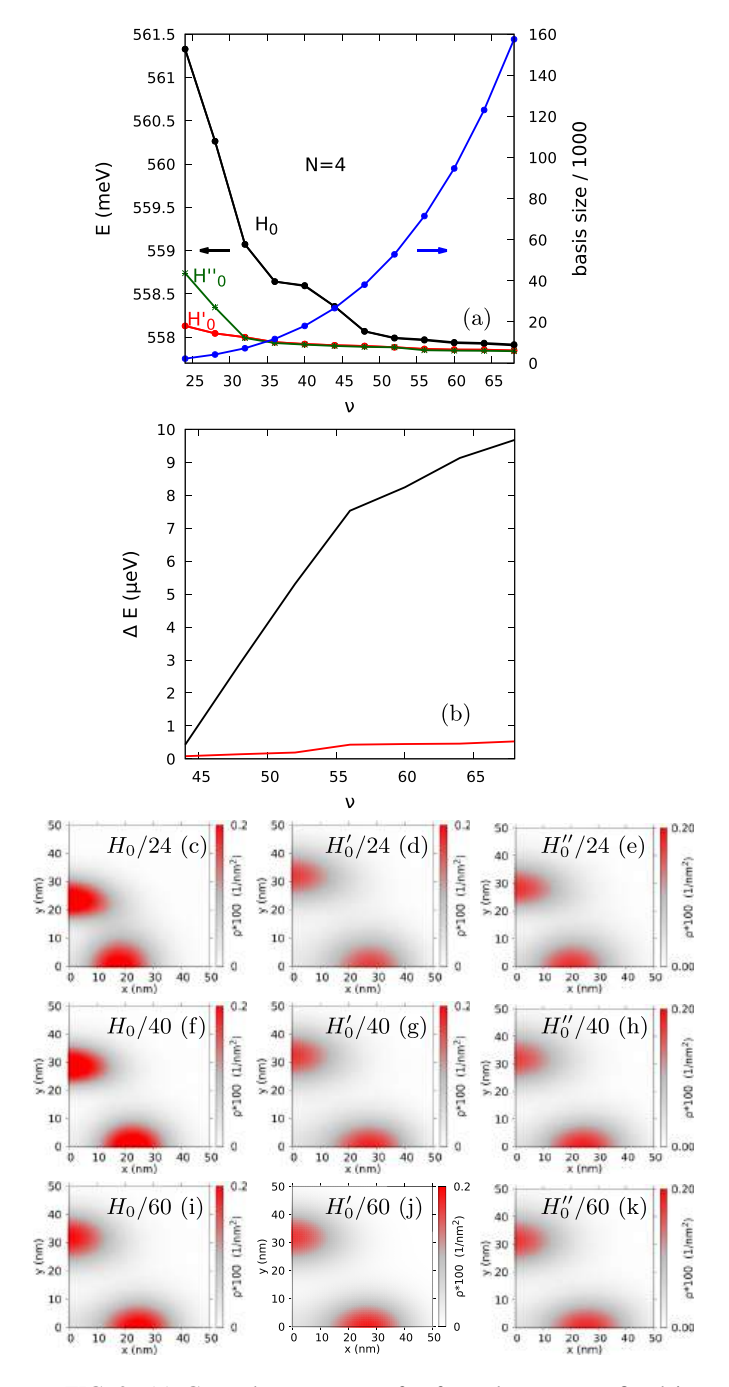


FIG. 2. (a) Ground-state energy for four electrons confined in circular quantum dot as a function of the number of single-electron eigenstates used for construction of the basis for B=0. For the black (red) line, the eigenstates of the single-electron Hamiltonian H_0 (Hamiltonian H_0) with the bare confinement (confinement with a central Gaussian with $V_0=8$ meV and $\sigma=35$ nm were used). (b) Energy shift that appears when the states with triple or quadruple excitations above the single-electron 32nd energy level are excluded from the basis constructed using H_0 (black) and H_0' (red) eigenstates. [(c)–(k)] The ground-state charge density in the x>0, y>0 quarter of the QD as obtained using the Slater determinants basis constructed with H_0 [(c), (f), and (i)], H_0' [(d), (g), and (j)], and H_0'' [(e), (h), and (k)] Hamiltonians using v=24 [(c)–(e)], 40 [(f)–(h)], and 60 [(i)–(k)] lowest-energy single electron wave functions.

used as variational parameters in terms of the *N*-electron energy [72]. The results for four electrons and the basis of the H_0' eigenstates for optimized Gaussian parameters given by the red line in Fig. 2(a) exhibit a substantial convergence speed-up with respect to H_0 basis. In particular, the basis of H_0' eigenstates with $\nu=36$ and about 12 thousand elements produce a similar ground-state energy estimate as the H_0 basis with $\nu=52$ and as much as about 53 thousand Slater determinants.

Figure 2(a) contains also the results obtained with eigenfunctions of Hamiltonian H_0'' (green line) using potential W''(x, y) = W(x)/s, where s is the scaling factor of the bare potential with its variationally optimal value of s = 2.13. The scaling enlarges the area covered by the low-energy single-electron wave functions in a manner that becomes equivalent in terms of the four-electron ground-state energy for the one using W' potential for v > 32. The low-energy single-electron wave functions for W, W', and W'' potentials are given in Appendix.

Figures 2(c)-2(k) shows the ground-state charge density in the x>0, y>0 quarter of the QD as obtained for $\nu=24$ (first row of plots), 40 (second row of plots), and 60 (third row of plots) with the H_0 (left column), H_0' (central column), and H_0'' (right column) eigenfunctions. For $\nu=60$ the results are similar for all the three bases. For lower ν , the results for H_0 [Figs. 2(c) and 2(f)] and H_0'' [Fig. 2(e)] the islands appear closer to the origin than in the convergent result.

In order to illustrate the role of the modified potential in the description of the electron-electron interaction, we plotted in Fig. 2(b) the energy overestimate that is obtained once the basis of Slater determinants is reduced by exclusion of all configurations with more than two electrons [56] above the 32nd single-electron energy level. For the Hamiltonian H_0 , the cost of the limited basis is much larger than for H'_0 and grows fast with ν . For H'_0 the overestimate is much lower. The single-electron effects due to W' potential are included in the basis, and the double excitations that stay in the basis cover most of the electron-electron correlation effects. A similar result is obtained in the HF+CI method [57,58].

D. Charge density and pair correlation function

For analysis of the electron localization, we extract the charge density and the pair correlation function from the N-electron wave function Ψ . The charge density is obtained as

$$\rho(\mathbf{r}) = \langle \Psi | \sum_{i=1}^{N} \delta(\mathbf{r}_{i} - \mathbf{r}) | \Psi \rangle.$$
 (5)

The pair correlation function extracts the relative localization of the electrons with one of the carrier positions fixed

$$\rho_{12}(\mathbf{r}, \mathbf{r}_f) = \langle \Psi | \sum_{i,i=1}^{N} \delta(\mathbf{r}_i - \mathbf{r}) \delta(\mathbf{r}_j - \mathbf{r}_f) | \Psi \rangle.$$
 (6)

In the following, we fix the position \mathbf{r}_f of one of the electrons near the local charge density maximum for a discussion of ρ_{12}

plots. The spin density can be calculated as

$$\rho^{\alpha_i}(\mathbf{r}) = \langle \Psi | \sum_{i=1}^N \delta(\mathbf{r}_i - \mathbf{r}) | \alpha_i \rangle \langle \alpha_i | | \Psi \rangle, \qquad (7)$$

where the projection on the spin eigenstates uses $|\alpha_i\rangle$ that stands for the single-electron spin eigenstate for *i*th electron. Similarly, the relative localization including the spin configuration of the electron pair can be included in the ρ_{12} pair-correlation function. In particular, opposite spin distribution can be obtained using spin projections

$$\rho_{12}^{\uparrow\downarrow}(\mathbf{r}, \mathbf{r}_f) = \langle \Psi | \sum_{i,j=1}^{N} \delta(\mathbf{r}_i - \mathbf{r}) \delta(\mathbf{r}_j - \mathbf{r}_f) \times (|\alpha_i \beta_f\rangle \langle \alpha_i \beta_f| + |\beta_i \alpha_f\rangle \langle \beta_i \alpha_f|) \Psi \rangle, \quad (8)$$

with the spin eigenstates $|\alpha\rangle \neq |\beta\rangle$.

III. RESULTS

In this section, we first (Sec. III A) discuss case for the circular external potential where the formation of Wigner molecules in the laboratory frame occurs due to anisotropy of the effective mass. Section III B contains the results for an elongated confinement potential near the quasi 1D confinement limit.

A. Circular potential

We discuss first the relatively simple case for $N \le 4$ (Sec. III A 1) where in the low-energy states the Wigner molecule formation in the laboratory frame is present (N = 2 and 4) or absent N = 3. Section III A 2 covers the case for N = 5 where states of both types are present in the low-energy part of the spectrum.

1. Results for $N \leq 4$ electrons

The energy spectra for the circular potential [see Fig. 1(c)] are plotted in Fig. 3. For N = 1 [Fig. 3(a)], the energy levels for B = 0 are degenerate with respect to spin. For N = 2 [Fig. 3(b)], the ground state is an even parity spin singlet which is replaced by an odd-parity spin-polarized triplet for $B \simeq 0.25$ T. The energy spacing between the lowest-energy states in Figs. 3(b)-3(f) are much smaller than for the single-electron spectra, which is a signature of strong electron-electron interaction [73]. The spin triplets that we find correspond to odd spatial parity which is characteristic to the two-electron system [19].

For N=3 electrons [Fig. 3(c)], three different symmetry states appear in the ground state starting from an odd-parity spin doublet for B=0. Above 1 T the ground state becomes spin-polarized first in the odd parity and next, above $\simeq 4$ T, in the even parity state.

For N=4 [Fig. 3(d)], the ground state at B=0 is nearly degenerate with respect to the parity and the spin. The ground state at B=0 is an even parity singlet. The spin polarization in the ground state appears already for $B \simeq 0.03$ T.

The results for $N \in [2, 4]$ can be summarized in the following manner.

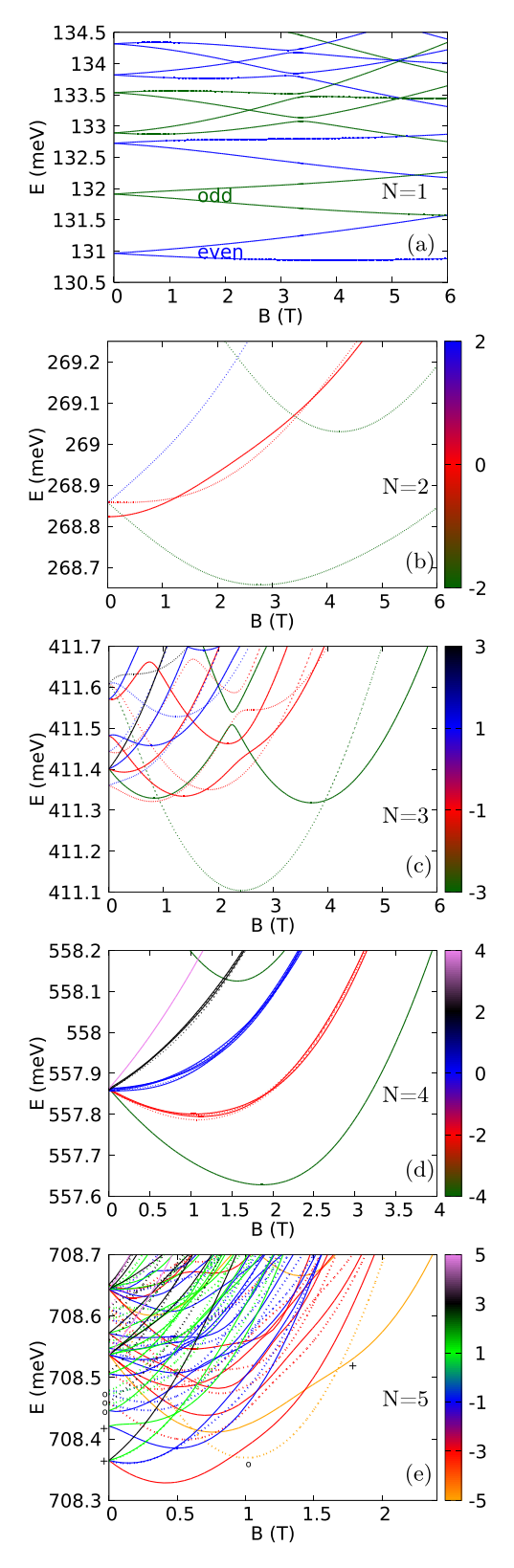


FIG. 3. Spectra for circular potential for N=1 (a), 2 (b), 3 (c), 4 (d), and 5 (e) electrons. In (a), even and odd parity energy levels are plotted with blue and green lines, respectively. In (b)–(e), the even parity energy levels are plotted with the solid lines and the odd parity energy levels with the dotted lines. In (e), the symbols of '+' and 'o' mark the states with (1,4) and (0,4) charge configurations, respectively (see text). The color scale is separate for each figure and given to the right of the plot.

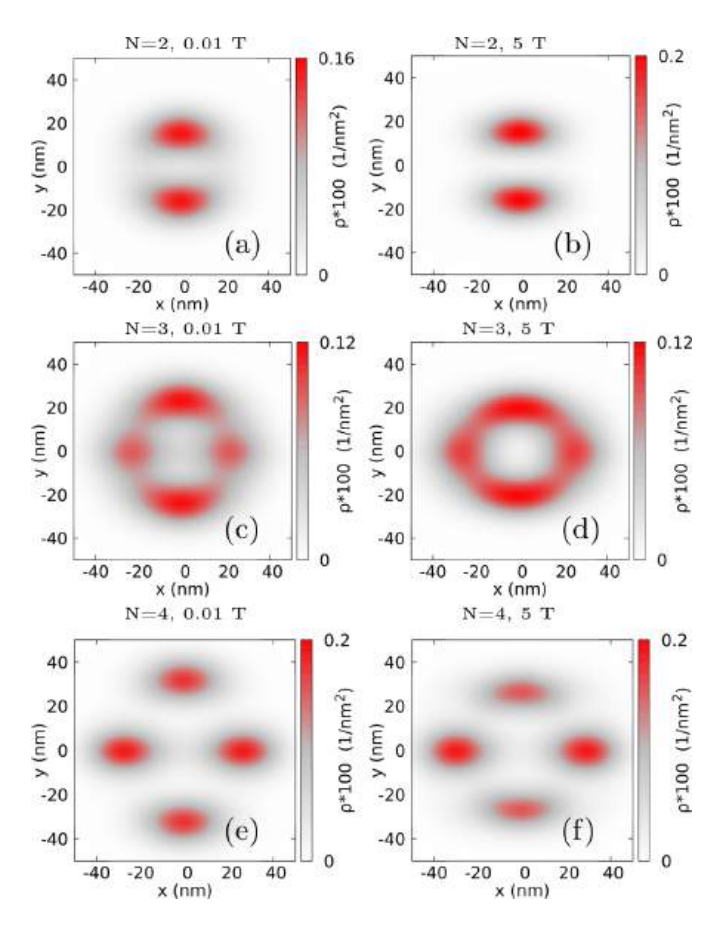


FIG. 4. The ground-state charge density in the circular confinement for N=2 [(a) and (b)], 3 [(c) and (d)], and 4 [(e) and (f)] for B=0.01 (left column) and 5 T (right column).

(i) For even N the spectrum at B=0 contains a few nearly degenerate energy levels near the ground state. Already a low magnetic field of a fraction of tesla leads to a complete spin polarization in the ground state. The systems with N=2 and 4 are also similar from the point of view of the Wigner molecular charge density, which contains separate N single-electron islands [Figs. 4(a), 4(b) and 4(e), 4(f)].

(ii) For N=3 the ground state at B=0 is exactly twofold degenerate with respect to the spin, and a few ground-state transitions appear in the field of the order of a few tesla before the high field symmetry is established. The charge density exhibits 4 local charge maxima Figs. 4(c) and 4(d). These are not the single-electron islands. Furthermore, the charge density is smeared over the area between the maxima [Figs. 4(c) and 4(d)] and does not vanish as effectively as for even N [Figs. 4(a) and 4(b)] The three-electron charge density is not ordered in the Wigner-molecule form.

The effects of the electron-electron correlation in the localization of the carriers can be observed in the pair-correlation function plots given in Fig. 5. For these plots, we fix the position of one of the electrons [see \mathbf{r}_f in Eq. (6)] that is marked by the cross in each panel of Fig. 5. For illustration of the system reaction to the electron position, we fixed one of the electrons slightly off the local density maxima of Fig. 5 near the left (top) edge of the charge distribution in the left (right) column of Fig. 5. For three electrons [Figs. 5(a) and 5(b)]

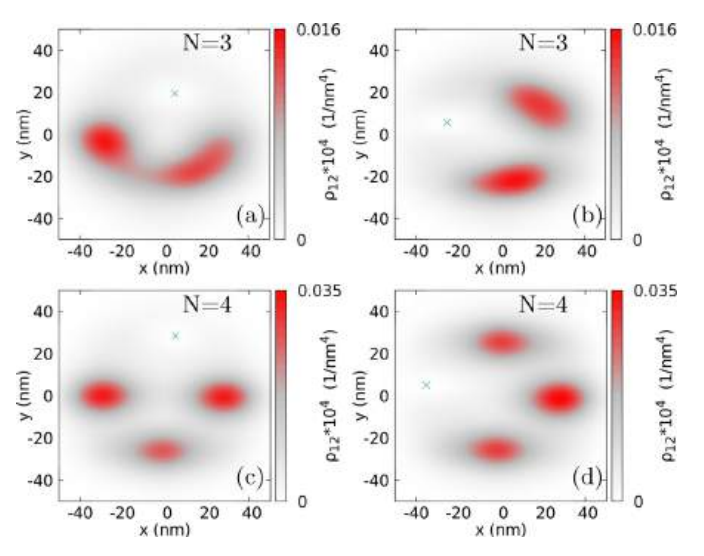


FIG. 5. Pair correlation function plots for the circular confinement potential. The spin-polarized ground state at B=5 T is considered. The crosses indicate the position of the fixed electron [see Eq. (6)].

the conditional probability exhibits two separate maxima. The maxima move once the fixed electron position is changed [cf. Figs. 5(a) and 5(b)], which corresponds to the ringlike charge distribution in Figs. 4(c) and 4(d). On the other hand, for N = 4, the probability maxima at the right and bottom edges of the quantum dot stay in the same place when the fixed electron position is changed [Figs. 5(c) and 5(d)]. Note that for N = 4, the charge density produces the pronounced single-electron maxima [Figs. 4(e) and 4(f)].

For N=3, the single-electron islands forming a Wigner molecule in the real space are not observed since the number of local charge maxima is not equal to N [Figs. 4(c) and 4(d)]. The single-electron charge maxima can appear in the real space when the symmetry of the confinement potential is lowered [24] by, e.g., an off-center impurity. We use a weak Gaussian perturbation introduced to the confinement potential used in H_0 ,

$$V_p(x, y) = D \exp(-(x^2 + (y - y_0)^2)/R_p^2),$$
 (9)

with parameters D = 0.125 meV, $R_p = 5$ nm, and $y_0 = 20$ nm.

We considered the spin-polarized states at the magnetic field, near the ground-state symmetry transition from even to odd parity, below 4 T for N=3 [Fig. 3(c)]. The blue lines in Fig. 6 present the energy levels of a clean system adopted from Fig. 3(c). The red lines show the energy levels for the perturbed system. The off-center Gaussian impurity opens avoided crossings between the energy levels (Fig. 6), which for the clean potential correspond to opposite parity.

The charge density for the ground (excited) state of N=3 is given in Figs. 7(a)–7(c) for the magnetic field that is swept across the avoided crossing. The charge density outside the avoided crossing [Figs. 7(a), 7(c), 7(d), and 7(f)] produces four maxima along the ringlike charge distribution, which deviates from the point symmetry due to the V_p potential. At the avoided crossing the wave functions from otherwise crossing levels mix. In the ground state [Fig. 7(b)], three well-separated

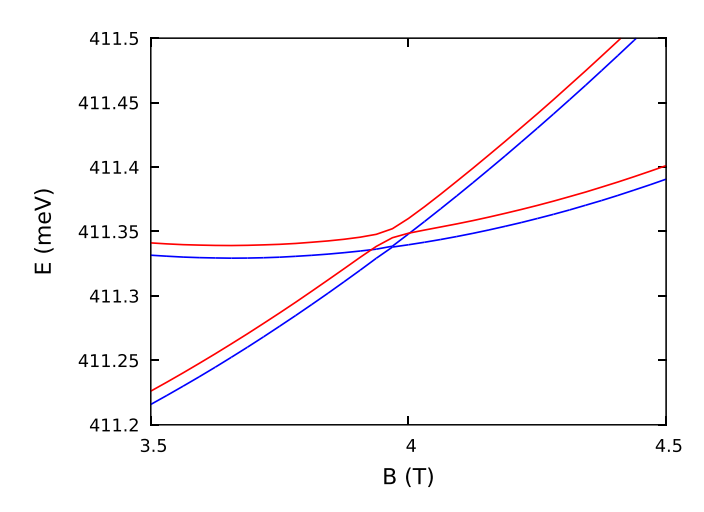


FIG. 6. The energy spectra with (red lines) and without (blue lines) a Gaussian impurity [Eq. (9)] that perturbs the circular symmetry of the confinement potential. The energy levels for the clean system (blue lines) are taken from Fig. 3(c). In Eq. (9), we apply D = 0.125 meV, $y_0 = 20$ nm, and $R_p = 5$ nm.

single-electron islands appear and the charge density is low at the center of the perturbation $[(x, y) = (0, y_0)]$. The excited state [Fig. 7(e)] at the avoided crossing produces a Wigner molecule that is rotated by the π angle. In this sense, the even and odd-parity N=3 states for a clean potential can be understood as superposition of states producing Wigner crystallization in real space with two equivalent but rotated charge distribution. This result for three electrons in circular potential but anisotropic effective mass is similar to the ones found previously for isotropic mass but anisotropic confinement potential [74,75].

2. Five-electron system in the circular quantum dot

The five-electron systems has a more complex structure than systems with two to four electrons due to two charge distributions that appear in the low-energy spectrum [see Fig. 3(e)]. In the ground state at B = 0, we find six nearly de-

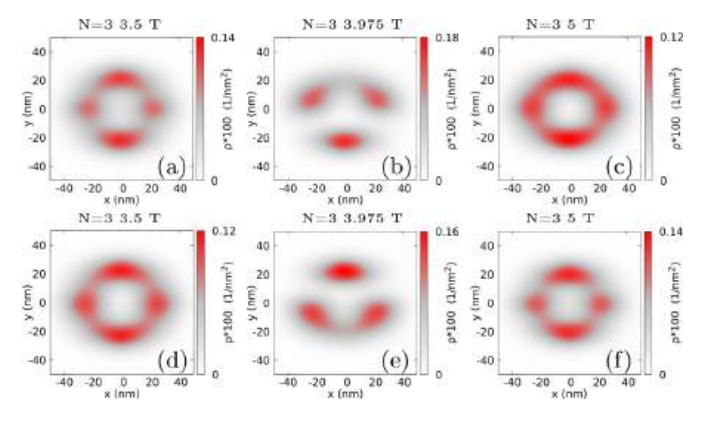


FIG. 7. The charge density for N=3 [(a)–(f)] levels marked in red in Fig. 6 for the circular quantum dot with an off-center Gaussian impurity. The first row [(a)–(c)] shows the data for N=3 ground state. The excited state for 3 electrons is shown in the second row [(d)–(f)]. The central column [(b) and (e)] shows the results at the center of the avoided crossing displayed in Fig. 6.

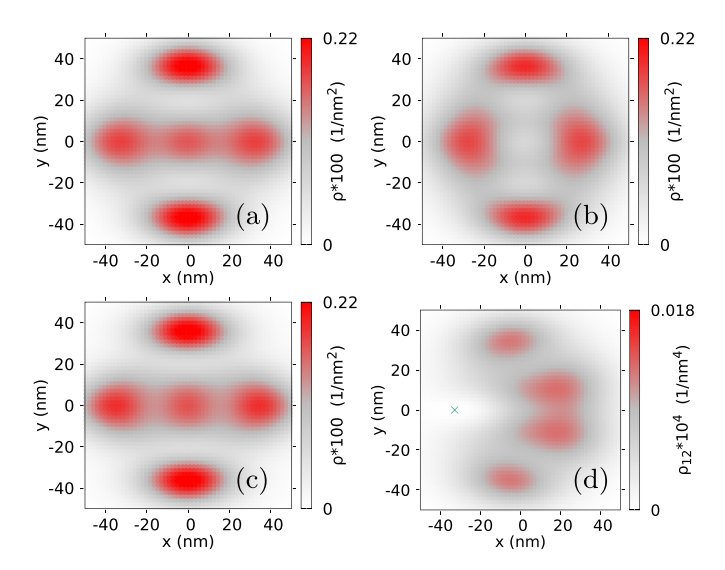


FIG. 8. The ground-state charge density for N = 5 electrons in B = 0.01 (a), 1 (b), and 1.75 T (c)—see the spectrum in Fig. 3(e). In (d), we plot the pair correlation function for the state of (b) one of the electrons fixed at the position marked by the cross.

generate energy levels: a $S_z = \pm 1$ odd-parity doublet slightly below $S_z = -3$, -1, 1, 3 even parity quartet. The charge density in all these energy levels is organized in the Wigner molecule form that is plotted in Fig. 8(a) with one central electron island and four others shifted off the center of the QD forming a crosslike structure that we will denote as (1,4). The near degeneracy of the ground state is a counterpart of the four-electron ground state for N = 4, where the Wigner molecule is also found. For five electrons the first excited energy level at B = 0 is a even parity $S_z = \pm 1$ doublet also with (1,4) charge distribution. In several higher excited energy levels the states at the energy of $\simeq 708.45$ meV the charge density is organized in a ringlike structure with four charge density maxima without the single-electron islands. We will denote this structure as (0,4). In higher excited levels, the states with (1,4) and (0,4) structure interlace on the energy scale. For B > 0.9 T, the ground state becomes fully spinpolarized [Fig. 3(e)] and the (0,4) structure [Fig. 8(b)] appear in the ground state. Above 1.7 T the spatial parity of the ground state change from odd to even and the (1,4) structure [Fig. 8(c)] reappears in the ground state. In presence of both types of states near the ground state—with and without single-electron islands in the laboratory frame—the spectrum contains the features of both N = 2, 4 (ground state near degeneracy at B = 0) and symmetry transformations at higher field as for N = 3.

The (0,4) state for five electrons has a similar character as the three-electron ground state. For three electrons, the charge density is a superposition of two equivalent configurations one being an inversion of the other. The five-electron charge configurations with the (0,4) state correspond to the superposition one or two electrons at the right/left ends of the charge density near y=0 line. One of the two equivalent structures for five electrons can be observed in the pair correlation function plot of Fig. 8(d) for one of the electrons fixed at point (-29.4 nm,0).

B. A linear confinement

We discuss two perpendicular orientations of the elongated quantum dot to study the interplay of the potential and effective mass anisotropies.

1. Confinement along the zigzag direction

The spectra for the potential of Fig. 1(d) with the confinement potential elongated along the y axis, i.e. in the direction where the effective mass is larger, are given in Fig. 9. The numbers (n_x, n_y) given in Fig. 9(a) near the energy levels at B = 0 (for B = 0 and N = 1 the parity with respect to inversion along the x and y axes of the H_0 eigenstates are definite). The first excitation within x, the direction of thinner confinement, occurs 3 meV above the ground state [see the energy level marked by (1,0) in Fig. 9(a)] above five states excited in the y direction. For N = 2 [Fig. 9(b)], the singlettriplet ground state the degeneracy is nearly perfect at B = 0. For B > 0, the $S_z = 0$ state remains twofold degenerate with spin-singlet and spin-triplet energy levels that coincide in energy. The separation of the electron charges [Fig. 10(a)] is complete, and the system is effectively equivalent to a pair of electrons in a double quantum dot with vanishing tunneling between the dots, which produces a vanishing exchange energy [19,76,77]. The ground-state degeneracy at B = 0 is also obtained for N = 3 [Fig. 9(c)]. The Wigner crystallized charge density of the three-electron system at B = 0 is shown in Fig. 10(b). Parity has no significant impact on energy once the electron charges are separated and the $S_z = \pm 1$ energy levels are twofold degenerate with respect to parity. Low-energy spin-polarized states $S_z = \pm 3$ occur only in the odd parity.

For N=4, the ground state at B=0 is only close to the degeneracy [Fig. 9(d)] with the even parity ground state at B=0. The spin polarization $S_z=\pm 4$ occurs only in even parity states. The structure of the low-energy spectrum is similar to the one found for the circular quantum dot [Fig. 3(e)] with even-odd parity splitting of energy levels reduced almost to zero

The results of Figs. 9(c) and 9(d) for B > 0 indicate that for N = 3 (N = 4) the low-energy spin-polarized energy levels occur only with the odd (even) parity symmetry. This is in agreement with Ref. [16] that indicated that in 1D Wigner molecules for N = 2M or N = 2M + 1 with integer M the low-energy spin-polarized state has the spatial parity that agrees with the number M. Note that for N = 3 in the circular potential [Fig. 3(c)], for which the Wigner molecules were not formed in the real-space charge density, both odd and even parity spin-polarized states appear in the ground state for a range of magnetic field.

2. Confinement along the armchair direction

For the rectangular gate of Fig. 1(a) with the longer side oriented along the x direction, the electron mass along the dot is light and in the transverse direction the mass is heavy. For the preceding subsection with confinement along the zigzag direction [Fig. 9(a)], several lowest energy single-electron states correspond to the same—ground state—energy level of the quantization in the direction perpendicular to the quantum dot axis. For the confinement along the armchair direction, the large m_y mass allow the states with excitations in the

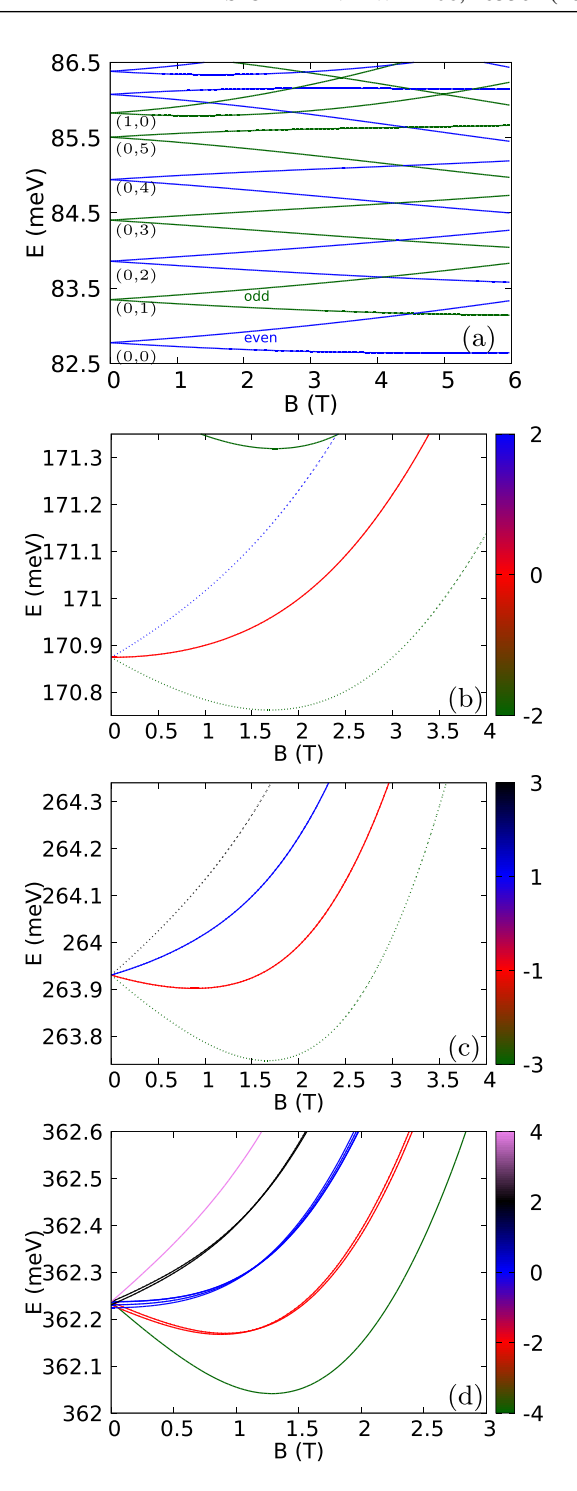


FIG. 9. Spectra for the potential of Fig. 1(d) elongated along the zigzag crystal direction (y) for N = 1 (a), 2 (b), 3 (c), and 4 (d). In (a), even and odd parity levels are plotted with blue and green lines, respectively. Notation (n_x, n_y) close to B = 0 shows the number of excitations (sign changes) in the wave function at 0T. In (b)–(e), the even parity levels are plotted with the solid lines and the odd parity levels with the dotted lines. The color of the lines stands for S_z . The color of the lines in (b)–(d) shows the S_z value.

direction perpendicular to the confinement axis to appear low in the energy spectrum [Fig. 11(a)]. The first single-electron state excited in the transverse direction is the second excited energy level in Fig. 11(a) [see the energy level described by

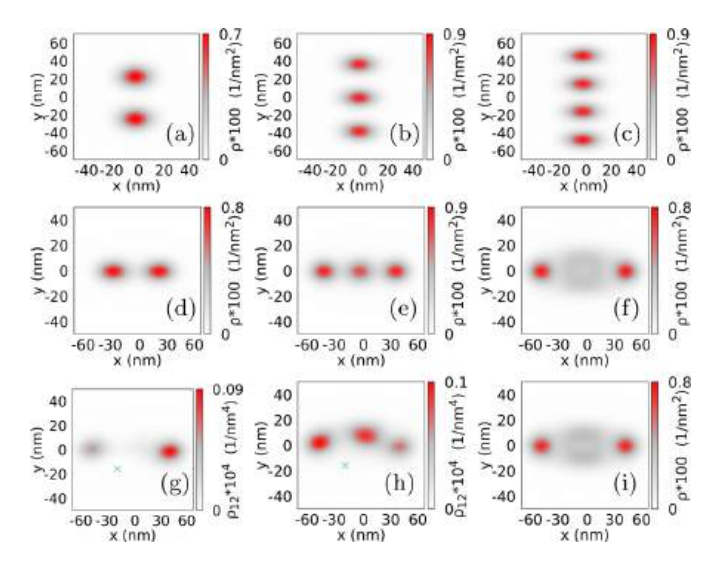


FIG. 10. Charge density for the B=0.01 T ground state of the quantum dot elongated along the y axis (zigzag direction, spectra given in Fig. 9) for N=2 (a), 3(b), and 4 electrons (c). The second row of the plots indicates the results for the dot elongated along the x direction (armchair direction, the spectra given in Fig. 11) for N=2 (d), 3 (e), and 4 electrons (f). (i) corresponds to N=4 and B=5 T. (g) and (h) show the pair correlation function for N=4 and the dot elongated along the x direction. The fixed position of one of the electrons is marked by the cross. (g) shows the pair correlation function for the other electrons with the same spin as the fixed one. In (h), the spin of the other electrons is opposite to the one of the fixed one.

(0,1)]. From this point of view, the system deviates from the quasi 1D confinement, which should be characterized by a large number of excitations along the quantum dot below the energy when the first transverse excitation occurs. However, the charge density of the N-electron states is elongated along the x direction [see Figs. 10(d)-10(f)]. The lifting of the evenodd degeneracy is observed in the spectrum for N=2 and 3 [Figs. 11(b) and 11(c)]. A lower value of m_x allows for a non-negligible electron tunneling between the single-electron islands [cf. the charge density in between the single-electron maxima for N=2 and 3 in Figs. 10(a), 10(d) and 10(b), 10(e)], thus lifting the degeneracy at B=0. Near B=0, the spectrum for N = 4 [Fig. 11(d))] has a distinctly different character than for the zigzag confinement [Fig. 9(d)] and for the circular confinement [Fig. 3(e)]. In both preceding cases the electrons were separated in the single-electron islands [Figs. 4(e), 4(f) and 10(c)]. The ground-state charge density for the armchair confinement possesses two single-electron islands at the ends of the dot and a lower but more extended central maximum [Fig. 10(f) for B = 0.01 T and Fig. 10(i) for B = 5 T]. The charge densities of the two central electrons do not separate into single-electron islands. The effect can be attributed to both a large value of m_v that allows the states excited in the y direction to contribute to the interacting states and a small value of m_x which makes the formation of the single-electron islands along the x direction more expensive in terms of the kinetic energy.

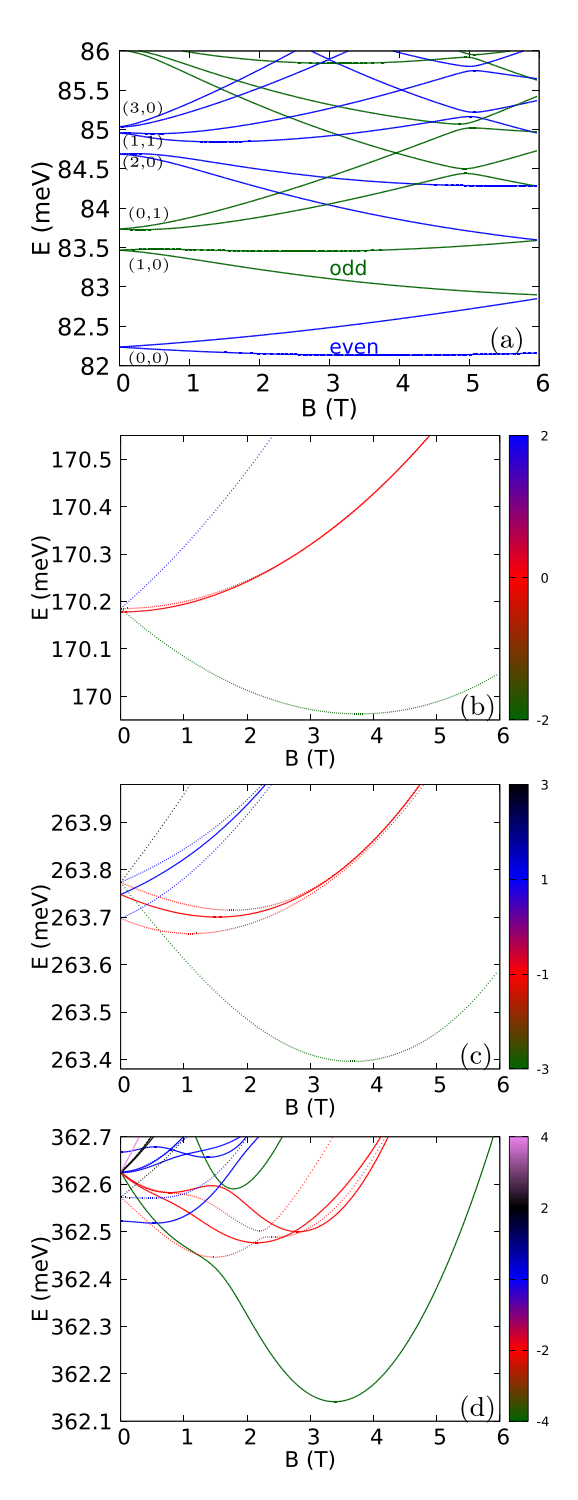


FIG. 11. Spectra for the potential of Fig. 1(d) elongated along the armchair crystal direction (x) for N=1 (a), 2 (b), 3 (c),and 4 (d). In (a), even and odd parity energy levels are plotted with blue and green lines, respectively. The notation (n_x, n_y) close to B=0 axis shows the number of excitations (sign changes) observed in the wave function at zero magnetic field. The spin degeneracy is lifted for B>0 with the spin-down energy levels promoted by the Zeeman interaction. In (b)–(d), the even parity energy levels are plotted with the solid lines and the odd parity energy levels with the dotted lines. The color of the lines stands for the spin. The color of the lines in (b)–(d) shows the S_z value. The color scale is separate for each figure and given to the right of the plot.

Fig. 10(g,h) shows the spin-resolved pair correlation function for one of the electron positions fixed in the point marked by the cross for B=0.01T. Fig. 10(g) (Fig. 10(h)) corresponds to the electron distribution with the same (opposite) spin as the fixed electron spin. The electrons at the central maximum of the charge distribution [Fig. 10(f)] possess opposite spin. Note that, with the electrons of the extreme ends of the dots, separated from the central density island, the system at B=0 acquires a singlet/triplet spectral structure (Fig. 11(d)) similar to the one for the two-electron system in the circular quantum dot (Fig. 3(b))—the central two-electron system governs the form of the low-energy part of the spectrum.

IV. DISCUSSION

The systems confined in quantum dots weakly coupled to electron reservoirs are studied with the transport spectroscopy using the Coulomb blockade phenomenon [51,78]. In the Coulomb blockade regime, the flow of the current across the dot is stopped when the chemical potential of the confined Nelectron is outside the transport window defined by the Fermi levels of the source and drain. For a small voltage drop between the reservoirs, the position of the chemical potential can be very precisely determined. The chemical potential $\mu_N =$ $E_N - E_{N-1}$ is defined by the ground-state energies of systems with N and N-1 electrons [51,78]. The ground-state energy crossing in the N electron system produces Λ -shaped cusps in the charging line as a function of the external magnetic field for the N-th electron added to the confined system, while the ground-state transitions for the N-1 system produces V-shaped cusps. Transport spectroscopy allows reconstruction of the energy spectra with a precision of the order of a few μeV [79]. The results presented above indicate that the formation of the Wigner molecule in the laboratory frame leads to a near degeneracy of the ground state near B = 0. The larger the electron separation in the single-electron charge islands, the closer the degeneracy at B = 0. The ground state becomes spin-polarized at low magnetic field and no further ground-state transitions are observed. The systems without the Wigner molecular charge density undergo a number of ground-state transitions that also appear at higher magnetic field. The transport spectroscopy technique can also be used for detection of the excited part of the spectra when the corresponding energy level enters the transport window [78,79]. Detection of a dense set of levels near the ground state can be used as a signature of Wigner molecule formation [10,11].

V. SUMMARY AND CONCLUSIONS

We have studied the system of a few electrons in an electrostatic quantum dot confinement induced within a phosphorene layer. A version of the configuration interaction approach dealing with the strong electron-electron interaction effects has been developed. We indicated formation of Wigner molecules with single-electron islands separated in the real space in a system of realistic yet small size. In circular quantum dots, Wigner crystallization in the laboratory frame occurs due to the lowered Hamiltonian symmetry with the anisotropy of the electron effective mass. The Wigner

molecules appear in the laboratory frame when the distribution of the single-electron islands is consistent with the Hamiltonian symmetry. For circular quantum dots we found Wigner molecules for two and four electrons but not for three electrons, for which two-semiclassical configurations form a resonance due to the conservation of the parity. For five electrons in the circular confinement, two forms of the charge density with or without single-electron islands appear in the ground state depending on the value of the external magnetic field. Formation of the Wigner molecules in a quasi-1D confinement calls for orientation of the confinement potential with longer axis along the zigzag direction since larger effective mass promotes the single-electron islands localization and the smaller armchair mass supports the quasi 1D confinement. We studied the spectra for both circular and elongated quantum dots to find the signatures of the Wigner crystallization in real space. The systems with single-electron islands forming Wigner molecules in the laboratory frame are characterized by near degeneracy of the ground state at B = 0 followed by spin polarization in low magnetic field and an energy gap between the nearly degenerate ground state and excited states. These features are missing for systems that do not form singleelectron islands. Resolution of these signatures is within the reach of transport spectroscopy techniques.

ACKNOWLEDGMENT

This work was supported by the National Science Centre (NCN) according to decision DEC-2019/35/O/ST3/00097. Calculations were performed on the PLGrid infrastructure.

APPENDIX

1. Single-electron eigen-states with H_0 , H'_0 , and H''_0

Figure 2 presents the convergence of the CI method the single-electron Hamiltonians H_0 , H'_0 and H''_0 using the bare QD potential W, the potential with the central repulsive Gaussian (W') and the reduced potential W'', respectively. The low-energy single-electron wave functions are plotted in Fig. 12 for the three Hamiltonians starting from the ground state in the first row, and the subsequent excited states presented in the lower panels of Fig. 12. The seven lowest-energy states have the same character for all Hamiltonians only with states for H'_0 (central column of plots) and H''_0 (right column) covering a larger area than the ones for H_0 , which turns out to speed-up the convergence of the CI method for the system of size increased by the strong electron-electron interaction.

2. Choice of the computational box

The CI method uses the single-electron wave functions that are obtained with the finite difference approach in a finite computational box with the boundary conditions of vanishing wave function at the edges of the box. The edges of the box form effectively an infinite quantum well that has to be chosen large enough to contain the few-electron system without perturbation to the low-energy states. The influence of the size of the box on the results is given in Fig. 13 for the circular quantum dot. For the circular quantum dot, we use the square grid of points of the spacing of $\Delta x = R/nx$ where R is the

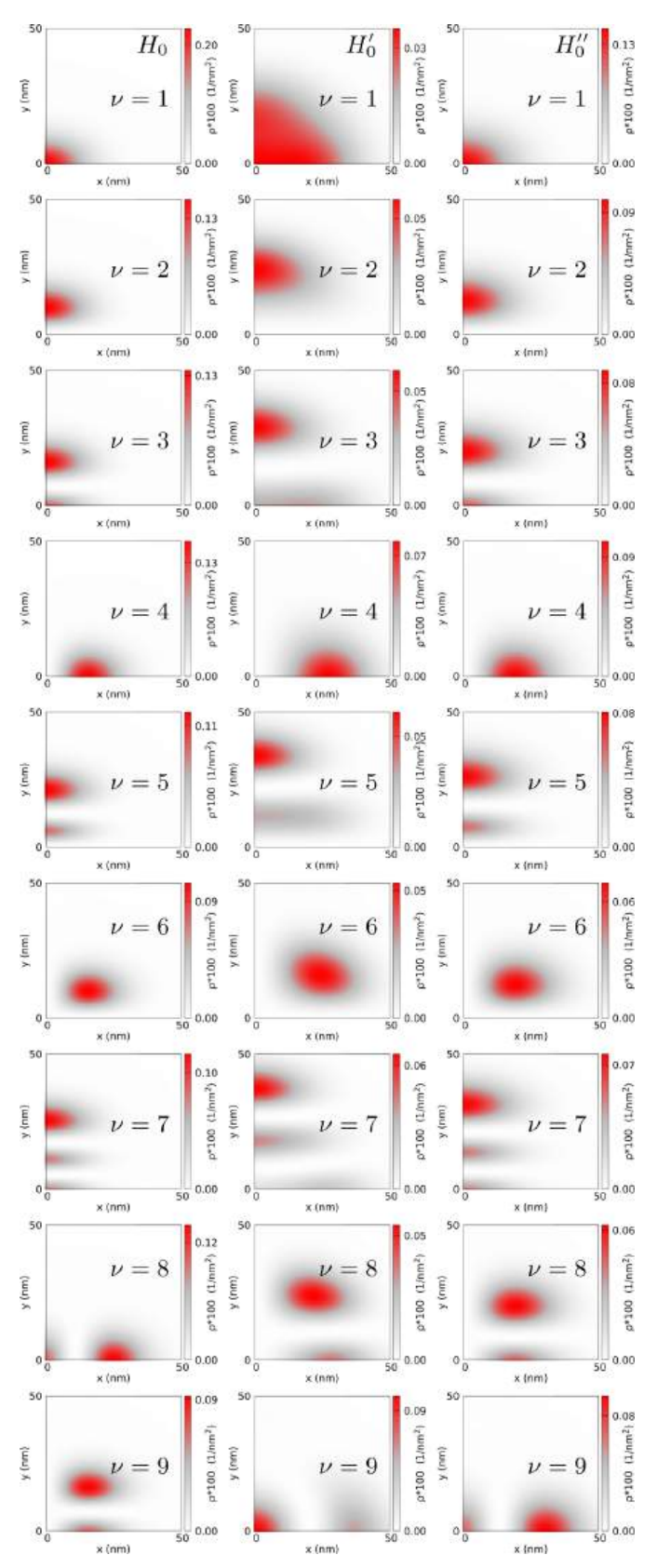


FIG. 12. Probability density of spin-down single-electron states ordered from the ground state ($\nu=1$ – the first row) to eighth excited spin-down energy level ($\nu=9$ – the last row). The left column corresponds to the states of the bare circular confinement with potential W (Hamiltonian H_0). The central column to the potential W' – with an added central Gaussian with 8 meV, 35 meV

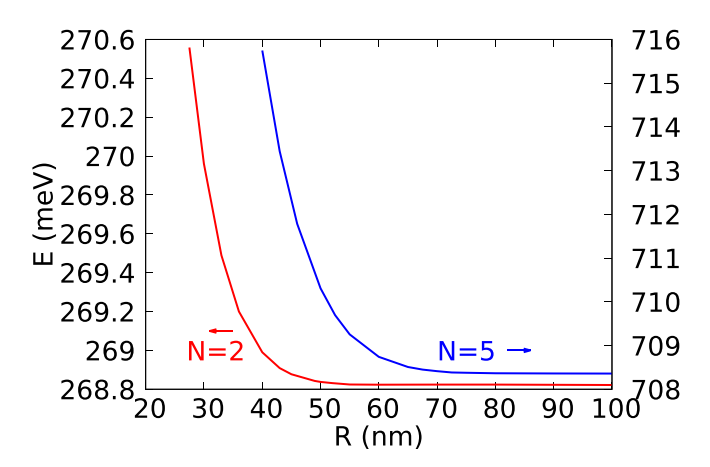


FIG. 13. The ground-state energy for a circular quantum dot holding two (red line, left energy axis) and five electrons (blue line, right energy axis) as a function of the radius of the computational box for 60 single-electron eigenstates of Hamiltonian H'_0 used in construction of the basis for configuration interaction.

radius of the computational box and we take $n_x = 111$. The red (black) line in Fig. 13 shows the ground-state energy for N = 2 (N = 5). The growth of the energy for small R is due to the finite-size effect with the quantum well ground state changing as $1/R^2$. For calculations for N = 2 the radius of R = 50 nm is large enough while for N = 5 is has to be taken as large as R = 80 nm.

3. Spectra without the spin Zeeman interaction

A striking difference in the energy spectra states with or without the Wigner molecule in the ground state is revealed for the circular potential once the spin Zeeman interaction is removed. This is illustrated in Fig. 14 which reproduces the data from Fig. 3 for g = 0. The systems with Wigner form of the charge density, i.e., the single-electron islands in the charge density, N = 2 [Fig. 14(a)] and N = 4 [Fig. 14(c)] contain a nearly degenerate ground state with energy levels of different parity that interlace in increasing B. The separation of the electron charges in the separate, weakly coupled, maxima produces a small energy difference due to the parity, which is similar to the nearly degenerate ground state for identical, weakly coupled quantum dots. The single electron islands are formed by a relatively strong electronelectron interaction and the weakness of the electron tunneling between the islands can be deduced from the charge density plots of Figs. 4(a), 4(b) and 4(e), 4(f) for N=2 and 4. In both cases, the bunch of energy levels of the ground state is separated by a distinct energy gap from the excited states.

For N = 3 [Fig. 8(b)], the parity of the ground state changes in growing B as for even N but the spacing between

(Hamiltonian H_0'). The right column correspond to states obtained with potential $W''=0.455\times W$ (Hamiltonian H_0''). The parameters of the central and the right column are optimized for diagonalization of the four-electron system.

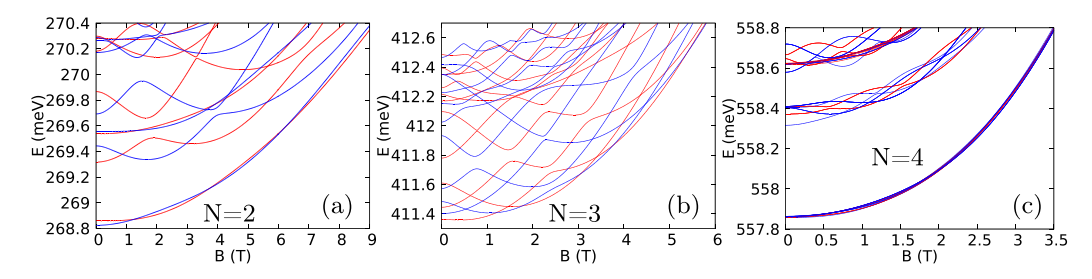


FIG. 14. Spectra of N = 2, 3, and 4 electron systems in circular potential (as in Fig. 3) but without the spin Zeeman interaction. The blue (red) lines show the energy levels of even (odd) parity.

the even and odd parity energy levels near the ground state is much larger than for even N and no energy gap is observed

between the nearly degenerate ground state and the rest of the spectrum.

- [1] E. Wigner, Phys. Rev. 46, 1002 (1934).
- [2] D. S. Fisher, B. I. Halperin, and P. M. Platzman, Phys. Rev. Lett. 42, 798 (1979).
- [3] T. Smolenski et al., Nature (London) 595, 53 (2021).
- [4] H. Li et al., Nature (London) 597, 650 (2021).
- [5] G. W. Bryant, Phys. Rev. Lett. 59, 1140 (1987).
- [6] K. Jauregui, W. Häusler, and B. Kramer, Europhys. Lett. 24, 581 (1993).
- [7] R. Egger, W. Häusler, C. H. Mak, and H. Grabert, Phys. Rev. Lett. 82, 3320 (1999).
- [8] I. Shapir, A. Hamo, S. Pecker, C. P. Moca, O. Legeza, G. Zarand, and S. Ilani, Science 364, 870 (2019).
- [9] A. Diaz-Marquez, S. Battaglia, G. L. Bendazzoli, S. Evangelisti, T. Leininger, and J. A. Berger, J. Chem. Phys. 148, 124103 (2018).
- [10] S. Pecker, F. Kuemmeth, A. Secchi, M. Rontani, D. C. Ralph, P. L. McEuen, and S. Ilani, Nat. Phys. 9, 576 (2013).
- [11] J. Corrigan, J. P. Dodson, H. Ekmel Ercan, J. C. Abadillo-Uriel, B. Thorgrimsson, T. J. Knapp, N. Holman, T. McJunkin, S. F. Neyens, E. R. MacQuarrie, R. H. Foote, L. F. Edge, M. Friesen, S. N. Coppersmith, and M. A. Eriksson, Phys. Rev. Lett. 127, 127701 (2021).
- [12] M. Modarresi and A. D. Güçlü, Phys. Rev. B 95, 235103 (2017).
- [13] C. Yannouleas and U. Landman, Phys. Rev. Lett. 82, 5325 (1999).
- [14] S. M. Reimann, M. Koskinen, and M. Manninen, Phys. Rev. B 62, 8108 (2000).
- [15] A. V. Filinov, M. Bonitz, and Y. E. Lozovik, Phys. Rev. Lett. 86, 3851 (2001).
- [16] B. Szafran, F. M. Peeters, S. Bednarek, T. Chwiej, and J. Adamowski, Phys. Rev. B 70, 035401 (2004).
- [17] C. Ellenberger, T. Ihn, C. Yannouleas, U. Landman, K. Ensslin, D. Driscoll, and A. C. Gossard, Phys. Rev. Lett. 96, 126806 (2006).
- [18] S. Kalliakos, M. Rontani, V. Pellegrini, C. P. García, A. Pinczuk, G. Goldoni, E. Molinari, L. N. Pfeiffer, and K. W. West, Nat. Phys. 4, 467 (2008).
- [19] J. C. Abadillo-Uriel, B. Martinez, M. Filippone, and Y.-M. Niquet, Phys. Rev. B 104, 195305 (2021).
- [20] E. Cuestas, P. A. Bouvrie, and A. P. Majtey, Phys. Rev. A 101, 033620 (2020).
- [21] D. D. Vu and S. Das Sarma, Phys. Rev. B 101, 125113 (2020).

- [22] M. Reimann and M. Manninen, Rev. Mod. Phys. 74, 1283 (2002).
- [23] J. Zhao, Yuhe Zhang, and J. K. Jain, Phys. Rev. Lett. 121, 116802 (2018).
- [24] C. Yannouleas and U. Landman, Rep. Prog. Phys. 70, 2067 (2007).
- [25] H. Liu, A. T. Neal, Z. Zhu, Z. Luo, X. Xu, D. Tomanek, and P. D. Ye, ACS Nano 8, 4033 (2014).
- [26] L. Li, Y. Yu, G. J. Ye, Q. Ge, X. Ou, H. Wu, D. Feng, X. H. Chen, and Y. Zhang, Nat. Nanotechnol. 9, 372 (2014).
- [27] S. Fukuoka, T. Taen, and T. Osada, J. Phys. Soc. Jpn. 84, 121004 (2015).
- [28] M. Akhtar, G. Anderson, R. Zhao, A. Alruqi, J. E. Mroczkowska, G. Sumanasekera, and J. B. Jasinski, npj 2D Mater. Appl. 1, 5 (2017).
- [29] R. Schuster, J. Trinckauf, C. Habenicht, M. Knupfer, and B. Büchner, Phys. Rev. Lett. 115, 026404 (2015).
- [30] J. Qiao, X. Kong, Z. X. Hu, F. Yang, and W. Ji, Nat. Commun. 5, 4475 (2014).
- [31] A. N. Rudenko and M. I. Katsnelson, Phys. Rev. B **89**, 201408(R) (2014).
- [32] A. N. Rudenko, S. Yuan, and M. I. Katsnelson, Phys. Rev. B **92**, 085419(R) (2015).
- [33] P. E. Faria Junior, M. Kurpas, M. Gmitra, and J. Fabian, Phys. Rev. B **100**, 115203 (2019).
- [34] X. Zhou, W.-K. Lou, D. Zhang, F. Cheng, G. Zhou, and K. Chang, Phys. Rev. B 95, 045408 (2017).
- [35] B. Szafran, Phys. Rev. B 101, 235313 (2020).
- [36] M. Lee, Y. H. Park, E. B. Kang, A. Chae, Y. Choi, S. Jo, Y. J. Kim, S. J. Park, B. Min, T. K. An, J. Lee, S. I. In, S. Y. Kim, S. Y. Park, and I. In, ACS Omega 2, 7096 (2017).
- [37] Z. Sun, H. Xie, S. Tang, Y. Xue-Fang, G. Zhinan, J. Shao, H. Zhang, H. Huang, H. Wang, and P. K. Chu, Angew. Chem. 127, 11688 (2015).
- [38] M. Wang, Y. Liang, Y. Liu, G. Ren, Z. Zhang, S. Wu, and J. Shen, Analyst **143**, 5822 (2018).
- [39] R. Gui, H. Jin. Z. Wang, and J. Li, Chem. Soc. Rev. 47, 6795 (2018).
- [40] V. A. Saroka, I. Lukyanchuk, M. E. Portnoi, and H. Abdelsalam, Phys. Rev. B **96**, 085436 (2017).
- [41] H. Abdelsalam, V. A. Saroka, I. Lukyanchuk, and M. E. Portnoi, J. Appl. Phys. **124**, 124303 (2018).

- [42] F. X. Liang, Y. H. Ren, X. D. Zhang, and Z. T. Jiang, J. Appl. Phys. 123, 125109 (2018).
- [43] L. L. Li, D. Moldovan, W. Xu, and F. M. Peeters, Phys. Rev. B 96, 155425 (2017).
- [44] D. He, Y. Wang, Y. Huang, Y. Shi, X. Wang, and X. Duan, Nano Lett. 19, 331 (2019).
- [45] X. Li, Z. Yu, X. Xiong, T. Li, T. Gao, R. Wang, R. Huang, and Y. Wu, Sci. Adv. 5, eaau3194 (2019).
- [46] N. Gillgren, D. Wickramaratne, Y. Shi, T. Espiritu, J. Yang, J. Hu, J. Wei, X. Liu, Z. Mao, K. Watanabe, and T. Taniguchi, 2D Mater. 2, 011001 (2014).
- [47] L. Li, F. Yang, G. J. Ye, Z. Zhang, Z. Zhu, W. Lou, X. Zhou, L. Li, K. Watanabe, T. Taniguchi, and K. Chang, Nat. Nano. 11, 593 (2016).
- [48] G. Long, D. Maryenko, S. Pezzini, S. Xu, Z. Wu, T. Han, J. Lin, C. Cheng, Y. Cai, U. Zeitler, and N. Wang, Phys. Rev. B 96, 155448 (2017).
- [49] G. Long, D. Maryenko, J. Shen, S. Xu, J. Hou, Z. Wu, W. K. Wong, T. Han, J. Lin, Y. Cai, R. Lortz, and N. Wang, Nano Lett. 16, 7768 (2016).
- [50] J. Yang, S. Tran, J. Wu, S. Che, P. Stepanov, T. Taniguchi, K. Watanabe, H. Baek, D. Smirnov, R. Chen, and C. N. Lau, Nano Lett. 18, 229 (2018).
- [51] R. Hanson, L. P. Kouwenhoven, J. R. Petta, S. Tarucha, and L. M. K. Vandersypen, Rev. Mod. Phys. 79, 1217 (2007).
- [52] Y. Sajeev and N. Moiseyev, Phys. Rev. B 78, 075316 (2008).
- [53] N. A. Bruce and P. A. Maksym, Phys. Rev. B 61, 4718 (2000).
- [54] H. Saarikoski and A. Harju, Phys. Rev. Lett. 94, 246803 (2005).
- [55] A. Secchi and M. Rontani, Phys. Rev. B 82, 035417 (2010).
- [56] F. Salihbegović, A. Gallo, and A. Grüeneis, Phys. Rev. B 105, 115111 (2022).
- [57] R. M. Abolfath and P. Hawrylak, J. Chem. Phys. 125, 034707 (2006).
- [58] X. Hu and S. Das Sarma, Phys. Rev. A 64, 042312 (2001).
- [59] F. Yang, Z. Zhang, N. Z. Wang, G. J. Ye, W. Lou, X. Zhou, K. Watanabe, T. Taniguchi, K. Chang, X. H. Chen, and Y. Zhang, Nano Lett. 18, 6611 (2018).
- [60] T. Thakur and B. Szafran, Phys. Rev. B 105, 165309 (2022).
- [61] M. Governale and C. Ungarelli, Phys. Rev. B 58, 7816 (1998).

- [62] S. Bednarek, B. Szafran, K. Lis, and J. Adamowski, Phys. Rev. B 68, 155333 (2003).
- [63] B. Szafran, Phys. Rev. B 104, 235402 (2021).
- [64] R. C. Ashoori, H. L. Stormer, J. S. Weiner, L. N. Pfeiffer, K. W. Baldwin, and K. W. West, Phys. Rev. Lett. 71, 613 (1993).
- [65] A. Szabo and N. S. Ostlund, Modern Quantum Chemistry (Dover, Mineola, NY, 1996).
- [66] L. W. Bertels, H. R. Grimsley, S. E. Economou, E. Barnes, and N. J. Mayhall, J. Chem. Theory Comput. 18, 6656 (2022).
- [67] R. Ahlrichs, H. Lischka, and V. Staemmler, J. Chem. Phys. 62, 1225 (1975).
- [68] P. J. Fasano, C. Constantinou, M. A. Caprio, P. Maris, and J. P. Vary, Phys. Rev. C 105, 054301 (2022).
- [69] E. R. Davidson, Rev. Mod. Phys. 44, 451 (1972).
- [70] B. B. Brandt, C. Yannouleas, and U. Landman, Nano Lett. 15, 7105 (2015).
- [71] P.-O. Löwdin, Phys. Rev. 97, 1474 (1955).
- [72] For the circular potential of Fig. 1(a) the optimal (V_0, d) parameters for N = 3, 4, and 5 electrons are equal to (4 meV, 35 nm), (8 meV, 35 nm), and (10 meV, 40 nm), respectively.
- [73] C. Yannouleas and U. Landman, Phys. Rev. B 105, 205302 (2022).
- [74] Y. Li, C. Yannouleas, and U. Landman, Phys. Rev. B 76, 245310 (2007).
- [75] C. Yannouleas, B. B. Brandt, and U. Landman, New J. Phys. 18, 073018 (2016).
- [76] G. Burkard, G. Seelig, and D. Loss, Phys. Rev. B 62, 2581 (2000).
- [77] J. R. Petta, A. C. Johnson, J. M. Taylor, E. A. Laird, A. Yacoby, M. D. Lukin, C. M. Marcus, M. P. Hanson, and A. C. Gossard, Science 309, 2180 (2005).
- [78] L. P. Kouwenhoven, C. M. Marcus, P. L. McEuen, S. Tarucha, R. M. Westervelt, and N. S. Wingreen, in *Mesoscopic Electron Transport*, edited by L. L. Sohn, L. P. Kouwenhoven, and G. Schön, NATO ASI Series (Series E: Applied Sciences) Vol. 345 (Springer, Dordrecht, 1997).
- [79] A. Fuhrer, S. Luescher, T. Ihn, T. Heinzel, K. Ensslin, W. Wegscheider, and M. Bichler, Nature (London) 413, 822 (2001).

Chapter 7

Vortex structure in Wigner molecules

Thakur, T., & Szafran, B. Vortex structure in Wigner molecules. Scientific Reports, 13(1), 9707 (2023). Licensed under CC BY 4.0.

scientific reports



OPEN Vortex structure in Wigner molecules

Tanmay Thakur & Bartłomiej Szafran[™]

We study clusters of vortices for Wigner molecules formed in the laboratory frame induced by anisotropy of the external potential or electron effective mass. For anisotropic systems the groundstate vortex structure undergoes a continuous evolution when the magnetic field is varied in contrast to isotropic systems where it changes rapidly at angular momentum transitions. In fractional quantum Hall conditions the additional vortices first appear on the edges of the confined system far from the axis of a linear Wigner molecule and then approach the electron positions in growing magnetic field. For an isotropic mass the vortices tend to stay at the line perpendicular to the Wigner molecule axis and pass to the axis for the lowest Landau level filling factor of $v \simeq \frac{1}{5}$. In phosphorene the behaviour of the vortices is influenced by a strong anisotropy of the electron effective mass. The vortices are stabilized off the axis of the molecule when it is oriented along the armchair crystal direction. For the molecule oriented along the zigzag direction the vortices are transfered to the molecule axis already at $\nu \simeq \frac{1}{3}$. The transfer is associated with an antivortex creation and annihilation near the electron position.

In fractional quantum Hall conditions, high magnetic field induces freezing of the kinetic energy to the lowest Landau level that results in appearance of strong electron-electron correlations. As a result of the correlations clusters of vortices appear in the ground-state wave function 1-6. The vortices are zeroes of the wave functions accompanied by phase winding¹⁻⁹ that are attributed to the external magnetic field flux quanta piercing the electron system³. Electron-vortices structures are used for construction of the composite fermion³ wave functions. The vortices with phase winding for the electrons at high magnetic field have their counterparts in the trapped rotating Bose–Einstein condensates^{10–12}.

Structures of vortices for circular quantum dots in isotropic mass materials have been discussed for the exact diagonalization wave functions⁷⁻⁹. In addition to the formation of vortices, the electron-electron correlations lead to Wigner localization 13-16. The finite counterparts of the Wigner crystal in laterally confined systems are called Wigner molecules ¹⁷⁻³⁰. For circularly symmetric quantum dots, Wigner molecules are formed in the inner coordinates of the system¹³ and for lowered symmetry they may appear in the laboratory frame^{25–31} with distinct single-electron islands in the charge density distribution. A lower symmetry of the system can be induced by external potential $^{25-31}$ or by the effective mass anisotropy 32 .

The venue of new materials motivated the research on quantum Hall states³³⁻⁴⁰ and Wigner crystallization^{32,41} for anisotropic Fermi surface. Effects of anisotropic electron-electron interactions for quantum Hall states were also studied 42-45. The anisotropic effective mass for a single electron can be readily accounted for in the structure of the Landau levels or Fock-Darwin states^{36,46} with rescaling the electron coordinates producing a modified angular momentum operator that commutes with the Hamiltonian. However, the central Coulomb interaction is not compatible with the rescaled coordinates and calls for further theoretical treatment of the interacting eigenstates 33-39,46.

The purpose of the present paper is to study the fractional quantum Hall effect clusters of vortices in the presence of Wigner crystallization in the laboratory frame space induced by anisotropy of external potential or effective mass. We chose for the case study the phosphorene 47-50 a material that exhibits a strong anisotropy of the effective mass. The quantum Hall effects in phosphorene were subject to theoretical³⁹ and experimental⁵¹⁻⁵⁴ investigations. Relatively large carrier effective masses in phosphorene provide favorable conditions for formation of Wigner localization, and their strong anisotropy^{55–60} paves the way for formation of Wigner molecules to be observed in the laboratory frame³² and not only in the inner structure of the electron system. We find that in quasi one-dimensional Wigner molecules the additional vortex clusters that appear with decreasing lowest Landau level filling factor tend to stay off the axis of the molecule for an isotropic effective mass. The anisotropy of the effective mass interferes with this process, strengthening or weakening this tendency depending on the orientation of the Wigner molecule axis with the heavier mass direction.

Faculty of Physics and Applied Computer Science, AGH University, al. Mickiewicza 30, 30-059 Kraków, Poland. [™]email: bszafran@agh.edu.pl

Theory

We work with a two-dimensional single-electron Hamiltonian with anisotropic effective mass and parabolic confinement⁶¹

$$h = \left(-i\hbar \frac{\partial}{\partial x} + eA_x\right)^2 / 2m_x + \left(-i\hbar \frac{\partial}{\partial y} + eA_y\right)^2 / 2m_y + \frac{1}{2} \left(m_x \omega_x^2 x^2 + m_y \omega_y^2 y^2\right)$$
(1)

with the symmetric gauge $\mathbf{A}=(A_x,A_y,A_z)=(-By/2,Bx/2,0)$ for perpendicular magnetic field B. In Eq. (1) we use the effective masses⁶¹ for phosporene $m_x=0.17037m_0$ for the armchair crystal direction (x) and $m_y=0.85327m_0$ for the zigzag direction (y). The Hamiltonian with these mass parameters⁶¹ reproduces the results of the tight-binding approximation⁵⁷ for electron states confined laterally within the monolayer phosphorene.

The single-electron wave functions ϕ are obtained by diagonalization of h in the basis of a product of polynomials and a Gaussian

$$\phi_{\mu}(\mathbf{r}) = \sum_{\nu} c_{\nu}^{\mu} x^{\nu_{x}} y^{\nu_{y}} \exp(-a_{x} x^{2} - a_{y} y^{2}), \tag{2}$$

where a_x and a_y are determined variationally and μ numbers the h eigenstates in the energy order.

For analysis of the zeroes in the fractional quantum Hall regime we consider a spin-polarized system and consider three electrons, which is the minimal electron number that allows for discussion of the zeroes of the reduced wave function^{7–9}.

For three electrons, we use the configuration interaction approach, i.e. we build a basis of antisymmetrized products (Slater determinants) of single-electron wave functions

$$\Phi(\mathbf{r}_{1}, \mathbf{r}_{2}, \mathbf{r}_{3}) = \sum_{\eta} d_{\eta} \mathcal{A} \left[\phi_{\mu_{1}}(\mathbf{r}_{1}) \phi_{\mu_{2}}(\mathbf{r}_{2}) \phi_{\mu_{3}}(\mathbf{r}_{3}) \right], \tag{3}$$

where \mathcal{A} is the antisymmetrization operator and $\mu_1 < \mu_2 < \mu_3$. The expansion coefficients d_η are obtained by diagonalization of the three-electron Hamiltonian

$$H = \sum_{i=1}^{3} h(\mathbf{r}_i) + \sum_{i=1,j>1}^{3} \frac{e^2}{4\pi \epsilon \epsilon_0 r_{ij}}.$$
 (4)

We use the dielectric constant $\epsilon = 9$ for the phosphorene embedded in Al₂O₃.

The calculations for the discussion of wave function zeroes require highly convergent results. After diagonalization of the h operator, we use 98 lowest energy single-electron eigenstates for the construction of about 150 thousand three-electron Slater determinants that are used as a basis to provide convergence in the total energy of a fraction of a μ eV.

Results and discussion

This section is organized as follows. We first provide the results for isotropic effective mass to set the reference for discussion of the effects of the mass anisotropy. For the isotropic mass we discuss the passage from the circular confinement to the quasi 1D confinement with the Wigner molecule in the laboratory frame. Next, we present the results for phosphorene with the Wigner molecule oriented along the zigzag or armchair crystal directions.

Isotropic effective mass. The results for a circular potential $\hbar\omega=\hbar\omega_x=\hbar\omega_y=3$ meV with an isotropic effective mass $m=m_x=m_y=0.17037m_0$ are summarized in Fig. 1. At high magnetic field the single-electron energy levels with non-negative angular momenta form a band that tends to the lowest Landau level (Fig. 1a). The three-electron spectrum presented in Fig. 1b exhibits the angular momentum transitions in the ground state¹³. The spin-polarized ground-state angular-momentum quantum numbers L take values that are multiples of 3°. The eigenvalue of the spatial parity operator for a given L is $(-1)^L$. In the following, we will refer to the states with the negative (positive) eigenvalue of the spatial parity as odd (even) parity states. The Laughlin wave function L in form of the antisymmetric Jastrow factor attenuated by a Gaussian—provides an approximate eigenstates for the ground states of odd parity. For the three-electron state at the lowest Landau level filling factor of $\nu=\frac{1}{n}$ with odd n this wave function has the form

$$\Psi_{\nu = \frac{1}{n}}(z_1, z_2, z_3) = \exp\left(-\frac{|z_1|^2 + |z_2|^2 + |z_3|^2}{2l_B^2}\right) \times \left[(z_1 - z_2)(z_2 - z_3)(z_1 - z_3)\right]^n,$$
(5)

where z = x + iy, $l_B^2 = \frac{\hbar}{m\omega_h}$, with $\omega_h^2 = \omega^2 + \omega_c^2/4$ and the cyclotron frequency $\omega_c = \frac{eB}{m}$. This wave function is an eigenstate of the angular momentum for L = 3n, hence the relation between the angular momentum and the lowest Landau level filling factor $v = \frac{37-9}{L}$.

In the following we discuss the position of vortices of the reduced wave function^{7,8}, e.g. the three-electron wave function for two fixed electron positions

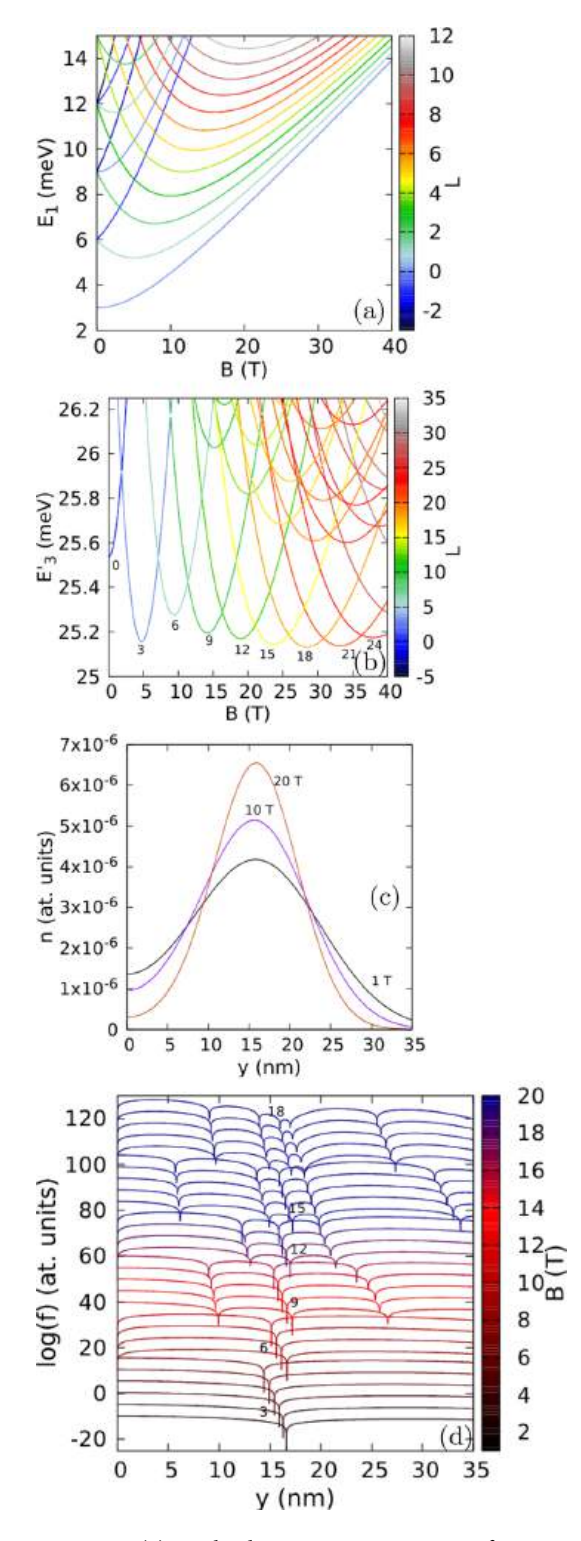


Figure 1. (a) Single-electron energy spectrum for an isotropic effective mass $m_x=m_y=0.17037m_0$ and confinement potential $\hbar\omega_x=\hbar\omega_y=3$ meV. The color of the lines corresponds to the angular momentum eigenvalue. (b) The three-electron energy spectrum for the spin-polarized states calculated with respect to the non-interacting ground state. (c) The electron density cross sections for the lowest-energy three-electron spin-polarized states density for B=1 T, 10 T, and 20 T. (d) The logarithm of the reduced wave function f for two electrons localized at $(x=0,y=\pm y_{max})$, where y_{max} corresponds to the maximal electron density calculated along the y axis. The dip corresponding to the electron at $y=y_{max}$ is close to the numbers that denote the ground-state angular momentum. The plots are calculated for $B=1,2,\ldots 29$ T. The lines for subsequent magnetic fields are shifted by +5 on the plot for clarity. Here, for presentation, we plot $\log(f+10^{-15})$ instead of $\log(f)$ to make the dips of the wave function shallower.

$$g(z; z_1, z_2) \equiv \Phi(z_1, z_2, z).$$
 (6)

The reduced Laughlin wave function is a complex polynomial of degree $2n = \frac{2}{\nu} = \frac{2}{3}L$, that possesses two n-fold zeroes at the electron positions: one at $z = z_1$ and the other at $z = z_2$. In the context of phase circulation, these zeroes are giant vortices with the phase of g that changes by $2\pi n$ under a rotation around the zero.

The Laughlin wave function is the exact² solution for the contact electron–electron interaction potential within the lowest Landau level. For the Coulomb interaction potential 2n-2 zeroes detach from the fixed electron positions^{7,8} and the zeroes are single vortices with rotation of the phase by 2π . In Fig. 1d we plot the logarithm of the absolute value of the reduced wave function $f(z) = |g(z; z_1, z_2)|$ with one electron fixed at $(0, y_{max})$ and the other at $(0, -y_{max})$, where y_{max} corresponds to the maximum of the electron density (Fig. 1c). The value of y_{max} decreases with increasing B for fixed value of the angular momentum, and increases in a discontinuous manner once a larger L appears in the ground state at an angular momentum transition. In Fig. 1d, y_{max} corresponds to the central dip of the reduced wave function. We denote the ground-state angular momentum with integer values placed near zero at $y = y_{max}$ in the figure. For L = 3, the reduced wave function has only the zeroes that correspond to the fixed positions of electrons. The next ground state at higher field, with L = 6 is of the even spatial parity and does not correspond to the Laughlin wave function. For L = 9 and the filling factor $v = \frac{1}{3}$ —covered with a Laughlin wave function—the number of zeroes is 6, e.g. three per fixed electron. We find that the extra zeroes appear also on the y axis, one closer and one further apart from the potential center than the electron position. The state with L = 12 is a non-Laughlin state with an extra zero in the confinement potential center. For L = 15 (Laughlin filling factor $v = \frac{1}{5}$) we find 5 zeroes per fixed electron position, etc.

Generally, for the state of the total angular momentum L diagonalized on the lowest Landau level basis with single-electron states of non-negative angular momenta $L=L_1+L_2+L_3$, the maximal degree of the reduced wave function is L-1 (for the minimal value of a sum $L_1+L_2=1$). Therefore, for L=15 one could expect up to 7 zeroes per fixed electron and not 5 as in the Laughlin wave function. Since our calculation is not limited to the lowest Landau level and covers also the states with negative single-electron angular momenta, the maximal degree of the polynomial, and the number of zeroes of the reduced wave function could be even larger, but for the circular quantum dot in the Laughlin state we resolve only the number of zeroes expected for the Laughlin wave function, i.e. L/3 or n per electron. More zeroes may still appear in the region far away from the dots center, where the electron density is negligible. The presence and location of zeroes far away from the region occupied by the electron density have no significant effect for the system energy.

For confinement that deviates from the circular symmetry we find a mechanism of formation and annihilation of antivortices, when the number of zeroes changes at a small magnetic field variation. To show this effect, let us now consider a deviation from the circular symmetry of the confinement potential. We increase the confinement energy in the x direction to $\hbar\omega_x=3.5$ meV. The three-electron spectrum (Fig. 2a) can no longer be described by the angular momentum, but the spatial parity is still defined for the Hamiltonian eigenstates. The quantum mechanical expectation value of the angular momentum which is plotted in Fig. 2b possesses plateaux near even and odd integer values for even and odd parity states, respectively. The steps between the plateaux correspond to avoided crossings that open between the lowest- and second-energy states of the same parity (Fig. 2a). The electron density on the plateaux [(Fig. 2c,e,f,h) for odd-parity states near (L) = 3, 9 and 15] has the form of an elliptically deformed ring. At the steps between the plateaux (Fig. 2d,g) local maxima appear in the density. These densities are superpositions of two energy-equivalent semiclassical charge configurations with the central electron occupying one of the maxima at the x axis.

In Figs. 3, 4 and 5 we look at detailed behaviour of the zeroes of the reduced wave function of the lowestenergy odd state (see also Supplementary Fig. S1 in the Supplementary Information) in the region of non-zero charge density. Below 10 T—at the plateaux of $\langle L \rangle \simeq$ 3—the zeroes appear only at the fixed electron positions. At the step between the plateaux with average L of 3 and 9 two additional zeroes appear on the edges of the reduced wave function [see the dips for 10.5 T in Fig. 3b]. These zeroes approach the fixed electron position as B grows. At 12 T already at the plateaux of $\langle L \rangle \simeq 9$ the additional zeroes appear at the y axis (Fig. 3a) as for the circular quantum dot (cf. Fig. 1d). The mechanism of the transition of the zeroes to the y axis is presented in Fig. 4. Between 10.7 T and 10.8 T, the zero associated with the electron position is split into three zeroes, all aligned at the y axis. In Fig. 4b the zero at the electron position is the central one in the cross configuration. The phase of the reduced wave function plotted in Fig. 4c shows that four of the zeroes at the arms of the cross are associated with a growth of the phase in the clockwise rotation around the zeroes. Only the phase at the central zero decreases in the clockwise direction. In this sense, splitting of the zero at the fixed electron position corresponds to transformation of a single vortex (Fig. 4a) to a central antivortex and two vortices above and below the antivortex (Fig. 4b,c). As B is increased further (Fig. 4d) the additional vortices at the y axis go further away from the electron position and the two at the sides approach the central antivortex. Due to the vortex-antivortex annihilation we are left with a single vortex at the electron position.

The reduced wave function for B = 20.5 T (Fig. 3b), that is, at the step between the plateaux with $\langle L \rangle$ of 9 and 15 (Fig. 2b) another two extra zeroes appear at a distance from the y axis. These zeroes approach the fixed electron position as B grows (Fig. 3b) and the highest one on the y axis moves away from the electron position (Fig. 3a) and leaves the picture. Between 22 T and 28 T the zeroes on the sides of the system relocate to the y axis with a process involving the formation of an antivortex at the electron position (Fig. 5b,c) and two additional vortices and next annihilation of the two vortices that approach the electron position along the x axis with the antivortex at z_1 (Fig. 5d). This process is similar to the one seen above in Fig. 4.

Note that for a circular system and a state of a fixed angular momentum, the variation of the magnetic field reduces to scaling the electron coordinates⁶³ accompanied by a scaling of the positions of the vortices. For systems with broken rotational symmetry we find a continuous evolution of the geometry of the vortex cluster beyond a simple scaling.

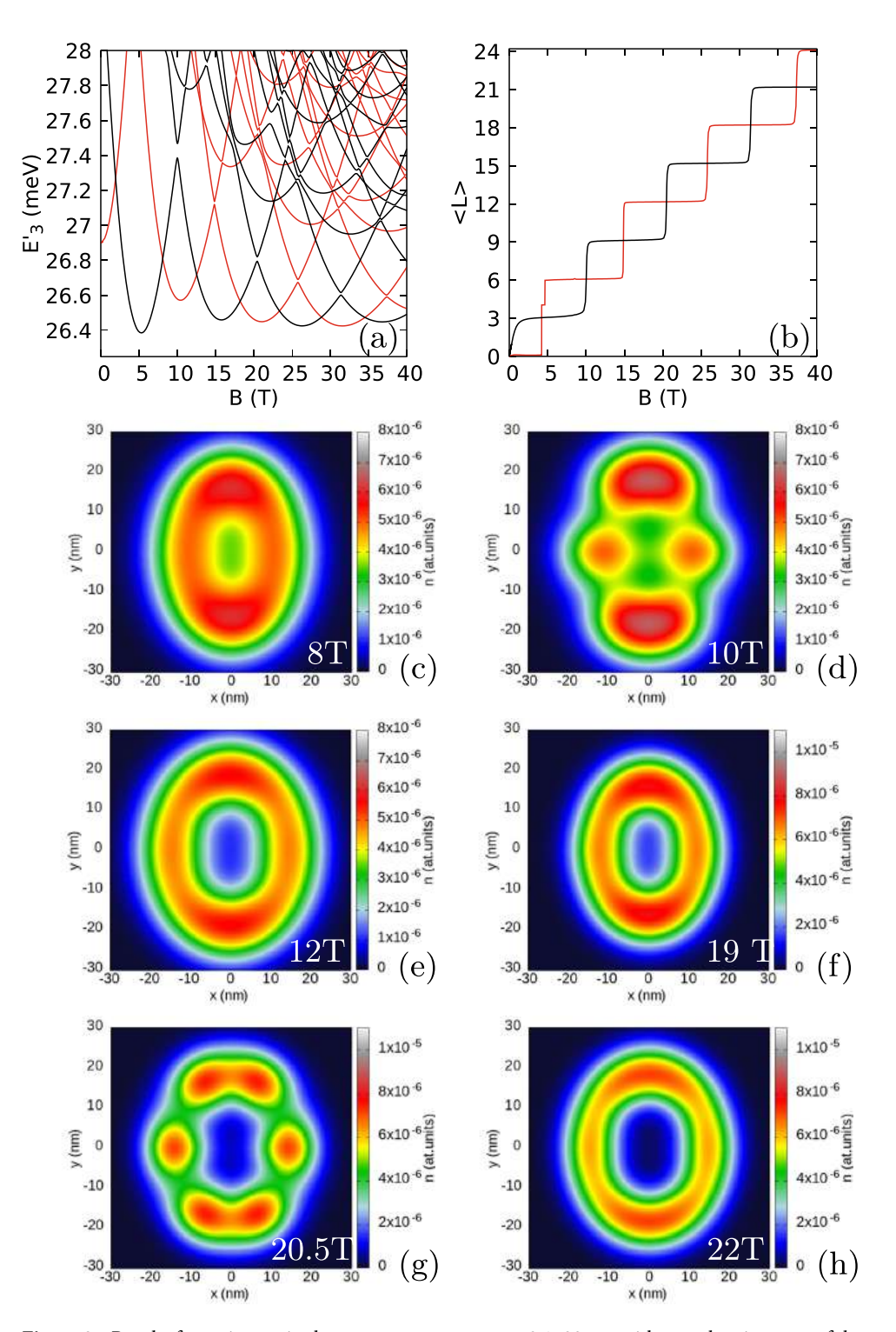


Figure 2. Results for an isotropic electron mass $m_x = m_y = 0.17037m_0$ with a weak anisotropy of the confinement potential $\hbar\omega_x = 3.5$ meV and $\hbar\omega_y = 3$ meV. (a) The energy spectrum for spin-polarized three-electron states minus three times the single-electron ground state energy. (b) The average value of the angular momentum for the lowest-energy odd and even parity states. In (a) and (b) the values for odd parity states are plotted in black and for the even parity ones in red. (c-h) The electron density for the lowest-energy odd parity states.

Let us now look at the system with strong anisotropy of the external potential ($\hbar\omega_x = 6 \text{ meV}$ and $\hbar\omega_y = 3 \text{ meV}$). The three-electron ground state is odd in the spatial parity (Fig. 6b) for any *B* and the spacings between the

ground state and the higher energy levels are too wide for the avoided crossings to be resolved. The dependence of the average angular momentum on B is smooth (Fig. 6c). The charge density is organized in a linear Wigner molecule (Fig. 6d–f) with single-electron islands that are increasingly localized in growing magnetic field.

For 8 T, the zeroes are observed only at the fixed electron position both in the exact calculation (Fig. 7a,b). Additional zeroes appear at the edges of the plot for 16 T (Fig. 7b) and approach the zero associated with the localized electron for higher field (Fig. 7b). At 34 T (Fig. 7b) two new zeroes appear at the sides of the Wigner molecule, while the old ones remain aligned perpendicular to the orientation of the Wigner molecule. At still higher magnetic field (Fig. 7c-h) we see (Fig. 7c,e,g) the flip of two zeroes close to the electron to the axis of the Wigner molecule from the perpendicular alignment, which appears in the mechanism involving formation and annihilation of the antivortex as seen above.

In Fig. 6b,c we additionally plotted with the dashed lines the results obtained for the ground state with a basis limited to single-electron states with non-negative angular momentum. In the context of the number of zeroes of the reduced wave function the limited basis is equivalent to the lowest Landau-level approximation. Although at a high magnetic field the energies are similar on the scale of the plot, the differences are resolved on the structure of the reduced wave function zeroes (Fig. 7c-h). In the limited basis (Fig. 7d,f,h) the antivortex is

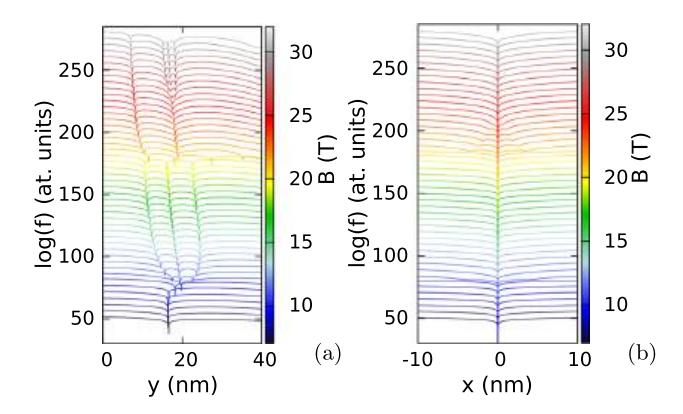


Figure 3. Logarithm of the reduced wave function for the lowest-energy odd-parity state for $m_x = m_y = 0.17037m_0$, $\hbar\omega_x = 3.5$ meV and $\hbar\omega_y = 3$ meV (as in Fig. 2) for two electrons localized at $(x = 0, y = \pm y_{max})$, where y_{max} corresponds to the maximal electron density calculated along the y axis. (a) Shows the cross section along the y axis, and (b) the cross section along the x direction for $y = y_{max}$. The plots are calculated for y = 7 T do 30 T with steps of 0.5 T. The lines for subsequent magnetic fields are shifted by y = 10 on the plot for clarity. In (a) we plot y = 10 instead of y = 10 to make the dips of the wave function shallower. The snapshots of the reduced wave function on y = 10 plane for selected values of the magnetic field are given in the Supplementary information (Supplementary Fig. S1). The dips in (b) are shallower since the zeroes that appear off the y axis are displaced along the y axis by an amount that changes with y = 10 (see Supplementary Fig. S1 in the Supplementary information).

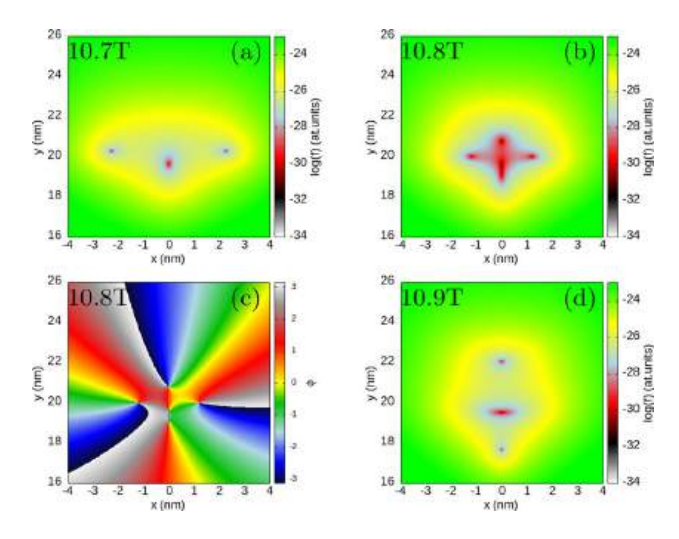


Figure 4. Logarithm of the reduced wave function for the lowest-energy odd-parity state for $m_x = m_y = 0.17037 m_0$, $\hbar \omega_x = 3.5$ meV and $\hbar \omega_y = 3$ meV as in Fig. 2. Two electrons are fixed at $(0, \pm y_{max})$, where y_{max} corresponds to the maximal value of the electron density for B = 10.7 T (a), 10.8 T (b) and 10.9 T (d), respectively. In (c) we plot the phase of the reduced wave function for B = 10.8 T.

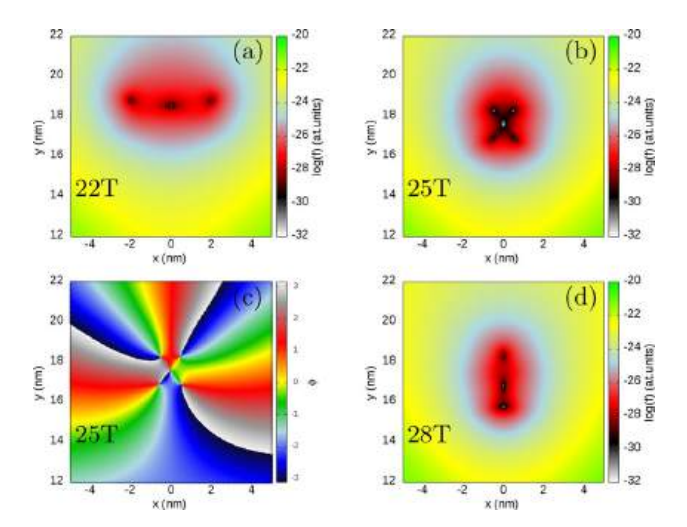


Figure 5. (**a,b,d**) same as Fig. 4 only for B = 22 T, 25 T and 28 T, respectively. In (**c**) we plot the phase of the reduced wave function for B = 25 T.

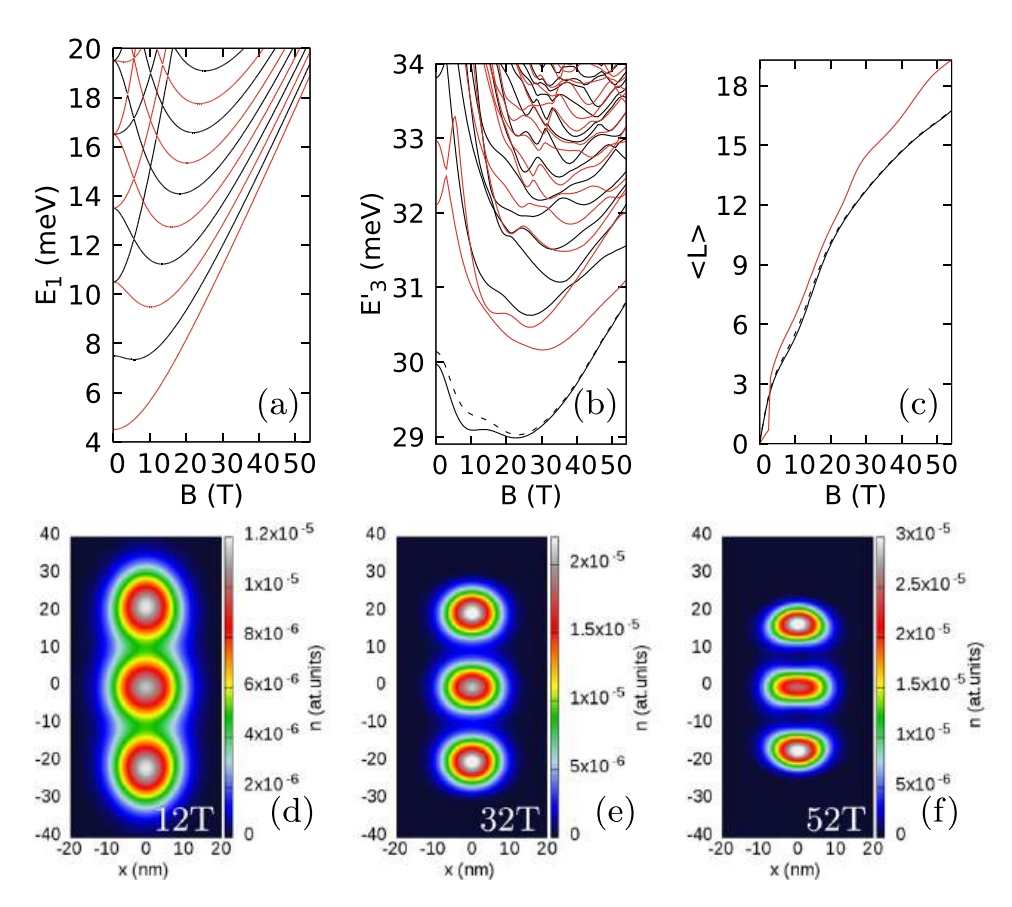


Figure 6. Results for an isotropic electron mass $m_x = m_y = 0.17037m_0$ with a strong anisotropy of the confinement potential $\hbar\omega_x = 6$ meV and $\hbar\omega_y = 3$ meV. (a) Single electron spectrum. (b) The energy spectrum for three electrons minus three times the single-electron ground state energy. (c) Average angular momentum of the three electron system. In $(\mathbf{a}-\mathbf{c})$ the values for the even (odd) parity states are plotted in red (black). In (b) and (c) the dashed black line shows the results for the ground-state calculated in the basis limited to the non-negative average value of the angular momentum. (d,e,f) The electron densities at 12 T, 32 T, and 52 T, respectively.

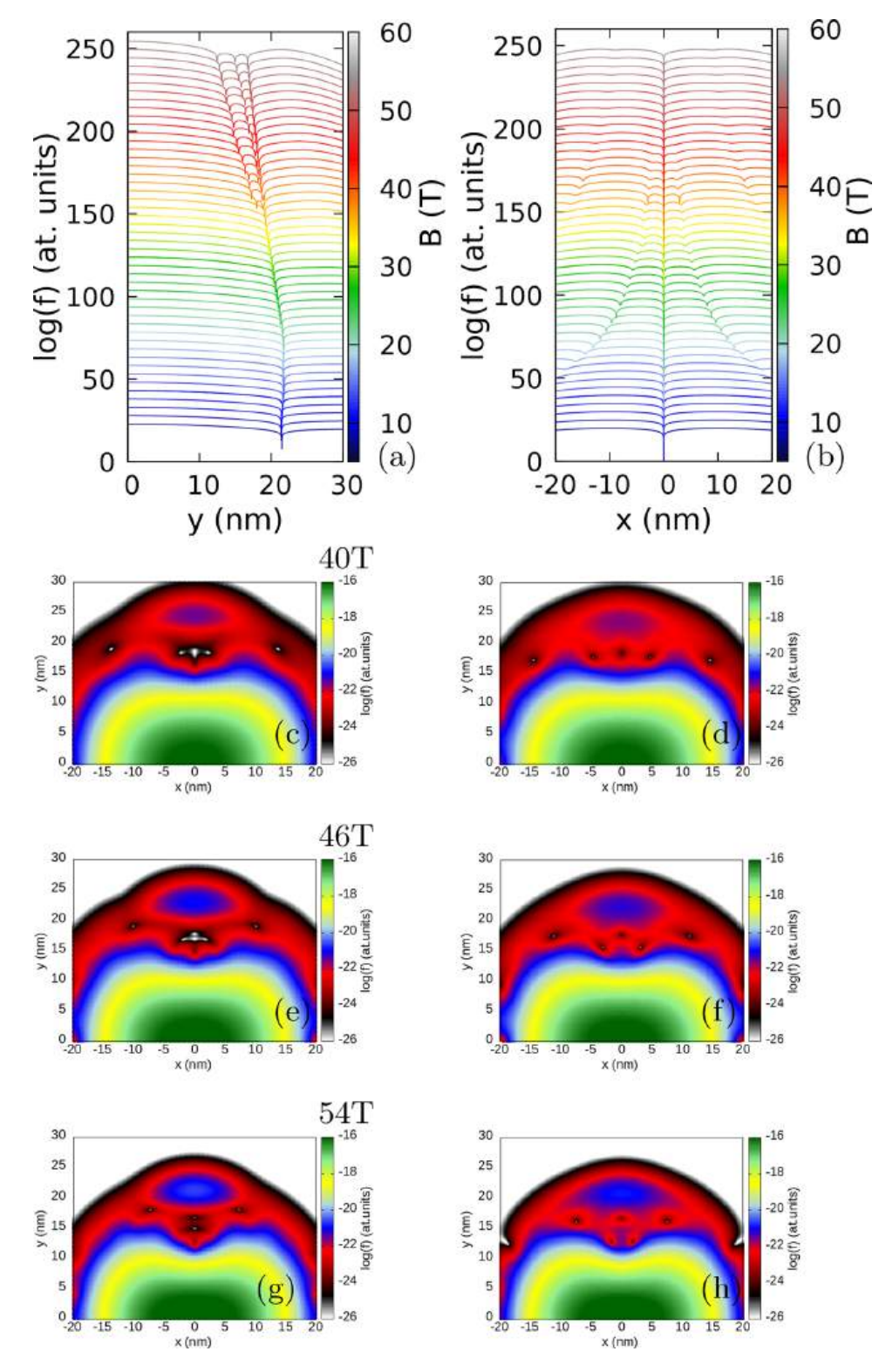


Figure 7. Logarithm of the reduced wave function for the lowest-energy odd-parity state for $m_x = m_y = 0.17037m_0$, $\hbar\omega_x = 6$ meV and $\hbar\omega_y = 3$ meV as in Fig. 6. In the plots two electrons are localized at positions (x = 0, $y = y_{max}$) where y_{max} corresponds to the maximal electron density calculated along the y axis. (a) Shows the cross section along the y axis and (b) the cross section along the x direction for $y = y_{max}$. The lines are plotted from 8 T to 54 T with steps of 1 T. In (a,b) the lines for subsequent magnetic fields are shifted by + 5 on the plot for clarity. In (a) $\log(f + 10^{-14})$ is plotted instead of $\log(f)$ to make the dips of the wave function shallower. In (c-h) we plot the reduced wave function on the (x, y) plane to illustrate the behaviour of the vortices which move away from the $y = y_{max}$ position at higher B. The left column of plots—the complete basis as everywhere else in this paper. The right column of plots—the basis limited to the single-electron states with nonnegative average angular momenta (the energy level marked with the dashed line in Fig. 6). Each row of plots corresponds to the same value of the magnetic field. The vortex corresponding to the electron at $(0, y_{max})$ is the one at the most central position on the y axis. See also Supplementary Fig. S2 for the magnetic fields.

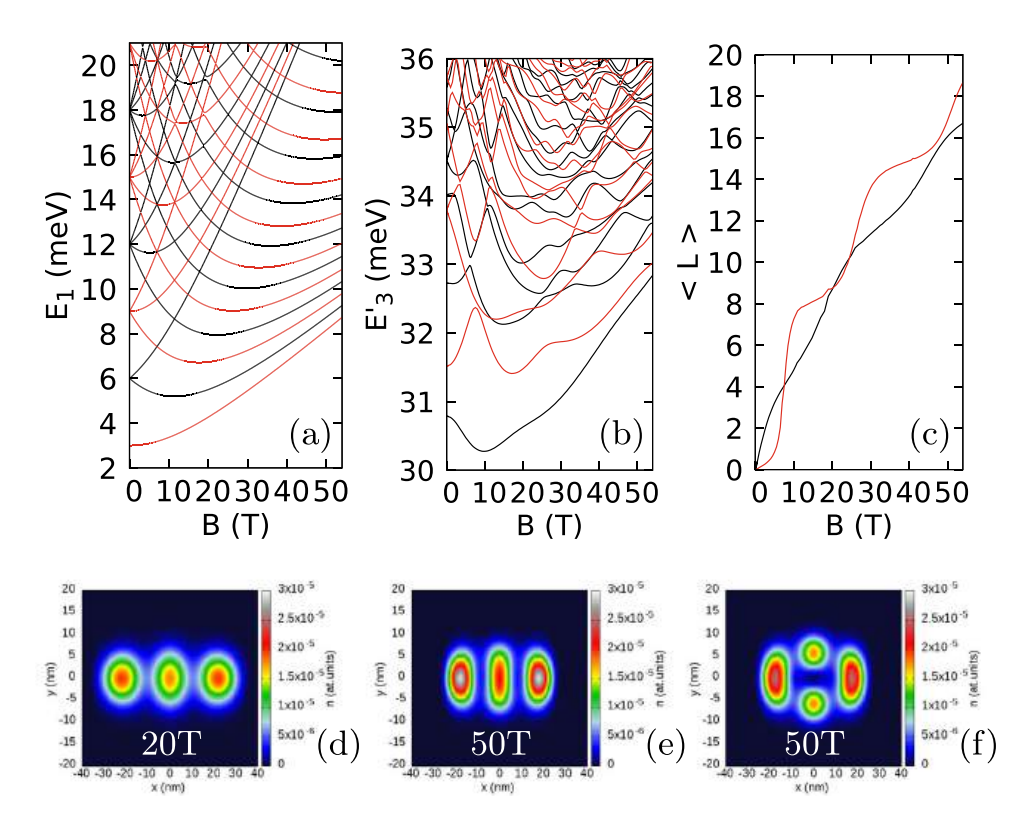


Figure 8. Results for the phosphorene $m_x = 0.17037m_0$, $m_y = 0.85327m_0$ for confinement potential with equal oscillator energies $\hbar\omega_x = \hbar\omega_y = 3$ meV. (a) The single-electron energy levels. (b) The three-electron spectrum minus three times the single-electron ground-state energy. In (a–b) the red (black) color stands for the even (odd) parity states. (c) The average angular momentum for the even (red) and odd (black) parity energy level. (d,e) The ground electron density for 20 and 50 T, respectively. (f) The electron density for the lowest even-parity state at B = 50 T.

not formed, and the extra zeroes accumulate around the electron position, but do not approach it as close as in the exact calculation (Fig. 7c,e,g).

Phosphorene: anisotropic effective mass. We now adopt the phosphorene parameters for the anisotropic electron mass $m_x=0.17037m_0$ and $m_y=0.85327m_0$ (Fig. 8). For equal oscillator confinement energies $\hbar\omega_x=\hbar\omega_y=3$ meV (Fig. 8) the Wigner molecular form of the density appears along the x axis due to the large mass in the y direction (Fig. 8d,e). The three-electron spectrum and the dependence of the angular momentum on B is similar to the one for the isotropic effective mass (Fig. 6b,c): the ground state has the odd spatial parity for all B and the angular momentum for the ground state is a smooth function of B with no clearly defined plateaux. The structure of zeroes is shown in Fig. 9. The extra zeroes appear and stay near the line perpendicular to the axis of the Wigner molecule for the entire considered magnetic field range. No passage to the axis of the molecule is found, as in the case with isotropic electron mass (Fig. 7a,c,e,g). For the maximal magnetic field considered (54 T) the ground state average angular momentum exceeds $16\hbar$ (Fig. 8c). For the isotropic mass, the passage of the zeroes from the axis perpendicular to the molecule axis to this axis appeared for $\langle L \rangle$ was around 15 (Figs. 6c, 7c,e,g) for 5 vortices per electron only for $\nu \simeq \frac{1}{5}$.

To separate the effect of the anisotropy of the Wigner molecule from the anisotropy of the mass, we have produced the Wigner molecule oriented along the y axis by decreasing the confinement energy $\hbar\omega_y$ to 1 meV (Fig. 10). The character of the spectrum and angular momentum dependence on B remains similar to that for the molecule oriented along the x axis, but the zeroes structure is very different. In Fig. 10f,g we have plotted the cross sections of the reduced wave function along the axis of the molecule (Fig. 10f) and a line perpendicular to the axis along the x direction for $y=y_{max}$. Now, the axis of the molecule is aligned with the direction of the heavier mass. The zeroes come from the sides of the main zero (Fig. 10g—the first extra two for 8 T and 9 T, and the next extra pair for 16 T and 17 T), but get aligned with the y axis (Fig. 10f). The behaviour of the zeroes in Fig. 10f,g resemble rather the case of a weakly anisotropic confinement for isotropic effective mass (Fig. 3) than the results for the Wigner molecule presented above.

The tendency of the vortices to stay at the line perpendicular to the Wigner molecule was present for the isotropic mass (Fig. 7). This tendency is strengthened for the Wigner molecule with the anisotropic effective mass when the axis of the molecule is perpendicular to the direction of the heavier mass (Fig. 9) and weakened or nearly lifted (Fig. 10f,g) for the axis of the Wigner molecule aligned with the direction of the heavier mass.

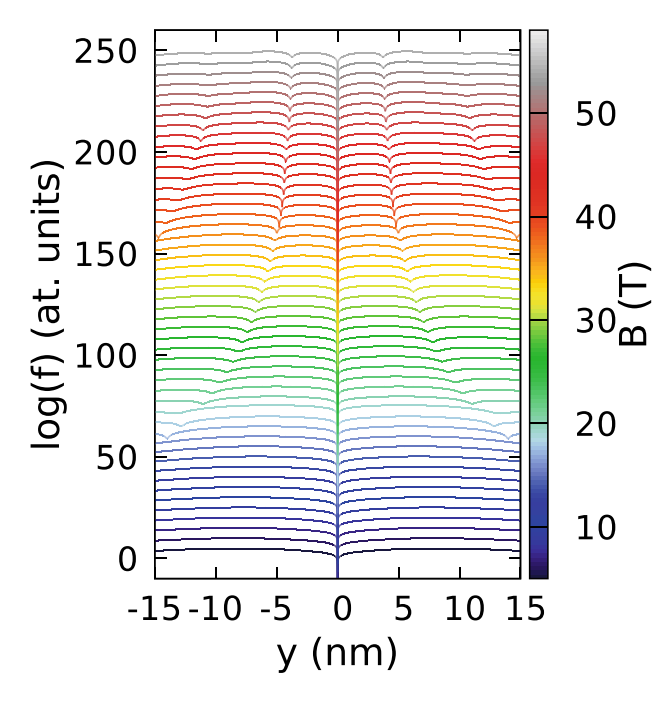


Figure 9. Logarithm of the reduced wave function for the lowest-energy odd-parity state for phosphorene $m_x = 0.17037m_0$, $m_y = 0.85327m_0$ and equal oscillator energies $\hbar\omega_x = \hbar\omega_y = 3$ meV (the same parameters as in Fig. 8). Two electrons are fixed at $(0, \pm x_{max})$ points where x_{max} corresponds to the maximal value of the electron density. The vortex corresponding to the electron at $(0, x_{max})$ is the one at the most central position on the x axis. The lines show the cross section along y direction for $x = x_{max}$ and are plotted from 5 T to 54 T with steps of 1 T. Each line for growing magnetic field is shifted along the vertical axis by + 5. x_{max} stands for the location of the maximal charge density of the extreme charge islands—see Fig. 8e,d. Maps at (x, y) plane for selected magnetic fields are given in Supplementary Fig. S3 in the Supplementary information.

The strong tendency of the vortices to be repelled from the Wigner molecule axis when it is aligned with the lighter magnetic field (Figs. 8 and 9) can be understood in the following manner. The effect is observed for both the exact calculation and in the limited basis corresponding to the lowest Landau level approximation (Fig. 7c–h). Diagonalization of the three-electron Hamiltonian in the basis of the lowest Landau level is equivalent to the diagonalization of the Coulomb interaction only, since all the states correspond to the same kinetic-energy^{7,8}. Within the quasi-1D Wigner molecule the electrons are ordered along its axis in a way that does not essentially change with the magnetic field. Incorporation of the vortices to the axis of the molecule affect the electron distribution in the inner coordinates of the system. The variation of the wave function in the direction of the lighter electron mass is associated with a larger increase in the kinetic energy. When the axis of the Wigner molecule coincides with the lighter electron mass the basis of the accessible low energy states does not allow the relocation of the vortices to the axis, while it is still possible for the orthogonal orientation of the molecule (Figs. 6, 7).

The charge density distribution in Wigner phase can be studied using the scanning probe techniques 14 . However, the location of the vortices is a feature of the wave function that is not directly accessible to the experiment. The number of vortices per electron is deduced from conductance plateaux in experiments on electron gas in the fractional quantum Hall conditions. For systems confined in the quantum dots the quantity that is readily derived from the Coulomb blockade spectroscopy is the energy of the system. This experimental technique provides resolution of the energy with a precision below $10\,\mu\text{eV}$ at temperature of $0.1\,\text{K}^{64}$. The positions of the vortices are relevant for the energy. The exact diagonalization results of this work provide information for modeling with simpler variational wave functions.

At large magnetic fields the odd-parity ground-state is separated by an energy gap of only about 0.25 meV from the first excited state which is of an even parity (see Fig. 6b or Fig. 8b at the end of the magnetic field scale. Small spacings between the energy levels is used as a signature of the Wigner physics³⁰. The gap corresponds to a thermal excitation of about 2.9 K. For a strictly 1D quantum wires a thermal enhancement of Wigner oscillations in a range of temperatures at the onset of the formation of a Wigner molecule was reported⁶⁵. The present system is not strictly 1D. In Fig. 8f we plotted the charge density of the lowest excited state. The central single-electron island is split in two, so one should expect that the thermal excitations will in our case rather destablize the charge density in terms of islands containing a single electron each. However, as pointed above experiments can be carried out at temperatures as low as 0.1 K^{64} .

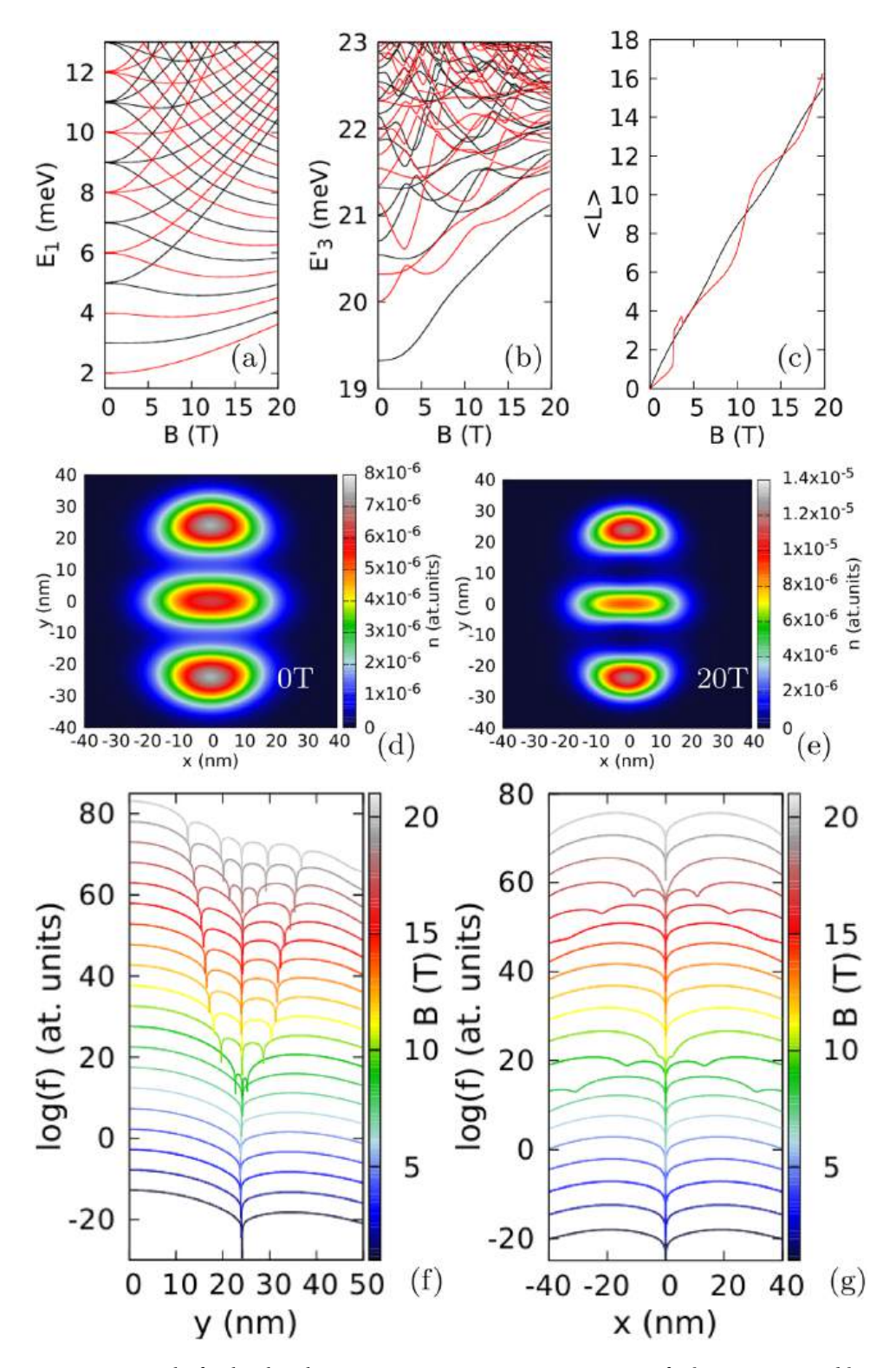


Figure 10. Results for the phosphorene $m_x = 0.17037m_0$, $m_y = 0.85327m_0$ for $\hbar\omega_x = 3$ meV and $\hbar\omega_y = 1$ meV. (a) The single-electron energy levels. (b) The three-electron spectrum minus three times the single-electron ground-state energy. In (a,b) the red (black) color stands for the even (odd) parity states. (c) The average angular momentum for the even (red) and odd (black) parity energy level. (d,e) The ground electron density for 0 and 20 T, respectively. (f,g) Logarithm of the reduced wave function for the lowest-energy odd-parity state for phosphorene—cross sections along the y (f) and x axis (g). Two electrons are fixed at $(0, \pm y_{max})$ points where x_{yax} corresponds to the maximal value of the electron density. The vortex corresponding to the electron at $(0, y_{max})$ is the one at the most central position on the y axis. The plots are calculated from 1 T to 20 T with steps of 1 T. The values for each subsequent B is shifted up by 5 along the scale.

Summary and conclusions

We have discussed the vortex clusters for Wigner molecules induced by anisotropy of confinement and anisotropy of the effective mass using an exact diagonalization approach. The ground states in one-dimensional Wigner molecules possess negative spatial parity as the Laughlin wave function. The observed number of vortices per electron for average angular momentum agrees with the ones predicted by the Laughlin function. As the magnetic field and average angular momentum increase, additional vortices appear from the lateral sides of the Wigner molecule and next approach the electron position. For the anisotropy of confinement alone, the vortex clusters tend to appear off the axis of the molecule and pass to the axis only for filling factor of $\nu \simeq \frac{1}{5}$. When the axis of the molecule coincides with the lighter hole mass, the additional vortices are stabilized off the Wigner molecule axis. On the contrary, for the Wigner molecule axis aligned with the heavier mass direction, the vortices are transferred to the axis of the molecule already at $\nu \simeq \frac{1}{3}$. The transfer of vortices from the perpendicular to the parallel to the axis of the molecule is accompanied with antivortex formation and annihilation that can be described only with the basis not limited to the lowest Landau level.

Data availability

The data that support the findings of this study are available from the first author (T.T.) upon reasonable request.

Received: 6 April 2023; Accepted: 7 June 2023 Published online: 15 June 2023

References

- 1. Laughlin, R. B. Anomalous quantum Hall effect: An incompressible quantum fluid with fractionally charged excitations. *Phys. Rev. Lett.* **50**, 1395 (1983).
- 2. Trugman, S. A. & Kivelson, S. Exact results for the fractional quantum Hall effect with general interactions. *Phys. Rev. B* 31, 5280 (1985).
- 3. Jain, J. K. Composite-fermion approach for the fractional quantum Hall effect. Phys. Rev. Lett. 63, 199 (1989).
- 4. Jain, J. K. Theory of the fractional quantum Hall effect. Phys. Rev. B 41, 7653 (1990).
- 5. Graham, K. L., Mandal, S. S. & Jain, J. K. Nodal correlations in the incompressible composite fermion liquid. *Phys. Rev. B* 67, 235302 (2003).
- 6. Saarikoski, H., Harju, A., Puska, M. J. & Niemiinen, R. M. Vortex clusters in quantum dots. Phys. Rev. Lett. 93, 116802 (2004).
- 7. Tavernier, M. B., Anisimovas, E. & Peeters, F. M. Correlation between electrons and vortices in quantum dots. *Phys. Rev. B* 70, 155321 (2004).
- 8. Tavernier, M. B., Anisimovas, E. & Peeters, F. M. Ground state and vortex structure of the N = 5 and N = 6 electron quantum dot. *Phys. Rev. B* 74, 125305 (2006).
- 9. Stopa, T., Szafran, B., Tavernier, M. B. & Peeters, F. M. Dependence of the vortex structure in quantum dots on the range of the inter-electron interaction. *Phys. Rev. B* **73**, 075315 (2006).
- 10. Fetter, A. L. Rotating trapped Bose-Einstein condensates. Rev. Mod. Phys. 81, 647 (2009).
- 11. Biasi, A., Evnin, O. & Malomed, B. A. Fermi-Pasta-Ulam phenomena and persistent breathers in the harmonic trap. *Phys. Rev. E* **104**, 034210 (2021).
- 12. Yu Okulov, A. Structured light entities, chaos and nonlocal maps. Chaos Solitons Fractals 133, 109638 (2020).
- 13. Reimann, S. M. & Manninen, M. Electronic structure of quantum dots. Rev. Mod. Phys. 74, 1283 (2002).
- 14. Zhao, J., Zhang, Y. & Jain, J. K. Crystallization in the fractional quantum Hall regime induced by landau-level mixing. *Phys. Rev. Lett.* 121, 116802 (2018).
- 15. Smolenski, T. et al. Signatures of Wigner crystal of electrons in a monolayer semiconductor. Nature **595**, 53 (2021).
- 16. Li, H. et al. Imaging two-dimensional generalized Wigner crystals. Nature 597, 650 (2021).
- 17. Egger, R., Haeusler, W., Mak, C. H. & Grabert, H. Crossover from fermi liquid to Wigner molecule behavior in quantum dots. *Phys. Rev. Lett.* 82, 3320 (1999).
- 18. Yannouleas, C. & Landman, U. Spontaneous symmetry breaking in single and molecular quantum dots. *Phys. Rev. Lett.* **82**, 5325 (1999).
- 19. Reimann, S. M., Koskinen, M. & Manninen, M. Formation of Wigner molecules in small quantum dots. *Phys. Rev. B* **62**, 8108 (2000).
- 20. Filinov, A. V., Bonitz, M. & Lozovik, Y. E. Wigner crystallization in mesoscopic 2D electron systems. *Phys. Rev. Lett.* **86**, 3851 (2001).
- 21. Kalliakos, S. et al. A molecular state of correlated electrons in a quantum dot. Nat. Phys. 4, 467 (2008).
- 22. Shapir, I. et al. Imaging the electronic Wigner crystal in one dimension. Science 364, 870 (2019).
- 23. Pecker, S. et al. Observation and spectroscopy of a two-electron Wigner molecule in an ultraclean carbon nanotube. Nat. Phys. 9, 576 (2013).
- 24. Abadillo-Uriel, J. C., Martinez, B., Filippone, M. & Niquet, Y.-M. Two-body Wigner molecularization in asymmetric quantum dot spin qubits. *Phys. Rev. B* **104**, 195305 (2021).
- 25. Jauregui, K., Haeusler, W. & Kramer, B. Wigner molecules in nanostructures. Europhys. Lett. 24, 581 (1993).
- 26. Szafran, B., Peeters, F. M., Bednarek, S., Chwiej, T. & Adamowski, J. Spatial ordering of charge and spin in quasi-one-dimensional Wigner molecule. *Phys. Rev. B* 70, 035401 (2004).
- 27. Diaz-Marquez, A. et al. Signatures of Wigner localization in one-dimensional systems. J. Chem. Phys. 148, 124103 (2018).
- 28. Vu, D. & Das Sarma, S. One-dimensional few-electron effective Wigner crystal in quantum and classical regimes. *Phys. Rev. B* **101**, 125113 (2020).
- 29. Cuestas, E., Bouvrie, P. A. & Majtey, A. P. Fermionic versus bosonic behavior of confined Wigner molecules. *Phys. Rev. A* 101, 033620 (2020).
- 30. Corrigan, J. et al. Coherent control and spectroscopy of a semiconductor quantum dot Wigner molecule. Phys. Rev. Lett. 127, 127701 (2021).
- 31. Yannouleas, C. & Landman, U. Symmetry breaking and quantum correlations in finite systems: Studies of quantum dots and ultracold Bose gases and related nuclear and chemical methods. *Rep. Prog. Phys.* **70**, 2067 (2007).
- 32. Thakur, T. & Szafran, B. Wigner molecules in phosphorene quantum dots. Phys. Rev. B 106, 205304 (2022).
- 33. Qiu, R.-Z., Hu, Z.-X. & Wan, Xin. Single-mode approximation for quantum Hall states with broken rotational symmetry. *Phys. Rev. B* 88, 235118 (2013).
- 34. Balram, A. C. & Jain, J. K. Exact results for model wave functions of anisotropic composite fermions in the fractional quantum Hall effect. *Phys. Rev. B* **93**, 075121 (2016).

- 35. Mueed, M. A. et al. Anisotropic composite fermions and fractional quantum Hall effect. Phys. Rev. B 93, 195436 (2016).
- 36. Bo Yang, Z., Papić, E. H., Rezayi, R.N. Bhatt. & Haldane, F. D. M. Band mass anisotropy and the intrinsic metric of fractional quantum Hall systems. *Phys. Rev. B* 85, 165318 (2012).
- 37. Jo, I. et al. Transference of fermi contour anisotropy to composite fermions. Phys. Rev. Lett. 119, 016402 (2017).
- 38. Kumar, Prashant & Bhatt, R. N. Anisotropic quantum Hall states in the presence of interactions with fourfold rotational symmetry. *Phys. Rev. B* **104**, 035147 (2021).
- 39. Ghazaryan, A. & Chakraborty, T. Aspects of anisotropic fractional quantum Hall effect in phosphorene. *Phys. Rev. B* **92**, 165409 (2015).
- 40. Johri, S., Papic, Z., Schmitteckert, P., Bhatt, R. N. & Haldane, F. D. M. Probing the geometry of the Laughlin state. New J. Phys. 18, 025011 (2016).
- 41. Hossain, M. S. et al. Anisotropic two-dimensional disordered Wigner solid. Phys. Rev. Lett. 129, 036601 (2022).
- 42. Yang, Kun. Geometry of compressible and incompressible quantum Hall states: Application to anisotropic composite-fermion liquids. *Phys. Rev. B* 88, 241105 (2013).
- 43. Krishna, A., Chen, F., Ippoliti, M. & Bhatt, R. N. Interaction-dependent anisotropy of fractional quantum Hall states. *Phys. Rev. B* 100, 085129 (2019).
- 44. Ciftja, O. Two-dimensional finite quantum Hall clusters of electrons with anisotropic features. Sci. Rep. 12, 2383 (2022).
- 45. Wang, Hao, Narayanan, Rajesh, Wan, Xin & Zhang, Fuchun. Fractional quantum Hall states in two-dimensional electron systems with anisotropic interactions. *Phys. Rev. B* **86**, 035122 (2012).
- Thakur, T. & Szafran, B. Aharonov-Bohm oscillations in phosphorene quantum rings: Mass anisotropy compensation by confinement potential. *Phys. Rev. B* 105, 165309 (2022).
- 47. Li, L. et al. Black phosphorus field-effect transistors. Nat. Nanotechnol. 9, 372 (2014).
- 48. Fukuoka, S., Taen, T. & Osada, T. Electronic structure and the properties of phosphorene and few-layer black phosphorus. *J. Phys. Soc. Jpn.* 84, 121004 (2015).
- 49. Akhar, M. et al. Recent advances in synthesis, properties, and applications of phosphorene. NPJ 2D Mater. Appl. 1, 5 (2017).
- 50. Liu, H. et al. Phosphorene: An unexplored 2D semiconductor with a high hole mobility. ACS Nano 8, 4033 (2014)
- 51. Yang, J. et al. Integer and fractional quantum Hall effect in ultrahigh quality few-layer black phosphorus transistor. Nano Lett. 18, 229 (2018).
- 52. Li, L. et al. Quantum Hall effect in black phosphorus two-dimensional electron system. Nat. Nano. 11, 593-597 (2016).
- 53. Long, G. et al. Achieving ultrahigh carrier mobility in two-dimensional hole gas of black phosphorus. Nano Lett. 16, 7768 (2016).
- 54. Long, G. et al. Ambipolar quantum transport in few-layer black phosphorus. Phys. Rev. B 96, 155448 (2017).
- 55. Schuster, R., Trinckauf, J., Habenicht, C., Knupfer, M. & Büchner, B. Anisotropic particle-hole excitations in black phosphorus. *Phys. Rev. Lett.* **115**, 026404 (2015).
- 56. Qiao, J., Kong, X., Hu, Z. X., Yang, F. & Ji, W. High-mobility transport anisotropy and linear dichroism in few-layer black phosphorus. *Nat. Commun.* 5, 4475 (2014).
- 57. Rudenko, A. N. & Katsnelson, M. I. Quasiparticle band structure and tight-binding model for single- and bilayer black phosphorus. *Phys. Rev. B* **89**, 201408(R) (2014).
- 58. Rudenko, A. N., Yuan, S. & Katsnelson, M. I. Toward a realistic description of multilayer black phosphorus: From GW approximation to large-scale tight-binding simulations. Phys. Rev. B 92, 085419(R) (2015).
- 59. Faria Junior, P., Kurpas, M., Gmitra, M. & Fabian, J. $k \cdot p$ theory for phosphorene: Effective *g*-factors, Landau levels, and excitons. *Phys. Rev. B* **100**, 115203 (2019).
- 60. Zhou, X. et al. Effective g factor in black phosphorus thin films. Phys. Rev. B 95, 045408 (2017)
- 61. Szafran, B. Electrostatic quantum dot confinement in phosphorene. Phys. Rev. B 101, 235313 (2020).
- 62. Li, Y., Yannouleas, C., & Landman, U. Three-electron anisotropic quantum dots in variable magnetic fields: Exact results for excitation spectra, spin structures, and entanglement. Phys. Rev. B 245310 (2007).
- 63. Tavernier, M. B. et al. Four-electron quantum dot in a magnetic field. Phys. Rev. B 68, 205305 (2003).
- 64. Fuhrer, A. et al. Energy spectra of quantum rings. Nature 413, 822 (2001).
- 65. Kylanpaa, I., Cavaliere, F., Traverso Ziani, N., Sassetti, M. & Rasanen, E. Thermal effects on the Wigner localization and Friedel oscillations in many-electron nanowires. *Phys. Rev. B* **94**, 115417 (2016).

Acknowledgements

This work was supported by the National Science Centre (NCN) according to decision DEC-2019/35/O/ST3/00097. Calculations were performed on the PLGrid infrastructure.

Author contributions

Both authors participated in calculations, analysis and preparation of the manuscript.

Competing interests

The authors declare no competing interests.

Additional information

Supplementary Information The online version contains supplementary material available at https://doi.org/10.1038/s41598-023-36659-3.

Correspondence and requests for materials should be addressed to B.S.

Reprints and permissions information is available at www.nature.com/reprints.

Publisher's note Springer Nature remains neutral with regard to jurisdictional claims in published maps and institutional affiliations.

Open Access This article is licensed under a Creative Commons Attribution 4.0 International License, which permits use, sharing, adaptation, distribution and reproduction in any medium or format, as long as you give appropriate credit to the original author(s) and the source, provide a link to the Creative Commons licence, and indicate if changes were made. The images or other third party material in this article are included in the article's Creative Commons licence, unless indicated otherwise in a credit line to the material. If material is not included in the article's Creative Commons licence and your intended use is not permitted by statutory regulation or exceeds the permitted use, you will need to obtain permission directly from the copyright holder. To view a copy of this licence, visit http://creativecommons.org/licenses/by/4.0/.

© The Author(s) 2023

Chapter 8

Nagaoka ferromagnetism in an array of phosphorene quantum dots

Thakur, T., & Szafran, B. Nagaoka ferromagnetism in an array of phosphorene quantum dots. Scientific Reports, 13(1), 18796 (2023). Licensed under CC BY 4.0.

scientific reports



OPEN

Nagaoka ferromagnetism in an array of phosphorene quantum dots

Tanmay Thakur & Bartłomiej Szafran⊠

We consider an array of four quantum dots defined in phosphorene containing three excess electrons, i.e., in the conditions of near half filling when itinerant Nagaoka ferromagnetism is expected to appear in a square array with isotropic interdot hopping. The interdot hopping in the array arranged in a square inherits the anisotropy from the form of the phosphorene conduction band. We apply the configuration interaction method for discussion of the appearance and stability of the spin-polarized ground state and discuss the compensation of the effective mass anisotropy by the geometry of the quantum dot array. Our study shows strong stability of Nagaoka ferromagnetism for optimized geometry of the array, with the Nagaoka gap as large as \sim 230 μeV . A phase diagram for the ground-state spin ordering versus the geometric parameters of the array is presented. We study the suppression of the ferromagnetism in a transition of the 2 x 2 array to a quasi-1D chain and indicate that the shift of one of the quantum dots away from the array center is enough to transform the system to a quantum dot chain. A shift in the zigzag crystal direction induces the low-spin ground state more effectively than a shift along the armchair direction. We also discuss the robustness of the spin ordering against detuning one of the dots. The ferromagnetic ground-state survives as long as the detuning is not large enough to trap one of the electrons within a single quantum dot (for positive detuning) or remove one of the quantum dots of the accessible energy range (for negative detuning).

The Hubbard model has been a catalyst for the development of novel and fascinating physics since it first appeared. Although originally meant to provide an understanding of itinerant ferromagnetism in transition metals¹, the variants of this model explain complex phenomena like Mott transition², superconductivity^{3,4}, ferrimagnetism⁵, antiferromagentism⁶, etc. The model has not only been used to theoretically investigate strongly correlated systems, but also been physically implemented in the form of quantum simulations utilizing quantum dots in semiconductors^{7,8}. The quantum dot systems are a playground for verification of the results of the Hubbard model experimentally. One of the results is Nagaoka ferromagnetism predicted for the ground state of single-band systems nearly half filled by strongly interacting electrons^{9,10}. Complete spin polarization of the system is favorable to reduce kinetic energy due to interference of the hole hopping paths in the array¹¹. The Nagaoka ferromagnetism was experimentally demonstrated using a square quantum dots system in GaAs¹¹ validating the theoretical results^{12,13} for a 2D array. Small systems such as quantum dot plaquettes as in Ref.¹² are feasible systems to test and investigate the Nagaoka theorem in depth. The experimental realization of such systems still requires that the energy gap be at least a few μ eV and its tolerance to disorder and imperfections.

Recently, black phosphorene¹⁴ a monolayer form of black phosphorus has been on the rise and is extensively studied for its strongly correlated phenomena^{15–18}. The anisotropic characteristics and tunability of its optical properties by the number of layers make black phosphorene an attractive candidate for applications such as optoelectronics^{19–22}. The material is particularly interesting in the context of electron hopping within the array due to the highly anisotropic carrier effective masses^{23–25}. Additionally, the effective mass of the electrons in phosphorene is much higher than that of GaAs. The large effective electron mass reduces the contribution of kinetic energy, and then the physics is largely affected by electron–electron interactions, which makes quantum dots in phosphorene an appealing choice for studies of the interaction-driven Nagaoka ferromagnetism.

The Hubbard model for GaAs in Ref. 11 —an isotropic effective mass material—employs isotropic hopping between the sites (i.e. the quantum dots) that is not suitable for phosphorene. The anisotropy in the effective masses in x and y directions will lead to the anisotropy of the hopping integrals. Although, investigation of a rectangular geometry with anisotropic hopping has also been reported 26 . Nevertheless, accurate results based on the anisotropic effective mass model are missing. The purpose of this paper is to fill this gap. For phosphorene, the

Faculty of Physics and Applied Computer Science, AGH University of Krakow, al. Mickiewicza 30, 30-059 Kraków, Poland. [™]email: bszafran@agh.edu.pl

anisotropy of the effective mass calls for an anisotropic geometry of the array, which in turn induces anisotropy of the interdot interaction energy. We show that the Nagaoka gap in the quantum dot plaquette in phosphorene is greater than just a few μ eV and therefore verification should be within the experimental reach. We illustrate the robustness of this state against different conditions, revealing the underlying physics, using the configuration interaction method with the effective mass Hamiltonian²⁴ for phosphorene.

The paper is organized as follows: First, we establish the theory and describe the computational approach in detail. In Section "Nagaoka spin polarization" we optimize the parameters and the geometry to get the largest Nagaoka gap. We discuss the ground-state phase diagram with respect to the array parameters. Next, in "Shift from the rectangular geometry" section we discuss the physics of the transition of the rectangular structure of dots to a pseudo-chain structure. In the last subsection of the results, we detune one of the potential wells to simulate the effect of system imperfection and test the Nagaoka phase against it. Lastly, the conclusions and summary of the work are given in Section "Summary and conclusion".

Theory

In this section "Single electron" we describe the applied continuum Hamiltonian for phosphorene. The system parameters and the potential applied for the quantum dots are discussed in Section "Model potential" and finally, the calculation methods and techniques are elaborated in Section "Three-electron Hamiltonian and electron density".

Single electron

An electron in the phosphorene monolayer can be described with the single-band continuum Hamiltonian^{24,27},

$$H_{0} = \left(-i\hbar \frac{\partial}{\partial x} + eA_{x}\right)^{2} / 2m_{x} + \left(-i\hbar \frac{\partial}{\partial y} + eA_{y}\right)^{2} / 2m_{y}$$

$$+ g\mu_{B}B\sigma_{z} / 2 + V(x, y),$$
(1)

with effective masses $m_x = 0.17037m_0$ along the armchair direction (see Fig. 1) and $m_y = 0.85327m_0$ along the zigzag direction, derived using a tight-binding Hamiltonian in Ref.²⁴ and V(x, y) is the confinement potential. The effective masses were obtained by fitting the energy spectra of the single-band continuum Hamiltonian to the tight-binding model for the harmonic oscillator²⁴ and the ring-like confinement potential²⁷. The magnetic field is applied perpendicular to the plane of 2D phosphorene crystal for non-zero Zeeman term and is introduced with symmetric gauge $\mathbf{A} = (A_x, A_y, A_z) = (-yB/2, xB/2, 0)$. In Eq. (1), we use the Landé g-factor, $g = g_0 = 2$. The value is taken from Ref.²⁸ where $k \cdot p$ theory was used to extract the Landé g-factors. The purpose of including the Zeeman term in the Hamiltonian is to remove the degeneracy of spin eigenstates. A range of g values were reported^{29–32}. The specific value of g changes the magnitude of the magnetic field required to lift the degeneracy.

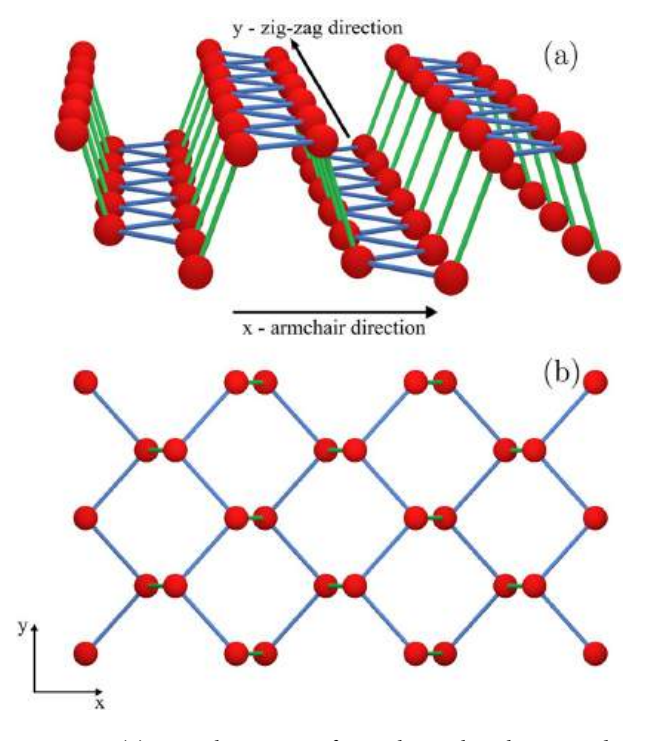


Figure 1. (a) Crystal structure of monolayer phosphorene indicating the zigzag direction (y-axis) and the armchair direction (x-axis). (b) Top view of the phosphorene crystal.

We introduce the external magnetic field for a residual lifting of the spin degeneracy which is useful for the characterization of the spectrum. In the discussion of Nagaoka ferromagnetism, for convenience, we set a residual magnetic field B=1 mT to lift the degeneracies with respect to the z component of the spin σ_z . The Nagaoka gap measured experimentally for the GaAs system was of the order of a few μeVs^{11} . We expect our system to have a much larger gap for the strongest ferromagnetic state. The magnetic field produces splitting between states of the z component of the total spin $\sigma_z=-3/2$ and $\sigma_z=-1/2$ of about 0.22 μeV . As we will see in further results, this energy will be small compared to the largest Nagaoka gap, and will affect the ground state only when the Nagaoka gap is of the same order (near the phase transition) and not the results near the point of largest gap. The energy gap is calculated as $\Delta E=E_{3/2}-E_{1/2}$ where $E_{3/2}$ is the energy of the spin quantum number S=3/2 state and $E_{1/2}$, the energy of the spin S=1/2 state.

The Hamiltonian in Eq. (1) is solved using the finite difference method with gauge-invariant discretization³³. We use a square mesh with spacing Δx in both directions so that the action of Hamiltonian on the wave-function $\Psi_{\alpha,\beta} = \Psi(x_{\alpha},x_{\beta}) = \Psi(\alpha \Delta x,\beta \Delta x)$ is given by

$$H_{0}\Psi_{\alpha,\beta} \equiv \frac{\hbar^{2}}{2m_{x}\Delta x^{2}} \left(2\Psi_{\alpha,\beta} - C_{y}\Psi_{\alpha,\beta-1} - C_{y}^{*}\psi_{\alpha,\beta+1}\right)$$

$$+ \frac{\hbar^{2}}{2m_{y}\Delta x^{2}} \left(2\Psi_{\alpha,\beta} - C_{x}\Psi_{\alpha-1,\beta} - C_{x}^{*}\psi_{\alpha+1,\beta}\right)$$

$$+ V_{\alpha,\beta}\Psi_{\alpha,\beta} + \frac{g\alpha_{B}B}{2}\sigma_{z}\Psi_{\alpha,\beta},$$

$$(2)$$

with Peierls phases³³ $C_x = \exp(-i\frac{e}{\hbar}\Delta x A_x)$ and $C_y = \exp(-i\frac{e}{\hbar}\Delta x A_y)$ to account for orbital effects of the magnetic field. The Hamiltonian in Eq. (2) is diagonalized in a finite computational box of size 50 nm × 50 nm and the spacing Δx of 0.4 nm. The numerical diagonalization is carried out using the Lanczos algorithm as in Ref.²⁴.

Model potential

Inside the computational square box of side length 50 nm, the model quantum dots are arranged in a rectangle with distance between the centers of dots $2\mu_x$ in the armchair direction (x) and $2\mu_y$ in the zigzag crystal direction (y). The spacings influence both the interdot tunneling rates (hopping energy) and the interdot electron–electron interaction. The applied model confinement potential is

$$V(x,y) = -V_d \sum_{i=1}^{2} \sum_{j=1}^{2} \exp\left(\frac{-(x + (-1)^{i} \mu_x)^2}{s^2}\right) \cdot \exp\left(\frac{-(y + (-1)^{j} \mu_y)^2}{s^2}\right)$$
(3)

such that the centers of the dots are located at $(\pm \mu_x, \pm \mu_y)$. Each dot is determined by a Gaussian potential with the size given by the parameter s and the depth of the potential by V_d . Throughout the work, the size of the dots is taken to be s=7 nm. The chosen soft Gaussian potential is a good approximation for the electrostatic quantum dots³⁴ and the construction of four such electrostatic quantum dots setup should be within the experimental reach with the help of a pair of flat gate electrodes with circular intrusion near the center of the dots^{35–37}.

Three-electron Hamiltonian and electron density

The energy spectrum for three interacting electrons in our system is calculated in a continuum approach using the following Hamiltonian

$$H_{3e} = \sum_{i=1}^{3} H_0(i) + \sum_{j>i}^{3} \frac{e^2}{4\pi \epsilon_0 \epsilon r_{ij}},$$
(4)

where H_0 is a single electron Hamiltonian in Eq. (1) and the dielectric constant has the value $\epsilon=9$ for all calculations in the work. The present study calls for an exact treatment of the electron–electron correlation due to the strong electron–electron interaction in phosphorene²⁹. We employ the configuration interaction approach^{38,39}. In this method, the Hamiltonian H_{3e} is diagonalized in the basis of three-electron Slater determinants constructed with the lowest 52 eigenfunctions of the single-electron Hamiltonian H_0 . The Slater determinants are built by filling the three electrons in the single-electron states in all available combinations. The three-electron ground state and excited states are then written as the linear combination of these configurations of electrons. The number of single-electron eigenfunctions spanning the basis of the Slater determinants was chosen on the basis of convergence of the three-electron energy eigenvalues. For 52 single-electron eigenfunctions, the basis of three-electron Slater determinants contains $\binom{52}{3} = 22100$ elements. The Hamiltonian matrix is then numerically diagonalized to obtain three-electron eigenfunctions and corresponding energies.

We investigate the electron distribution in the dots by extracting the electron density from the three electron wave-functions Ψ ,

$$\rho(\mathbf{r}) = \langle \Psi | \sum_{i=1}^{3} \delta(\mathbf{r} - \mathbf{r}_{i}) | \Psi \rangle$$
 (5)

where Ψ is the three-electron ground-state wave function.

Results

We discuss our results in the following order: First, we discuss the parameters of the system for the energy spectrum and the electron density, including the spin ground-state configuration. Next, we calculate a complete phase diagram for the nonferromagnetic and Nagaoka ferromagnetic phases. This gives us insight on the configuration for which the Nagaoka ferromagnetism is the most robust. We then discuss a similar phase diagram but with a shallower potential. We investigate the case where we gradually change the configuration of dots to form a pseudo-1D chain of dots to understand the competition between the ferromagnetic and nonferromagnetic states and the effect of anisotropy on this competition. Lastly, we observe the effect on the Nagaoka phase of a changed potential of one of the quantum dots.

Nagaoka spin polarization

The anisotropy of the effective mass causes the x and y axes of the system to be inequivalent. Therefore, we vary both parameters, μ_x and μ_y to search for the high-spin configuration in the ground state. The potential and square root of the density of the ground state for different combinations of the parameters are plotted in Fig. 2. The potential depth considered for the following calculations is $V_d = 125$ meV. The densities are calculated using Eq.

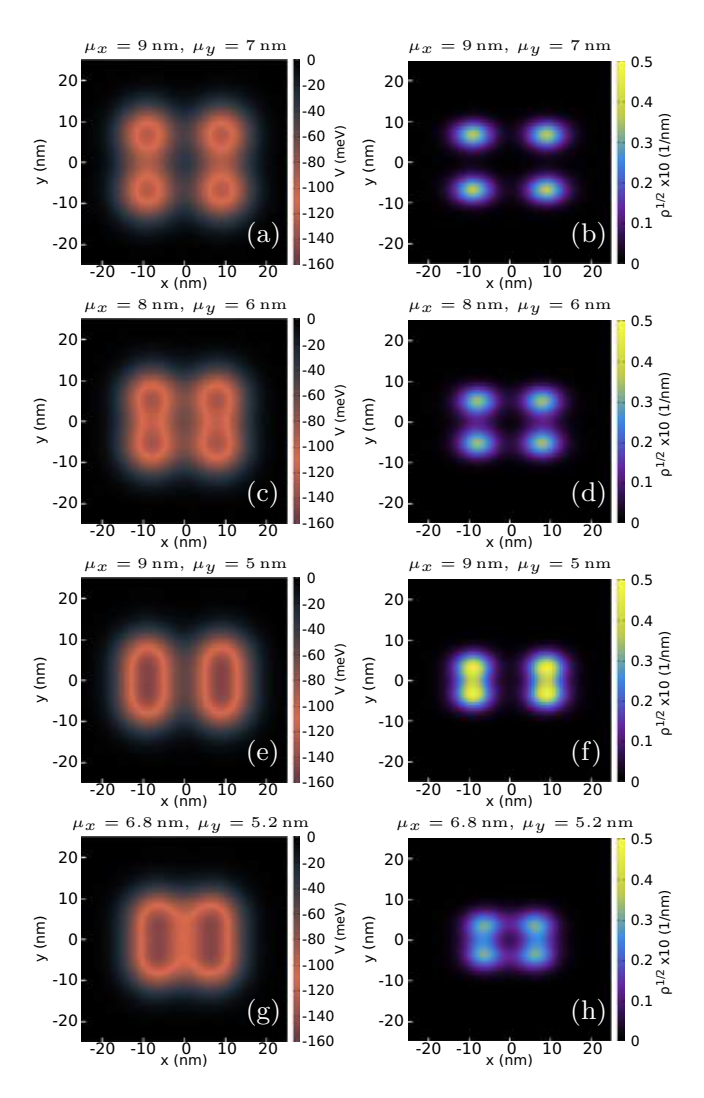


Figure 2. The potential (left column) and the square root of electron density (right column) with parameters, $\mu_x = 9$ nm, $\mu_y = 7$ nm (**a**, **b**); $\mu_x = 8$ nm, $\mu_y = 6$ nm (**c**, **d**); $\mu_x = 9$ nm, $\mu_y = 5$ nm (**e**, **f**); $\mu_x = 6.8$ nm, $\mu_y = 5.2$ nm (**g**, **h**). For all the cases, the magnetic field is 1 mT and the potential depth $V_d = 125$ meV. The color scale for each plot is to the right of each plot. Subfigures (**g**, **h**) indicate the potential and square root of the density for the configuration of dots with the largest Nagaoka gap.

(5) for the ground state. For spacings $\mu_x=9$ nm, $\mu_y=7$ nm (Fig. 2a) the electrons are located near the center of four dots, the charge densities of the array are distinctly separated with little or no density overlap (Fig. 2b). Note that even though the dots are far away, the square root density in the center of dots is not circular, but is more spread in the x direction (Fig. 2a), which is a consequence of the mass anisotropy. For the rest of the plots with $\mu_y\leq 6$ nm the potential [see Fig. 2c,e,g] resembles two dumbbell-like shapes due to the electron tunneling in the zigzag direction, for which the assumed distance between the dots is smaller than in the armchair direction. The trace of electron tunneling between the dots can be observed in Fig. 2d for $\mu_x=8$ nm, $\mu_y=6$ nm. As we move the dots closer together in the y direction, we can observe in Fig. 2f that the square root densities of the top-bottom pair of dots now overlap considerably. Finally, for dots arranged in a rectangle with $\mu_x=6.8$ nm, $\mu_y=5.2$ nm, the square root electron density is highest along the edges of the rectangle.

The energy spectra for the same parameters are plotted in Fig. 3. For $\mu_x = 9$ nm and $\mu_y = 7$ nm, the ground state at B = 0 is a four-fold degenerate state with spin eigenvalue S = 3/2 but the spin doublet 1/2 is above with the energy difference of $40 \,\mu\text{eV}$ (Nagaoka gap $\Delta E = -40 \,\mu\text{eV}$). The low-energy spectra are illustrated in Fig. 3a. Although the tunneling coupling between the dots is weak, it is already large enough to promote the spin-polarized quadruplet with the total spin eigenvalue of S = 3/2 and the z component eigenvalues $\sigma_z = -3/2, -1/2, 1/2, 3/2$ in the ground state. An asymptotic case of large interdot distances corresponds to tunneling and interaction being negligible so that the quadruplet becomes degenerate with the spin S = 1/2 doublet.

Reducing the spacing between the dots to $\mu_x = 8$ nm and $\mu_y = 6$ nm, the energy gap between the lowest spin S = 1/2 and spin S = 3/2 states becomes 100 μ eV with the high-spin ground state [see Fig. 3b].

The energy spectrum for $\mu_x = 9$ nm and $\mu_y = 5$ nm is plotted in Fig. 3c. In this case, the electrons interact weakly in the *x*-direction and strongly in the *y*-direction. We have effectively two extended quantum dots with an electron in one of the other two dots. Since the ground state of the two electrons for negligible magnetic field is a singlet state⁴⁰, the top-bottom pair of dots will contain two electrons of opposite spins, resulting in the ground state being a spin S = 1/2 state due to the spin of the solitary electron. The ground state becomes spin-polarized by the Zeeman interaction only at a high magnetic field of about 1.9 T.

The spin singlet state is removed from the ground state when the tunneling in the x direction is enhanced for a reduced distance in x direction to $\mu_x=6.8$ nm with $\mu_y=5.2$ nm we obtain the ground state, which is again spin polarized with a large energy gap of $\Delta E=-230~\mu {\rm eV}$ in Fig. 3d. This is the maximal gap that we obtain for the applied single-dot potential depth.

The energy gap ΔE for various geometry of the quantum dot array is given in a phase diagram that displays the nonferromagnetic and Nagaoka ferromagnetic phases in Fig. 4. The diagram is calculated for a small magnetic field of 1 mT. For the case with $\mu_y \geq 7$ nm, the four dots are located far away from each other, rendering tunneling negligible, and hence the lowest spin S=1/2 and spin S=3/2 states are nearly degenerate, as seen on the right side of the figure. In the case where the dots are located much closer to each other in y direction (left side of the diagram), the ground state tends to be the spin-1/2 state as in Fig. 3c. This is a quantitative result for the strong tunnel coupling forming two double-dot subsystems. The region in between corresponds to the extended ferromagnetic system with a spin-polarized ground state. In this region, the tunneling between neighbouring dots is enough for the 'hole' to move around the four dots. The largest gap is $\Delta E=-230~\mu {\rm eV}$ and is located at $\mu_x=6.8~{\rm nm},\,\mu_y=5.2~{\rm nm}.$

To understand in detail the effects of the interactions depending on the location of the dots, we study the cross sections of the phase diagram to see the energy gap as a function of the parameter μ_y for various ($\mu_x - \mu_y$) in Fig. 5a. The top-most (bluest) line shows the change in the energy gap ΔE with μ_y for $\mu_x - \mu_y = 1$ nm. It barely goes below the zero line, indicating a very weak Nagaoka ferromagnetic phase near $\mu_y = 6$ nm. As the difference $\mu_x - \mu_y$ increases, the next four lines from the top slowly start to go much lower than the zero line, indicating that the system is in a stronger ferromagnetic phase and that it would take more energy to invert one of the spins and break the phase. The lowest line is the one that goes the lowest under the zero line, which is for the difference $\mu_x - \mu_y = 1.6$ nm. The second line from the bottom (greenest) is for the difference of 1.9 nm and is now higher than the difference of 1.6 nm. At this point, the electron density begins to take the shape of two dumbbells with decreasing x-direction overlap.

Fig. 5b shows the energy gap as a function of μ_x for different y spacings. The plot has few interesting features that give insight on the system. First, every plot has a peak at low values of μ_x slightly below the fixed μ_y distance. The initial growth of the energy gap at the left side of the plot is due to an extension of the region accessible for electrons that has a larger influence on the spin-unpolarized state than on the spin-polarized state for which the electrons cannot occupy the same location anyway. When the system is separated to single-electron islands maxima the lines dip to a certain value before tending to a constant value as μ_x increases. This constant itself tends to zero for the lines as the parameter μ_y becomes large, indicating a vanishing tunnel coupling. In order from topmost (red) line in Fig. 5b, for $\mu_y = 4.5$ nm the energy gap is always positive and for this y spacing, the system never attains the ferromagnetic ordering. For other parameters, a ferromagnetic ground state is found for a range of μ_x .

The maximal Nagaoka gap is expected to shift on the μ_x , μ_y plane for a varied potential depth that affects the strength of the tunnel coupling. The phase diagram for the potential depth of $V_d=60$ meVis plotted in Fig. 6. The results are qualitatively similar to the case of $V_d=125$ meV presented above. The largest Nagaoka gap $\Delta E=-211~\mu {\rm eV}$ occurs for the parameters $\mu_x=7.52$ nm and $\mu_y=5.35$ nm. Because of the shallower potential, the electrons are less localized within the separate dots. This results in a larger tunnel coupling and the Nagaoka phase is achieved for larger inter-dot distances compared to the case of $V_d=125$ meV. Note that the parameter μ_x changed from 6.8 nm to 7.5 nm, while the parameter μ_y changed only about 0.15 nm. This can be attributed to the heavier electron effective mass in y direction and the tunneling energy changing more strongly with the interdot distance.

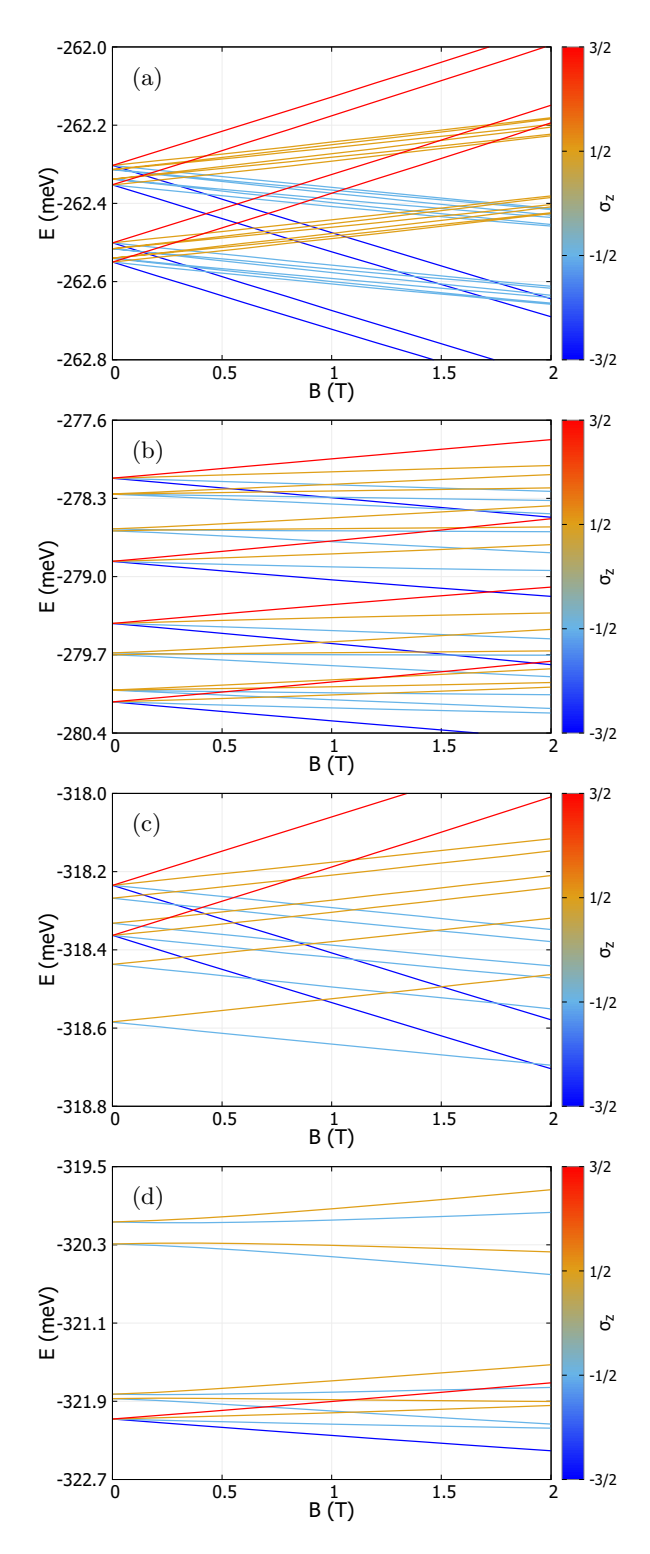


Figure 3. The energy spectrum as a function of magnetic field *B* for parameter sets of $\mu_x = 9$ nm (**a**), $\mu_y = 7$ nm, (**b**) $\mu_x = 8$ nm, $\mu_y = 6$ nm, (**c**) $\mu_x = 9$ nm, $\mu_y = 5$ nm, (**d**) $\mu_x = 6.8$ nm, $\mu_y = 5.2$ nm. Potential depth is set $V_d = 125$ meV for all the chosen sets in (**a**-**d**). The colour of each line denotes the spin eigenvalue of the energy state, and the scale is shown to right of each plot. The spectra show the shifting of ground states and the changing Nagaoka gap as the configurations of the dots change. Subfigure (**d**) shows the spectrum for the configuration with the largest Nagaoka gap.

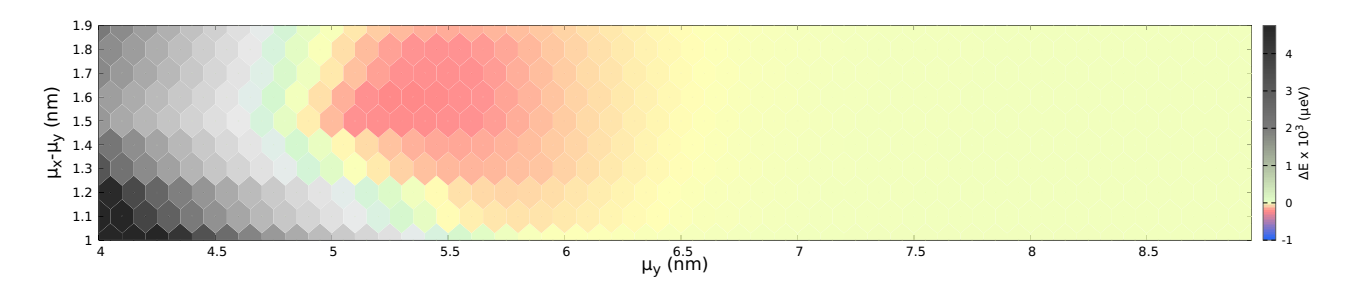


Figure 4. The energy gap, ΔE as a function of the parameters μ_y and $(\mu_x - \mu_y)$ with potential depth, $V_d = 125$ meV. The energy gap is calculated for every point at the center of the hexagons. The green and grey regions in the diagram indicate the configurations for which the ground state is a low-spin state. The red and yellow regions show the configurations with a spin polarized ground state. The largest energy gap $\Delta E = -230~\mu \text{eV}$ occurs at $\mu_y = 5.2$ nm and $\mu_x - \mu_y = 1.6$ nm and is indicated with the most saturated red color.

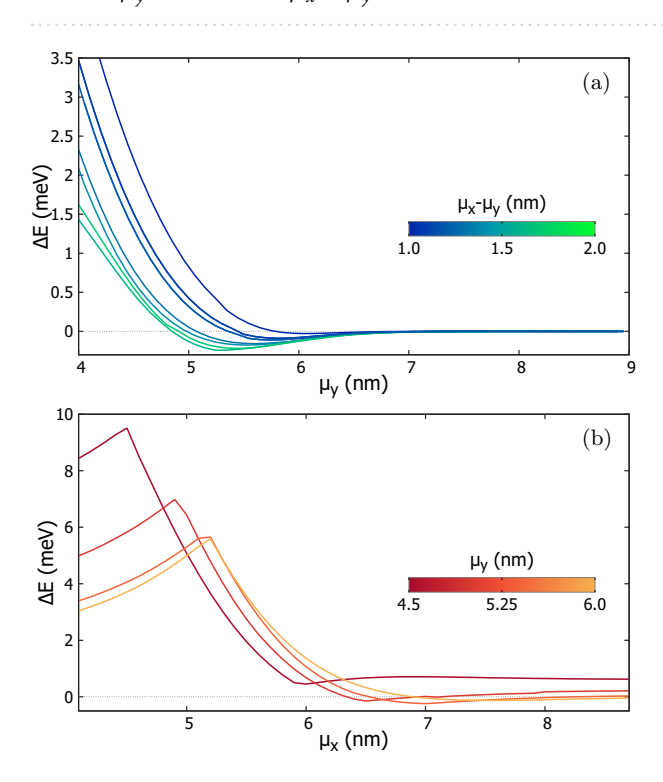


Figure 5. (a) The Nagaoka gap as a function of the parameters μ_y for different values of $(\mu_x - \mu_y)$. (b) as a function of parameter μ_x for various μ_y 's. The lines shift towards the negative sides as the system parameters approach the largest Nagaoka gap point, after which the lines in both subfigures approach zero.

Shift from the rectangular geometry

In order to investigate the robustness of the spin-polarized ground state we deform the rectangular arrangement of dots so that electrons are trapped in a finite pseudo-1D chain. Starting from the initial state with the largest energy gap, i.e. $\mu_x = 6.8$ nm, $\mu_y = 5.2$ nm, we shift the location of the top-right dot in both x and y directions separately. The energy gap as a function of the shift $\Delta\mu$ is plotted in Fig. 7. The anisotropy in the effective mass makes the nature of Nagaoka transition different in armchair (x) and zigzag (y) direction. For a shift in armchair direction, the spin-1/2 states have much lower energy than the high-spin state and the electrons from a 1D pseudo chain structure as seen in inset (f) of Fig. 7. The electron occupancy of the lower right dot is low for the shift of $\Delta \mu_V = 3.5$ nm in the zigzag direction. One of the electrons get fixed in the shifted dot, which is far away from the rest, which minimizes the Coulomb interaction energy. The two remaining electrons occupy the deeper left dumbbell instead of the shallower lower right dot [see inset (a) and (b) of Fig. 7]. No tunneling is possible between the rightmost dots and only a trace tunneling in the topmost dots. A similar effect is seen in the x-direction shift, but the geometry of the dots is such that the electrons form a chain with no tunneling between the two upper dots. Ref.²⁴ showed that when the dot arrays are deformed to form a quantum dot chain, the spin polarization in the ground state is excluded by the Lieb-Mattis theorem⁴⁰, which restricts the ground state solutions of such a 1D chain to low spin values. However, the anisotropy of the masses leads to an asymmetry in the tunneling of electrons between the dots. In the case of a shift in the zigzag direction, the system can

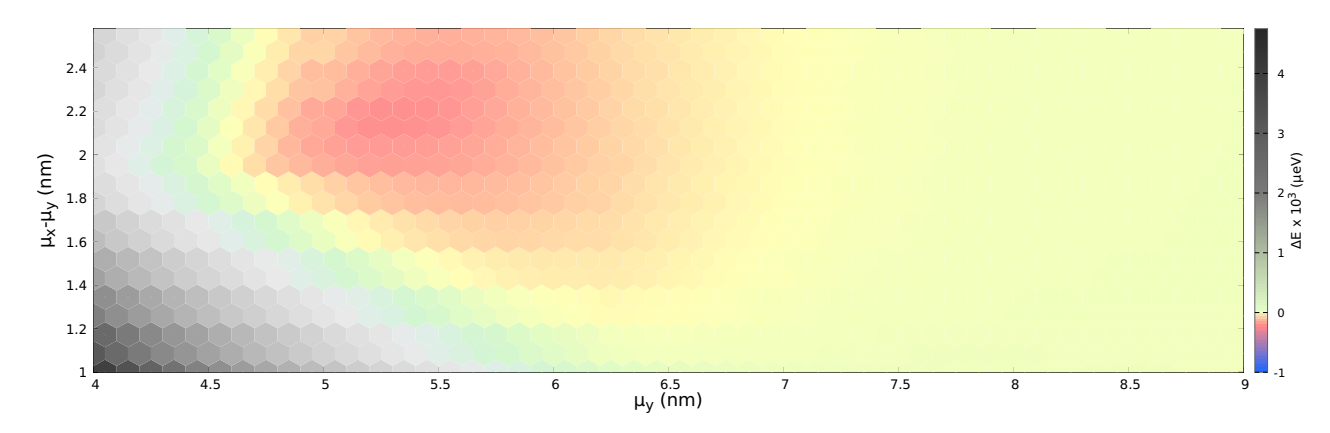


Figure 6. The energy gap, ΔE as a function of the parameters μ_y and $(\mu_x - \mu_y)$ with potential depth, $V_d = 60$ meV. The energy gap is calculated for every point at the center of the hexagons. The largest energy gap $\Delta E = -211~\mu \text{eV}$ occurs at $\mu_y = 5.35$ nm and $\mu_x - \mu_y = 2.21$ nm. The diagram is similar as Fig. 4, but the lower potential depth has resulted in a major shift of the largest Nagaoka gap up on the $\mu_x - \mu_y$ scale and a minor shift on μ_y scale.

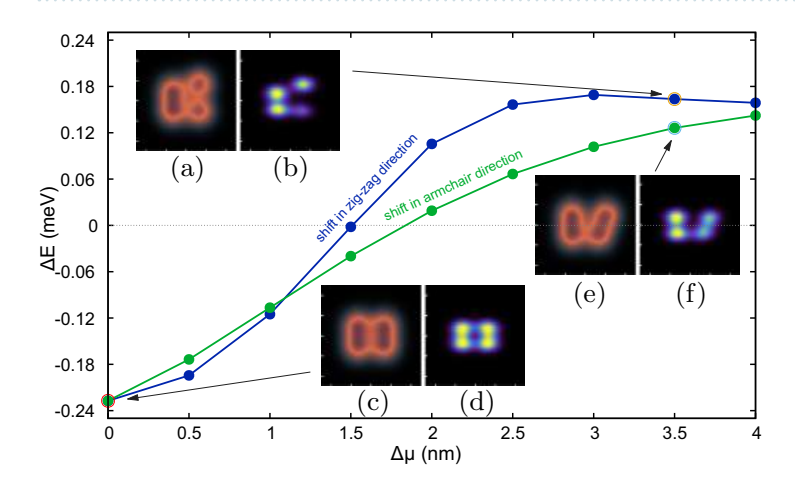


Figure 7. The Nagaoka gap as a function of shift $\Delta\mu$ for both in armchair direction (shown in blue) and zigzag direction (shown in green) from the starting point of $\mu_x = 6.8$ nm, $\mu_y = 5.2$ nm. The insets $(\mathbf{a}, \mathbf{c}, \mathbf{e})$ show the external potential and insets $(\mathbf{b}, \mathbf{d}, \mathbf{f})$ show the square root of ground state electron density. The insets (\mathbf{a}, \mathbf{b}) are for shift $\Delta\mu_x = 3.5$ nm and (\mathbf{e}, \mathbf{f}) are for shift $\Delta\mu_y = 3.5$ nm. The starting potential and square root density are shown in insets (\mathbf{c}, \mathbf{d}) . The colors scale for insets is same as in Fig. (2). The difference in the curves can be explained using different mechanisms as discussed in Section "Shift from the rectangular geometry".

be divided into two parts: the left double-dot subsystem and two single dots. As in the case of Fig. 3c, the double dot holds the singlet state of two electrons, and the third electron lowers the Coulomb repulsion by occupying the shifted dot. Tunnel coupling in the y direction decreases rapidly due to the higher effective mass, resulting in a transition occurring at a shift of about ~ 1.5 nm. In contrast, lifting the Nagaoka ground-state polarization requires a shift of approximately 1.85 nm in the x-direction.

Potential detuning

In addition to moving the dots, it is possible to assess the tolerance of the ferromagnetic state to disorder by changing the potential depth of one of the dots. We vary the potential depth V_d of just the top right dot by an amount dV. Fig. 8 shows the Nagaoka gap as a function of the change dV in the range -20 meV to 20 meV. The changes in the electron density as the potential changes are also shown in the insets of Fig. 8.

The most evident feature of the plot in Fig. 8 is the asymmetry in the energy gap variation for negative and positive potential changes. More precisely, for the positive change dV the Nagaoka ferromagnetic transitions to the low-spin state at $dV \approx 7.0$ meV, while the same transition occurs at a bit smaller change of $dV \approx -5.4$ meV for the negative change. The transition to the low-spin ground state for positive detuning is due to the localization of an electron in the detuned dot and the transition for negative detuning is due to the delocalization of an electron from the detuned dot which is excluded from the array by the energy mismatch leaving the three dots with an exact half-filling. When the top right dot is made deeper [insets (c) and (d)] the electron occupancy of this dot becomes larger than 1. When the dot is made shallower [insets (a) and (b)] the dot is emptied. In both cases the conditions for observation of the itinerant ferromagnetism are lifted, and the ground state acquires the low spin.

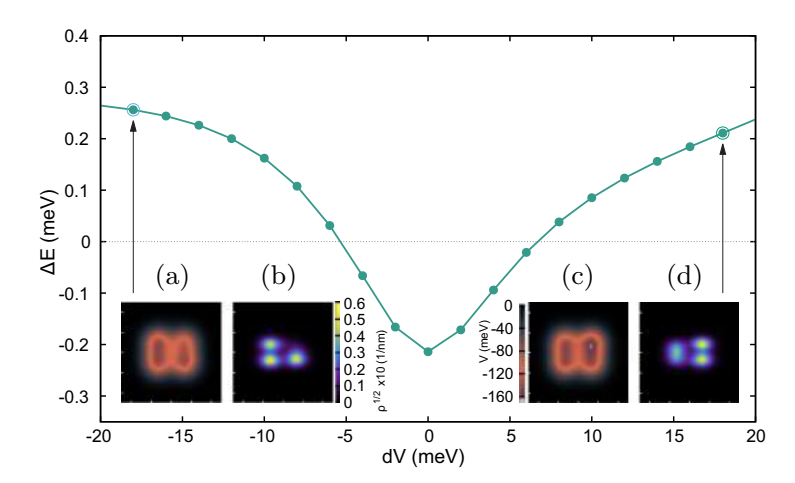


Figure 8. The Nagaoka gap as a function of an alteration in the potential of one of the dots, dV (meV). The insets (a, b) show the potential and square root electron density for value dV = -18 meV and insets (c, d) show the potential and the square root electron density for change in potential of dV = 18 meV. The color scale for the potential and square root of density is shown. Unlike the case in Section "Shift from the rectangular geometry", the anisotropy of the curve is inherent and is not unique to phosphorene.

Summary and conclusions

We have investigated the Nagaoka ferromagnetic state in the phosphorene quantum-dot plaquette using an effective mass Hamiltonian nearly half-filled system. We determined the geometry of the plaquette for the maximal stability of the spin-polarized ground state. For the chosen parameters of the isotropic single-dot Gaussian confinement the largest Nagaoka gap of $\Delta E = -230 \,\mu\text{eV}$ occurs for the parameters $\mu_x = 6.8 \,\text{nm}$ and $\mu_v = 5.2 \,$ nm. Shifting one of the dots in x or y direction breaks the ferromagnetic ordering of spins stopping the carrier hopping between now nonequivalent locations and forming a quasi-1D chain with low spin ground state on the ground of the Lieb-Mattis theorem. Our results indicate that the Nagaoka state in the phosphorene quantum dots exhibits strong resistance to disorder, which we tested in the form of detuning one of the dots. We showed that the mechanisms breaking the Nagaoka ordering are different for positive and negative detuning, and hence the transition occurs for uneven values of detuning.

Data availability

The data that support the findings of this study are available from the first author (T.T.) upon reasonable request.

Received: 10 May 2023; Accepted: 25 October 2023 Published online: 01 November 2023

References

- 1. Hubbard, J. Electron correlations in narrow energy bands. Proc. R. Soc. A 276, 238-257 (1963).
- 2. Hubbard, J. Electron correlations in narrow energy bands. II. The degenerate band case. Proc. R. Soc. A 277, 237-259 (1964).
- 3. Scalapino, D. J., Loh, E. Jr. & Hirsch, J. E. D-wave pairing near a spin-density-wave instability. Phys. Rev. B 34, 8190(R) (1986).
- 4. Dagotto, E. & Riera, J. Indications of $d_x^2 y^2$ superconductivity in the two dimensional t-J model. *Phys. Rev. Lett.* **70**, 682 (1993).
- 5. Shen, S. Q., Qiu, Z. M. & Tian, G. S. Ferrimagnetic long-range order of the Hubbard model. *Phys. Rev. Lett.* **72**, 1280 (1994). 6. Liu, S. H. Quasispin model for itinerant magnetism-effects of short-range order. *Phys. Rev. B* **17**, 3629 (1978).
- Wang, X. et al. Experimental realization of an extended Fermi-Hubbard model using a 2D lattice of dopant-based quantum dots. Nat. Commun. 13, 6824 (2022).
- 8. Hensgens, T. et al. Quantum simulation of a Fermi-Hubbard model using a semiconductor quantum dot array. Nature 548, 70-73 (2017).
- 9. Nagaoka, Y. Ferromagnetism in a narrow, almost half-filled s band. Phys. Rev. 147, 392 (1966).
- 10. Tasaki, H. From Nagaoka's ferromagnetism to flat-band ferromagnetism and beyond: An introduction to ferromagnetism in the Hubbard model. Prog. Theor. Phys. 99, 489 (1998).
- 11. Dehollain, J. P. et al. Nagaoka ferromagnetism observed in a quantum dot plaquette. Nature 579, 528 (2020).
- 12. Mattis, D. C. Eigenvalues and magnetism of electrons on an artificial molecule. Int. J. Nanosci. 02, 165-170 (2003).
- Wang, Y. et al. Ab initio exact diagonalization simulation of the Nagaoka transition in quantum dots. Phys. Rev. B 100, 155133 13. (2019).
- 14. Liu, H. et al. Phosphorene: An unexplored 2D semiconductor with a high hole mobility. ACS Nano 8(4), 4033-4041 (2014).
- 15. Long, G. et al. Achieving ultrahigh carrier mobility in two-dimensional hole gas of black phosphorus. Nano Lett. 16(12), 7768–7773
- 16. Long, G. et al. Ambipolar quantum transport in few-layer black phosphorus. Phys. Rev. B 96, 155448 (2017).
- Yang, J. et al. Integer and fractional quantum hall effect in ultrahigh quality few-layer black phosphorus transistors. Nano Lett. 18(1), 229-234 (2018).
- 18. Zhong, J., Xie, J. & Sheng, W. Negative quasiparticle shifts in phosphorene quantum dots. Phys. Rev. B 103(23), 235405 (2021).
- Bui, H. D., Phuong, L. T. & Yarmohammadi, M. On the influence of dilute charged impurity and perpendicular electric field on the electronic phase of phosphorene: Band gap engineering. Europhys. Lett. 124(2), 27001 (2018).
- Neupane, B., Tang, H., Nepal, N. K. & Ruzsinszky, A. Bending as a control knob for the electronic and optical properties of phosphorene nanoribbons. Phys. Rev. Mater. 6(1), 014010 (2022).

- 21. Yarmohammadi, M., Hoi, B. D. & Phuong, L. T. T. Systematic competition between strain and electric field stimuli in tuning EELS of phosphorene. Sci. Rep. 11(1), 3716 (2021).
- 22. Derball, S. & Moudam, O. Insights into the application of 2D phosphorene in dye-sensitized solar cells. *Energy Technol.* 11(9), 2300353 (2023).
- 23. Schuster, R., Trinckauf, J., Habenicht, C., Knupfer, M. & Büchner, B. Anisotropic particle-hole excitations in black phosphorus. *Phys. Rev. Lett.* **115**, 026404 (2015).
- 24. Szafran, B. Electrostatic quantum dot confinement in phosphorene. Phys. Rev. B 101, 235313 (2020).
- 25. Qiao, J., Kong, X., Hu, Z. X., Yang, F. & Ji, W. High-mobility transport anisotropy and linear dichroism in few-layer black phosphorus. *Nat. Commun.* 5, 4475 (2014).
- 26. Buterakos, D. & Sarma, S. D. Ferromagnetism in quantum dot plaquettes. Phys. Rev. B 100, 224421 (2019).
- 27. Thakur, T. & Szafran, B. Aharonov–Bohm oscillations in phosphorene quantum rings: Mass anisotropy compensation by confinement potential. *Phys. Rev. B* **105**, 165309 (2022).
- 28. Junior, P. E. F., Kurpas, M., Gmitra, M. & Fabian, J. $k \cdot p$ theory for phosphorene: Effective g-factors, Landau levels, and excitons. *Phys. Rev. B* 100, 115203 (2019).
- 29. Yang, F. et al. Quantum hall effect in electron-doped black phosphorus field-effect transistors. Nano Lett. 18, 6611 (2018).
- 30. Zhou, X. et al. Effective g factor in black phosphorus thin films. Phys. Rev. B 95, 045408 (2017).
- 31. Li, L. et al. Quantum Hall effect in black phosphorus two-dimensional electron system. Nat. Nanotechnol. 11, 593 (2016).
- 32. Gillgren, N. et al. Gate tunable quantum oscillations in air-stable and high mobility few-layer phosphorene heterostructures. 2D Mater. 2, 011001 (2014).
- 33. Governale, M. & Ungarelli, C. Gauge-invariant grid discretization of the Schrödinger equation. Phys. Rev. B 58, 7816 (1998).
- 34. Lis, K., Bednarek, S., Szafran, B. & Adamowski, J. Electrostatic quantum dots with designed shape of confinement potential. *Phys. E* 17, 494–497 (2003).
- 35. Bednarek, S., Szafran, B., Lis, K. & Adamowski, J. Modeling of electronic properties of electrostatic quantum dots. *Phys. Rev. B* 68, 155333 (2003).
- 36. Szafran, B. Annular confinement for electrons on liquid helium. Phys. Rev. B 104, 235402 (2021).
- 37. Ashoori, R. C. et al. N-electron ground state energies of a quantum dot in magnetic field. Phys. Rev. Lett. 71, 613 (1993).
- 38. Thakur, T. & Szafran, B. Wigner molecules in phosphorene quantum dots. Phy. Rev. B 106(20), 205304 (2022).
- 39. Rontani, M., Cavazzoni, C., Bellucci, D. & Goldoni, G. Full configuration interaction approach to the few-electron problem in artificial atoms. *J. Chem. Phys.* **124**(12), 124102 (2006).
- 40. Lieb, E. & Mattis, D. Theory of ferromagnetism and the ordering of electronic energy levels. Phys. Rev. 125, 164 (1962).

Acknowledgements

This work was supported by the National Science Centre (NCN) according to decision DEC-2019/35/O/ST3/00097. We gratefully acknowledge Poland's high-performance computing infrastructure PLGrid (HPC Center Cyfronet) for providing computer facilities and support within computational grant no. PLG/2023/016317. Research was partly supported by program "Excellence initiative - research university" for the AGH University of Krakow.

Author contributions

T.T. performed the calculations analyzed the results and prepared the manuscript. B.S. selected and tested the calculation method, participated in the discussion of the results and editing the text. The authors declare no competing interests.

Competing interests

The authors declare no competing interests.

Additional information

Correspondence and requests for materials should be addressed to B.S.

Reprints and permissions information is available at www.nature.com/reprints.

Publisher's note Springer Nature remains neutral with regard to jurisdictional claims in published maps and institutional affiliations.

Open Access This article is licensed under a Creative Commons Attribution 4.0 International License, which permits use, sharing, adaptation, distribution and reproduction in any medium or format, as long as you give appropriate credit to the original author(s) and the source, provide a link to the Creative Commons licence, and indicate if changes were made. The images or other third party material in this article are included in the article's Creative Commons licence, unless indicated otherwise in a credit line to the material. If material is not included in the article's Creative Commons licence and your intended use is not permitted by statutory regulation or exceeds the permitted use, you will need to obtain permission directly from the copyright holder. To view a copy of this licence, visit http://creativecommons.org/licenses/by/4.0/.

© The Author(s) 2023

8. Nagaoka ferromagnetism in an array of phosphorene quantum dots

Chapter 9

Electrical manipulation of the spins in phosphorene double quantum dots

Thakur, T., Peeters, F. M., & Szafran, B. Electrical manipulation of the spins in phosphorene double quantum dots. Scientific Reports, 14(1), 18966 (2024). Licensed under CC BY 4.0.

scientific reports



OPEN Electrical manipulation of the spins in phosphorene double quantum dots

Tanmay Thakur^{1,2}, Francois M. Peeters^{2,3,4} & Bartłomiej Szafran^{1⊠}

We investigate electric dipole spin resonance (EDSR) induced by an oscillating electric field within a system of double quantum dots formed electrostatically in monolayer phosphorene. Apart from the observed anisotropy of effective masses, phosphorene has been predicted to exhibit anisotropic spin-orbit coupling. Here, we examine a system consisting of two electrons confined in double quantum dots. A single-band effective Hamiltonian together with the configuration interaction theory is implemented to simulate the time evolution of the ground state. We examine spin flips resulting from singlet-triplet transitions driven by external AC electric fields, both near and away from the Pauli blockade regime, revealing fast sub-nanosecond transition times. Furthermore, we analyze the impact of anisotropy by comparing dots arranged along a different crystal axis. The sub-harmonic multi-photon transitions and Landau-Zener-Stückelberg-Majorana transitions are discussed. We show modulation of spin-like and charge-like characteristics of the qubit through potential detuning.

In the fast-evolving landscape of quantum technology, precise control and manipulation of spin emerges as a topic of prime importance. Coupling of spin with the magnetic field facilitates the control of electron spins in the system. If this magnetic field has an alternating component, it induces rotation of spin on the Bloch sphere by electron spin resonance (ESR)¹⁻³ and thus one of the simplest spin manipulation can be achieved. Such spin rotations are crucial in spintronics⁴⁻⁶ and quantum computing applications⁶⁻⁸. However, because of the small moments of the spin, a very strong alternating magnetic field is required to realise fast rotations, making ESR a demanding experimental task. Spin-orbit coupling (SOC) in the materials, either inherent or engineered^{9,10}, offers a practical alternative for this task by coupling the spin moment to the electric field through electric dipole spin resonance (EDSR)^{11,12}. It is an optimal choice for spin manipulations, since a fine-tuned electric field of desired features can be produced using advanced engineering methods. Although EDSR is observed in a variety of systems like bulk crystals^{11,13} and quantum wells^{14,15}, its ideal use is in quantum dots where discrete states can

The EDSR is investigated in double quantum dots with two electrons, with spin manipulations lifting the Pauli spin blockade of the current flow 19,20. SOC hybridization between the spin singlet and triplet states results in an avoided crossing, which can be used to determine the SOC energy²¹. Effects of tunneling with the SOC in strongly electrically driven double quantum dot system were examined theoretically 22,23 and showed a nonlinear character of the spin resonance. Spins in III-V semiconductor quantum dots are subject to dephasing due to electron-nucleus effects^{24–26} which, when comparable with the spin-flip times, will hinder precise spin control. For this reason, fast manipulation and control of the spins are pursued by researchers 10,26 and remains a considerable challenge to develop quantum dots as qubits. The states of the bottom of the conduction band in phosphorene are constructed of p-type orbitals²⁷ which eliminates the dephasing effects of the hyperfine interaction.

The anisotropic spin-orbit magnetic field, produced by combined Rashba and Dresselhaus SOC, results in anisotropic avoided crossings and relaxation times^{28–30}. Such anisotropy affects also the rate of spin-flip tunneling in double quantum dots. A similar but inherent anisotropy in Rashba SOC alone was predicted in phosphorene 31,32. The phoshophorene has an inversion symmetry and the Dresselhaus coupling occurs only when the symmetry is intentionally broken³³.

Phosphorene³⁴, a monolayer form of black phosphorous, is a material with rapidly evolving interest and is extensively studied for its strongly correlated properties^{35–37} and anisotropic characteristics^{38,39}. The band's anisotropy reflects itself in the effective masses of the electron in phosphorene and results in different Rashba SOC

¹Faculty of Physics and Applied Computer Science, AGH University of Krakow, al. Mickiewicza 30, 30-059 Kraków, Poland. ²Department of Physics, University of Antwerp, Groenenborgerlaan 171, 2020 Antwerp, Belgium. ³Nanjing University of Information Science and Technology, Nanjing 210044, China. ⁴Departamento de Física, Universidade Federal do Ceará, Campus do Pici, Fortaleza, Ceará 60455-900, Brazil. [™]email: bszafran@agh.edu.pl

parameters for zig-zag and armchair direction. Phosphorene quantum dots in the form of nano flakes have been studied for various applications^{40,41}. In this work, we study electrostatically confined double quantum dots in phosphorene with electric field driving. This system is promising to study the majority of the physics concerned with quantum spin control. We investigate the interplay between the anisotropy of the effective masses, tunneling and SOC and spin flip-rates. We also examine the effects of asymmetry of the dot potentials, which can be exploited as a control knob in experiments to fine-tune the nature of qubit and spin manipulations. Additionally, we take a look at low frequency electric driving, i.e. Landau-Zener^{42,43} sweep near the avoided crossing of the lowest energy spin-singlet and spin-triplet states of double quantum dot. We will also see the occurrence of spin-flip transitions, which are forbidden by parity selection rules through higher order processes and explain the mechanism behind it.

The paper is organised as follows: In Sect. "Theory", we discuss the theory and setup that were considered to study the system. Then we move on to the discussion of our results in Sect. "Results & discussions", where we first discuss the effects of asymmetry on the system in Sect. "Effects of asymmetry at t=0" and study the main focus of the work of spin manipulations and spin-flip transitions in Sect. Spin-flip transitions. Later in Sect. Dots arranged in the zig-zag direction we discuss the effects of anisotropy of phosphorene by changing the arrangement of the dots in a different lattice direction. Finally, we conclude and summarize our results in Sect. Summary and conclusions.

Theory

The system under consideration is lateral double quantum dots with spin orbit coupling, external constant perpendicular magnetic field and external time dependent electric field as illustrated in Fig. 1. The single electron the Hamiltonian is.

$$H(t) = H_0 + H_{SO} + V'(t),$$
 (1)

where H_0 is the effective mass continuum model for phosphorene derived from the tight-binding Hamiltonian⁴⁴, H_{SO} is the spin-orbit coupling and V'(t) is the external time dependent electric field for the control of spins in the dots. The single electron effective mass Hamiltonian is given by

$$H_{0} = \left(-i\hbar \frac{\partial}{\partial x} + eA_{x}\right)^{2} / 2m_{x} + \left(-i\hbar \frac{\partial}{\partial y} + eA_{y}\right)^{2} / 2m_{y}$$

$$+g \mu_{B} B \sigma_{z} / 2 + V(x, y),$$
(2)

with effective masses $m_x = 0.17037m_0$ ($m_y = 0.85327m_0$) along armchair (zig-zag) direction of the phosphorene crystal. The Landé g-factor for the material is taken to be g = 2. The corrections to the bare g-factor for phosphorene vary and are reported in previous theoretical 45,46 and experimental works 47,48. The precise value of the g-factor is of less significance for our work as variations primarily impact the position of avoided crossings rather than qualitative conclusions regarding the spin control and spin-flip transitions.

The confinement potential V(x, y) is modelled by two inverted Gaussians centered at +d and -d (c.f.Fig. 1) in the x (armchair) direction with parameters d = 8 nm, s = 7 nm and is given by

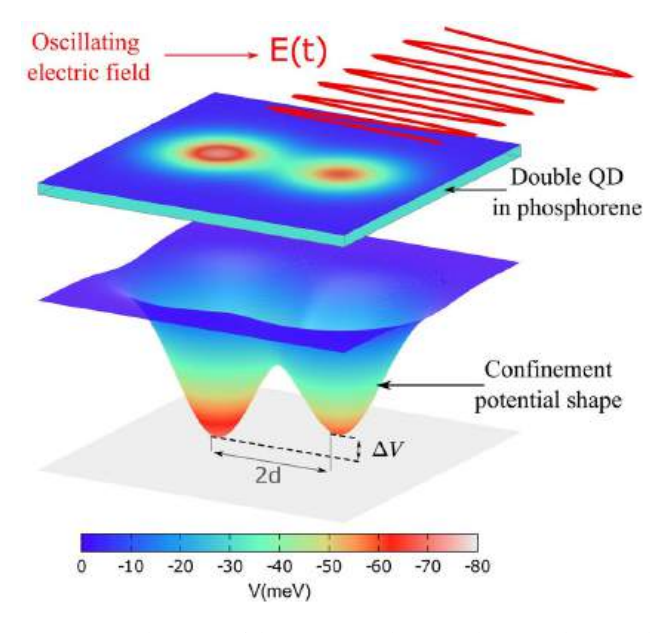


Figure 1. Schematic of the system under consideration showing double quantum dot formed in phosphorene due to electrostatic confinement potential and the applied oscillating electric field for driving the transitions.

$$V(x,y) = V_R \exp\left(-\frac{((x-d)^2 + y^2)}{s^2}\right) + V_L \exp\left(-\frac{((x+d)^2 + y^2)}{s^2}\right).$$
(3)

For the case of phosphorene electrons with strong correlation effects⁴⁹⁻⁵¹, as well as transitions induced by external driving fields, it is anticipated that higher energy states will have contributions to the physics of the system. While the parabolic potential serves as a convenient approximation for examining quantum dots near the ground states, we expect that the Gaussian potential will be a more realistic model for EDSR experiments involving quantum dots in phosphorene⁵².

The spin-orbit coupling is a relativistic effect where the electric field induces a momentum dependent magnetic field which then couples with the spin. These effects especially in 2D materials were reviewed in Ref.⁵³. This coupling is essential for driving the spins electrically and the contribution of this interaction is given by

$$H_{SO} = \lambda_x \left(-i\hbar \frac{\partial}{\partial x} \right) \sigma_y + \lambda_y \left(-i\hbar \frac{\partial}{\partial y} \right) \sigma_x, \tag{4}$$

where σ_x and σ_y are Pauli matrices and the anisotropic Rashba parameters are $\lambda_x = -17.9 \,\mathrm{meV} \cdot \text{Å}$ and $\lambda_y = 10.3 \,\mathrm{meV} \cdot \text{Å}$. The values are taken to be ten times of that found by Farzaneh et. al for electric field of about 1 V/nm³¹. Another work³² reported much larger anisotropy and values with external field of about 2.6 V/Å. In comparison, Shubnikov-de Haas oscillations and spin precession studies for InAs quantum well gives a Rashba parameter of 67.1 meV Å⁵⁴. Experiments on other InAs heterostructures reported similar values⁵⁵⁵⁵⁵. Many other materials have been reported to have a larger SOC parameter than phosphorene⁵⁵³ and phosphorene can be considered to have weak spin orbit coupling but which is order of magnitude larger than for graphene.

In order to induce transitions, driving electric field E(t) can be applied experimentally with microwave radiation or simply by adding an AC voltage component to the confinement gate electrodes^{25,59-67}. In both cases the wavelength of the electric field is much larger than that of the dimensions of the system. Therefore the in-plane electric field V'(x,y,t) is taken to be spatially constant between the gates or throughout the size of the system. For field along x (armchair) direction,i.e. in the same orientation as the dots are arranged, the term V'(t) in Eq. (1) equates to $V'(t) = -eFx\Theta(t)\sin(\omega t)$ and the field is switched on at t = 0, where $\Theta(t)$ is Heaviside function.

We focus on double quantum dots populated with two interacting electrons. Hence, the Hamiltonian of the complete system is given by,

$$H_{2e}(t) = \sum_{i=1}^{2} H_i(t) + \sum_{i>i}^{2} \frac{e^2}{4\pi \epsilon_0 \epsilon r_{ij}},$$
 (5)

where the dielectric constant is $\epsilon=9$. For the diagonalization of the final Hamiltonian in Eq. (5) at t=0, we use the configuration interaction approach. The single electron eigenstates of the Hamiltonian H_0+H_{SO} are used to form Slater determinants for the possible configurations of two electrons in these eigenstates. The single electron eigenstates are themselves obtained using the discretization as performed in previous work⁵⁰. The final Hamiltonian is then diagonalized in the basis of these Slater determinants to get the stationary states $|i\rangle$ and corresponding energies of $H_{2e}(t=0)$. The states $|i\rangle$ is the total wavefunction containing spatial, spin and orbital state. The probability density of two electrons in state $|i\rangle$ is obtained using

$$\rho_i(\mathbf{r}) = \langle i | \sum_{i=1}^2 \delta(\mathbf{r} - \mathbf{r}_i) | i \rangle.$$
 (6)

Time dependent part of the Hamiltonian is solved subsequently using the Schrödinger equation. We assume that the final state of the system after the application of the time dependent field will be a linear combination of the original two electron energy eigenfunctions at t=0. Moreover, we assume the time evolution of the individual states itself is given by the time dependent Schrödinger equation without the field V'(t) and the extra potential evolves the coefficients of the linear combinations only. The final state is thus, $|\Psi(t)\rangle = \sum_i c_i(t) \exp[-iE_it\hbar]|i\rangle$ and the probability of system to be in state $|n\rangle$ at time t is then $|c_n(t)|^2$. Substituting this state into the time-dependent Schrödinger equation one obtains the coupled differential equations for the time evolution of the coefficients.

$$i\hbar \left(\frac{d}{dt}\right) c_n(t) = -eF \sum_m c_m(t) \exp[i(E_m - E_n)t/\hbar]$$

$$\cdot \sin(\omega t) \langle m|x_1 + x_2|n\rangle.$$
(7)

The coupled differential equations are then solved using the Crank-Nicolson method to obtain the probabilities $|c_n(t)|^2$ at any given time. The system is evolved for a finite time with a fixed initial condition $c_i(t=0) = \delta_{i1}$.

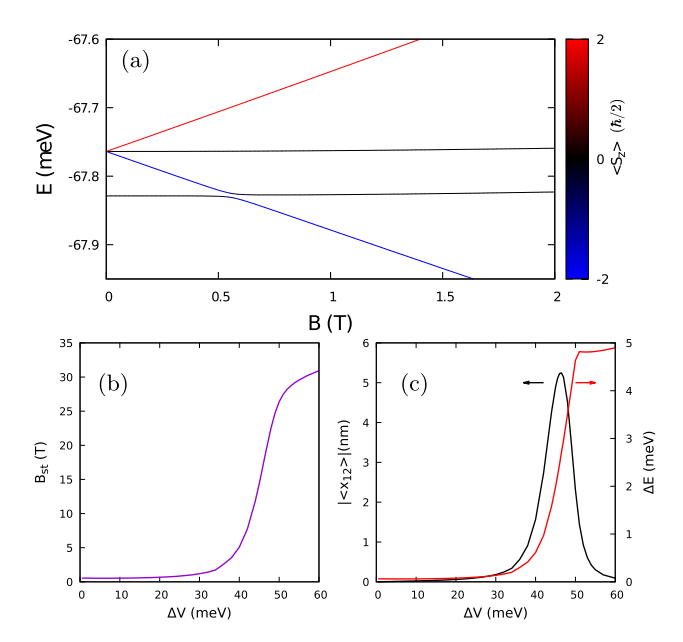


Figure 2. (a) Lowest energy eigenstates without the external electric field with the singlet-triplet avoided crossing at $B_{st} = 0.56$ T for $\Delta V = 0$. The color scale shows the average eigenvalue of S_z operator. (b) The magnetic field corresponding to the center of singlet-triplet avoided crossing as a function of asymmetry of the double dot system. (c) The maximal value of matrix element (black curve, left axis) at center if the avoided crossing and the singlet-triplet energy difference (red curve, right axis) as function of asymmetry.

Results & discussions Effects of asymmetry at t=o

Figure 2a illustrates the two electron lowest eigenstates of the system at time t=0. With a symmetric potential, where V_L and V_R are equivalent [as defined in Eq. (3)], the singlet state emerges as the ground state, accompanied by the triplet state as the first excited state with $\langle S_z \rangle = -\hbar$. External magnetic field along z-axis promotes the triplet as ground state, eventually. As a result, a crossing between the singlet and triplet states occurs which turns into an anti-crossing by the SO coupling. As we remove the symmetry by increasing $\Delta V = V_L - V_R$, the position of this avoided crossing shifts, as shown in Fig. 2b. The magnetic field at the center of this singlet-triplet (S/T) avoided crossing B_{ac} varies slowly for initial values of ΔV and increases rapidly after 40 meV and starts to saturate near 60 meV, suggesting that the system is sensitive to even small changes in potential between $\Delta V = 40$ meV and $\Delta V = 50$ meV. The single-triplet energy difference ΔE at magnetic field B=0 shown in Fig. 2c with red curve. We discover a similar sensitive nature of ΔE due to the detuning, but the value flattens considerably after $\Delta V = 50$ meV suggesting further detuning has very little impact on the system.

A better understanding can be gained by examining the square root of electron densities calculated using Eq. (6) as plotted in Fig. 3 to give insight on the wavefunction. The square root densities of the singlet and the triplet state are plotted at zero magnetic field for detuning values $\Delta V = 0$ meV, $\Delta V = 46$ meV and $\Delta V = 60$ meV. It is crucial to note the fact that for a symmetric phosphorene dot system where the depth of dots is 60 meV a detuning of about even 10 meV renders very little change in the S/T energy difference. This robustness against detuning can be attributed to the large effective mass of the electrons, which leads to strong localization and electron-electron interaction⁶⁸. For a symmetric system [Fig. 3a,b], the singlet and triplet states look very similar, with two electrons occupying both dots. The difference between square root density in between the two dots near x = 0 nm exhibit the bonding nature of the singlet state and the anti-bonding nature of the triplet state for $\Delta V = 0$. For $\Delta V = 46$ meV we see a different character of the singlet [3c] state. While the triplet state [3d] maintains similarity to the $\Delta V = 0$ case but with unequal occupation in the dots, the singlet state shows that almost both electrons occupy a single dot. The triplet state consists of two electrons with the same individual spin orientations. Due to the Pauli exclusion principle they cannot occupy a single dot with the same single electron energy states, responsible for blocking of transport through the dots, i.e. Pauli spin blockade^{19,20} which was first reported in Ref.⁶⁹. Whereas the singlet electrons can occupy a single dot where both electrons are in the lowest single electron energy levels with just the Coulomb repulsion and tunnel barrier to overcome. Hence, the steeper slope of the curves in Fig. 2b,c are due to significant density changes in the ground state and first excited state with respect to ΔV . Once the detuning becomes sufficiently large at $\Delta V = 60$ meV, both electrons occupy mostly the left dot and a further increase of detuning only increases the strength of confinement of the electrons.

Given the focus of this study is on spin-flip transitions, it is important to investigate the matrix element $\langle 1|x_1+x_2|2\rangle$ since for a given field amplitude F and frequency ν , the transition probability is upper bounded by the value of this matrix element. Fig. 2c shows the transition matrix element (black curve) as a function of the detuning ΔV . For the symmetric system the Hamiltonian commutes with a generalized parity operator $\Pi = \Pi_1(1) \otimes \Pi_1(2)$, where Π_1 is the single-electron operator

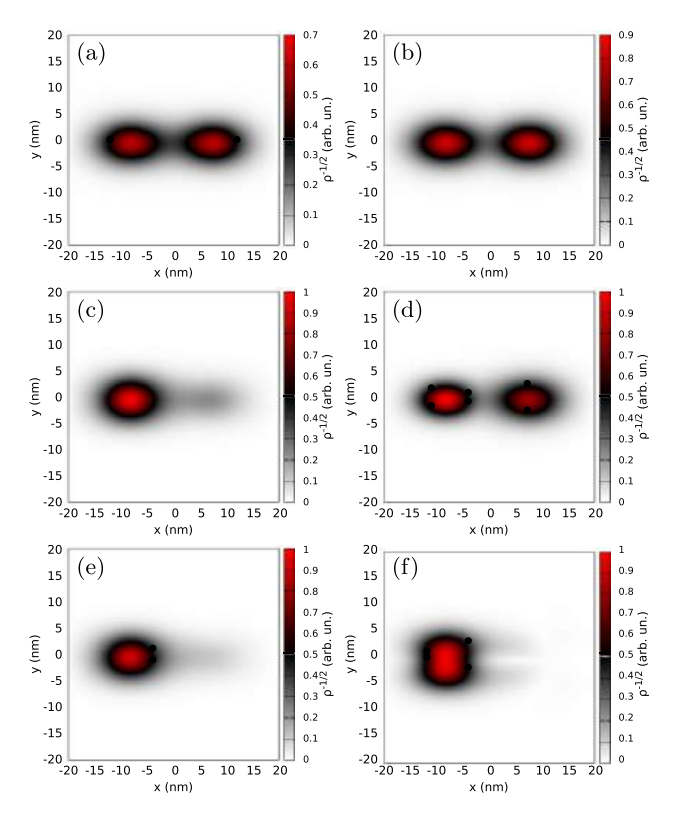


Figure 3. The square root of the charge density for the singlet $(\mathbf{a}, \mathbf{c}, \mathbf{e})$ and the triplet $(\mathbf{b}, \mathbf{d}, \mathbf{f})$ at B = 0 for a symmetric double dot system (\mathbf{a}, \mathbf{b}) , $\Delta V = 46$ meV (\mathbf{c}, \mathbf{d}) and $\Delta V = 60$ meV (\mathbf{e}, \mathbf{f}) .

$$\Pi_1 = \begin{pmatrix} P & 0 \\ 0 & -P \end{pmatrix},\tag{8}$$

and P is the scalar parity operator Pf(x,y) = Pf(-x,-y). For a symmetric potential the spin-up and spin-down components of the single-electron Hamiltonian wave functions have opposite parities. For two electrons, both the lowest-energy singlet and the lowest-energy triplet state with spin component $S_z = -\hbar$ correspond to negative eigenvalue of the Π operator. Due to the parity symmetry the transition dipole matrix elements $\langle n|x_1+x_2|m\rangle$ vanish for states n, m corresponding to the same Π eigenvalue ± 1 . This selection rule eliminates the possibility of a direct transition from singlet to the lowest triplet in the symmetric system as seen in Fig. 2c at $\Delta V = 0$, the value of matrix element is zero. The matrix element achieves its maximum value of 5.23 nm at $\Delta V = 46$ meV where the singlet has a charge state (2, 0) and the triplet with extended densities and charge state nearly (1, 1). This higher value of the transition matrix element is where we expect the largest chance in spin-flip transitions. Further beyond this point, the transition matrix reduces to lower values as the charge states for both states become the same, i.e. (2, 0).

The energy spectrum for the detuning $\Delta V=1$ meV and $\Delta V=46$ meV are presented in Fig. 4a and b respectively. In addition, the transition matrix element and the average $\langle S_z \rangle$ values are depicted in Fig. 4c and d. We observe that the avoided crossing is shifted to higher magnetic fields for the stronger detuning case just above 17 T, whereas for $\Delta V=1$ meV, the S/T avoided crossing occurs at 0.545 T. At these points the transition matrix element is the largest. Although non-zero, the transition matrix element for weak asymmetry is three orders of magnitude smaller than for the other case. We also see the exchange of the $\langle S_z \rangle$ values at the avoided crossings as seen in the second row of the figure by the red and blue curves. The most desirable region in the spectrum for fast electrical control of the spin is near these S/T avoided crossings. There have been EDSR experiments 59-66 where the frequency of microwave radiation or the AC frequency of voltages on the gates is of order of few to 10 GHz, which corresponds to energies of order 0.0414 meV. We shall now examine the spin-flip transitions near these S/T avoided crossings, where the energy differences exhibit comparable magnitudes, making the results more relevant to experimental observations. In the following two sections we present the analysis with the external time-dependent electric field for the two cases of a small and large potential asymmetry shown in Fig. 4.

Spin-flip transitions

We first consider the case with the largest transition matrix element, i.e. for $\Delta V=46$ meV. For such large asymmetry, as seen in the previous section, the spin singlet and triplet states are coupled with different charge states (1, 1) and (0, 2). The applied time-dependent electric field drives the system through spin orbit coupling. Using Eq. (7), the states were evolved typically for 20 ns for the plots presenting maximal occupation of spin flipped

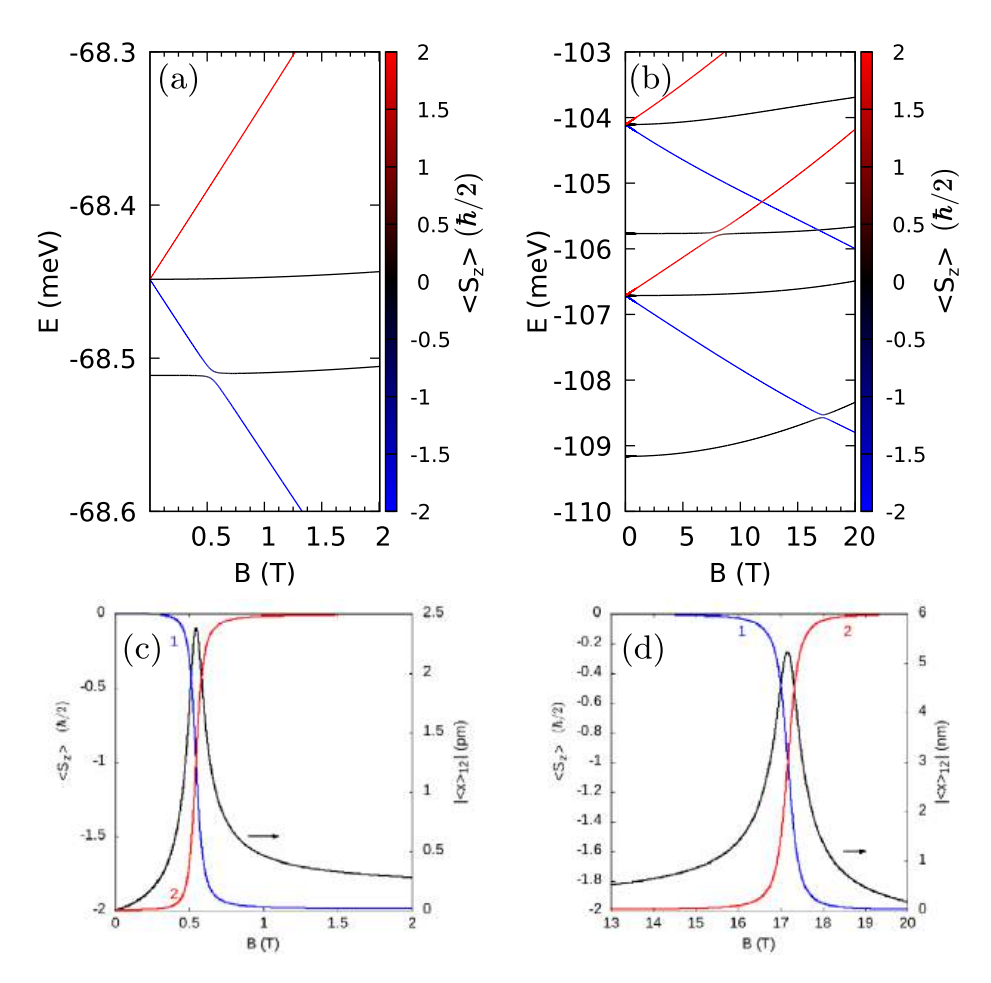


Figure 4. Two-electron energy spectrum for the double quantum dot system aligned with the x axis for asymmetry of the potential depth of (**a**) $\Delta V = 1$ meV and (**b**) $\Delta V = 46$ meV. The average $\langle S_z \rangle$ of the two lowest-energy levels referred to the left axis of (**c**) $\Delta V = 1$ meV and (**d**) $\Delta V = 46$ meV. Blue (Red) curves shows $\langle S_z \rangle$ value for ground (first excited) state. In (**c**) and (**d**) the black curve shows the dipole matrix element $\langle 1|x_1+x_2|2\rangle$ between the ground state and the first excited state referred to the right axis.

states as functions of hv. Even larger simulation times are used for evaluation of the spin-flip time when it exceeds 20ns. The calculations are performed for magnetic field 16 T near the S/T avoided crossing. Fig. 5a shows maximal occupation in the first excited state max $|c_2|^2 = p_f$ (the targeted final state) found during 20ns simulation time as a function of frequency of the applied field. We plot the resonance spectrum for three field amplitudes F and for each field strength. Notice the two peaks corresponding to first and second order transitions from singlet to triplet. The direct transition occurs near the S/T energy difference ΔE of about 0.14 meV, while the second order transition occurs at half this value. Similar harmonic resonances were observed in experiments in GaAs double QD⁶¹ and in GaAs heterostructures⁹ in InAs nanowire double QD⁷⁰. As the field strength increases, the peaks become broader with the second order transition always being sharper than the direct transition. Despite the increasing amplitudes, the positions of the peaks remain unchanged for both orders. This second order transition can be considered as two-photon transitions mediated by a virtual state. First the system undergoes an energy non-conserving transition to state $|m\rangle$ with the maximum probability determined by the transition matrix element x_{1m} and then from state $|m\rangle$ to state $|2\rangle$ with transition matrix element x_{m2} . The energy is conserved overall over the two transitions. Along with the matrix element, the contribution from each state of the system is inversely proportional to $[(\omega_{1m} - \omega)(\omega_{12} - 2\omega)]$. A much rigorous understanding can be obtained from the equations derived for the perturbative expansion of coefficients in Appendix A, which describes every feature of the peaks. This driving amplitude can be considered as weak since at B = 16T the matrix element of $\langle x_{12} \rangle = 1.59$ nm leads to $\frac{eF\langle x_{12} \rangle}{hv_{12}} \ll 1$. Due to a low amplitude of the driving field, no significant Bloch-Siegert shift⁷¹ is observed in the resonance frequencies as seen from the figure. Note that the peaks in Fig. 5a are not visibly shifted when the amplitude of the driving field is altered.

At the resonance, time taken for spin-flip transition is plotted in Fig. 5b. Remarkably, even for amplitudes as small as 1 μ V/nm, the spin-flip times remain close to 1 ns for the direct transitions. Whereas for the second order, a nano-second spin-flip occurs at amplitudes larger than 3.8 μ V/nm. The second order transition times decrease as a function of $\frac{0.003872^2}{F^2}$ ns (nm/mV)², while the direct transition goes as $\frac{0.00105}{F}$ ns nm/mV. It is even possible to achieve a sub nano-second spin-flip time as we approach the field strength of 10 μ V/nm. For even

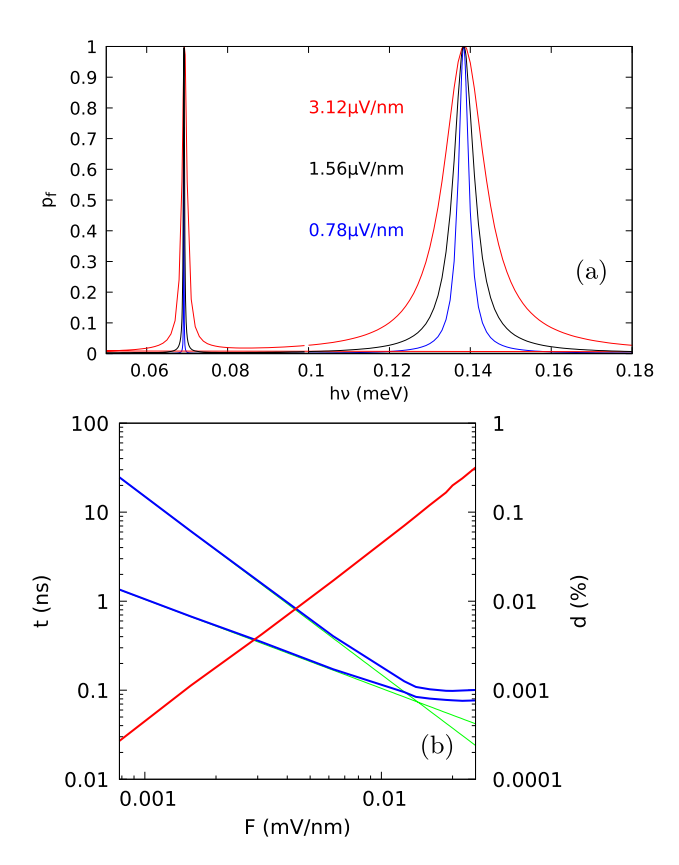


Figure 5. For $\Delta V=46$ meV at magnetic field B=16 T, (a) The maximal occupation of the triplet state for the time-dependent evolution of the system subject to the AC electric field with the amplitude of $0.78\mu V/nm$ (blue curve), $1.56\mu V/nm$ (black curve), and $3.12\mu V/nm$ (red curve) found in a simulation lasting 20 ns. (b) Blue solid and dashed lines show the singlet-triplet transition times as a function of the AC electric field amplitude for the first-order and second-order transitions, respectively. The two green thin lines show the linear and quadratic fits to the transition times vs the amplitude. The red line shows the contribution of the second and higher energy levels as a function of the AC field with slope of 2.

larger amplitudes, the lines lose their predicted dependence and deviate from the linear nature in the plot above 8 μ V/nm . This occurs due to the leakage of the system into higher energy states. Maximal leakage of probability into higher states as depicted with the red line in Fig. 5b. This leakage can be calculated with the formula $d=1-(|c_1(t)|^2+|c_2(t)|^2)$. When the leakage tends to zero, the system approaches an ideal two-level system, desirable for qubit applications and with dynamics accurately described by the Rabi model. We notice that even in the sub nano-second regime of the transitions, leakage is as low as 0.002% and grows quadratically with field amplitude F. A low leakage of the qubit is favoured to obtain norm conserving rotations on the Bloch sphere, which in turn is beneficial for higher gate fidelity and lower noise.

Such sub nanosecond transition between the two states of a qubit is reported often in charge qubits where the driving field is pulsed instead of sinusoidal, but it is still periodic⁷²⁻⁷⁴. This system can thus be used for fast sub-nanosecond spin manipulation operations without the practical intricacy of pulse generation and while retaining long coherence times due to weak spin-orbit coupling of phosphorene. These type of qubits are advantageous because of their quick operations, but they are also very vulnerable to material defects and charge noise from the quantum dot environment. The configuration described earlier with detuning of $\Delta V = 46$ meV can be regarded as a qubit where the spin and charge are strongly linked. It is possible to modify and tune this coupling via changing the original detuning, as shown in Fig. 2c. Weak coupling of the spin moment to the environment gives the advantage over a charge qubit in terms of large coherence times. A more spin-qubit like character can be obtained from the same setup by going to the other extreme end of detuning, i.e. a nearly symmetric system.

A similar analysis was therefore performed for $\Delta V = 1\,\mathrm{meV}$ and maximum of occupation $|c_2|^2$ with respect to the AC frequency of the electric field ν was obtained. Results for various electric field amplitudes are shown in Fig. 6. The magnetic field near the avoided crossing of 0.4 T and 0.9 T are chosen, the energy difference and its first few fractions are listed in Table 1. The simulation starts from the ground state, i.e. the singlet state for magnetic field 0.4 T and the triplet state for magnetic field 0.9 T. Immediately, we observe that despite the significantly smaller S/T energy difference in this scenario compared to the previous one, a much higher field is needed to induce the transition within the simulation time. This is because of the transition matrix elements being three orders of magnitude lower now [see Fig. 4c and d]. An amplitude $F = 0.2\,\mathrm{mV/nm}$ of the electric field produces a resonance spectrum as shown in the bottom part of Fig. 6a (for $B = 0.4\,\mathrm{T}$) and of Fig. 6b (for $B = 0.9\,\mathrm{meV/nm}$)

B (T)	Δ <i>E</i> ₁₂ (meV)	$\frac{\Delta E_{12}}{2}$ (meV)	$\frac{\Delta E_{12}}{3}$ (meV)	$\langle x_{12} \rangle (pm)$
0.4	0.017232	0.0086160	0.0057440	0.593
0.9	0.042037	0.0210185	0.0140123	0.531

Table 1. Energy difference and transition matrix element between singlet and triplet states near the avoided crossing for detuning $\Delta V = 1$ meV.

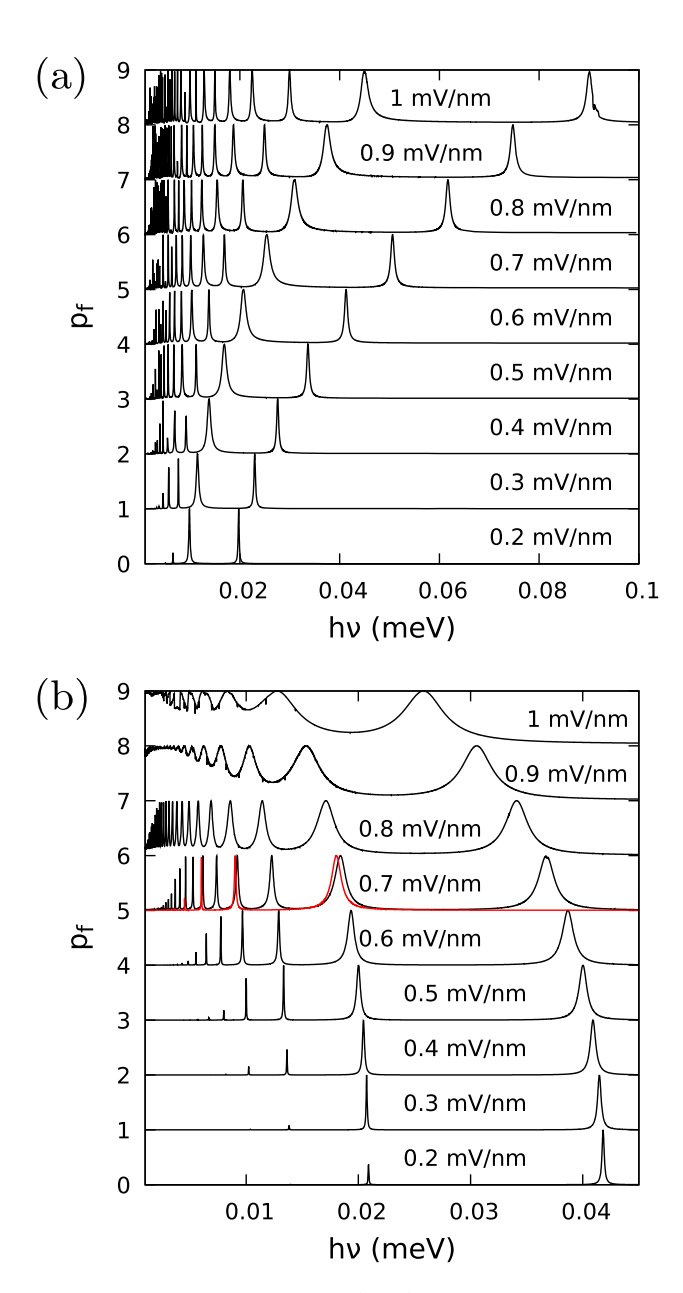


Figure 6. Maximal occupation of the first excited state calculated similar to Fig. 5 for $\Delta V=1$ meV in the external magnetic field of (a) 0.4 T and (b) 0.9 T. The plots for an increasing amplitude of the AC field are shifted by 1 in panels (a) and (b). The red curve in panel (b) shows the results for an ideally symmetric double dot and the amplitude of F=0.7 mV/nm with presence of only even order transitions. The simulation time in both the plots is set to 20 ns.

T). We detect resonances occurring near frequencies where the corresponding energies match the energy differences and their fractions. First resonance peak from the right corresponds to a direct spin-flip transition where $h\nu \approx \Delta E_{12}$. At the peak, we find that the direct spin-flip time is above 12 ns. The second peak from the right is the second order transition where $h\nu \approx \Delta E_{12}/2$. Higher order transitions can be explained using expansion of the coefficients $c_i(t)$ and recursively solving for higher orders of the coefficients (cf. Appendix A). The nth order

transition (or *n*-photon transition) coefficient is proportional to $(eF/2\hbar)^n$. Thus, as the amplitudes get larger, the peak heights of higher order resonances grow one order of *F* faster. The transition rates for the higher order resonances can further be increased by tuning the interdot tunnel barrier⁷⁵.

The resonance spectra for higher amplitudes of the electric fields are shifted by one along the y-axis in the plot. We see that resonance peaks blue-shift as a result of higher amplitudes before the S/T avoided crossing where the initial state is singlet [Fig. 6a]. On the contrary even with similar size of the transition matrix elements (Table 1), the resonance peaks red-shift to lower energies with increasing amplitude of the electric field after the crossing (B = 0.9 T) when the initial state is the triplet [See Fig. 6b]. Here as well, the higher order peaks occur with increasing amplitude, which agrees well with the energy differences for lower amplitudes of field. But at amplitudes higher than 0.7 mV/nm, at lower frequencies, the occupancy is no longer zero and for amplitudes more than 0.9 mV/nm, the occupancy is almost one. This corresponds to the adiabatic triplet to singlet transitions governed by the Landau-Zener-Stückelberg-Majorana (LZSM) formula 42,43. Such adiabatic transition only occurs for the case when the triplet is the ground state due to singlet state being pushed down as a result of the asymmetry created by the electric field. Fig. 7a shows the lowest four energy levels as a function of constant electric field with the singlet as the ground state. We observe that the field pushes the singlet state down for large values of 1 mV/nm or -1 mV/nm. Similar behaviour is seen in Fig. 7b for B = 0.9 T except we see an avoided crossing at about 0.76 mV/nm. Thus for small frequency of electric field, the state sweeps adiabatically from triplet to singlet causing the spin flip transition. LZSM mechanism was also reported to induce the multiple harmonic generation in multilevel systems 76. For a perfectly symmetric system, the resonance spectrum is shown in Fig. 6b by the red curve. Clearly showing the absence of the direct transition, as well as the absence of the higher peaks of odd n-order due to the parity selection rule.

The higher amplitude required to drive the transitions indicates that such a system where the charge states are not strongly linked with spin states will be more robust against the external charge noise and material defects. As we notice from Fig. 2c, a detuning of even 10 meV will keep the system more or less the same, with the transition matrix element as well as the avoided crossing vary by smaller amount as compared to the previous case. A trade-off of this extreme being weak coupling to the external electric field which influences the transition times.

Spin-flip times of the nearly symmetric system before and after the S/T avoided crossing are shown in Fig. 8. The solid (dotted) lines indicate the first (second) order transition times. For even amplitudes 10 to 100 times larger than the previous case, spin-flip times are about 80 ns. Spin-flip time at B=0.9 T for direct transitions is similar to that of B=0.4 T case for lower amplitudes. However, once the amplitude exceeds 0.2 mV/nm and the peaks red-shift, the triplet transitions to singlet state are more rapid compared to the reverse transition. The second order transitions, even though slower than direct transitions for lower amplitudes, become much faster than the direct transitions and follow the trend of $1/F^2$. Whereas the direct transitions evolve proportional to 1/F. This proportionality breaks down as the amplitude approaches 1 mV/nm and contribution from higher states reaches up to 4%. These amplitudes can then drive the spin-flip transitions at sub nano-second scale, but the fidelity of such operations would be very low because of leakage.

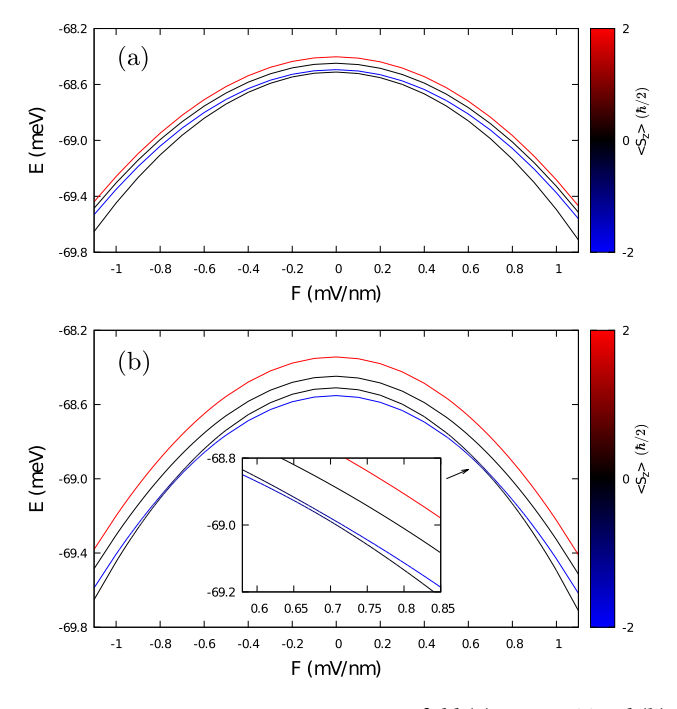


Figure 7. For $\Delta V = 1$ meV at magnetic field (**a**) B = 0.4 T and (**b**) B = 0.9 T. Energy levels as function of constant electric field perturbation showing the avoided crossing in (**b**) for B = 0.9 T which is shown more clearly in the inset figure.

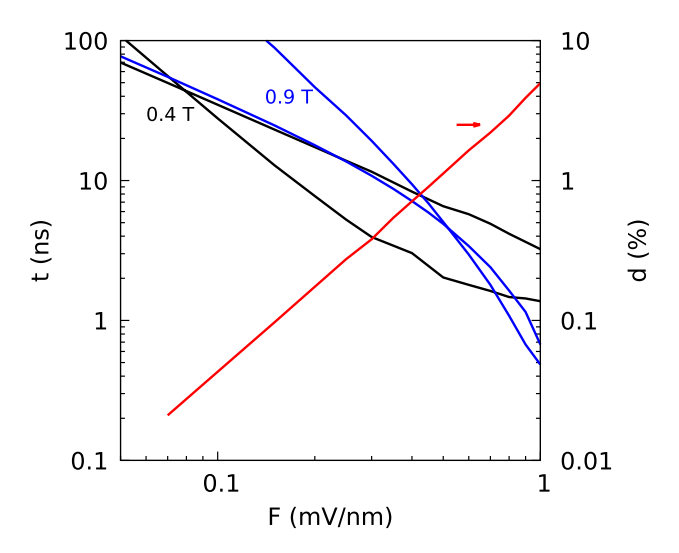


Figure 8. Same as Fig. 5b but for $\Delta V = 1$ meV. The black and blue lines correspond to B = 0.4 T (Fig. 4(a)) and B = 0.9 T [cf. Fig. 6b], respectively.

Dots arranged in the zig-zag direction

Weaker inter-dot coupling can be achieved by arranging the dots in the y-direction within the same material and geometric parameters. By modifying Eq. (3) so that the center of Gaussians are at $y=\pm d$ and changing the electric field to be $V'(t)=-eFy\Theta(t)\sin(\omega t)$, we can investigate the effects of asymmetry and spin-flip transitions analogous to previous sections and compare the results for a different inter-dot coupling.

Figure 9a and b show the energy spectrum for the dots arranged vertically at the detuning $\Delta V = 42 \, \text{meV}$ and $\Delta V = 46$ meV, respectively. We see similar features as seen for dots arranged in x-direction. The ground state is a singlet and is replaced by the triplet after the avoided crossing. It occurs for a very small value as compared to the previous cases, with the center of avoided crossing for $\Delta V = 42 \, \text{meV}$ at about 50 mT. Which is in contrast to the dots in x-direction, where the detuning of about $\Delta V = 42$ meV moved the center of avoided crossing above 5 T. At $\Delta V = 45$ meV, the position of avoided crossing has reached about 5.5 T. Due to the lower tunneling coupling between the dots, the slope of the position of avoided crossing [see Fig. 9c] is much steeper. It occurs at very low values for up to $\Delta V = 42$ meV and then shoots up to values more than 10 T before ΔV even reaches 50 meV. This sensitivity to the detuning is also reflected in the transition matrix and S/T energy gaps in Fig. 9d. The transition matrix element between singlet-triplet achieves its maximum at 45 meV with values of about 7 nm. Because of the strong electron-electron interaction in y-direction, detuning of about 35 meV has basically no effect on the S/T energy difference and the transition matrix, meaning the densities are largely unaffected. The square root densities of the lowest singlet and triplet of this system for symmetric, $\Delta V = 45$ meV and $\Delta V = 50$ meV are plotted in Fig. 10. Note the smaller values of square root densities between the dots [see Figs. 10a,b], indicating a much weaker inter-dot coupling compared to Fig. 4a,b for symmetric dots arrange in x-direction. The effect of this is also seen for the case where transition matrix element is the largest. The square root density of singlet [Fig. 10c] shows both electrons completely occupied in the bottom dot with almost no leakage to the other dot because of weak tunneling, contrary to singlet in Fig. 4c. With the large enough detuning [Fig. 9e,f], both the triplet states electrons eventually occupy the lower dot. Once the electrons have both occupied the lower dot, the position of avoided crossing and the S/T energy difference saturates similar to the situation in the earlier sections.

We now focus the case with the largest transition matrix element, i.e. for $\Delta V = 45$ meV. An analysis similar to that of horizontal dots was performed to obtain the spin-flip times illustrated in Fig. 11. The magnetic field was chosen to be 4.5 T near the avoided crossing in Fig. 9b where the electric field drives the system from the ground state singlet to the spin polarized triplet. At the field amplitude of 2 μ V/nm, we see that the spin flip time is 2.875 ns, whereas due to stronger coupling and tunneling, spin flip time for dots in horizontal orientation at this amplitude was already 0.525 ns [cf. Fig. 5b]. A sub-nanosecond spin-flip occurs for amplitudes great than $5.75 \,\mu\text{V/nm}$. The first and second order transitions follow a similar trend, the first order transition time reduces as $\frac{0.00575}{F}$ ns nm/mV and the second order as $\frac{0.00866^2}{F^2}$ ns (nm/mV)² resulting in a second-order nanosecond spinflip at an amplitude of 8.6 μ V/nm. Although the sub-nanosecond spin manipulation is possible in this case, cost of it is paid in the leakage due to higher amplitudes. A half nano-second spin-flip occurs with leakage of about 0.005% for dots with stronger inter-dot coupling (dots in x-direction) while for dots with weaker coupling the same spin-flip time is not observed as a consequence of leakage to higher states. The contribution of higher energy states is shown in red referred to the right axis in Fig. 11. Higher amplitudes increase the contribution of higher states, with the trend being quadratic for lower amplitudes. The leakage grows rapidly to about 2% as the amplitude approaches 30 μ V/nm. When the contribution of the higher state reaches about 0.05%, transition time lines deviate away from linear and quadratic fits.

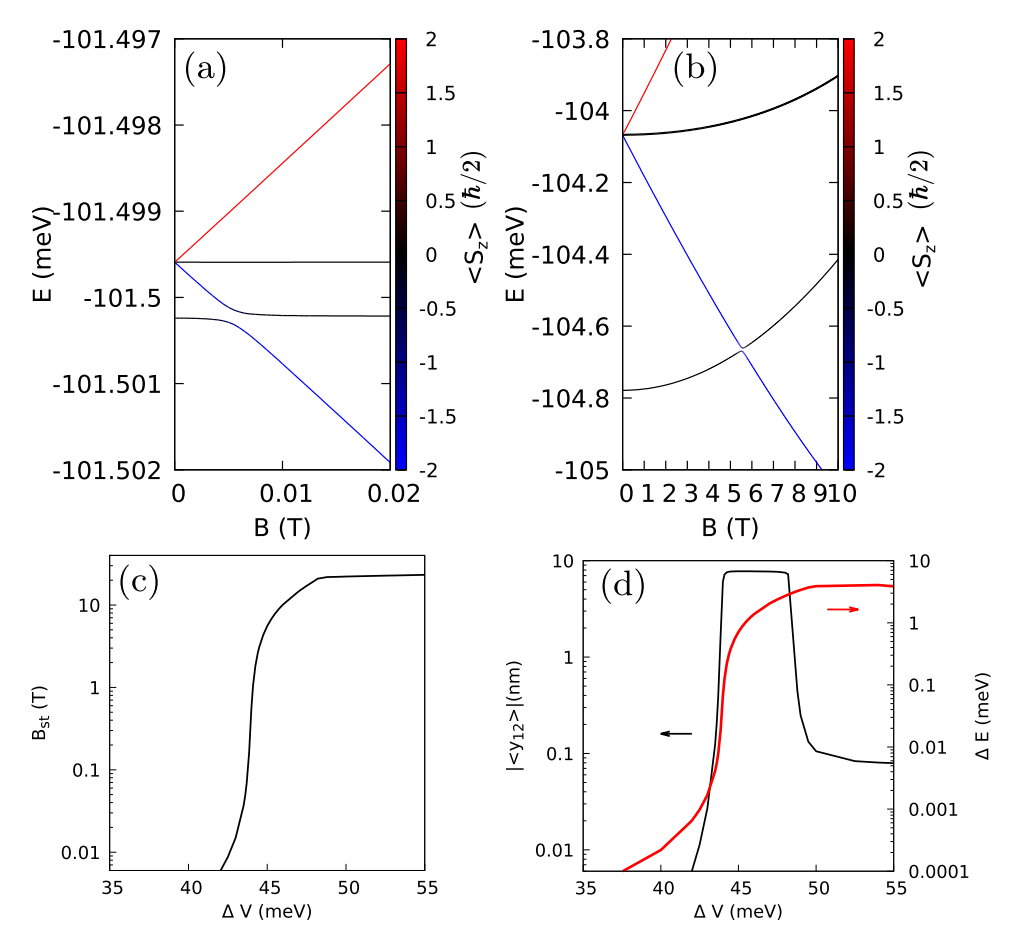


Figure 9. The energy spectrum for (a) $\Delta V = 42$ meV and (b) $\Delta V = 45$ meV. (c) The magnetic field position of the singlet-triplet avoided crossing vs ΔV . The field is basically zero unless both the electrons in the singlet drop in the deeper dot. (d) The maximal value of the transition matrix element (black curve) for the S/T transition referred to left axis and the exchange energy (red curve) at B = 0 referred to the right axis.

Summary and conclusions

We presented an analysis of the singlet-triplet energy splitting and singlet-triplet transitions driven by oscillating electric field in double quantum dots with the effective mass and spin-orbit coupling anisotropy in phosphorene using an exact numerical treatment involving configuration interaction method and the two-electron eigenstates used as a basis for integrating the time evolution of the driven system. The potential asymmetry and orientation of the confinement potential was discussed. The first order singlet-triplet transition turns out to be forbidden by the parity symmetry selection rules in symmetric system of quantum dots. The dipole matrix element for the transition depends strongly on the asymmetry of the confinement potential in a non-monotonic way, with a maximum corresponding to an asymmetry which localizes the singlet in one of the quantum dots and the triplet state still extended over both the dots.

We studied the times of the resonant spin flips including the first and higher-order transitions and the fidelity of the flip versus the amplitude of the driving electric field. Fast sub-nanosecond singlet-triplet transitions involving only the initial and final states are easily achieved for anisotropic quantum dots arranged in the armchair direction. This is possible due to the strong electron-electron interaction in the phosphorene. Detuning can be used to control the sensitivity to charge noise and increase fidelity of operation while simply using the oscillating driving without even employing optimization methods. For the quantum dots arranged in the zig-zag direction fast spin transition times are obtained only at the cost of the leakage of the two-electron wave function to higher excited energy levels. The advantage of using phosphorene for spin manipulation in gated double quantum dots is that the interdot coupling, the spin-transition times and the leakage of the states beyond the two lowest-energy states can be additionally controlled by orientation of the axis of the double dot system with respect to the crystalographic axes of the 2D crystal.

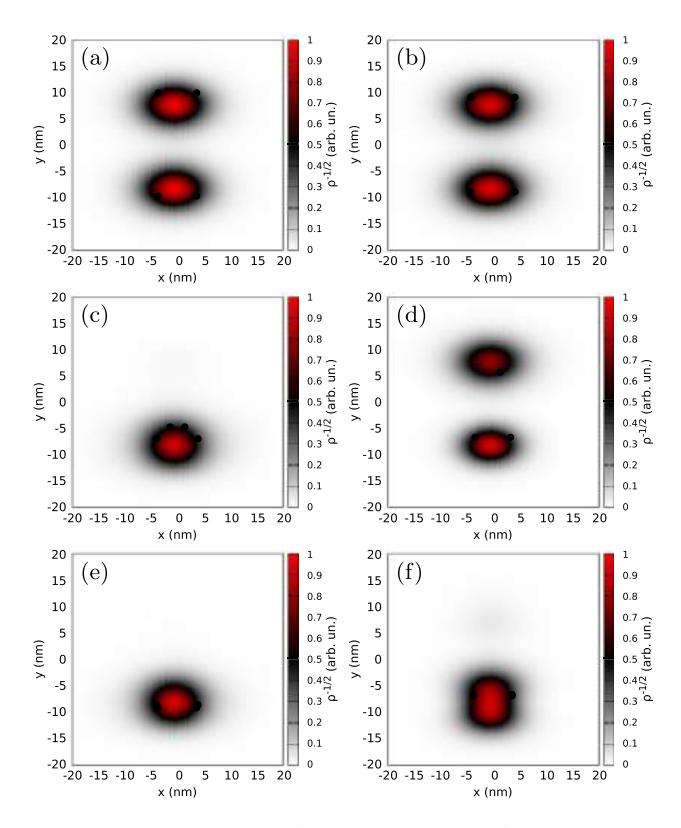


Figure 10. A square root of the electron density for a symmetric double dot system (\mathbf{a},\mathbf{b}) , $\Delta V = 45$ meV (\mathbf{c},\mathbf{d}) and $\Delta V = 50$ meV (\mathbf{e},\mathbf{f}) . The left panel $(\mathbf{a},\mathbf{c},\mathbf{e})$ shows the lowest singlet state and the right panel $(\mathbf{b},\mathbf{d},\mathbf{f})$ the lowest triplet state. The results were calculated for B = 0.

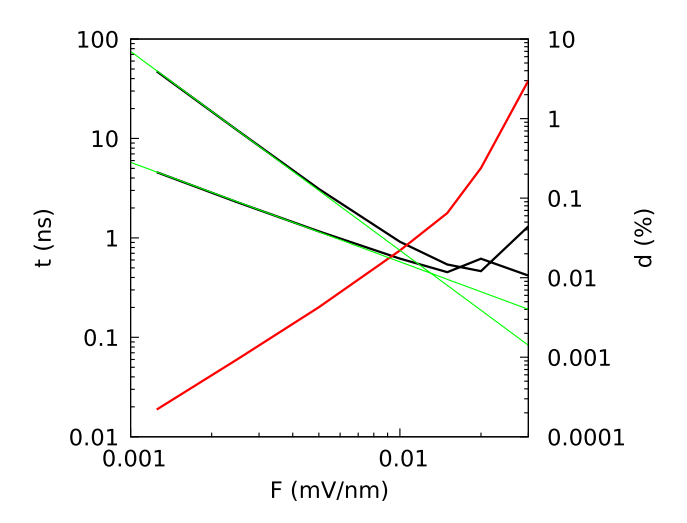


Figure 11. Same as Fig. 5b but for dots arranged in zig-zag direction with $\Delta V = 45$ meV at B = 4.5 T. The black solid (dashed) line indicates spin-flip time for first (second) order transitions. Green lines show the linear and quadratic fits.

For lower asymmetry of the confinement potential with both the singlet and the triplet states extended the dipole matrix element is by order magnitudes smaller than its optimal value and the singlet-triplet transition times of the order of several ns are obtained only at high amplitude of the driving field which is accompanied by a series of subharmonic resonances and Landau-Zener transitions at low frequencies driving the system across the singlet-triplet avoided crossings.

Data availability

The datasets used and/or analysed during the current study available from the corresponding author on reasonable request.

Expansion of coefficients

The coefficients for any n-level system in Eq. (7) can be solved using perturbative expansion,

$$c_n(t) = c_n^{(0)}(t) + c_n^{(1)}(t) + c_n^{(2)}(t) + \dots,$$
 (A1)

where zeroth order simply being the initial condition. Subsequent orders of expansion can be obtained by substituting previous order in the right hand side of Eq. (7). Without using the rotating-wave approximation (RWA) we obtain the expressions for the coefficients by integrating up to time t as

$$c_{n}^{(1)}(t) = \frac{eFx_{1n}}{2i\hbar} \cdot \left\{ \frac{1 - \exp[i(\nu_{1n} + \nu)t]}{\nu_{1n} + \nu} + \frac{1 - \exp[i(\nu_{1n} - \nu)t]}{\nu_{1n} - \nu} \right\}$$

$$c_{n}^{(2)}(t) = -\left(\frac{eF}{2i\hbar}\right)^{2} \cdot \sum_{m} x_{mn} x_{1m}$$

$$\left\{ \frac{1 - \exp[i(\nu_{mn} + \nu)t]}{(\nu_{mn} + \nu)(\nu_{1m} + \nu)} - \frac{1 - \exp[i(\nu_{mn} + \nu_{1m} + 2\nu)t]}{(\nu_{1m} + \nu)(\nu_{mn} + \nu_{1m} + 2\nu)} + \frac{1 - \exp[i(\nu_{mn} + \nu)t]}{(\nu_{mn} + \nu)(\nu_{1m} - \nu)} - \frac{1 - \exp[i(\nu_{mn} + \nu_{1m})t]}{(\nu_{1m} - \nu)(\nu_{mn} + \nu_{1m})} - \frac{1 - \exp[i(\nu_{mn} - \nu)t]}{(\nu_{mn} - \nu)(\nu_{1m} + \nu)} + \frac{1 - \exp[i(\nu_{mn} + \nu_{1m})t]}{(\nu_{1m} - \nu)(\nu_{mn} + \nu_{1m})} - \frac{1 - \exp[i(\nu_{mn} - \nu)t]}{(\nu_{mn} - \nu)(\nu_{1m} - \nu)} + \frac{1 - \exp[i(\nu_{mn} + \nu_{1m} - 2\nu)t]}{(\nu_{1m} - \nu)(\nu_{mn} + \nu_{1m} - 2\nu)} \right\}$$

where x_{mn} is the matrix element $\langle m|x|n\rangle$ and $v_{mn}=(E_m-E_n)/h$. We can obtain a much convenient form of these expressions under RWA by removing fast moving components as,

$$c_{n}^{(1)}(t) = \frac{eF}{2i\hbar} x_{1n} \frac{\exp[it(\nu_{1n} - \nu)/2] \sin(it(\nu_{1n} - \nu)/2)}{(\nu_{1m} - \nu)}$$

$$c_{n}^{(2)}(t) = \left(\frac{eF}{2i\hbar}\right)^{2} \sum_{m} x_{1m} x_{mn}$$

$$\cdot \left\{ \frac{\exp[it(\nu_{mn} - \nu)/2] \sin(it(\nu_{mn} - \nu)/2)}{(\nu_{mn} - \nu)(\nu_{1m} - \nu)} + \frac{\exp[it(\nu_{mn} + \nu_{1m} - 2\nu)/2] \sin(it(\nu_{mn} + \nu_{1m} - 2\nu)/2)}{(\nu_{1m} - \nu)(\nu_{1m} + \nu_{mn} - 2\nu)} \right\}$$
(A3)

The coefficients reach their maximum when the arguments of sine function tend to zero. The absolute values of nth order coefficient is proportional to nth power of F, thus nth order transition times will be proportional to $1/F^n$.

Received: 6 June 2024; Accepted: 17 July 2024

Published online: 16 August 2024

References

- 1. Atherton, N. M. Electron Spin Resonance: Theory and Applications (Halsted Press, 1973).
- Engel, H. A. & Loss, D. Single-spin dynamics and decoherence in a quantum dot via charge transport. Phys. Rev. B 65, 195321 (2002).
- 3. Koppens, F. H. et al. Driven coherent oscillations of a single electron spin in a quantum dot. Nature 442(7104), 766-771 (2006).
- 4. Wolf, S. A. et al. Spintronics: A spin-based electronics vision for the future. Science 294(5546), 1488–1495 (2001).
- Awschalom, D. & Loss, D. Semiconductor Spintronics and Quantum Computation (Springer Science & Business Media, 2002).
 Hanson, R., Kouwenhoven, L. P., Petta, J. R., Tarucha, S. & Vandersypen, L. M. Spins in few-electron quantum dots. Rev. Mod. Phys. 79(4), 1217 (2007).
- 7. Loss, D. & DiVincenzo, D. P. Quantum computation with quantum dots. Phys. Rev. A 57(1), 120 (1998).
- 8. Burkard, G., Loss, D. & DiVincenzo, D. P. Coupled quantum dots as quantum gates. *Phys. Rev. B* **59**(3), 2070 (1999).
- 9. Forster, F., Mühlbacher, M., Schuh, D., Wegscheider, W. & Ludwig, S. Electric-dipole-induced spin resonance in a lateral double quantum dot incorporating two single-domain nanomagnets. *Phys. Rev. B* **91**(19), 195417 (2015).
- Yoneda, J. et al. Fast electrical control of single electron spins in quantum dots with vanishing influence from nuclear spins. Phys. Rev. Lett. 113(26), 267601 (2014).
- 11. Bell, R. L. Electric dipole spin transitions in InSb. Phys. Rev. Lett. 9(2), 52 (1962).
- 12. Golovach, V. N., Borhani, M. & Loss, D. Electric-dipole-induced spin resonance in quantum dots. *Phys. Rev. B* 74(16), 165319 (2006).
- 13. Bemski, G. Spin resonance of conduction electrons in InSb. Phys. Rev. Lett. b(2), 62 (1960).
- 14. Meier, L. et al. Measurement of Rashba and Dresselhaus spin-orbit magnetic fields. Nat. Phys. 3(9), 650-654 (2007).

- Rashba, E. I. & Efros, A. L. Orbital mechanisms of electron-spin manipulation by an electric field. Phys. Rev. Lett. 91(12), 126405 (2003).
- 16. Reiner, J. et al. High-fidelity initialization and control of electron and nuclear spins in a four-qubit register. Nat. Nanotech. 1, 1–7 (2024).
- 17. Froning, F. N. Ultrafast hole spin qubit with gate-tunable spin-orbit switch functionality. Nat. Nanotech. 16(3), 308-312 (2021).
- 18. Takeda, K., Noiri, A., Yoneda, J., Nakajima, T. & Tarucha, S. Resonantly driven singlet-triplet spin qubit in silicon. *Phys. Rev. Lett.* 124(11), 117701 (2020).
- 19. Hanson, R. & Awschalom, D. D. Coherent manipulation of single spins in semiconductors. Nature 453(7198), 1043-1049 (2008).
- Petta, J. R. et al. Coherent manipulation of coupled electron spins in semiconductor quantum dots. Science 309(5744), 2180–2184 (2005).
- 21. Stepanenko, D., Rudner, M., Halperin, B. I. & Loss, D. Singlet-triplet splitting in double quantum dots due to spin-orbit and hyperfine interactions. *Phys. Rev. B* **85**(7), 075416 (2012).
- 22. Khomitsky, D. V., Gulyaev, L. V. & Sherman, E. Y. Spin dynamics in a strongly driven system: Very slow Rabi oscillations. *Phys. Rev. B* 85(12), 125312 (2012).
- 23. Khomitsky, D. V., Lavrukhina, E. A. & Sherman, E. Y. Spin rotation by resonant electric field in few-level quantum dots: Floquet dynamics and tunneling. *Phys. Rev. Appl.* 14(1), 014090 (2020).
- 24. Koppens, F. H. L., Nowack, K. C. & Vandersypen, L. M. K. Spin echo of a single electron spin in a quantum dot. *Phys. Rev. Lett.* 100(23), 236802 (2008).
- 25. Nadj-Perge, S., Frolov, S. M., Bakkers, E. P. A. M. & Kouwenhoven, L. P. Spin-orbit qubit in a semiconductor nanowire. *Nature* 468(7327), 1084–1087 (2010).
- 26. Van den Berg, J. W. G. et al. Fast spin-orbit qubit in an indium antimonide nanowire. Phys. Rev. Lett. 110(6), 066806 (2013).
- 27. Liu, B. et al. Tuning the Schottky contacts in the phosphorene and graphene heterostructure by applying strain. Phys. Chem. Chem. Phys. 18, 19918 (2016).
- 28. Stano, P. & Fabian, J. Orbital and spin relaxation in single and coupled quantum dots. Phys. Rev. B 74, 045320 (2006).
- 29. Hofmann, A. et al. Anisotropy and suppression of spin-orbit interaction in a GaAs double quantum dot. *Phys. Rev. Lett.* **119**(17), 176807 (2017).
- 30. Scarlino, P. et al. Spin-relaxation anisotropy in a GaAs quantum dot. Phys. Rev. Lett. 113(25), 256802 (2014).
- 31. Farzaneh, S. M. & Rakheja, S. Extrinsic spin-orbit coupling and spin relaxation in phosphorene. *Phys. Rev. B* **100**(24), 245429 (2019).
- 32. Popović, Z. S., Kurdestany, J. M. & Satpathy, S. Electronic structure and anisotropic Rashba spin-orbit coupling in monolayer black phosphorus. *Phys. Rev. B* **92**(3), 035135 (2015).
- 33. Low, T., Jiang, Y. & Guinea, F. Topological currents in black phosphorus with broken inversion symmetry. *Phys. Rev. B* **92**, 235447 (2015).
- 34. Liu, H. et al. Phosphorene: An unexplored 2D semiconductor with a high hole mobility. ACS Nano 8(4), 4033-4041 (2014).
- 35. Long, G. *et al.* Achieving ultrahigh carrier mobility in two-dimensional hole gas of black phosphorus. *Nano Lett.* **16**(12), 7768–7773 (2016).
- 36. Long, G. et al. Ambipolar quantum transport in few-layer black phosphorus. Phys. Rev. B 96(15), 155448 (2017).
- 37. Yang, J. et al. Integer and fractional quantum hall effect in ultrahigh quality few-layer black phosphorus transistors. Nano Lett. 18(1), 229–234 (2018).
- Derbali, S. & Moudam, O. Insights into the Application of 2D Phosphorene in Dye-Sensitized Solar Cells. Energy Technol. 11(9), 2300353 (2023).
- 39. Schuster, R., Trinckauf, J., Habenicht, C., Knupfer, M. & Büchner, B. Anisotropic particle-hole excitations in black phosphorus. *Phys. Rev. Lett.* **115**(2), 026404 (2015).
- 40. Tian, X. et al. Recent advances in the development of nanomedicines for the treatment of ischemic stroke. Bioact. Mater. 6(9), 2854–2869 (2021).
- 41. Sun, Z. et al. Ultrasmall black phosphorus quantum dots: synthesis and use as photothermal agents. Angew. Chem. Int. Ed. 54(39), 11526–11530 (2015).
- 42. Ivakhnenko, V., Shevchenko, S. N. & Nori, F. Nonadiabatic Landau-Zener-Stückelberg-Majorana transitions, dynamics, and interference. *Phys. Rep.* **995**, 1–89 (2023).
- 43. Kofman, P. O., Ivakhnenko, O. V., Shevchenko, S. N. & Nori, F. Majorana's approach to nonadiabatic transitions validates the adiabatic-impulse approximation. Sci. Rep. 13(1), 5053 (2023).
- 44. Szafran, B. Electrostatic quantum dot confinement in phosphorene. Phys. Rev. B 101(23), 235313 (2020).
- 45. Faria Junior, P. E., Kurpas, M., Gmitra, M. & Fabian, J. k·p theory for phosphorene: Effective g-factors, Landau levels, and excitons. *Phys. Rev. B* b(11), 115203 (2019).
- 46. Zhou, X. et al. Effective g factor in black phosphorus thin films. Phys. Rev. B 95(4), 045408 (2017).
- 47. Gillgren, N. et al. Gate tunable quantum oscillations in air-stable and high mobility few-layer phosphorene heterostructures. 2D Materials 2(1), 011001 (2014).
- 48. Li, L. et al. Quantum Hall effect in black phosphorus two-dimensional electron system. Nat. Nanotech. 11(7), 593–597 (2016).
- 49. Yang, F. C Quantum hall effect in electron-doped black phosphorus field-effect transistors. Nano Lett. 18(10), 6611-6616 (2018).
- 50. Thakur, T. & Szafran, B. Wigner molecules in phosphorene quantum dots. Phys. Rev. B 106(20), 205304 (2022).
- 51. Thakur, T. & Szafran, B. Vortex structure in Wigner molecules. Sci. Rep. 13(1), 9707 (2023).
- 52. Lis, K., Bednarek, S., Szafran, B. & Adamowski, J. Electrostatic quantum dots with designed shape of confinement potential. *Physica* E 17, 494–497 (2003).
- 53. Chen, J., Wu, K., Hu, W. & Yang, J. Spin-orbit coupling in 2D semiconductors: A theoretical perspective. *J. Phys. Chem. Lett.* 12(51), 12256 (2021).
- Ho Park, Y. Separation of Rashba and Dresselhaus spin-orbit interactions using crystal direction dependent transport measurements. Appl. Phys. Lett. 103(25), 252407 (2003).
- 55. Luo, J., Munekata, H., Fang, F. F. & Stiles, P. J. Effects of inversion asymmetry on electron energy band structures in GaSb/InAs/ GaSb quantum wells. *Phys. Rev. B* 41(11), 7685 (1990).
- 56. Nitta, J., Akazaki, T., Takayanagi, H. & Enoki, T. Gate control of spin-orbit interaction in an inverted In_{0.53}Ga_{0.47}As/In_{0.52}Al_{0.48} as heterostructure. *Phys. Rev. Lett.* **78**(7), 1335 (1997).
- 57. Liang, D. & Gao, X. P. Strong tuning of Rashba spin-orbit interaction in single InAs nanowires. Nano Lett. 12(6), 3263-3267 (2012).
- 58. Acosta, C. M., Ogoshi, E., Fazzio, A., Dalpian, G. M. & Zunger, A. The Rashba scale: Emergence of band anti-crossing as a design principle for materials with large rashba coefficient. *Matter* 3(1), 145–165 (2020).
- 59. van der Wiel, W. G., Fujisawa, T., Tarucha, S. & Kouwenhoven, L. P. A double quantum dot as an artificial two-level system. *Jpn. J. Appl. Phys.* 40(3S), 2100 (2001).
- 60. Forster, F. et al. Characterization of qubit dephasing by Landau-Zener-Stückelberg-Majorana interferometry. Phys. Rev. Lett. 112(11), 116803 (2014).
- 61. Laird, E. A. *et al.* A new mechanism of electric dipole spin resonance: Hyperfine coupling in quantum dots. *Semicond. Sci. Technol.* **24**(6), 064004 (2009).

- 62. Nadj-Perge, S. et al. Spectroscopy of spin-orbit quantum bits in indium antimonide nanowires. Phys. Rev. Lett. 108(16), 166801 (2012).
- Corna, A. et al. Electrically driven electron spin resonance mediated by spin-valley-orbit coupling in a silicon quantum dot. NPJ Quantum Information 4(1), 6 (2018).
- 64. Nowack, K. C., Koppens, F. H. L., Nazarov, Y. V. & Vandersypen, L. M. K. Coherent control of a single electron spin with electric fields. *Science* 318(5855), 1430–1433 (2007).
- 65. Hu, R. Z. et al. Flopping-mode spin qubit in a Si-MOS quantum dot. Appl. Phys. Lett. 122(13), 5 (2023).
- 66. Wagner, T. et al. Quantum stochastic resonance in an ac-driven single-electron quantum dot. Nat. Phys. 15(4), 330–334 (2019). 67. Castelano, L. K. et al. Optimal control of universal quantum gates in a double quantum dot. Phys. Rev. B 97(23), 235301 (2018).
- 68. Thakur, T. & Szafran, B. Nagaoka ferromagnetism in an array of phosphorene quantum dots. Sci. Rep. 13(1), 18796 (2023).
- 69. Ono, K., Austing, D. G., Tokura, Y. & Tarucha, S. Current rectification by Pauli exclusion in a weakly coupled double quantum dot system. *Science* 297(5585), 1313–1317 (2002).
- 70. Stehlik, J., Schroer, M. D., Maialle, M. Z., Degani, M. H. & Petta, J. R. Extreme harmonic generation in electrically driven spin resonance. *Phys. Rev. Lett.* **112**(22), 227601 (2014).
- 71. Romhanyi, J., Burkard, G. & Pályi, A. Subharmonic transitions and Bloch-Siegert shift in electrically driven spin resonance. *Phys. Rev. B* 92, 054422 (2015).
- 72. Hayashi, T., Fujisawa, T., Cheong, H. D., Jeong, Y. H. & Hirayama, Y. Coherent manipulation of electronic states in a double quantum dot. *Phys. Rev. Lett.* **91**(22), 226804 (2003).
- 73. Petersson, K. D., Petta, J. R., Lu, H. & Gossard, A. C. Quantum coherence in a one-electron semiconductor charge qubit. *Phys. Rev. Lett.* **105**(24), 246804 (2010).
- 74. Shi, Z. et al. Coherent quantum oscillations and echo measurements of a Si charge qubit. Phys. Rev. B 88(7), 075416 (2013).
- 75. Giavaras, G. & Tokura, Y. Spectroscopy of double quantum dot two-spin states by tuning the interdot barrier. *Phys. Rev. B* **99**(7), 075412 (2019).
- 76. Stehlik, J., Maialle, M. Z., Degani, M. H. & Petta, J. R. Role of multilevel Landau-Zener interference in extreme harmonic generation. *Phys. Rev. B* **94**, 075307 (2016).

Acknowledgements

This work was supported by the National Science Centre (NCN) according to decision DEC-2019/35/O/ST3/00097 and Polish National Agency for Academic Exchange (NAWA) under program Zagraniczne Staże Doktorskie NAWA Preludium BIS 1 according to decision PPN/STA/2021/1/00076/DEC/1. We gratefully acknowledge Poland's high-performance computing infrastructure PLGrid (HPC Center Cyfronet) for providing computer facilities and support within computational grant no. PLG/2024/017175. Research was partly supported by program "Excellence initiative - research university" for the AGH University of Krakow. We are sincerely grateful to Dr Diego Rabelo da Costa and Dr Andrey Chaves for very helpful discussions.

Author contributions

TT performed calculations, led the analysis of the results and wrote the manuscript. FMP and BS participated in setting the problem, selection of the calculation methods, analysis of the data and editing the manuscript.

Competing interests

The authors declare no competing interests.

Additional information

Correspondence and requests for materials should be addressed to B.S.

Reprints and permissions information is available at www.nature.com/reprints.

Publisher's note Springer Nature remains neutral with regard to jurisdictional claims in published maps and institutional affiliations.

Open Access This article is licensed under a Creative Commons Attribution-NonCommercial-NoDerivatives 4.0 International License, which permits any non-commercial use, sharing, distribution and reproduction in any medium or format, as long as you give appropriate credit to the original author(s) and the source, provide a link to the Creative Commons licence, and indicate if you modified the licensed material. You do not have permission under this licence to share adapted material derived from this article or parts of it. The images or other third party material in this article are included in the article's Creative Commons licence, unless indicated otherwise in a credit line to the material. If material is not included in the article's Creative Commons licence and your intended use is not permitted by statutory regulation or exceeds the permitted use, you will need to obtain permission directly from the copyright holder. To view a copy of this licence, visit http://creativecommons.org/licenses/by-nc-nd/4.0/.

© The Author(s) 2024

Chapter 10

Summary & Conclusions

In this thesis, we explored unique properties of confined states in electrostatic quantum dots based on phosphorene, motivated by phosphorene's strong anisotropy and its potential for realization into novel applications. The primary goal was to study theoretically how anisotropy influences electronic and spin states in phosphorene quantum dots and rings. We employed tight-binding model, effective mass approximation and computational techniques, including the configuration interaction method, and time-dependent simulations, to capture many-body effects accurately. Thus, not only filling the gap in theoretical literature, but also informing on potential future experiments.

We demonstrated that in phosphorene quantum rings, effect of mass anisotropy on the confined single electron states can be exactly compensated for a single-confined electron by confinement potentials, altering the Aharonov-Bohm interference pattern. Thus, opening the avenue of investigations based on quantum interference for anisotropic materials. With large and anisotropic effective masses in phosphorene, the electron-electron interactions lead to the formation of Wigner molecules in laboratory frame. The formation is affected by the symmetry of confinement potential, parity and magnetic field. We indicated the spectral features that can indicate formation of single-electron islands in the laboratory frame besides a direct density observation. We investigated the vortex structures forming in the fractional quantum Hall conditions. The evolution of these vortex structures with magnetic field is associated with antivortex creation and annihilation, which can only be described by basis beyond lowest Landau level, indicating a complex multi-body behavior. Under certain conditions, electron-electron interactions can lead to strong itinerant ferromagnetism predicted by Nagaoka's theorem in quantum dot array, fairly robust against detuning and small imperfections because of phosphorene's heavier effective mass in zigzag direction. Spin states in the double quantum dot system can be coherently controlled with sub-nanosecond spin flip times and low leakages. Such properties demonstrate feasibility for spin-based quantum computing or spintronics in anisotropic 2D materials like phosphorene.

We established the effects of anisotropy on electronic correlations, magnetic phenomena, and spin manipulation in phosphorene quantum dots and rings. By tailoring confinement geometries and external fields, it is possible to tune electronic and spin properties of the confined states in a controllable manner. This highlights phosphorene's potential as a platform for next-generation quantum devices.

Bibliography

- [1] Li, L. et al. Black phosphorus field-effect transistors. Nature Nanotechnology, 9(5), 372-377 (2014).
- [2] Novoselov, K. S. *et al.* Electric field effect in atomically thin carbon films. *Science*, **306**(5696), 666-669 (2004).
- [3] Mak, K. F., Lee, C., Hone, J., Shan, J., & Heinz, T. F. Atomically thin MoS₂: a new direct-gap semi-conductor. *Physical Review Letters*, **105**(13), 136805 (2010).
- [4] Kong, D., Wang, H., Cha, J. J., Pasta, M., Koski, K. J., Yao, J., & Cui, Y. Synthesis of MoS₂ and MoSe₂ films with vertically aligned layers. *Nano Letters*, **13**(3), 1341-1347 (2013).
- [5] Ovchinnikov, D., Allain, A., Huang, Y. S., Dumcenco, D., & Kis, A. Electrical transport properties of single-layer WS₂. *ACS Nano*, **8**(8), 8174-8181 (2014).
- [6] Allain, A., & Kis, A. Electron and hole mobilities in single-layer WSe₂. *ACS Nano*, **8**(7), 7180-7185 (2014).
- [7] Netzer, F. P., Allegretti, F., & Surnev, S. Low-dimensional oxide nanostructures on metals: Hybrid systems with novel properties. *Journal of Vacuum Science & Technology B*, **28**(1), 1-16 (2010).
- [8] Balendhran, S. *et al.* Two-dimensional molybdenum trioxide and dichalcogenides. *Advanced Functional Materials*, **23**(32), 3952-3970 (2013).
- [9] Novoselov, K. S., Jiang, D., Schedin, F., Booth, T. J., Khotkevich, V. V., Morozov, S. V., & Geim, A. K. Two-dimensional atomic crystals. *Proceedings of the National Academy of Sciences*, 102(30), 10451-10453 (2005).
- [10] Kalantar-Zadeh, K. et al. Synthesis of nanometre-thick MoO₃ sheets. Nanoscale, 2(3), 429-433 (2010).
- [11] Naguib, M. *et al.* MXene: a promising transition metal carbide anode for lithium-ion batteries. *Electrochemistry Communications*, **16**(1), 61-64 (2012).
- [12] Feng, B., Ding, Z., Meng, S., Yao, Y., He, X., Cheng, P., *et al.* Evidence of silicene in honeycomb structures of silicon on Ag(111). *Nano Letters*, **12**(7), 3507-3511 (2012).
- [13] Tao, L. *et al.* Silicene field-effect transistors operating at room temperature. *Nature Nanotechnology*, **10**(3), 227-231 (2015).

[14] Dávila, M. E., Xian, L., Cahangirov, S., Rubio, A., & Le Lay, G. Germanene: a novel two-dimensional germanium allotrope akin to graphene and silicene. *New Journal of Physics*, **16**(9), 095002 (2014).

- [15] Saxena, S., Chaudhary, R. P., & Shukla, S. Stanene: atomically thick free-standing layer of 2D hexagonal tin. *Scientific Reports*, **6**(1), 31073 (2016).
- [16] Murali, G. *et al.* A review on MXene synthesis, stability, and photocatalytic applications. *ACS Nano*, **16**(9), 13370-13429 (2022).
- [17] Jose, D., & Datta, A. Structures and chemical properties of silicene: unlike graphene. *Accounts of Chemical Research*, **47**(2), 593-602 (2014).
- [18] Gillgren, N. *et al.* Gate tunable quantum oscillations in air-stable and high mobility few-layer phosphorene heterostructures. *2D Materials*, **2**(1), 011001 (2014).
- [19] Pei, J. *et al.* Producing air-stable monolayers of phosphorene and their defect engineering. *Nature Communications*, **7**(1), 10450 (2016).
- [20] Yang, S. *et al.* Thermal annealing of black phosphorus for etching and protection. *Applied Surface Science*, **457**, 773-779 (2018).
- [21] Wu, R. J. et al. Atomic and electronic structure of exfoliated black phosphorus. *Journal of Vacuum Science & Technology A*, **33**(6) (2015).
- [22] Li, X. et al. High-speed black phosphorus field-effect transistors approaching ballistic limit. *Science Advances*, **5**(6), eaau3194 (2019).
- [23] Mamori, H. *et al.* Dynamic stability in phosphorene bilayer with different stacking orders: A first principle study. *Materials Science in Semiconductor Processing*, **140**, 106341 (2022).
- [24] Margot, F. *et al.* Electronic structure of few-layer black phosphorus from μ -ARPES. *Nano Letters*, **23**(14), 6433-6439 (2023).
- [25] Tran, V., Soklaski, R., Liang, Y., & Yang, L. Layer-controlled band gap and anisotropic excitons in few-layer black phosphorus. *Physical Review B*, **89**(23), 235319 (2014).
- [26] Yang, J., Xu, R., Pei, J., Myint, Y. W., Wang, F., Wang, Z., *et al.* Optical tuning of exciton and trion emissions in monolayer phosphorene. *Light: Science & Applications*, **4**(7), e312-e312 (2015).
- [27] Long, G. *et al.* Achieving ultrahigh carrier mobility in two-dimensional hole gas of black phosphorus. *Nano Letters*, **16**(12), 7768-7773 (2016).
- [28] Shao, D. F., Lu, W. J., Lv, H. Y., & Sun, Y. P. Electron-doped phosphorene: a potential monolayer superconductor. *Europhysics Letters*, **108**(6), 67004 (2014).
- [29] Lee, M. *et al.* Highly efficient visible blue-emitting black phosphorus quantum dot: Mussel-inspired surface functionalization for bioapplications. *ACS Omega*, **2**(10), 7096-7105 (2017).

[30] Vishnoi, P., Mazumder, M., Barua, M., Pati, S. K., & Rao, C. N. R. Phosphorene quantum dots. *Chemical Physics Letters*, **699**, 223-228 (2018).

- [31] Tataka, R., Sharma, A., Shinozaki, M., Johmen, T., Kumasaka, T., Chen, Y. P., & Otsuka, T. Surface Gate-Defined Quantum Dots in MoS₂ with Bi Contacts. *Journal of the Physical Society of Japan*, **93**(9), 094601 (2024).
- [32] Song, X. X. *et al.* A gate-defined quantum dot on the two-dimensional transition metal dichalcogenide semiconductor WSe₂. *Nanoscale*, **7**(40), 16867-16873 (2015).
- [33] Angus, S. J., Ferguson, A. J., Dzurak, A. S., & Clark, R. G. Gate-defined quantum dots in intrinsic silicon. *Nano Letters*, **7**(7), 2051-2055 (2007).
- [34] Biercuk, M. J., Garaj, S., Mason, N., Chow, J. M., & Marcus, C. M. Gate-defined quantum dots on carbon nanotubes. *Nano Letters*, **5**(7), 1267-1271 (2005).
- [35] Jing, F. M., Zhang, Z. Z., Qin, G. Q., Luo, G., Cao, G., Li, H. O., *et al.* Gate-controlled quantum dots based on 2D materials. *Advanced Quantum Technologies*, **5**(6), 2100162 (2022).
- [36] Liu, H. *et al.* Phosphorene: an unexplored 2D semiconductor with a high hole mobility. *ACS Nano*, **8**(4), 4033-4041. (2014).
- [37] Carvalho, A., Wang, M., Zhu, X., Rodin, A. S., Su, H., & Castro Neto, A. H. Phosphorene: from theory to applications. *Nature Reviews Materials*, **1**(11), 1-16. (2016).
- [38] Koleśnik-Gray, M. *et al.* Unconventional conductivity increase in multilayer black phosphorus. *npj 2D Materials and Applications*, **7**(1), 21. (2023).
- [39] Qiao, J., Kong, X., Hu, Z. X., Yang, F., & Ji, W. High-mobility transport anisotropy and linear dichroism in few-layer black phosphorus. *Nature Communications*, **5**(1), 4475. (2014).
- [40] Luo, Z. *et al.* Anisotropic in-plane thermal conductivity observed in few-layer black phosphorus. *Nature Communications*, **6**(1), 8572. (2015).
- [41] Jang, H., Wood, J. D., Ryder, C. R., Hersam, M. C., & Cahill, D. G. Anisotropic Thermal Conductivity of Exfoliated Black Phosphorus. *Advanced Materials*, **27**(48), 8017-8022. (2015).
- [42] Qin, G., Yan, Q. B., Qin, Z., Yue, S. Y., Hu, M., & Su, G. Anisotropic intrinsic lattice thermal conductivity of phosphorene from first principles. *Physical Chemistry Chemical Physics*, **17**(7), 4854-4858. (2015).
- [43] Flores, E., Ares, J. R., Castellanos-Gomez, A., Barawi, M., Ferrer, I. J., & Sánchez, C. Thermoelectric power of bulk black-phosphorus. *Applied Physics Letters*, **106**(2). (2015).
- [44] Zare, M., Rameshti, B. Z., Ghamsari, F. G., & Asgari, R. Thermoelectric transport in monolayer phosphorene. *Physical Review B*, **95**(4), 045422. (2017).

[45] Popović, Z. S., Kurdestany, J. M., & Satpathy, S. Electronic structure and anisotropic Rashba spin-orbit coupling in monolayer black phosphorus. *Physical Review B*, **92**(3), 035135. (2015).

- [46] Farzaneh, S. M., & Rakheja, S. Extrinsic spin-orbit coupling and spin relaxation in phosphorene. *Physical Review B*, **100**(24), 245429. (2019).
- [47] Jung, J. H., Park, C. H., & Ihm, J. A rigorous method of calculating exfoliation energies from first principles. *Nano Letters*, **18**(5), 2759-2765. (2018).
- [48] Wang, H., Wang, X., Xia, F., Wang, L., Jiang, H., Xia, Q., et al. Black phosphorus radio-frequency transistors. *Nano Letters*, **14**(11), 6424-6429. (2014).
- [49] He, D., Wang, Y., Huang, Y., Shi, Y., Wang, X., & Duan, X. High-performance black phosphorus field-effect transistors with long-term air stability. *Nano Letters*, **19**(1), 331-337. (2018).
- [50] Bolotin, K. I. *et al.* Ultrahigh electron mobility in suspended graphene. *Solid State Communications*, **146**(9-10), 351-355. (2008).
- [51] Balandin, A. A., Ghosh, S., Bao, W., Calizo, I., Teweldebrhan, D., Miao, F., & Lau, C. N. Superior thermal conductivity of single-layer graphene. *Nano Letters*, **8**(3), 902-907. (2008).
- [52] Lim, S., Park, H., Yamamoto, G., Lee, C., & Suk, J. W. Measurements of the electrical conductivity of monolayer graphene flakes using conductive atomic force microscopy. *Nanomaterials*, 11(10), 2575. (2021).
- [53] Zuev, Y. M., Chang, W., & Kim, P. Thermoelectric and magnetothermoelectric transport measurements of graphene. *Physical Review Letters*, **102**(9), 096807. (2009).
- [54] Min, H., Hill, J. E., Sinitsyn, N. A., Sahu, B. R., Kleinman, L., & MacDonald, A. H. Intrinsic and Rashba spin-orbit interactions in graphene sheets. *Physical Review B—Condensed Matter and Materials Physics*, **74**(16), 165310. (2006).
- [55] Kane, C. L., & Mele, E. J. Quantum spin Hall effect in graphene. *Physical Review Letters*, **95**(22), 226801. (2005).
- [56] Xia, F., Farmer, D. B., Lin, Y. M., & Avouris, P. Graphene field-effect transistors with high on/off current ratio and large transport band gap at room temperature. *Nano Letters*, **10**(2), 715-718. (2010).
- [57] Liao, L., Bai, J., Cheng, R., Lin, Y. C., Jiang, S., Huang, Y., & Duan, X. Top-gated graphene nanoribbon transistors with ultrathin high-k dielectrics. *Nano Letters*, **10**(5), 1917-1921. (2010).
- [58] Wang, S. Y., Ko, T. S., Huang, C. C., & Huang, Y. S. Optical and electrical properties of MoS₂ and Fe-doped MoS₂. *Japanese Journal of Applied Physics*, **53**(4S), 04EH07. (2014).
- [59] Kim, S., Konar, A., Hwang, W. S., Lee, J. H., Lee, J., Yang, J., *et al.* High-mobility and low-power thin-film transistors based on multilayer MoS₂ crystals. *Nature Communications*, **3**(1), 1011. (2012).

[60] Ayari, A., Cobas, E., Ogundadegbe, O., & Fuhrer, M. S. Realization and electrical characterization of ultrathin crystals of layered transition-metal dichalcogenides. *Journal of Applied Physics*, **101**(1). (2007).

- [61] Li, X., Mullen, J. T., Jin, Z., Borysenko, K. M., Buongiorno Nardelli, M., & Kim, K. W. Intrinsic electrical transport properties of monolayer silicene and MoS₂ from first principles. *Physical Review B*, **87**(11), 115418. (2013).
- [62] Sahoo, S., Gaur, A. P., Ahmadi, M., Guinel, M. J. F., & Katiyar, R. S. Temperature-dependent Raman studies and thermal conductivity of few-layer MoS₂. *The Journal of Physical Chemistry C*, **117**(17), 9042-9047. (2013).
- [63] Jo, I., Pettes, M. T., Ou, E., Wu, W., & Shi, L. Basal-plane thermal conductivity of few-layer molybdenum disulfide. *Applied Physics Letters*, **104**(20). (2014).
- [64] Garadkar, K. M., Patil, A. A., Hankare, P. P., Chate, P. A., Sathe, D. J., & Delekar, S. D. MoS₂: Preparation and their characterization. *Journal of Alloys and Compounds*, **487**(1-2), 786-789. (2009).
- [65] Buscema, M., Barkelid, M., Zwiller, V., van der Zant, H. S., Steele, G. A., & Castellanos-Gomez, A. Large and tunable photothermoelectric effect in single-layer MoS₂. *Nano Letters*, **13**(2), 358-363. (2013).
- [66] Kayyalha, M., Maassen, J., Lundstrom, M., Shi, L., & Chen, Y. P. Gate-tunable and thickness-dependent electronic and thermoelectric transport in few-layer MoS₂. *Journal of Applied Physics*, **120**(13). (2016).
- [67] Peng, Q., Lei, Y., Deng, X., Deng, J., Wu, G., Li, J., *et al.* Giant and tunable Rashba spin splitting in MoS₂/Bi₂Te₃ heterostructures. *Physica E: Low-Dimensional Systems and Nanostructures*, **135**, 114944. (2022).
- [68] Sebastian, A., Pendurthi, R., Choudhury, T. H., Redwing, J. M., & Das, S. Benchmarking monolayer MoS₂ and WS₂ field-effect transistors. *Nature Communications*, **12**(1), 693. (2021).
- [69] Nourbakhsh, A. *et al.* MoS_2 field-effect transistor with sub-10 nm channel length. *Nano Letters*, **16**(12), 7798-7806. (2016).
- [70] Faria Junior, P. E., Kurpas, M., Gmitra, M., & Fabian, J. $k \cdot p$ theory for phosphorene: Effective g-factors, Landau levels, and excitons. *Physical Review B*, **100**(11), 115203. (2019).
- [71] Zhang, G., Chaves, A., Huang, S., Wang, F., Xing, Q., Low, T., & Yan, H. Determination of layer-dependent exciton binding energies in few-layer black phosphorus. *Science Advances*, 4(3), eaap9977. (2018).
- [72] Seixas, L., Rodin, A. S., Carvalho, A., & Castro Neto, A. H. Exciton binding energies and luminescence of phosphorene under pressure. *Physical Review B*, **91**(11), 115437. (2015).

[73] Zhou, X. Y. *et al.* Landau levels and magneto-transport property of monolayer phosphorene. *Scientific Reports*, **5**(1), 12295. (2015).

- [74] Pereira Jr, J. M., & Katsnelson, M. I. Landau levels of single-layer and bilayer phosphorene. *Physical Review B*, **92**(7), 075437. (2015).
- [75] Szafran, B. Electrostatic quantum dot confinement in phosphorene. *Physical Review B*, **101**(23), 235313. (2020).
- [76] Li, H., Li, S., Regan, E. C., Wang, D., Zhao, W., Kahn, S., *et al.* Imaging two-dimensional generalized Wigner crystals. *Nature*, **597**(7878), 650-654. (2021).
- [77] Peng, X., Wei, Q., & Copple, A. Strain-engineered direct-indirect band gap transition and its mechanism in two-dimensional phosphorene. *Physical Review B*, **90**(8), 085402. (2014).
- [78] Landau, L.D. and Lifshitz, E.M., Quantum Mechanics (Non-Relativistic Theory). 3rd Edition, Pergamon Press, Oxford (1977).
- [79] Ashcroft, N.W. and Mermin, N.D., Solid State Physics. Saunders College, Philadelphia, pg 5,342 (1976).
- [80] Ferry, D. K., Grubin, H. L., Jacoboni, C., & Jauho, A. P. (Eds.), Quantum Transport in Ultrasmall Devices: Proceedings of a NATO Advanced Study Institute on Quantum Transport in Ultrasmall Devices, Held July 17–30, 1994, in II Ciocco, Italy (Vol. 342). Springer Science & Business Media pg 81 (2012).
- [81] Yan, Zijun, General thermal wavelength and its applications. *European Journal of Physics* **21**.6, 625 (2000).
- [82] Tang, T. W., O'Regan, T., & Wu, B., Thomas–Fermi approximation for a two-dimensional electron gas at low temperatures. *Journal of Applied Physics* **95**(12), 7990-7997 (2004).
- [83] Siddiki, A., & Gerhardts, R. R., Thomas-Fermi-Poisson theory of screening for laterally confined and unconfined two-dimensional electron systems in strong magnetic fields. *Physical Review B* **68**(12), 125315 (2003).
- [84] Davis, D., Thomas-Fermi screening in one dimension. *Physical Review B* **7**(1), 129 (1973).
- [85] Reyes, J. A., & del Castillo-Mussot, M., Screened Coulomb potential for a quantum wire in the Thomas-Fermi approximation. *Physical Review B* **57**(16), 9869 (1998).
- [86] Stoddart, J. C., March, N. H., & Stott, M. J., Electronic structure of point defects and impurities in metals. *Physical Review* **186**(3), 683 (1969).
- [87] Almeida, A. J., *et al.*, Charge trapping defects in CdSe nanocrystal quantum dots. *The Journal of Physical Chemistry C* **120**(25), 13763-13770 (2016).

[88] Rabeya, R., et al., Structural defects in graphene quantum dots: A review. *International Journal of Quantum Chemistry* **122**(12), e26900 (2022).

- [89] Li, X., *et al.*, Effect of single point defect on local properties in BiFeO3 thin film. *Acta Materialia* **170**, 132-137 (2019).
- [90] Yang, W., et al., Point defects in two-dimensional RuCl₃. Physical Review Materials **7**(6), 064004 (2023).
- [91] Zhang, L., *et al.*, Probing interlayer shear thermal deformation in atomically-thin van der Waals layered materials. *Nature Communications* **13**(1), 3996 (2022).
- [92] Wang, F., *et al.*, Difference analysis model for the mismatch effect and substrate-induced lattice deformation in atomically thin materials. *Physical Review B* **98**(24), 245403 (2018).
- [93] Jung, S. W., Fujisawa, T., Hirayama, Y., & Jeong, Y. H., "Background charge fluctuation in a GaAs quantum dot device," *Applied Physics Letters* **85**(5), 768-770 (2004).
- [94] Connors, E. J., *et al.*, Low-frequency charge noise in Si/SiGe quantum dots. *Physical Review B* **100**(16), 165305 (2019).
- [95] Sohn, L. L., Kouwenhoven, L. P., & Schön, G. (Eds.), Mesoscopic electron transport, Chapter: ELECTRON TRANSPORT IN QUANTUM DOTS (2013).
- [96] Fulton, T. A., & Dolan, G. J., Observation of single-electron charging effects in small tunnel junctions. *Physical Review Letters* **59**(1), 109 (1987).
- [97] Ashoori, R. C., *et al.*, Single-electron capacitance spectroscopy of discrete quantum levels. *Physical Review Letters* **68**(20), 3088 (1992).
- [98] Weis, J., Haug, R. J., Klitzing, K. V., & Ploog, K., Competing channels in single-electron tunneling through a quantum dot. *Physical Review Letters* **71**(24), 4019 (1993).
- [99] Weis, J., Haug, R. J., Von Klitzing, K., & Ploog, K., Transport spectroscopy on a single quantum dot. Semiconductor Science and Technology **9**(11S), 1890 (1994).
- [100] Brodsky, M., *et al.*, Localization in artificial disorder: two coupled quantum dots. *Physical Review Letters* **85**(11), 2356 (2000).
- [101] Van der Wiel, W. G., et al., Electron transport through double quantum dots. Reviews of Modern Physics 75(1), 1 (2002).
- [102] Elzerman, J. M., *et al.*, Few-electron quantum dot circuit with integrated charge read out. *Physical Review B* **67**(16), 161308 (2003).
- [103] Zajac, D. M., *et al.*, Scalable gate architecture for a one-dimensional array of semiconductor spin qubits. *Physical Review Applied* **6**(5), 054013 (2016).

[104] Borsoi, F., *et al.*, Shared control of a 16 semiconductor quantum dot crossbar array. *Nature Nanotechnology* **19**(1), 21-27 (2024).

- [105] Fuhrer, A., et al., Energy spectra of quantum rings. Nature **413**(6858), 822-825 (2001).
- [106] Zhang, X., et al., Black phosphorus quantum dots. Angewandte Chemie International Edition **54**(12), 3653-3657 (2015).
- [107] Niu, X., Li, Y., Shu, H., & Wang, J., Anomalous size dependence of optical properties in black phosphorus quantum dots. *The Journal of Physical Chemistry Letters* **7**(3), 370-375 (2016).
- [108] Han, S. T., *et al.*, Black phosphorus quantum dots with tunable memory properties and multilevel resistive switching characteristics. *Advanced Science* **4**(8) (2017).
- [109] Sun, Z., *et al.*, Ultrasmall black phosphorus quantum dots: synthesis and use as photothermal agents. *Angewandte Chemie International Edition* **54**(39), 11526-11530 (2015).
- [110] Ge, S., Zhang, L., Wang, P., & Fang, Y., Intense, stable and excitation wavelength-independent photoluminescence emission in the blue-violet region from phosphorene quantum dots. *Scientific Reports* **6**(1), 27307 (2016).
- [111] Shutt, R. R., et al., Synthesis of Black Phosphorene Quantum Dots from Red Phosphorus. Chemistry—A European Journal 29(55), e202301232 (2023).
- [112] Valappil, M. O., Alwarappan, S., & Pillai, V. K., Phosphorene quantum dots: Synthesis, properties and catalytic applications. *Nanoscale* **14**(4), 1037-1053 (2022).
- [113] Riel, B. J., An introduction to self-assembled quantum dots. *American Journal of Physics* **76**(8), 750-757 (2008).
- [114] Dhanabalan, S. C., *et al.*, Emerging trends in phosphorene fabrication towards next generation devices. *Advanced Science* **4**(6), 1600305 (2017).
- [115] Kouwenhoven, L. P., Austing, D. G., & Tarucha, S., Few-electron quantum dots. *Reports on Progress in Physics* **64**(6), 701 (2001).
- [116] Allen, M. T., Martin, J., & Yacoby, A., Gate-defined quantum confinement in suspended bilayer graphene. *Nature Communications* **3**(1), 934 (2012).
- [117] Vandersypen, L. M. K., *et al.*, Real-time detection of single-electron tunneling using a quantum point contact. *Applied Physics Letters* **85**(19), 4394-4396 (2004).
- [118] Kouwenhoven, L. P., *et al.*, Excitation spectra of circular, few-electron quantum dots. *Science* **278**(5344), 1788-1792 (1997).
- [119] Cronenwett, S. M., Oosterkamp, T. H., & Kouwenhoven, L. P., A tunable Kondo effect in quantum dots. *Science* **281**(5376), 540-544 (1998).

[120] Sasaki, S., et al., Kondo effect in an integer-spin quantum dot. Nature 405(6788), 764-767 (2000).

- [121] Hanson, R., Kouwenhoven, L. P., Petta, J. R., Tarucha, S., & Vandersypen, L. M., Spins in fewelectron quantum dots. *Reviews of Modern Physics* **79**(4), 1217-1265 (2007).
- [122] Culcer, D., Hu, X., & Das Sarma, S., Interface roughness, valley-orbit coupling, and valley manipulation in quantum dots. *Physical Review B—Condensed Matter and Materials Physics* **82**(20), 205315 (2010).
- [123] Lim, W. H., Yang, C. H., Zwanenburg, F. A., & Dzurak, A. S., Spin filling of valley–orbit states in a silicon quantum dot. *Nanotechnology* **22**(33), 335704 (2011).
- [124] Yang, C. H., *et al.*, Spin-valley lifetimes in a silicon quantum dot with tunable valley splitting. *Nature Communications* **4**(1), 2069 (2013).
- [125] Borselli, M. G., *et al.*, Measurement of valley splitting in high-symmetry Si/SiGe quantum dots. *Applied Physics Letters* **98**(12) (2011).
- [126] Yang, C. H., Lim, W. H., Lai, N. S., Rossi, A., Morello, A., & Dzurak, A. S., Orbital and valley state spectra of a few-electron silicon quantum dot. *Physical Review B* **86**(11), 115319 (2012).
- [127] Yoneda, J., et al., A quantum-dot spin qubit with coherence limited by charge noise and fidelity higher than 99.9%. *Nature Nanotechnology* **13**(42), 102-106 (2018).
- [128] Kawakami, E., *et al.*, Gate fidelity and coherence of an electron spin in an Si/SiGe quantum dot with micromagnet. *Proceedings of the National Academy of Sciences* **113**(42), 11738-11743 (2016).
- [129] Yacoby, A., Heiblum, M., Mahalu, D., & Shtrikman, H., Coherence and phase sensitive measurements in a quantum dot. *Physical Review Letters* **74**(20), 4047 (1995).
- [130] Zajac, D. M., Hazard, T. M., Mi, X., Wang, K., & Petta, J. R., A reconfigurable gate architecture for Si/SiGe quantum dots. *Applied Physics Letters* **106**(22) (2015).
- [131] Wang, L. J., *et al.*, A graphene quantum dot with a single electron transistor as an integrated charge sensor. *Applied Physics Letters* **97**(26) (2010).
- [132] Marcus, C. M., *et al.*, Quantum chaos in open versus closed quantum dots: Signatures of interacting particles. *Chaos, Solitons & Fractals* **8**(7-8), 1261-1279 (1997).
- [133] Ponomarenko, L. A., et al., Chaotic Dirac billiard in graphene quantum dots. Science **320**(5874), 356-358 (2008).
- [134] Ferry, D. K., et al., Quantum transport in single and multiple quantum dots. *Japanese Journal of Applied Physics* **36**(6S), 3944 (1997).
- [135] Möller, S., Buhmann, H., Godijn, S. F., & Molenkamp, L. W., Charging energy of a chaotic quantum dot. *Physical Review Letters* **81**(23), 5197 (1998).

[136] Corrigan, J., et al., Coherent control and spectroscopy of a semiconductor quantum dot Wigner molecule. *Physical Review Letters* **127**(12), 127701 (2021).

- [137] Kinaret, J. M., Meir, Y., Wingreen, N. S., Lee, P., & Wen, X. G., Conductance through a quantum dot in the fractional quantum Hall regime. *Physical Review B* **45**(16), 9489 (1992).
- [138] Beenakker, C. W. J., & Rejaei, B., Single-electron tunneling in the fractional quantum Hall effect regime. *Physica B: Condensed Matter* **189**(1-4), 147-156 (1993).
- [139] Kinaret, J. M., A quantum dot in the fractional quantum Hall regime. *Physica B: Condensed Matter* **189**(1-4), 142-146 (1993).
- [140] Geller, M. R., & Loss, D., Coulomb blockade in the fractional quantum Hall effect regime. *Physical Review B* **62**(24), R16298 (2000).
- [141] Balram, A. C., & Jain, J. K., Exact results for model wave functions of anisotropic composite fermions in the fractional quantum Hall effect. *Physical Review B* **93**(7), 075121 (2016).
- [142] Mueed, M. A., *et al.*, Anisotropic composite fermions and fractional quantum Hall effect. *Physical Review B* **93**(19), 195436 (2016).
- [143] Hossain, M. S., *et al.*, Anisotropic two-dimensional disordered Wigner solid. *Physical Review Letters* **129**(3), 036601 (2022).
- [144] Slater, J. C., Exchange in spin-polarized energy bands. *Physical Review* **165**(2), 658 (1968).
- [145] Mattis, D. C., The theory of magnetism I: Statics and Dynamics (Vol. 17). Springer Science & Business Media (2012).
- [146] Tokura, Y., & Seki, S., Multiferroics with spiral spin orders. *Advanced Materials* **22**(14), 1554-1565 (2010).
- [147] Fert, A., Reyren, N., & Cros, V., Magnetic skyrmions: advances in physics and potential applications. *Nature Reviews Materials* **2**(7), 1-15 (2017).
- [148] Hurd, C. M., Varieties of magnetic order in solids. Contemporary Physics 23(5), 469-493 (1982).
- [149] Kaplan, T. A., & Menyuk, N., Spin ordering in three-dimensional crystals with strong competing exchange interactions. *Philosophical Magazine* **87**(25), 3711-3785 (2007).
- [150] Kittel, C., & McEuen, P., Introduction to solid state physics. John Wiley & Sons, Pg.147 (2018).
- [151] Amusia, M. Y., Popov, K. G., Shaginyan, V. R., & Stephanovich, V. A., Theory of heavy-fermion compounds. *Springer series in solid-state sciences*, **182** 33 (2014).
- [152] Ekahana, S. A., *et al.*, Anomalous electrons in a metallic kagome ferromagnet. *Nature* **627**(8002), 67-72 (2024).

[153] Mishra, S., *et al.*, Observation of fractional edge excitations in nanographene spin chains. *Nature* **598**(7880), 287-292 (2021).

- [154] Milloch, A., Fabrizio, M., & Giannetti, C., Mott materials: unsuccessful metals with a bright future. *npj Spintronics* **2**(1), 49 (2024).
- [155] Fazekas, P., Lecture notes on electron correlation and magnetism (Vol. 5). World scientific, Chapter 4 & 5 (1999).
- [156] Wigner, E., On the interaction of electrons in metals. *Physical Review* **46**(11), 1002 (1934).
- [157] Fukuyama, H., Two dimensional wigner crystallization caused by magnetic field. *Solid State Communications* **19**(6), 551-554 (1976).
- [158] Ziani, N. T., Cavaliere, F., Becerra, K. G., & Sassetti, M., A short review of one-dimensional Wigner crystallization. *Crystals* **11**(1), 20 (2020).
- [159] Piot, B. A., *et al.*, Wigner crystallization in a quasi-three-dimensional electronic system. *Nature Physics* **4**(12), 936-939 (2008).
- [160] Tanatar, B., & Ceperley, D. M., Ground state of the two-dimensional electron gas. *Physical Review B* **39**(8), 5005 (1989).
- [161] Drummond, N. D., & Needs, R. J., Phase diagram of the low-density two-dimensional homogeneous electron gas. *Physical Review Letters* **102**(12), 126402 (2009).
- [162] Tsui, Y. C., *et al.*, Direct observation of a magnetic-field-induced Wigner crystal. *Nature* **628**(8007), 287-292 (2024).
- [163] Ellenberger, C., *et al.*, Excitation Spectrum of Two Correlated Electrons in a Lateral Quantum Dot with Negligible Zeeman Splitting. *Physical Review Letters* **96**(12), 126806 (2006).
- [164] Yannouleas, C., & Landman, U., Symmetry breaking and quantum correlations in finite systems: studies of quantum dots and ultracold Bose gases and related nuclear and chemical methods. *Reports on Progress in Physics* **70**(12), 2067 (2007).
- [165] Mendez-Camacho, R., & Cruz-Hernandez, E., Asymmetric Wigner molecules in nanowire Y-junctions. *Scientific Reports* **12**(1), 20183 (2022).
- [166] Li, H., *et al.*, Wigner molecular crystals from multielectron moiré artificial atoms. *Science* **385**(6704), 86-91 (2024).
- [167] Klitzing, K. V., Dorda, G., & Pepper, M., New method for high-accuracy determination of the fine-structure constant based on quantized Hall resistance. *Physical Review Letters* **45**(6), 494 (1980).
- [168] Laughlin, R. B., Quantized motion of three two-dimensional electrons in a strong magnetic field. *Physical Review B* **27**(6), 3383 (1983).

[169] Laughlin, R. B., Anomalous quantum Hall effect: an incompressible quantum fluid with fractionally charged excitations. *Physical Review Letters* **50**(18), 1395 (1983).

- [170] Tsui, D. C., Stormer, H. L., & Gossard, A. C., Two-dimensional magnetotransport in the extreme quantum limit. *Physical Review Letters* **48**(22), 1559 (1982).
- [171] Pan, W., et al., Fractional quantum Hall effect of composite fermions. *Physical Review Letters* **90**(1), 016801 (2003).
- [172] Jain, J. K., Composite-fermion approach for the fractional quantum Hall effect. *Physical Review Letters* **63**(2), 199 (1989).
- [173] Jain, J. K., Composite fermions. Cambridge University Press (2007).
- [174] Tavernier, M. B., Anisimovas, E., & Peeters, F. M., Correlation between electrons and vortices in quantum dots. *Physical Review B* **70**(15), 155321 (2004).
- [175] Saarikoski, H., Harju, A., Puska, M. J., & Nieminen, R. M., Vortex clusters in quantum dots. *Physical Review Letters* **93**(11), 116802 (2004).
- [176] Aharonov, Y., & Bohm, D., Significance of electromagnetic potentials in the quantum theory. *Physical Review* **115**(3), 485 (1959).
- [177] Webb, R. A., Washburn, S., Umbach, C. P., & Laibowitz, R. B., Observation of h e aharonov-bohm oscillations in normal-metal rings. *Physical Review Letters* **54**(25), 2696 (1985).
- [178] Ford, C. J. B., *et al.*, The Aharonov-Bohm effect in electrostatically defined heterojunction rings. *Journal of Physics C: Solid State Physics* **21**(10), L325 (1988).
- [179] Grbić, B., Leturcq, R., Ihn, T., Ensslin, K., Reuter, D., & Wieck, A. D., Aharonov–Bohm oscillations in p-type GaAs quantum rings. *Physica E: Low-dimensional Systems and Nanostructures* **40**(5), 1273–1275 (2008).
- [180] Keyser, U. F., Borck, S., Haug, R. J., Bichler, M., Abstreiter, G., & Wegscheider, W., Aharonov–Bohm oscillations of a tuneable quantum ring. *Semiconductor Science and Technology* **17**(5), L22 (2002).
- [181] Cheung, H. F., Gefen, Y., Riedel, E. K., & Shih, W. H., Persistent currents in small one-dimensional metal rings. *Physical Review B* **37**(11), 6050 (1988).
- [182] Ambegaokar, V., & Eckern, U., Coherence and persistent currents in mesoscopic rings. *Physical Review Letters* **65**(3), 381 (1990).
- [183] Cheung, H. F., Riedel, E. K., & Gefen, Y., Persistent currents in mesoscopic rings and cylinders. *Physical Review Letters* **62**(5), 587 (1989).
- [184] Aronov, A. G., & Lyanda-Geller, Y. B., Spin-orbit Berry phase in conducting rings. *Physical Review Letters* **70**(3), 343 (1993).

[185] Bogachek, E. N., Krive, I. V., Kulik, I. O., & Rozhavsky, A. S., The Aharonov-Casher and Berry'S Phase Effects in Solids. *Modern Physics Letters B* **5**(23), 1607-1611 (1991).

- [186] Leykam, D., & Yuan, L., Topological phases in ring resonators: recent progress and future prospects. *Nanophotonics* **9**(15), 4473-4487 (2020).
- [187] Orlando, T. P., et al., Superconducting persistent-current qubit. Physical Review B **60**(22), 15398 (1999).
- [188] Weinstock, H. (Ed.), SQUID sensors: fundamentals, fabrication and applications (2012).
- [189] Hung, T. Q., Terki, F., Kamara, S., Kim, K., Charar, S., & Kim, C., Planar Hall ring sensor for ultralow magnetic moment sensing. *Journal of Applied Physics* **117**(15) (2015).
- [190] Chang, D. I., *et al.*, Quantum mechanical complementarity probed in a closed-loop Aharonov–Bohm interferometer. *Nature Physics* **4**(3), 205-209 (2008).
- [191] Kobayashi, K., Aikawa, H., Katsumoto, S., & Iye, Y., Tuning of the Fano effect through a quantum dot in an Aharonov-Bohm interferometer. *Physical Review Letters* **88**(25), 256806 (2002).
- [192] Vladimir M. Fomin, Physics of Quantum Rings. Springer Science & Business Media. Chapter 2,7,8 (2013).
- [193] Hartmann, N. F., *et al.*, Uniaxial transition dipole moments in semiconductor quantum rings caused by broken rotational symmetry. *Nature Communications* **10**(1), 3253 (2019).
- [194] Li, X. L., & Yang, G. W., Growth mechanisms of quantum ring self-assembly upon droplet epitaxy. *The Journal of Physical Chemistry C* **112**(20), 7693-7697 (2008).
- [195] Lee, J. H., Wang, Z. M., Sablon, K., & Salamo, G. J., Formation of hybrid molecules composed of Ga metal particle in direct contact with InGaAs semiconductor quantum ring. *Crystal Growth & Design* **8**(2), 690-694 (2008).
- [196] Heinzel, T., *et al.*, Electronic properties of nanostructures defined in Ga [Al] As heterostructures by local oxidation. *Physica E: Low-dimensional Systems and Nanostructures* **9**(1), 84-93 (2001).
- [197] Fuhrer, A., Brusheim, P., Ihn, T., Sigrist, M., Ensslin, K., Wegscheider, W., & Bichler, M., Fano effect in a quantum-ring–quantum-dot system with tunable coupling. *Physical Review B—Condensed Matter and Materials Physics* **73**(20), 205326 (2006).
- [198] Corfdir, P., *et al.*, Excitonic Aharonov–Bohm oscillations in core–shell nanowires. *Advanced Materials* **31**(3), 1805645 (2019).
- [199] Banszerus, L. et al. Nano Letters 20(3), 2005-2011 (2020).
- [200] Johnson, A. C., Petta, J. R., Marcus, C. M., Hanson, M. P., and Gossard, A. C. *Physical Review B* **72**(16), 165308 (2005).

[201] Nagaoka, Y. Ferromagnetism in a narrow, almost half-filled s band. *Physical Review*, **147**(1), 392 (1966).

- [202] Tasaki, H. From Nagaoka's ferromagnetism to flat-band ferromagnetism and beyond: An introduction to ferromagnetism in the Hubbard model. *Progress of Theoretical Physics*, **99**(4), 489-548 (1998).
- [203] Hubbard, J. Electron correlations in narrow energy bands. *Proceedings of the Royal Society of London. Series A. Mathematical and Physical Sciences*, **276**(1365), 238-257 (1963).
- [204] Hubbard, J. Electron correlations in narrow energy bands. II. The degenerate band case. *Proceedings of the Royal Society of London. Series A. Mathematical and Physical Sciences*, **277**(1369), 237-259 (1964).
- [205] Hubbard, J. Electron correlations in narrow energy bands III. An improved solution. *Proceedings of the Royal Society of London. Series A. Mathematical and Physical Sciences*, **281**(1386), 401-419 (1964).
- [206] Buluta, I. & Nori, F. Quantum simulators. Science, **326**(5949), 108-111 (2009).
- [207] Georgescu, I. M., Ashhab, S., & Nori, F. Quantum simulation. *Reviews of Modern Physics*, **86**(1), 153-185 (2014).
- [208] Bloch, I., Dalibard, J., & Nascimbene, S. Quantum simulations with ultracold quantum gases. *Nature Physics*, **8**(4), 267-276 (2012).
- [209] Gross, C. & Bloch, I. Quantum simulations with ultracold atoms in optical lattices. *Science*, **357**(6355), 995-1001 (2017).
- [210] Hensgens, T. *et al.* Quantum simulation of a Fermi–Hubbard model using a semiconductor quantum dot array. *Nature*, **548**(7665), 70-73 (2017).
- [211] Wang, X. *et al.* Experimental realization of an extended Fermi-Hubbard model using a 2D lattice of dopant-based quantum dots. *Nature Communications*, **13**(1), 6824 (2022).
- [212] Dehollain, J. P. *et al.* Nagaoka ferromagnetism observed in a quantum dot plaquette. *Nature*, **579**(7800), 528-533 (2020).
- [213] Manchon, A., Koo, H. C., Nitta, J., Frolov, S. M., & Duine, R. A. New perspectives for Rashba spin-orbit coupling. *Nature Materials*, **14**(9), 871-882 (2015).
- [214] Koppens, F. H. L., Nowack, K. C., & Vandersypen, L. M. K. Spin echo of a single electron spin in a quantum dot. *Physical Review Letters*, **100**(23), 236802 (2008).
- [215] Nadj-Perge, S., Frolov, S. M., Bakkers, E. P. A. M., & Kouwenhoven, L. P. Spin-orbit qubit in a semiconductor nanowire. *Nature*, **468**(7327), 1084-1087 (2010).
- [216] Van den Berg, J. W. G. *et al.* Fast spin-orbit qubit in an indium antimonide nanowire. *Physical Review Letters*, **110**(6), 066806 (2013).

[217] Yoneda, J. *et al.* Fast electrical control of single electron spins in quantum dots with vanishing influence from nuclear spins. *Physical Review Letters*, **113**(26), 267601 (2014).

- [218] Liu, B., Wu, L. J., Zhao, Y. Q., Wang, L. Z., & Caii, M. Q. Tuning the Schottky contacts in the phosphorene and graphene heterostructure by applying strain. *Physical Chemistry Chemical Physics*, **18**(29), 19918-19925 (2016).
- [219] Shi, Z. *et al.* Coherent quantum oscillations and echo measurements of a Si charge qubit. *Physical Review B*, **88**(7), 075416 (2013).
- [220] Nowack, K. C., Koppens, F. H. L., Nazarov, Y. V., & Vandersypen, L. M. K. Coherent control of a single electron spin with electric fields. *Science*, **318**(5855), 1430-1433 (2007).
- [221] Hu, R. Z. et al. Flopping-mode spin qubit in a Si-MOS quantum dot. Applied Physics Letters, **122**(13) (2023).
- [222] Khomitsky, D. V., Bastrakova, M. V., Munyaev, V. O., Zaprudnov, N. A., & Studenikin, S. A. Controllable single-spin evolution at subharmonics of electric dipole spin resonance enhanced by four-level Landau-Zener-Stückelberg-Majorana interference. *Physical Review B*, **108**(20), 205404 (2023).
- [223] Stano, P., & Loss, D. Review of performance metrics of spin qubits in gated semiconducting nanostructures. *Nature Reviews Physics*, **4**(10), 672-688 (2022).
- [224] Kloeffel, C., & Loss, D. Prospects for spin-based quantum computing in quantum dots. *Annual Review of Condensed Matter Physics*, **4**(1), 51-81 (2013).
- [225] Burkard, G., Ladd, T. D., Pan, A., Nichol, J. M., & Petta, J. R. Semiconductor spin qubits. *Reviews of Modern Physics*, **95**(2), 025003 (2023).
- [226] Rudenko, A. N., & Katsnelson, M. I. *et al.* Quasiparticle band structure and tight-binding model for single-and bilayer black phosphorus. *Physical Review B*, **89**(20), 201408 (2014).
- [227] Governale, M., & Ungarelli, C. Gauge-invariant grid discretization of the Schrödinger equation. *Physical Review B*, **58**(12), 7816 (1998).
- [228] Pfannkuche, D., Gudmundsson, V., & Maksym, P. A. Comparison of a Hartree, a Hartree-Fock, and an exact treatment of quantum-dot helium. *Physical Review B*, **47**(4), 2244 (1993).
- [229] Reusch, B., & Grabert, H. Unrestricted Hartree-Fock for quantum dots. *Physical Review B*, **68**(4), 045309 (2003).
- [230] Jiang, H., Baranger, H. U., & Yang, W. Density-functional theory simulation of large quantum dots. *Physical Review B*, **68**(16), 165337 (2003).
- [231] Schenk, S., Schwab, P., Dzierzawa, M., & Eckern, U. Density functional theory for a model quantum dot: Beyond the local-density approximation. *Physical Review B—Condensed Matter and Materials Physics*, **83**(11), 115128 (2011).

[232] Hirose, K., & Wingreen, N. S. Spin-density-functional theory of circular and elliptical quantum dots. *Physical Review B*, **59**(7), 4604 (1999).

- [233] Bolton, F. Fixed-phase quantum Monte Carlo method applied to interacting electrons in a quantum dot. *Physical Review B*, **54**(7), 4780 (1996).
- [234] Ambrosetti, A., Pederiva, F., & Lipparini, E. Quantum Monte Carlo study of circular quantum dots in presence of Rashba interaction. *Physical Review B—Condensed Matter and Materials Physics*, **83**(15), 155301 (2011).
- [235] Olsen, V. K. B. Full configuration interaction simulation of quantum dots. Master's thesis, University of Oslo (2012).
- [236] Szabo, A., & Ostlund, N. S. Modern quantum chemistry: introduction to advanced electronic structure theory. Courier Corporation. Section 2.3 (1996).
- [237] Carmona-Tellez, S. *et al.* Electrical, optical, and structural characteristics of Al₂O₃ thin films prepared by pulsed ultrasonic sprayed pyrolysis. *Journal of applied physics*, **103**(3) (2008).
- [238] Lanczos, C. An iteration method for the solution of the eigenvalue problem of linear differential and integral operators (1950).
- [239] Arnoldi, W. E. The principle of minimized iterations in the solution of the matrix eigenvalue problem. *Quarterly of applied mathematics*, **9**(1), 17-29 (1951).